Diagnosis with near infrared spectroscopy during minimally invasive procedures

Rami Nachabé

Diagnosis with Near Infrared Spectroscopy during Minimally Invasive procedures

Diagnose met nabij infrarood spectroscopie tijdens minimale invasieve ingrepen

Thesis

to obtain the degree of Doctor from the
Erasmus University Rotterdam
by command of the
rector magnificus

Prof.dr. H.G. Schmidt

and in accordance with the decision of the Doctorate Board
The public defense shall be held on
Tuesday 29 May 2012 at 15.30 hrs

by

Rami Nachabé

born in Lebanon

ERASMUS UNIVERSITEIT ROTTERDAM

Dit proefschrift is goedgekeurd door:

Promotor	Prof.dr.ir. H.J.C.M. Sterenborg
Co-promotor	Dr. B.H.W. Hendriks
Overige leden	Prof.dr.ir. G.C. van Rhoon
	Prof.dr. A.G.J.M. van Leeuwen
	Dr.ir. G.J. Puppels

Contents

Introduction

In current medical practice, there is a clear trend towards minimally invasive procedures in surgery and radiology. Medical imaging is very often used for diagnosis but also in percutaneous image guidance. One of the challenges that physicians still encounter is to accurately guide interventional tools such as needles to the region of interest for an effective treatment. Most percutaneous image-guided procedures such as tissue biopsy are performed under ultrasound, CT, MR, or X-ray. Ultrasound is widely used for guidance however it requires a lot of experience for proper and accurate needle guidance to the region of interest. X-ray is another real-time imaging that has the drawback of lacking soft tissue contrast information. CT and MR enable soft tissue visualization; however they require to be combined with ultrasound or X-ray for real-time guidance and visualization of the distal end of the tip of the interventional tools. Thus, there is a clear need to have sensing capabilities at the tip of the interventional tools to confirm its position in the region of interest for an effective treatment. To this aim, several biomedical research groups investigated optical sensing at the tip of interventional probes to provide feedback on the tissue type during a procedure and subsequently confirm the position of the tip in the region of interest.

Diffuse reflectance spectroscopy is an optical technique that enables tissue characterization by measuring the spectral response of tissue-light interaction. Broadband light is emitted via an optical fiber and is collected with another optical fiber after light absorption and scattering in the tissue. The collected light is acquired with a spectrometer that can resolves light in the visible and near infrared wavelength range below a micron. The use of light is clinically appealing as it can detect physiological and biological changes whereas medical imaging only provides morphological information. Relevant biological parameters, namely blood oxygenation and content in the probed volume, could be extracted from the tissue spectral response to light illumination. These blood-derived parameters have shown to be of great relevance to distinguish between normal and dysplastic tissues. However, no existing studies investigated the potential of diffuse reflectance spectroscopy in the infrared beyond 1000 nm due to the limitation of silicon detectors to sense light at wavelengths above a micron.

This thesis focuses on investigating diffuse reflectance spectra acquired at the distal end of a custom-made needle in a wavelength range extended to 1800 nm as opposed to the commonly used wavelength range presented in existing studies in literature. Because of the limited sensitivity of silicon detectors to measure beyond 1000 nm, an InGaAs detector was added to a silicon detector to measure spectra between 500 and 1800 nm. The hypothesis is that additional biological chromophores, besides the blood-derived chromophores, have an optical signature in the infrared wavelength range which can be used for advanced tissue characterization. Different evaluation techniques have been used to validate a mathematical model that derives the physiological and biological tissue composition from the spectra. The impact of the wavelength range extension on the clinical diagnosis has been assessed for different medical applications in

the field of oncology. For each investigated organ such as breast, lung, and liver; a combination of parameters set enables discrimination of the abnormal tissue from healthy tissue. Multivariate data analysis methods and other statistical tools used throughout this thesis assessed the clinical performance of diffuse reflectance spectroscopy between 500 and 1800 nm for tissue diagnosis and confirmation of the location of the needle tip for tissue biopsy or treatment.

The ultimate goal of this thesis is to highlight the potential of diffuse reflectance spectroscopy in the demarcation of malignant and benign tissues from normal tissue based on the parameters that are derived from the spectral signals over a wide wavelength range in an image-guided clinical setting.

Chapter 1

Modeling diffuse reflectance spectroscopy: a review

Rami Nachabé

Benno H. W. Hendriks

Henricus J. C. M. Sterenborg

Abstract

Over the last decade, several groups working on biomedical optics have developed setups to perform diffuse reflectance spectroscopy measurements acquired with fiber optic probes for clinical diagnosis. Several clinical studies were conducted to discriminate healthy from dysplastic tissue using different classification methods. Two different approaches have been used: a purely statistical approach where the unprocessed spectra are directly related to the clinical diagnosis, and a method that first analyses the spectra making use of the knowledge of tissue optics and then relate the outcome to the clinical diagnosis. The aim of this review is to present an overview of various models for analyzing reflectance spectra that are employed by different groups as well as the type of clinical studies conducted by these groups.

1. **Introduction**

Optical spectroscopy is a field that has been growing over the last two decades with a strong emphasis on evaluating the diagnostic performance given a clinical application.

There are three methods used by the biomedical photonics community to describe the reflectance in order to extract the optical properties from which physical and physiological parameters can be deduced: time domain [1-4], frequency domain [2, 4-6] and steady-state domain [7-9]. In the case of time-resolved measurements, what is actually measured is not a spectrum but the temporal changes of a near infrared (NIR) femto- or pico- second pulsed laser source measured with a near infrared photo multiplier tube (NIR-PMT) in a single or narrow band wavelength. From the measured time response of the tissue, one could assess the peak time value in combination with the integral of the measured signal that enables the determination of the absorption and reduced scattering coefficients [7]. By using multiple lasers at different wavelengths, the optical properties over a wide wavelength range can be estimated. Similarly, in the frequency-resolved domain, modulated light is detected after its interaction with the tissue and it is subsequently phase-shifted and amplitude demodulated. From both the phase shift and the modulation of the detected signal for different frequencies, one can determine the absorption and scattering coefficients from the real and imaginary part of the wave number [10]. In the steady-state domain, a broadband white light source is most commonly used to illuminate the tissue by making use of optical fibers and the reflected light is collected with another or the same fiber after being subject to scattering and absorption. From this measured diffuse reflectance spectra the absorption and scattering coefficients can be deduced [9].

Various approaches were developed by different research groups to translate the acquired spectral data into clinically relevant parameters. There are three main approaches that can be distinguished in literature. The first approach is to directly correlate the raw measured spectra with the classical diagnosis. This method does not require any data processing and uses spectral analysis techniques such as principal component analysis, neural networks, and partially least squares discriminant analysis. The second approach consists of first translating the spectral data into physical properties such as the absorption and reduced scattering coefficients for different wavelengths on which the statistical analysis are performed and then investigate the correlation with the classical diagnosis. This method requires prior knowledge of light-tissue interaction. The third approach translates these optical properties into biologically relevant parameters. This uses additional prior knowledge on the optical properties of various biological substances that absorb and scatter light. These last methods require mathematical models that describe the measured diffuse reflectance spectra in terms of input parameters.

The third approach, having received the most attention, will be discussed in more detail here. An overview of the recent developments in this model based approach will be presented. A plethora of efforts in investigating the validity of these models was performed in order to validate the reliability of the parameterization of the measured optical spectra. Thorough validations and assessments of the models are generally done by evaluating their outcome when applied to measurements with actual *a priori* known

optical properties of phantoms [11]. A list of all the existing biological chromophores that have been used so far in literature is given. Finally, an overview of the clinical applications that were investigated with diffuse reflectance spectroscopy such as treatment monitoring, complication prediction, needle guidance, tumor margin assessment and optical biopsy.

The aim of this review is to present the wide panoply of ways of analyzing diffuse reflectance spectroscopy measurements aiming at extracting the relevant clinical parameters.

2. Modeling of optical spectra

Definition

Diffuse reflectance spectroscopy corresponds to the study of light absorption and scattering as a function of wavelength. Depending on the nature of the material that is being illuminated, light could either travel through the media along the direction of illumination or be diffused due to the turbidity of the media.

In the biomedical field, additionally to absorption, light interaction with tissue is influenced by the biological substructures that scatter light such as mitochondria, connective tissue, nuclei, etc.

Analytical models to translate spectral measurements into optical properties

Several groups use a derivation of the diffusion theory to describe the measured spectra with a well-defined analytical model. From the Boltzmann transport equation, the light propagation in turbid media can be described and is based on energy conservation by accounting for the amount of photons in a specific volume at a certain position per unit solid angle and time [12]. An analytical solution can be obtained by solving the Boltzmann transport equation under the diffusion approximation assumptions which are namely: (a) the fluence rate due to the highly forward scattering can be converted into fluence rate due to an isotropic scattering by expressing the scattering as reduced scattering using the similarity principle [1]. By doing such, the tissue anisotropy factor is taken into account with the scattering to obtain the reduced scattering

$$\mu_s' = \mu_s(1 - g) \,, \tag{1}$$

where μ_s and g are the tissue scattering and anisotropy, respectively. (b) In case of highly scattering media such as in tissue, the fluence rate φ satisifies the diffusion equation

$$\partial\varphi(r,t)/\partial t + c\mu_a\varphi(r,t) - cD\nabla^2\varphi(r) = -cS(r,t) \,, \tag{2}$$

with μ_a being the absorption coefficient of tissue, c the celerity of light in tissue, S being the source term truncated after the first order spherical harmonics corresponding to low anisotropy photon sources in the tissue, and D is the diffusion constant assumed to be constant for homogenous media and is expressed as

$$D = 1/[3(\mu_a + \mu_s')] \,. \tag{3}$$

This approximation holds as long as the tissue absorption is small compared to the reduced scattering while the inverse of the reduced scattering is larger than the source-detector separation ρ. (c) The third assumption is that the source terms in equation (2) consist of a distribution of single scattering sources along the axis normal to the boundary between the tissue and the source surface.

The diffusion equation can be solved analytically given specific boundary conditions that correspond to specific geometries. Throughout this review, the semi-infinite media geometry is described as it is the most commonly used in literature. The semi-infinite media geometry corresponds to the fact that the tissue medium is delimited by the non-scattering probe and the scattering tissue medium [9]. The boundary condition can mathematically be expressed as

$$\phi(z = 0, t) - 2AD\,\partial\phi/\partial z\,|_{z=0} = 0 \, , \tag{4}$$

meaning that the flux is null at the interface between the tissue and the probe [13] with $z = 0$ being the coordinate of the boundary along the normal to the interface. In Eq. (4), A is a parameter that depends on the refractive index of the tissue and the surrounding medium. From the fluence rate obtained by solving the diffusion equation (Eq.2) given the boundary condition in Eq. (4), the reflectance R from the medium is calculated as the current across the boundary via Fick's law i.e.

$$R(r, t) = D\,\partial\phi(r, t)/\partial z\,|_{z=0} \, . \tag{5}$$

In the case of the time-resolved domain, the reflectance of light R as a function of the absorption and reduced scattering coefficients as well as the radial distance ρ from the source at $z = 0$ as found by Farrell *et al.* [9]

$$R(\rho) = \frac{a\prime}{4\pi}\left[z_0\left(\mu_{eff} + \frac{1}{\tilde{r}_1}\right)\frac{e^{-\mu_{eff}\tilde{r}_1}}{\tilde{r}_1{}^2} + (z_0 + 2z_b)\left(\mu_{eff} + \frac{1}{\tilde{r}_2}\right)\frac{e^{-\mu_{eff}\tilde{r}_2}}{\tilde{r}_2{}^2}\right] \tag{6}$$

with $\mu_{eff} = [3\mu_a(\mu_s\prime + \mu_a)]^{1/2}$ being the effective attenuation coefficient, $a\prime = \mu_s\prime/(\mu_s\prime + \mu_a)$ being the albedo and $z_0 = (\mu_a + \mu_s\prime)^{-1}$ the location of the virtual scattering source. The extrapolated boundary condition is expressed as $z_b = 2AD$. Furthermore, $\tilde{r}_1 = (z_0^2 + \rho^2)^{1/2}$ is the distance between the single scattering source and the collecting fiber, and $\tilde{r}_2 = ((z_0 + 2z_b)^2 + \rho^2)^{1/2}$ is the distance between the image source and the collecting fiber.

Analytical models to transform optical properties into biological, biochemical and physiological parameters

Generally, a broadband white light source is used to illuminate the tissue and the reflected light is collected with a spectrometer. From a single reflectance measurement, it is not possible to extract both absorption and reduced scattering coefficients at a given

wavelength; therefore at least two different source-detector distance separations are required for that aim. On the other hand, by using *a priori* wavelength-dependent knowledge of the scattering and the absorption coefficient of the chromophores present in the measured tissue, it is possible to estimate the concentrations or volume fractions of the various biological substances from a single reflectance measurement. The absorption coefficient is generally expressed as the sum of the various chromophores absorption coefficients weighted by the corresponding concentration or volume fractions:

$$\mu_a(\lambda) = \sum_{i=1}^{N}[c_i] \cdot \mu_{a_i}(\lambda) \,, \tag{7}$$

with $[c_i]$ and $\mu_{a_i}(\lambda)$ are the concentration and the absorption coefficient of the i-th out of the total amount N of chromophores present in tissue. The absorption coefficients as a function of the wavelength of each chromophores are known from literature and are used as *a prori* knowledge to fit the measured absorption in order to estimate the concentrations $[c_i]$ of each of the various biological constituents. The reduced scattering can be expressed as a function of wavelength by considering a Mie and a Rayleigh scattering contribution [14]:

$$\mu_s'(\lambda) = a_{Mie}\lambda^{-b} + a_{Rayleigh}\lambda^{-4} \,, \tag{8}$$

with a_{Mie} and $a_{Rayleigh}$ corresponds to the Mie and Rayleigh reduced scattering amplitude, respectively. The b parameter corresponds to the Mie reduced scattering slope and correlates with the average particles size. When computing the reduced scattering with the Mie theory, it was observed that b decreases with the average diameter of the particles according to a Lorentzian cumulative function [15]. In a similar way as for the absorption coefficient, non wavelength-dependent parameters such as the reduced scattering amplitudes and slope are fitted from the estimated total reduced scattering μ_s'.

Regarding the steady-state domain, one could use a single reflectance measurement only and estimate the clinical related parameters without having to estimate the optical properties beforehand. Indeed, by implementing Eq. (7) and (8) in Eq. (6), the chromophores concentrations and reduced scattering amplitudes and slopes can be immediately determined because the wavelength-dependency is replaced by *a priori* knowledge of the absorption coefficient of the various chromophores and the reduced scattering was assumed to be a power law function. In this way, the fitting model locks onto the spectral features and shapes of the measured reflectance. In the case of time-resolved and frequency-resolved domain, only two equations are used to estimate the two optical parameters for each wavelength that is used for the light source. Subsequently, N parameters are derived by fitting the estimated absorption coefficient from the linear Eq. (7) and 3 parameters from Eq. (8) by applying a non-linear fit. In principle, min(N,3) number of wavelengths for light source is sufficient to estimate the various parameters of interest. However, in the case of the steady-state domain where only a single reflectance measurement is used to determine the parameters, there are N+3 parameters to fit from a highly non-linear equation such as Eq. (6).

Empirical models

In many cases, miniaturization of the optical probes requires a small source-detector optical fiber separation. As a result, the mathematical assumptions behind diffusion theory are no longer valid. Therefore empirical models were developed by several groups to extract the optical properties. In most cases, the mathematical empirical models are either developed by modeling the reflectance measurements of a wide range of phantoms with different known optical properties or by using Monte-Carlo based approach.

The group of Bigio has started diffuse reflectance spectroscopy measurements in the mid-90 [16] using elastic scattering spectroscopy approach and principal component analysis to evaluate the differences in the measured spectra. A decade later, they have modeled the reflectance measurement for a 250 μm fiber distance separation by using the following empirical expression for R:

$$R = (a_0\mu'_s + a_1)\exp(-\mu_a a_3/(\mu_a\mu'_s)^{a_4}) ,\qquad(9)$$

with $a_{i\in[\![1..4]\!]}$ being constant coefficients derived from reflectance Monte-Carlo simulations and experiments for different absorption and reduced scattering coefficients [17]. From this model, inserting Eq. (7) and (8) enables the extraction of the clinical relevant parameters.

Zonios *et al.* have slightly modified the expression derived from diffusion theory Eq. (6) making it suitable for short fiber distance separation [18-19]. From measurements in polystyrene bead suspensions with known optical properties, they empirically defined two parameters R_0 and r_c that are a scaling factor for the reflectance R and an effective radius replacing the actual fiber distance ρ, respectively. They have also developed an empirical model which seem to have similar performance than the modified diffusion theory approximation solution [20]

$$R = (k_1/\mu'_s + k_2\mu_a/\mu'_s)^{-1},\qquad(10)$$

with k_1 and k_2 being two parameters that are derived from a reflectance measurement of a phantom with known optical properties.

Another approach to estimate clinical relevant parameters is to make use of different path lengths in the steady-state domain as suggested by the group of Sterenborg in 2003 [21]. With this technique, the apparent path length is independent of the optical properties of the tissue but depends only on the fiber diameter as has been verified by Monte-Carlo simulations and experimental measurements on phantoms with known optical properties. Typically, for fiber diameters of 400 and 1000 microns, the apparent path length would be of 320 and 700 microns, respectively. Differential path length spectroscopy enables very shallow probing of the tissue. This has the advantage of assessing the optical properties of superficial tissue layers with a thickness below a millimeter and can be very useful to detect precancerous lesions with morphological and

physiological changes typically occurs in the mucosa. The reflectance model for the differential path length spectroscopy measurements is expressed as follows

$$R = C_1 \mu_s' \exp(-\tau \mu_a) \, , \tag{11}$$

with C_1 being a proportionality constant that depends on the distance between the fiber and the calibration standards (spectralon) and τ being the apparent path length that is proportional to the optical fiber diameter.

In 2008, the same group developed a similar model for single fiber measurements which is used for light delivery and collection. The reflectance is modeled by the mathematical expression in Eq. (11). Similarly to the differential path length configuration, the apparent path length is a function of the fiber diameter and depends on the optical properties of the probed tissue [22]. From Monte Carlo simulations and phantoms measurements with a wide range of optical properties, the apparent path is empirically found to be

$$\tau = \left[p_1 e^{-p_2 d_{fiber}}\right] / \left[(\mu_s' d_{fiber})^{p_3} (p_4 + (\mu_a d_{fiber})^{p_4})\right] \, , \tag{12}$$

with d_{fiber} being the optical fiber diameter and $[p_1, p_2, p_3, p_4] = [1.34 \pm 0.16, 0.17 \pm 0.08, 0.23 \pm 0.05, 0.52 \pm 0.16]$ four parameters derived from the Monte Carlo and phantoms study of known optical properties.

Probabilistic models

Analytical expressions derived from the diffusion equation work well for simple geometries such as for semi-infinite media. For more complicated geometries additional approximations are required to come to analytical expressions for the measured reflectance spectra that may impact the accuracy with which the optical properties can be derived from the model.

For complex geometries where the distance between the emitting and collecting fibers is small and for which the shape as well as the optical properties of the probe influence the reflectance measurements, an alternative to the analytical models is a probabilistic approach of solving the transport equation. This approach has the ability to cope with cases where the media is not highly scattering i.e. where the absorption coefficient greater than the reduced scattering coefficient. The most commonly used probabilistic model for the photon transport in tissue is the Monte Carlo approach [23-24]. This approach requires the absorption and scattering coefficients as well as the anisotropy factor as input parameters. The probability density function expressed as an exponential distribution is then given by

$$P(s) = (\mu_a + \mu_s)e^{-(\mu_a + \mu_s)s} \, , \tag{13}$$

which corresponds to the probability that a photon is being scattered and absorbed within a path length s along the photon direction of propagation. This distance is randomly sampled based on a uniformly distributed random number $k \in [0,1]$ as follows

$$s = -\ln(k)/(\mu_a + \mu_s) . \tag{14}$$

Two additional probability density functions, $P(\theta)$ and $P(\varphi)$, are required to determine the deflection angles along the polar and the azimuthal orientations, respectively. The probability density function for the polar distribution describes the angular distribution of the scattering and is often modeled by the formulation of the phase function suggested by Henyey-Greenstein yielding the polar angle to be expressed as [25]

$$\theta = \cos^{-1}\left[\frac{1}{2g}\left(1 + g^2 - \left(\frac{1-g^2}{1-g+2gk}\right)^2\right)\right], \tag{15}$$

whereas the azimuthal distribution is often assumed to be uniformly distribution ranging between zero and 2π and therefore the azimuthal angle is given by

$$\varphi = 2\pi k . \tag{16}$$

From these distributions, the reflectance can be computed by simulating for a large number of photons (typical several millions or more) their trajectories. Such a large number is required to statistically reduce the standard deviations of the reflectance for a given set of optical parameters. The photons are launched from the source into the tissue with a unity weight and are gradually decreased for each step with a weight that derives from the Beer-Lambert law which relates the absorption to the initial light intensity and the path length. Each photon is subject to angular deflections described by Eq. (15) and (16) at each scattering event. For each incremental step size, the position of each photon is recorded along the path length. Given its iterative aspect, this approach is much more time consuming than the analytical models whether they are empirical or derive from diffusion theory.

      Table 1 summarizes the types of modeling and measurement domains that are being used by the several research groups in the field of biomedical photonics. The amount of publications related to clinical studies is also displayed. Additionally, the fiber source-detector separation distance is also given.

Table 1. Overview of technological specification of the optical spectroscopy devices by several research groups.

Group, location	Type of model	Wavelength range	source-detector separation
Bigio, Boston University, USA	Empirical	350-800 nm	0.7-3.2 mm
Cubeddu, Politecnico Milano, Italy	Diffusion Theory	600-1100 nm	Larger than 1 cm
Feld, MIT, USA	Diffusion Theory	375-750 nm	1 mm
Jacques, Oregon University, USA	Diffusion Theory	450-950 nm	2.5-3 mm
Philips Research, The Netherlands	Diffusion Theory	500-1600 nm	2.5 mm
Ramanujam, Duke University, USA	Probabilistic	350-600 nm	Below 1 mm
Sterenborg, Erasmus MC, The Netherlands	Empirical	375-1060 nm	Single fiber, 0.2-1 mm
Tromberg, Beckman Laser Institute, USA	Diffusion Theory	650-1000 nm	Larger than 1 cm
Tunnell, Texas University, USA	Look-up table	375-700 nm	Below 1 mm
Zonios, University of Ioannina ,Greece	Diffusion Theory Empirical	450-1000 nm	Below 1 mm

Inhomogeneities

Diffusion theory assumes a semi-infinite homogenous medium but this is obviously an assumption that does not fully describe the morphological tissue complexity. The effects of inhomogeneities are expected to be largest for large sampling volumes and disappear for sampling volumes of dimensions smaller than the diffusion length. Doornbos *et al.* [26] used spatially resolved diffuse reflectance with source detector separations up to 20 mm. On the basis of diffusion theory calculated absorption spectra, the measurements could not be fitted properly with the absorption spectra of the present chromophores. He observed smoothening of the absorption spectra. He and others found that this artifact could be fitted by adding an offset to the fit of the absorption spectrum, i.e. a wavelength independent constant absorption coefficient. Sterenborg *et al.* [27] showed that the measured spectra could be fitted with the known set of absorbers up to the measurement noise with differential pathlength spectroscopy (DPS) technique using 400 micron fibers. That the sensitivity of the method to inhomogeneities is related to the size of the sampling volume with respect to the diffusion length and that the effects of inhomogeneities are expressed as misfits in certain spectral regions is illustrated by an

experiment by Nachabé *et al.* [28]. He used the method described above with a sampling volume of a couple of mm³. His measurements were performed through a needle inside tissue. Inside muscle and fat his spectra fitted perfectly, while close to a boundary spectral misfits occurred. The same smoothing was observed as in the spectra of Doornbos *et al.* The relation to the ratio between sampling volume and diffusion length is obvious: when sampling larger volumes, inhomogeneities cause spatial changes in fluence rates that diffusion theory mistakenly interprets by assuming incorrect optical properties.

3. **Fitting a model to measurements and fit quality assessment**
Model inversion

In order to extract the optical properties from a measurement, a non-linear inversion is used to minimize the residual between the reflectance measurement and the model. To derive the clinically related parameters, the absorption coefficients of the chromophores of interest are fixed parameters in the model whereas the concentrations parameters in Eq. (7) are free parameters. With respect to the reduced scattering, the amplitudes and the slope are the free parameters. The first step in the inversion problem is to use an initial starting guess values for the model which will be used for a forward computation of the reflectance and that will be compared to the measurement. The free parameters are then iteratively updated until the sum of squares error is minimized. The most commonly used nonlinear least-squares inversion algorithm that is used is the Levenberg-Marquardt algorithm whereas few people presented other inversion techniques such as Nelder-Mead direct search simplex method [29], genetic algorithm [30] and Gauss-Newton [31].

Some groups have different approaches with respect to the recovery of the free parameters such as look-up table principles based on Monte Carlo forward calculations of reflectance [32] or with phantoms with known optical properties are used to extract the physiological and biological constitution of the measured tissue [33]. Briefly, reflectance measurements from a set of phantoms with various absorption and reduced scattering coefficients are performed. The reflectance values can be mapped from the wavelength space to a 2D optical property space creating a sparse matrix for the reflectance. Subsequently, this space is interpolated to uniformly spaced data points of optical properties to obtain a look-up table for diffuse reflectance values.

Modifications to the absorption coefficient expression

Investigators that were interested in determining blood volumes and its oxygenation level could not estimate the proper values from phantoms with known blood content when measuring the spectra for short wavelengths. At the beginning it was thought that the assumptions of the diffusion theory did not hold due to the fact that absorption of blood at short wavelengths was very high [34]. However, in the mid-90s, some groups investigated whether the cause was due to the difference in path lengths of the photons for the different wavelengths. As a matter of fact, as blood is not homogenously distributed in tissue but confined in small structures such as vessels, the photons at wavelengths below 500 nm have a much higher chance to be completely absorbed when being in a vessel as compared to the photons at higher wavelengths (cf.

Figure 1). Several groups looked into correction factors for the non-homogenous distribution of chromophores and mainly hemoglobin derivatives. Computational studies modeled distributions of hemoglobin in blood vessels in order to assess a pigment packaging correction factor [35-37]. Although it took almost a decade after its publication to be used by the field, nowadays most of the algorithms apply this correction factor to the absorption coefficient in Eq. (7). The most commonly used expression of the pigment packaging factor that assumes that blood is confined in cylindrical shaped tubes of diameter δ derived by Verkruysse *et al.* and given by

$$C = [1 - \exp(-\mu_a\delta)]/(\mu_a\delta) . \tag{17}$$

In most cases, the absorption coefficient in Eq. (17) corresponds to the absorption of hemoglobin derived parameters only. In Eq. (7), the C factor is multiplied to the terms related to the chromophores that are considered to be subject to the pigment packaging effect [38]. More recently, a couple of experimental studies based on phantoms confirmed the importance of having such a factor to correct in the model [39, 40].

Often Eq. (7) is implemented in a slightly different form where the total blood volume fraction and the oxygen saturation in blood are estimated instead of the concentration of oxygenated and deoxygenated hemoglobin:

$$\mu_a^{Blood} = Cv_{Blood}\left[S_tO_2\mu_a^{HbO_2} + (1 - S_tO_2)\mu_a^{Hb}\right] , \tag{18}$$

with $\mu_a^{HbO_2}$ and μ_a^{Hb} being the absorption coefficient of oxygenated and deoxygenated hemoglobin, respectively; considering a concentration of hemoglobin in full human blood of 150g/L. The total blood volume fraction and the oxygen saturation level are noted as v_{Blood} and S_tO_2, respectively. This formulation has the advantage of self-constraining S_tO_2 parameter between 0 and 1. Furthermore, it also reduces the covariance between v_{Blood} and S_tO_2 than between the Hb and HbO_2 concentrations. Similarly, an equivalent notation is adopted for water and lipid where the sum of these two absorbers and the lipid fraction within this sum are estimated instead of their respective concentrations [28].

Modification of the reduced scattering expression

To obtain a more stable fit, the reduced scattering coefficient in Eq. (8) is often normalized to a specific wavelength in order to obtain amplitudes of the reduced scattering which is constrained to smaller ranges. Furthermore, instead of estimating separately the reduced scattering amplitudes due to Mie and Rayleigh scattering, fitting a Mie-to-total scattering fraction reduces the covariance. The implemented reduced scattering in the models could be thus expressed as follows

$$\mu_s'(\lambda) = a\left[\rho(\lambda/\lambda_0)^{-b} + (1 - \rho)(\lambda/\lambda_0)^{-4}\right] , \tag{22}$$

with λ_0 being a normalization wavelength, a the reduced scattering amplitude at λ_0 and ρ the Mie scattering fraction within Mie and Rayleigh scattering.

Confidence intervals

The first question that arises after fitting a model to the measurements is whether the estimated values of the free parameters do make sense. Amelink *et al.* [41] published an extensive study to demonstrate the added value of computing the confidence intervals of the estimated free parameters as it gives indication on the bias in the obtained values. The computation of the confidence interval is described in detail by Amelink *et al.* [41] and a comparison of confidence intervals on simulated spectra with different level of synthetic noises as well when fitting with a missing absorber where demonstrated to present the effect on the values of the intervals. Briefly, to compute the confidence interval for each free parameter, the covariance matrix is first approximated as the multiplication of the reduced chi-square by the inverse of the hessian of the chi-square with respect to the free parameters. The confidence intervals correspond to the square root of the diagonal elements of the covariance matrix.

F-test for number of parameters and model assessments

As in any research field that requires fitting a model to a measurement, researchers should be very careful when adding additional parameters to their model. By adding additional free parameters, it is possible to reduce the residual whilst biasing the actual values of the parameters.

As mentioned in section 3, the main absorbers in human tissue are Hb, HbO_2, H_2O and lipid which are also all together the most abundant biological substances in the human body. Therefore, the related parameters to these absorbers will properly lock onto the spectral shape. In principle, by including the free parameters related to the reduced scattering, the fit curve should overlay with the measurement curve yielding a small residual. However, in some cases the residual has a spectral shape suggesting a missing chromophore in the model or that the model does not describe well enough the measurements.

In order to evaluate whether adding a chromophore or improving the model by adding an extra free parameter is necessary, an F-test can be applied by using the chi-square values from fitting the measurement with and without the additional free parameters. If the obtained F-value is close to unity, the initial model is the one that describes the measurements best. However if the F-value is greater than unity there are two possible interpretations. Either, the model with the additional parameters describes the measurements best or the model with lower amount of fitting parameters is the most suitable. To know which of these two conditions is correct; the computation of the p-value from the F-value is required [27].

4. **Biological chromophores**

As most of the models use the absorption or extinction coefficients of the various chromophores of interest as fixed input arguments, it is of high importance to have the most accurate coefficients for each chromophore for which the concentration is estimated. This section gives an overview of most of the biological chromophores that were investigated in literature.

Blood derived chromophores

Deoxygenated and oxygenated hemoglobin (Hb and HbO_2) are the two main chromophores that are investigated by the biomedical photonics community as they are the two main optical absorbers that can be measured with silicon detector based spectrometers. These two biological substances are of great interest from a clinical point of view as they can be combined to define the oxygenation level of blood i.e. the concentration of HbO_2 over the sum of both hemoglobin derivatives. The oxygenation level of blood is an important indicator of hypoxia [42] as well as tumor [43-45].

Absorption coefficients of Hb and HbO_2 measured by Scott Prahl are available for the biomedical photonics community in the website of the Oregon Medical Laser Center [46]. Another set of coefficients is also available in a book written by Zijlstra *et al.* which also reports the coefficients for different pH and temperature of the blood samples as well as coefficients for various animals [47]. Additionally, the book contains absorption coefficients of other blood derivatives such as methemoglobin (metHb), sulfhemoglobin (SHb), and carboxyhemoglobin (COHb).

Amelink *et al.* investigated which of the sources provides the most reliable coefficients as it is very important to have the most accurate absorption coefficients to properly fit the measurements [48]. He concluded that the absorption coefficients reported by Zijlstra *et al.* allowed most accurate fitting of the measurements. **Figure 1** depicts the absorption coefficients of Hb and HbO_2 by Prahl and Zijlstra.
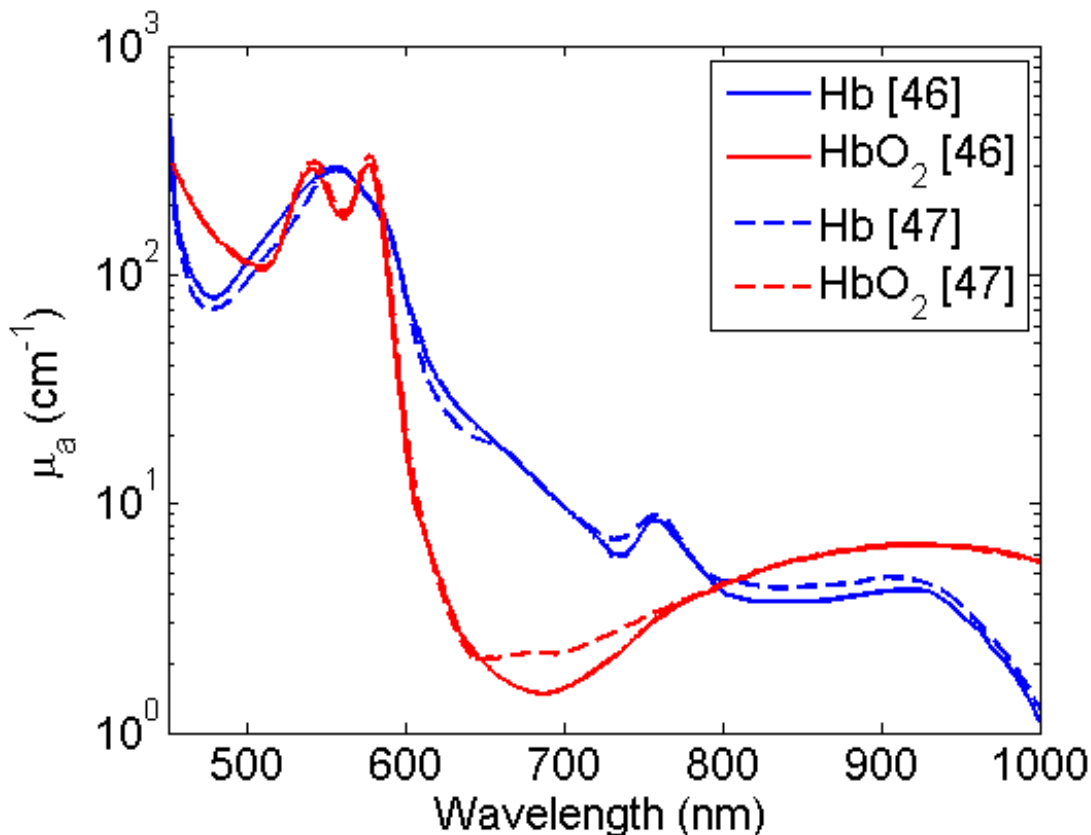

Figure 1. Hb and HbO_2 absorption coefficients by Prahl [61] and Zijlstra [47].

Water

Water is one of the most abundant biological substances in human body ranging from 60 to 80% in body weight [49]. Therefore, water is also one of the most important biological chromophore that is estimated with spectroscopy technique. Within the visible wavelength range, the absorption coefficient of water is insignificant. However, in the infrared, water has several absorption peaks with absolute values above one cm^{-1}, as depicted in **Figure 2**, which are the most dominant absorption peaks in the infrared range. Water absorption coefficients change significantly for different temperatures [50]. Measurements of water absorption coefficients made at different temperatures ranging from 30 °C up to 45 °C demonstrated that the higher the temperature, the more the 972-nm absorption peak of the water shifts to lower wavelengths. The shift is roughly 5 nm for an increase in temperature from 30 to 40 °C accompanied with typically 5% higher absorption values. Additionally, it appeared that the water absorption value at 1192 nm decreases with negligible shift of the peak [50].

Among the various research groups involved in estimating water volume fractions from spectroscopy measurements, the group of Tromberg and Cubeddu always estimate this component as they are mainly interested in water composition in breast (cf. **Table 2**). However, given the wavelength range for their measurements, only one single absorption peak at 972 enables determination of water fractions. Extending the measurement range at least up to 1600 nm is advisable as additional water absorption peaks exist (cf. **Fig. 2**). It was proven that in case of using the steady-state diffusion theory model, extension of the wavelength range significantly improved the confidence in estimating the water volume fractions [28]. The group of Sterenborg and Zonios occasionally determined water volume fractions in case of breast and skin measurements, respectively (cf. **Table 2**).
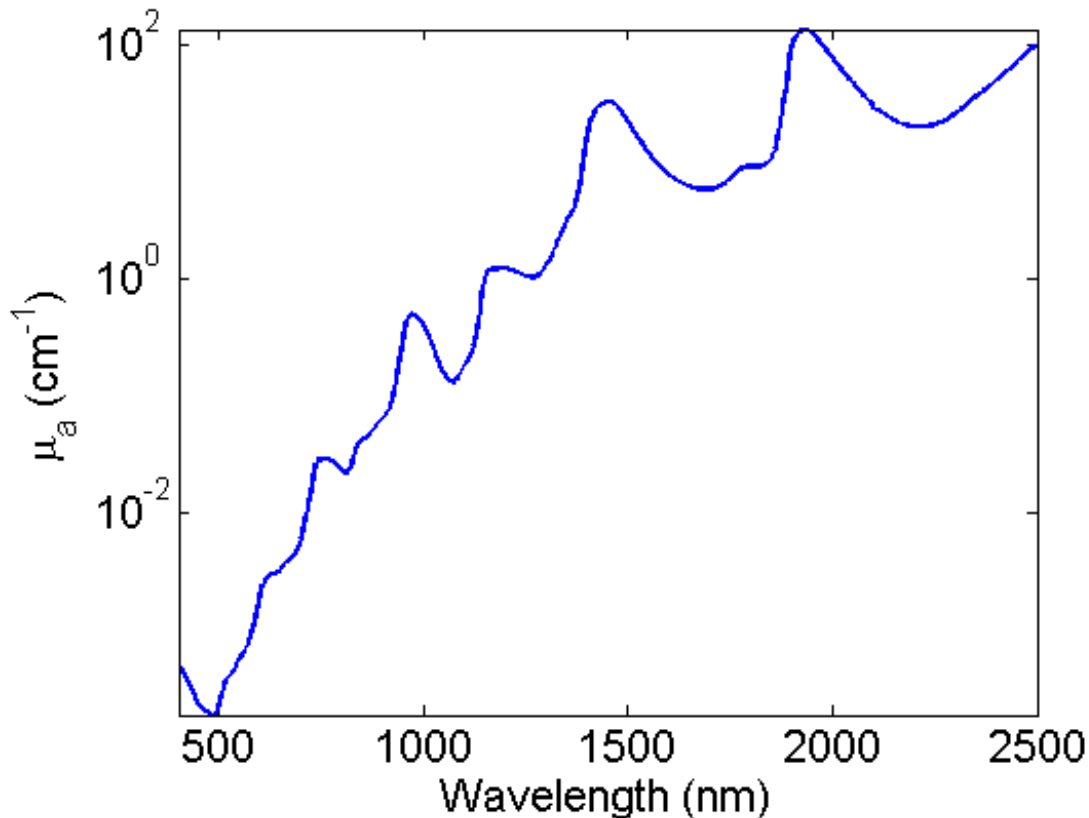
Figure 2. Water absorption coefficient [54].

Lipid

In the human body, lipids are mainly found in adipose tissue such as subcutaneous fat layers as well in visceral fat surrounding the organs. They are main components of cell membranes and therefore could be found everywhere in the body. The lipid concentration in adipose tissue ranges from 60 to 87% for adults and 23 to 47% for infants [51].

One of the very first lipid absorption coefficient measurements that was made available to the community was presented by Conway *et al.* who measured pork lard from 800 to 1080 nm [52]. This measurement was performed by Van Veen *et al.* starting from 400 nm and showed additional peaks of weak absorption coefficient up to 800 nm [53]. Nachabé *et al.* has performed measurement of lipid between 900 and 1600 nm [50] and re-measured the absorption coefficient from 400 up to 2200 nm as shown in **Figure 3** [54].

Lipid is composed of three types of fat: saturated, monounsaturated, and polyunsaturated fat. Typically, human subcutaneous fat is composed of 21%, 46%, and 33% of saturated, monounsaturated, and polyunsaturated fat, respectively. The variations in composition of fat types yield to slight variations in the absorption peaks. For example, lipid constituted of 42%, 46%, and 12% of saturated, monounsaturated and polyunsaturated, respectively, shows an additional absorption peak at 1170 nm [50].
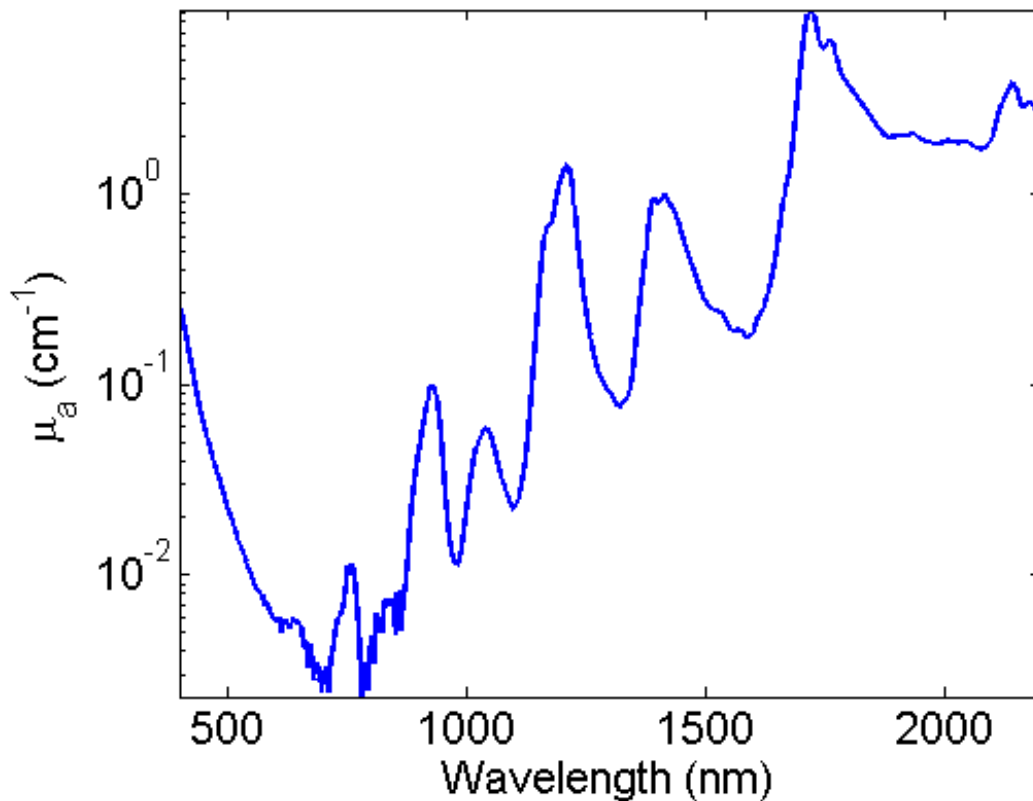
Figure 3. Lipid absorption coefficient [54].

β-Carotene

β-carotene is one of the carotenoids which is mainly found in the skin, blood stream, and adipose cells. In human breast studies [43, 55-57], it showed to be an important absorber in adipose tissue as well as in oral cancer clinical studies [58] and vessel plaque detection [59]. This chromophore has its main absorption peak at 482 nm as depicted in **Figure 4**. The extinction coefficient of β-carotene depends on the substance it was diluted. Comparing the extinction coefficients of this absorber when it is dissolved in hexane and in lipid-rich tissue, respectively, as depicted in **Figure 4**, it shows that the extinction peak is 25 nm broader in the green wavelengths when diluted in lipid-rich tissue. Besides, the absolute value of the extinction coefficient at 482 nm is lower.

Most of the groups that use β-carotene in their model consider the extinction coefficient with this absorber diluted in adipose cell as it is expected to be in human body.
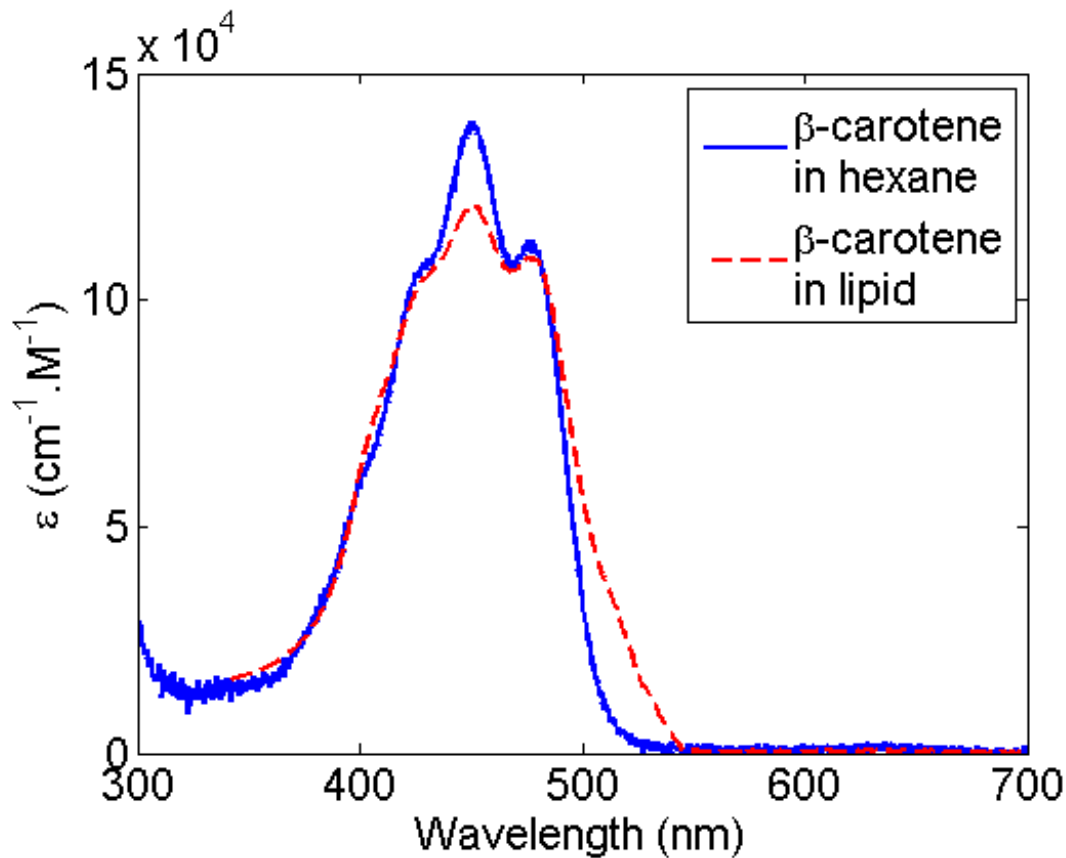
Figure 4. Absorption coefficient of β-carotene diluted in hexane and in adipose cells.

Bilirubin

Bilirubin is a yellow liquid that is mainly found in the spleen and in the liver. In case of an excess of bilirubin secretion in the liver, it can no longer be stored in bile and therefore it flows in the blood stream and leaks into the tissue yielding the skin to become yellowish.

Similarly to β-carotene, bilirubin extinction coefficients depend on the media in which it was diluted. Kanick *et al.* presented bilirubin diluted in albumin extinction coefficients and it appeared to have its maximum at 467 nm whereas bilirubin diluted in chloroform has its peak at 453 nm [60] as depicted in **Figure 5**.
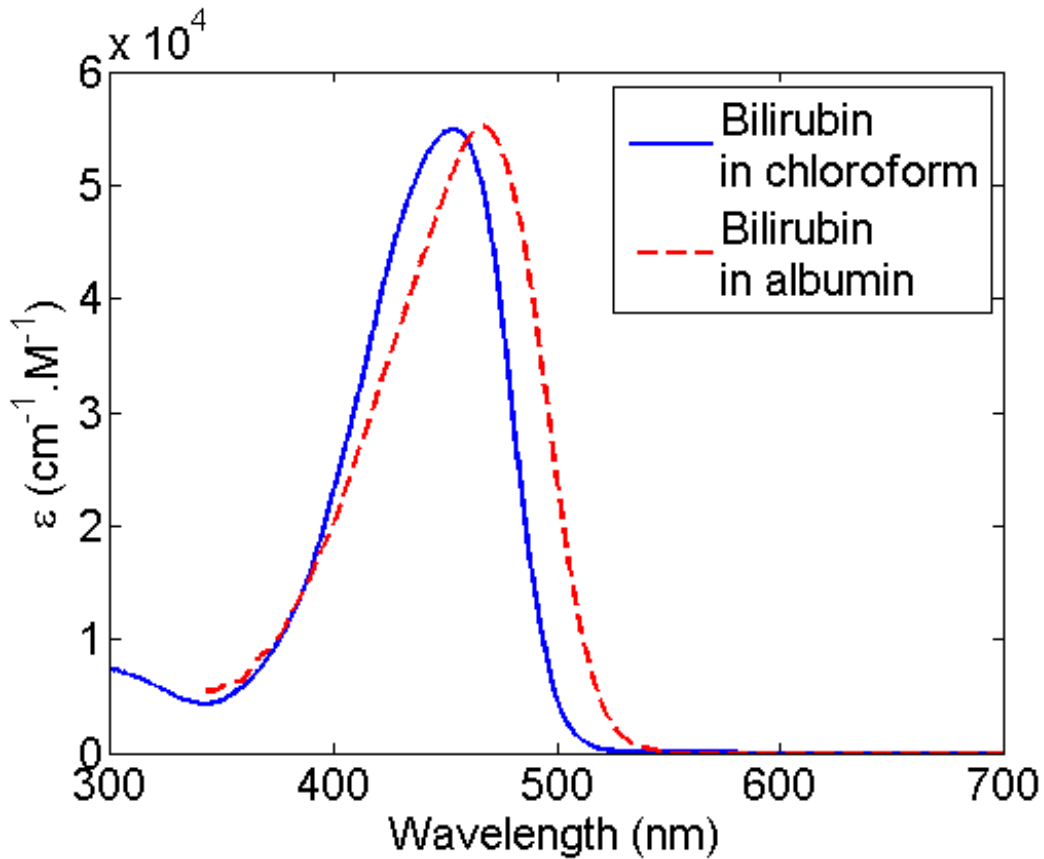
Figure 5. Absorption coefficient of bilirubin diluted in chloroform and in albumin [88].

Organ specific chromophores

Some other studies investigated other chromophores that are organ specific such as skin, liver and breast.

In the field of dermatology, melanin is an important absorber that is always taken into consideration in the model and is expressed as a power law $\mu_a^{melanin} = 142.(\lambda/800)^{-3.33}$ [61] or as an exponential decay function $\mu_a^{melanin} = \exp[-k_m((\lambda - \lambda_{min})/\lambda_{min})]$ with λ_{min} being the minimum wavelength value for the fitting range and k_m being a fit parameter [62].

Recently, measurements on liver showed the need to add the bile absorption coefficient for liver measurements as this organ is extremely abundant with bile ducts and demonstrated that bile concentrations are significantly different in liver metastases compared to healthy liver tissue [63].

Taroni *et al.* investigated the absorption coefficient of collagen in the wavelength range from 600 to 1100 nm and demonstrated that it improves the fit mainly for measurements performed on dense breast tissue [64-66]. Nachabe *et al.* measured the collagen absorption coefficient of collagen from 500 to 1600 nm and presented the collagen concentration in various tumors types of breast tissue [67].

Table 2 summarizes the different absorbers that are used in the different studies of various groups.

Table 2. Overview of biological chromophores used for specific organs by the various research groups developing optical spectroscopy tools for medical applications.

Group, location	Organ	Absorbers used in model
Bigio, Boston University, USA	Muscle [68]	Hb, HbO_2
Cubeddu, Politecnico Milano, Italy	Breast [64-66]	Hb, HbO_2, H_2O, Lipid, Collagen
Feld, MIT, USA	Breast [55] Oral [58, 69] Cardiovascular [59,70] Cervix [71]	Hb, HbO_2, β-carotene Hb, HbO_2, β-carotene Hb, HbO_2, β-carotene, Ceroid Hb, HbO_2, β-carotene
Jacques, Oregon University, USA	Gastrointestinal [72-74]	Hb, HbO_2
Philips Research, The Netherlands	Breast [67] Muscle [28] Neuro [75, 76] Liver [54, 63]	Hb, HbO_2, H_2O, Lipid, β-carotene, Collagen Hb, HbO_2, H_2O, Lipid Hb, HbO_2, H_2O, Lipid Hb, HbO_2, H_2O, Lipid, Bile
Ramanujam, Duke University, USA	Breast [45, 56, 57, 77-81] Cervix [82, 83] Head and Neck [84, 85]	Hb, HbO_2, β-carotene Hb, HbO_2, β-carotene Hb, HbO_2
Sterenborg, Erasmus MC, The Netherlands	Breast [43] Head and Neck [86] Lung [21, 42, 87] Lung [88] Oral [89] Oral [90] Gastrointestinal [91] Urology [92]	Hb, HbO_2, β-carotene Hb, HbO_2 Hb, HbO_2 Hb, HbO_2, Bilirubin Hb, HbO_2 Hb, HbO_2, β-carotene Hb, HbO_2 Hb, HbO_2
Tromberg, Beckman Laser Institute, USA	Breast [10, 44, 93-105]	Hb, HbO_2, H_2O, Lipid
Tunnell, Texas University, USA	Skin [33, 40] Skin [106, 107]	Hb, HbO_2 Hb, HbO_2, Melanin
Zonios, University of Ioannina ,Greece	Gastrointestinal [18] Skin [15, 19, 62, 108, 109] Skin [110] Skin [111]	Hb, HbO_2 Hb, HbO_2, Melanin Hb, HbO_2, H_2O, Melanin Hb, HbO_2, MetHb

5. Clinical applications

Diagnosis

The most common clinical application is cancer diagnosis where malignant tissue is discriminated from the surrounding healthy tissue in order to assess tumors margins. For this aim, several tools were developed ranging from hand-held probes [44, 81] to pen-like probes [55-57] and needle-like probes [21, 43, 75, 76]. Most of the studies clearly showed that there is a significant difference in blood oxygenation level between malignant and non-malignant tissues with non-malignant being less oxygenated. The same holds for the reduced scattering amplitude with higher values in malignant tissues compared to non-malignant tissues. These observations are independent of the organs. In many cases, the total amount of blood is also a discriminator with higher volume fractions in non-malignant tissues related to angiogenesis. It was also demonstrated that in the case of breast cancer the healthy tissue is rich in β-carotene compared to the malignant tissue as β-carotene is abundant in adipose tissue [43, 55-57, 67]. Groups that measure spectra above 900 nm are able to estimate water and lipid volume fractions and proved that obviously it is possible to discriminate non-malignant tissue as adipose tissue is rich in lipid [44, 67]. However, it is important to note that very often glandular tissue is included as non-malignant tissue and the statistics can be biased due to the fact that glandular is mainly rich in connective tissues.

Another organ that received a lot of attention is skin due to the fact that it is easily accessible. The group of Zonios has the largest experience in dermatological investigation with diffuse reflectance spectroscopy and showed that the main discriminator between the cancerous tissue and benign tissue is the melanin decay factor k_m. The group of Tunnell has been over the last five years active in investigating skin cancer diagnosis and showed that they can classify basal cell carcinoma from squamous cell carcinoma and benign skin tissue with a sensitivity and specificity ranging from 89% to 97% and 25% to 89%, respectively [106].

With respect to cervical cancer, several studies investigated the change in optical properties for different grades and it was demonstrated that blood volume fractions increases with the grade level [82, 83].

Colon tissues have also been investigated with diffuse reflectance spectroscopy to diagnose polyps and cancer [18, 112]. It was shown that blood volume fraction is the main discriminator between malignant and non-malignant and being less abundant in normal tissue. Another organ from the gastrointestinal system that was investigated by Amelink *et al.* is the esophagus where it was shown that blood volume fractions is also higher in cancer compared to healthy mucosa from the Barrett's esophagus.

Diffuse reflectance spectroscopy investigations on the oral cavity showed that blood is a discriminator between cancerous tissue and normal tissue as well as the scattering amplitude and slope [89].

The group of Sterenborg has a lot of experience in lung cancer diagnosis where they showed that the blood oxygenation level is lower in cancerous tissue compared to healthy tissue using differential pathlength spectroscopy technique [21, 42, 87]. More recently, they have investigated the difference between metastasis and normal lymph nodes in the lung by integrating a single fiber in a fine-needle and showed that both blood

volume fraction and its oxygenation level are significantly different for the two types of lymph nodes [88].

A paucity of liver studies cannot allow for a clear conclusion with respect to the parameters that show differences between tumors and healthy tissue. Nachabé *et al.* performed a study to investigate the difference between colorectal metastasis in liver and the surrounding healthy tissue. It was shown that bile is a very important discriminator being more abundant in healthy tissue than the tumors. Similarly to breast and cervical cancer, it was shown that the reduced scattering amplitude is significantly higher in tumors. Furthermore, water showed similar trends to the scattering amplitude; the reason being that water is attracted to necrotic tissue that is abundantly present in most colorectal liver metastases. The high water content of collagenous stroma in general, and tumor induced stroma play a role as well. Another type of diagnosis investigated by Nachabé *et al.* corresponds to non-alcoholic fatty liver disease (NAFLD) diagnosis [54]. NAFLD is considered to be positively diagnosed for hepatic lipid accumulation as low as 5% and therefore very accurate tools are required to properly estimate the fat fraction. Nachabé *et al.* showed by comparing fat estimation with diffuse reflectance spectroscopy with other commonly used methods such as MR spectroscopy, MAS-NMR spectroscopy, high performance thin layer chromatography and histopathology being the gold standard. They concluded that diffuse reflectance spectroscopy provides comparable hepatic fat quantification for the various methods as well as clear differences in fat between a chow control mice group and a high fat diet mice group.

Few studies exist with respect to the head and neck cancer. Breumer *et al.* [85] showed significant difference between squamous cell carcinomas and healthy tissue based on the blood oxygenation level. The cardiovascular field is also not very much investigated. The group of Feld did perform studies on distinguishing thrombotic plaques from vulnerable plaques and showed that they can classify both tissues with a sensitivity and specificity of 93% and 72%, respectively [59].

Tumor margins assessment

The group of Ramanujam has a wide experience in diffuse reflectance spectroscopy for breast cancer investigation and has recently developed a multiple fiber probe setup to evaluate breast tumor margins subject to surgery removal.
They have showed in a study by Wilke *et al.* [78] that they reached sensitivity of 79% of the pathological close/positive margins and a specificity of 67%. More recently, a study by Kennedy *et al.* [81] showed that the reduced scattering amplitude and the blood volume fraction are both significantly higher in malignant tissue compared to the surrounding healthy breast tissue.

Chemotherapy response monitoring

The group of Tromberg has investigated the relation between the fit parameters and breast cancer chemotherapy responses. Monitoring the response to therapy can improve survival and reduce morbidity [44, 99, 100, 113].

Jakubowsky *et al.* used diffuse reflectance spectroscopy to monitor tumor responses to neoadjuvant chemotherapy prior to doxorubicincyclophosphamide therapy as

well as at several time points over the course of three treatment cycles of 68 days [100]. By investigating the tumor to normal tissue contrast in blood, water, lipid and blood oxygenation prior to treatment and comparing the values over a 10-week period, they showed that blood and water fractions dropped more than 50%, whereas lipid remained constant and the oxygenation level increased. Within only 5 days, half of the blood and water changes occurred making these two chromophores of high interest for breast chemotherapy monitoring.

Shah *et al.* performed a similar study where diffuse reflectance spectroscopy measurements were employed in conjunction with magnetic resonance imaging (MRI) to assess tumor responses to presurgical neoadjuvant chemotherapy [99]. The study was conducted on patients with ductal carcinoma *in situ* breast tumors and the measurements were performed after the first and fourth cycles of doxorubicincyclophosphamide regimen. Spectral measurements are used to quantify bulk tissue optical and physiological parameters, which are mapped to T2- and T1-weighted contrast-enhanced MRI images. Initial spectroscopic measurements show high tumor/normal contrast in blood and water fraction colocalized with regions of strongly enhancing T2-wieghted signals. After the fourth cycle of chemotherapy, decreases in peak MRI contrast-enhancement values and apparent lesion volume (20% to 25% reduction in the spatial extent of the tumor) and a 38.7% drop in mean blood content were observed.

Tromberg *et al.* [113] performed a study on 12 young patients aged from 30 to 39 years and investigated the potential of detecting tumors in pre-menopausal women and monitor the neoadjuvant chemotherapy. They showed that blood, water, and lipid volume fractions as well as the blood oxygenation level showed significant differences between normal and tumor. They came up with an empirical parameter called tissue optical index (TOI) corresponding to the product of deoxygenated hemoglobin concentration multiplied by the water fraction and divided by the lipid fraction to evaluate the response of tumors to chemotherapy. A 50% decrease in TOI within a single week after neoadjuvant chemotherapy was observed.

Cerussi *et al.* [95] conducted a study where the goal was to investigate how early during the chemotherapy treatment can one predict whether a patient is a responder or not based on the fit-parameters derived from diffuse reflectance spectroscopy. Discrimination analysis based on the combination of deoxygenated hemoglobin concentration and water fractions classified responders from non-responders with 100% sensitivity and specificity within a single week after the treatment.

From all these studies conducted by the group of Tromberg, it can be suggested that diffuse reflectance spectroscopy has a strong potential in properly monitoring chemotherapy responses as well as developing new strategies for individualized patient care.

Photodynamic and radiotherapy monitoring
Photodynamic treatment (PDT) is an emerging treatment that is used to treat and reduce tumors size. It requires a photosensitizer such as aminolevulinic acid (ALA-5) that is absorbed by cells and coverted into protoporphoryn IX (PPIX). Subsequently, a single wavelength light is shined on the tumor causing light absorption by PPIX and causing

energy transfer from PPIX to oxygen. The reaction between the oxygen and the biological substances in the tumor provoke tissue damage. However the PDT dose of photosensitizer and light delivery can vary for patient to patient and therefore there is a crucial need in monitoring PDT. The group of Sterenborg performed several studies to monitor oxygenation during PDT procedures and showed increase in blood content as well its oxygenation at the treated tumor sites [86]. Similar study by Bargo *et al.* corroborated with these findings [72].

Another type of treatment monitoring corresponds to irradiation treatment monitoring. Vishwanath *et al.* performed a preclinical study to investigate whether a final treatment outcome could be estimated from optical signatures in a murine model of head and neck cancer when treated with radiation [84]. They performed the study on 23 nude mice exposed to 39 Gy of radiation and 11 other as control group exposed to sham radiation. The measurements were performed until 17 days after treatment and they demonstrated that an increase in blood oxygenation can be observed starting 5 days post-treatment and last up to 17 days.

Complications prediction

Recently, the group of Jacques has investigated the potential of diffuse reflectance spectroscopy to predict anastomotic complications and gastric ischemic conditions during conduit creation [73, 74]. They have demonstrated that patients that had anastomotic complications showed to have higher blood content with lower oxygenation level measured in the distal gastric conduit. This study was performed in 23 patients during esophagectomy from which 8 showed anastomotic complications. They came to the conclusion that decreased oxygenation level in blood at either the completion of conduit or anastomosis is predictive of complication with a sensitivity and specificity of 71%.

Needle guidance

Diffuse reflectance spectroscopy sensing integrated in needles (e.g. biopsy needles) has shown to be a promising real-time feedback tool for improving percutaneous procedures. Van Veen *et al.* clearly showed the advantage of having real-time optical sensing feedback for breast biopsies [43]. Being able to discriminate the tumor site from the healthy tissue is of great relevance for clinician to be able to acquire the biopsy in the tumor site for further histopathological analysis. As a consequence, the total amount of repeated biopsy could be reduced.

Rathmell *et al.* showed the added value of spinal needles with integrated optical fibers to be able to confirm the localization of the tip of a needle in the epidural space [75]. Based on the total amount of lipid that is estimated with diffuse reflectance spectroscopy, the epidural space can be accurately identified and discriminated from the surrounding tissues such as the ligamentum flavum or the cerebral spinal fluid (CSF).

6. **Conclusion**

Diffuse reflectance spectroscopy measurements acquired from fiber-optic hand-held probes are extremely relevant for several clinical applications. As emphasized in this

review, the choice of the model should be carefully made by taking into consideration the geometrical aspects of the probe. The most common way of validating a model is to recover the optical properties from phantoms measurements with known optical properties. Several mathematical tools exist to evaluate the reliability of the estimated parameters as well as to investigate whether additional parameters need to be added to the model.

Multitude of preclinical and clinical studies has been conducted and most of them converge to the same conclusions with respect to the analysis of the clinically relevant parameters in the aim to discriminate different types of tissues. However, the comparison between the different tools and the performance of the analysis is not always straightforward as there is a big variety of method, wavelength range, chromophores considered in the models, etc. that can influence the comparison.

Anyhow, using diffuse reflectance spectroscopy showed sensitivity and specificity to discriminate malignant from non-malignant tissues ranging from 53% to 100% and 70 to 100%, respectively. The performance of such diagnosis can be improved by combining fluorescence spectroscopy and also Raman spectroscopy.

Diffuse reflectance spectroscopy has been intensively used in the clinic and demonstrated great potential in several clinical applications thanks to its minimal invasiveness and high optical contrast between various chromophores that enables tissue discrimination.

References

1. M. S. Patterson, B. Chance, and B. C. Wilson, "Time resolved reflectance and transmittance for the non-invasive measurement of tissue optical properties", App. Opt. 28(12): 2331-2336 (1989).

2. J. D. Moulton, "Diffusion modeling of picoseconds laser pulse propagation of turbid media", Master's degree dissertation (McMaster University, Hamilton, Ontario, Canada, 1990).

3. A. H. Hielscher, S. L. Jacques, L. Wang, and F. K. Tittel, "The influence of boundary conditions on the accuracy of diffusion theory in time-resolved reflectance spectroscopy of biological tissue", Phys. Med. Biol. 40, 1957-1975 (1995).

4. A. Kienle, and M. S. Patterson, "Improved solutions of the steady-state and the time-resolved diffusion equations for reflectance from a semi-infinite turbid media" J. Opt. Soc. Am. A 14(1), 246-254 (1997).

5. S. Fantini, M. A. Franceschini, S. Fishkin, B. Barbieri, and E. Gratton, "Quantitative determination of the absorption spectra of chromophores in strongly scattering media", Appl. Opt. 33, 5204-5213 (1994).

6. R. C. Haskell, L. O. Svaasand, T. T. Tsay, T. C. Feng, M. McAdams, and B. J. Tromberg, "Boundary conditions for the diffusion equation in radiative transfer" J. Opt. Soc. Am. A 11, 2727-2741 (1994).

7. A. Kienle and M. S. Patterson, "Determination of the optical properties of turbid media from a single Monte Carlo simulations" Phys. Med. Biol. 41, 2221-2227 (1996).

8. T. J. Farrell, B. C. Wilson, and M. S. Patterson, "The use of a neural network to determine tissue optical properties from spatially resolved diffuse reflectance measurements" Phys. Med. Biol. 37, 2281-2286 (1992).

9. T. J. Farrell, M. S. Patterson, and B. Wilson, "A diffusion theory model of spatially resolved, steady-state diffuse reflectance for the noninvasive determination of tissue optical properties *in vivo*" Med. Phys. 19(4), 879-888 (1992).

10. F. Bevilacqua, A. J. Berger, A. E. Cerussi, D. Jakubowski, and B. J. Tromberg, "Broadband absorption spectroscopy in turbid media by combined frequency-domain and steady-state methods", App. Opt. 39(34), 6498-6507 (2000).

11. B. W. Pogue and M. S. Patterson, "Review of tissue simulating phantoms for optical spectroscopy, imaging and dosimetry" J. Biomed. Opt. 11(4), 041102 (2006).

12. S. L. Jacques and B. W. Pogue, "Tutorial on diffuse light transport", J. Biomed. Opt. 13(4), 041302 (2008).

13. M. Keijzer, W. M. Star, and P. R. Storchi, "Optical diffusion in layered media" Appl. Opt. 27, 1820-1824 (1988).

14. I. S. Saidi, S. L. Jacques, and F. K. Tittel, "Mie and Rayleigh modeling of visible light scattering in neonatal skin", App. Opt. 34(31), 7410-7418 (1995).

15. G. Zonios and A. Dimou, "Light scattering spectroscopy of human skin *in vivo*" Opt. Exp. 17(3), 1256-1267 (2009).

34

16. J. R. Mourant, I. J. Bigio, J. Boyer, R. L. Conn, T. Johnson, and T. Shimada, "Spectroscopic diagnosis of bladder cancer with elastic light scattering" Lasers Surg. Med. 17, 350-357 (1995).

17. R. Reif, O. A'Amar, and I. J. Bigio, "Analytical model of light reflectance for extraction of the optical properties in small volumes of turbid media" Appl. Opt. 48(29), 7317-7328 (2007).

18. G. Zonios, L. T. Perelman, V. Backman, R. Manoharan, M. Fitzmaurice, J. Van Dam, and M. S. Feld, "Diffuse reflectance spectroscopy of human adenomatous colon polyps *in vivo*" Appl. Opt. 38(31), 6628-6637 (1999).

19. G. Zonios, J. Bykowski, and N. Kollias, "Skin melanin, hemoglobin, and light scattering properties can be quantitatively assessed *in vivo* using diffuse reflectance spectroscopy" J. Invest. Dermatol. 117, 1452-1457 (2001).

20. G. Zonios, I. Bassukas, and A. Dimou, "Comparative evaluation of two simple diffuse reflectance models for biological tissue applications" Appl. Opt. 47(27), 4965-4973 (2008).

21. A. Amelink, M. P. Bard, S. A. Burgers, and H. J. C. M. Sterenborg, "*In vivo* measurement of the local optical properties of tissue by use of differential path-length spectroscopy" Opt. Let. 29(10), 1087-1089 (2004).

22. S. C. Kanick, H. J. C. M. Sterenborg, and A. Amelink, "Empirical model of the photon path length for a single fiber reflectance spectroscopy device" Opt. Exp. 17(2), 860-871 (2009).

23. B. C. Wilson and G. Adam, "A Monte Carlo model for the absorption and flux distributions of light in tissue" Med. Phys. 10(6), 824-830 (1983).

24. M. Keijzer, S. L. Jacques, S. A. Prahl, and A. J Welch, "Light distribution in artery tissue: Monte Carlo simulations for finite-diameter laser beams" Lasers Surg. Med. 9(2), 148-154 (1989).

25. G. Henyey and JL Greenstein, "Diffuse radiation in the galaxy", Astrophys. J. **93**, 70-83 (1941).

26. R. M. P. Doornbos, R. Lang, M. C. Aalders, F. W. Cross, and H. J. C. M. Sterenborg, "The determination of *in vivo* human tissue optical properties and absolute chromophore concentrations using spatially resolved steady-state diffuse reflectance spectroscopy" Phys. Med. Biol. 44, 967-981 (1999).

27. Adam Wax and Vadim Backman. *Biomedical applications of light scattering.* McGraw-Hill 2010; ISBN: 978-0-07-159881-1.

28. R. Nachabe, B.H.W. Hendriks, M. van der Voort, A. E. Desjardins, and H. J. C. M. Sterenborg, "Estimation of biological chromophores using diffuse optical spectroscopy: benefit of extending the UV-VIS wavelength range to include 1000 to 1600 nm" Biomed Opt Exp. 1(5): 1432-1442 (2010).

29. L. F. Douven, G. W. Lucassen, "Retrieval of optical properties of skin from measurement and modeling the diffuse reflectance" Proc. SPIE 3914, 312 (2000).

30. R. Zhang, W. Verkruysse, B. Choi, J. A. Viator, B. Jung, L. O. Svaasand, G. Aguilar, and J. S. Nelson, "Retrieval of human skin optical properties from spectrophotometer measurement based on the application of genetic algorithm" J. Biomed. Opt. 10(2), 024030 (2005).

31. G. M. Palmer and N. Ramanujam, "Monte Carlo-based inverse model for calculating tissue optical properties. Part I: theory and validation on synthetic phantoms" Appl. Opt. 45(5), 1062-1071 (2006).

32. W. Verkruysse, R. Zhang, B. Choi, G. Lucassen, L. O. Svaasand, and J. S. Nelson, "A library based fitting method for visual reflectance spectroscopy of human skin" Phys. Med. Biol. 50, 57-70 (2005).

33. N. Rajaram, T. H. Nguyen, and J. W. Tunnell, "Lookup table-based inverse model for determining optical properties of turbid media" J. Biomed. Opt. 13(5), 050501 (2008).

34. K. Furutsu, "On the diffusion equation derived from the space-time transport equation" J. Opt. Sco. Am. 70, 360-366 (1980).

35. W. Verkruysse, G. W. Lucassen, J. F. De Boer, D. J. Smithies, J. S. Nelson and M. J. C. Van Gemert, "Modelling light distributions of homogenous versus discrete in light irradiated turbid media" Phys. Med. Biol. 42, 51-65 (1997).

36. L. O. Svaasand, E. J. Fiskerstrand, G. Kopstad, L. T. Norvang, E. K. Svaasand, J. S. Nelson, and M. W. Berns, "Therapeutic response during pulsed laser treatment of port-wine stains: dependence on vessel diameter and depth in dermis" Lasers Med. Sci. 10, 235 (1995).

37. A. Talsma, B. Chance and R, Graaf, "Corrections for inhomogeneities in biological tissue caused by blood vessels" J. Opt. Soc. Am. A. 4, 932-939 (2001).

38. R. L. P. van Veen, W. Verkruysse, and H. J. C. M. Sterenborg, "Diffuse reflectance spectroscopy from 500 to 1060 nm by correction for inhomogeneously distributed absorbers" Opt. Let. 27(4), 246-248 (2002).

39. J. C. Finlay and T. H. Foster, "Effect of pigment packaging on diffuse reflectance spectroscopy of samples containing red blood cells" Opt. Let. 29(9), 965-967 (2004).

40. N. Rajaram, A. Gopal, X. Zhang, and J. W. Tunnell, "Experimental validation of the effects of microvasculature pigment packaging on *in vivo* diffuse reflectance spectroscopy" Lasers Surg. Med. 42, 680-688 (2010)

41. A. Amelink, D. J. Robinson, and H. J. C. M. Sterenborg, "Confidence intervals on fit parameters derived from optical reflectance spectroscopy measurements" J. Biomed. Opt. 13(5), 054044 (2008).

42. M. P. L. Bard, A. Amelink, V. N. Hegt, W. J. Graveland, H. J. C. M. Sterenborg, H. C. Hoogsteden, and J. G. J. V. Aerts, "Measurement of hypoxia-related parameters in bronchial mucosa by use of optical spectroscopy" Am. J. Respir. Crit. Care Med. 171, 1178-1184 (2005).

43. R. L. P van Veen, A. Amelink, M. Menke-Pluymers, C. Van der Pol, and H. J. C. M. Sterenborg, "Optical biopsy of breast tissue using differential path-length spectroscopy" Phys. Med. Biol. 50 2573-2581 (2005).

44. A. Cerussi, N. Shah, D. Hsiang, A. Durkin, J. Butler, and B. J. Tromberg, "*In vivo* absorption, scattering, and physiologic properties of 58 malignant breast tumors determined by broadband diffuse optical spectroscopy" J. Biomed. Opt. 11(4), 044005 (2006).

45. J. Q. Brown, Lee. G. Wilke, J. Geradts, S. A. Kennedy, G. M. Palmer, and N. Ramanujam, "Quantitative optical spectroscopy: a robust tool for direct measurement of breast cancer vascular oxygenation and total hemoglobin content *in vivo*" Cancer Res. 69(7), 2919-2926 (2009).

46. S. A. Prahl, "Optical properties of hemoglobin" http://www.omlc.ogi.edu/spectra/hemoglobin/summary.html (retrieved October 20, 2011).

47. W. G. Zijlstra, A. Buursma, and O. W. Assendelft, *Visible and Near Infrared Absorption Spectra of Human and Animal Haemoglobin,* VSP Publishing, Utrecht, The Netherlands (2000).

48. A. Amelink, T. Christiaanse, and H. J. C. M. Sterenborg, "Effect of hemoglobin extinction spectra on optical spectroscopic measurements of blood oxygen saturation" Opt. Let. 34(10), 1525-1527 (2009).

49. Marieb, E.N., *Human Anatomy and Physiology*. Third ed. 1995, Redwood City, California: Benjamin/Cummings.

50. R. Nachabe, B. H. W. Hendriks, A. E. Desjardins, M. Van der Voort, and H. J. C. M. Sterenborg, "Estimation of lipid and water in scattering media with diffuse optical spectroscopy from 900 to 1600 nm". J Biomed Opt. 15(3): 037015 (2010).

51. H. Q. Woodard and D. R. White, "The Composition of Body-Tissues", British Journal of Radiology, 59(708), 1209-1219 (1986).

52. Conway, J.M., Norris, K.H. and Bodwell, C.E. "A new approach for the estimation of body composition: infrared interactance" Am. J. Clin. Nutri., 40,1123-1130 (1984).

53. R. L. P. van Veen, H. J. C. M. Sterenborg, A. Pifferi, A. Torricelli, E. Chikoidze, and R. Cubeddu, "Determination of visible near-IR absorption coefficients of mammalian fat using time and spatially resolved diffuse reflectance and transmission spectroscopy" J. Biomed. Opt. 10(5), 054004 (2005).

54. R. Nachabe, J. W. A. van der Hoorn, R. A. van de Molengraaf, R. Lamerichs, J. Pikkemaat, C. F. Sio, B. H. W. Hendriks, and H. J. C. M. Sterenborg, "Validation of interventional fiber optic spectroscopy with MR spectroscopy, MAS-NMR spectroscopy, high performance thin layer chromatography and histopathology for accurate hepatic fat quantification" Investigative Radiol. 47(4): (2012).

55. Z. Volynskaya, A. S. Haka, K. L. Bechtel, M. Fitzmaurice, R. Shenk, N. Wang, J. Nazemi, R. R. Dasari, M. S. Feld, "Diagnosing breast cancer using diffuse reflectance spectroscopy and intrinsic fluorescence spectroscopy" J. Biomed. Opt. 13(2), 024012 (2008).

56. C. Zhu, G. M. Palmer, T. M. Breslin, J. Harter, and N. Ramanujam, "Diagnosis of breast cancer using diffuse reflectance spectroscopy: comparison of a Monte Carlo versus partial least squares analysis based feature extraction technique" Lasers Surg. Med. 38, 714-724 (2006).

57. C. Zhu, G. M. Palmer, T. M. Breslin, J. Harter, and N. Ramanujam, "Diagnosis of breast cancer using fluorescence and diffuse reflectance spectroscopy: a Monte-Carlo-model-based approach" J. Biomed. Opt. 13(3), 034015 (2008).

58. S. McGee, V. Mardirossian, A. Elackattu, J. Mirkovic, R. Pistey, G. Gallagher, S. Kabani, C. Chieh, Z. Wang, K. Badizadegan, G. Grillone, and M. S. Feld, "Anatomy-based algorithms for detecting oral cancer using reflectance and fluorescence spectroscopy" Ann. Otol. Rhinol. Laryngol. 118(11): 817-826 (2009).

59. O. R. Scepanovic, M. Fitzmaurice, J. A. Gardecki, G. O. Angheloiu, S. Awasthi, J. R. Kramer, R. R. Dasari, and M. S. Feld, "Detection of morphological markers of vulnerable atherosclerotic plaque using multimodal spectroscopy" J. Biomed. Opt. 11(2), 021007 (2006).

60. S. C. Kanick, C. van der Leest, J. G. V. Aerts, H. C. Hoogsteden, S. Kascakova, H. J. C. M. Sterenborg, "Integration of single-fiber reflectance spectroscopy into ultrasound-guided endoscopic lung cancer staging of mediastinal lymph nodes" J. Biomed. Opt. 15(1), 017004 (2010).

61. S. Jacques, "Optical absorption of melanin", http://omlc.ogi.edu/spectra/melanin/index.html (retrieved October 20, 2011).

62. G. Zonios, A. Dimou, I. Bassukas, D. Galaris, A. Tsolaskidis, E. Kaxiras, "Melanin absorption spectroscopy: new method for noninvasive skin investigation and melanoma detection" J. Biomed. Opt. 13(1), 014017 (2008).

63. R. Nachabe, D. J. Evers, B. H. W. Hendriks, G. W. Lucassen, M. van der Voort, J. Wesseling, and T. J. M. Ruers, "Effect of bile absorption coefficients on the estimation of liver tissue optical properties and related implications in discriminating healthy and tumorous samples" Biomed. Opt. Exp. 2(3), 600-614 (2011).

64. P. Taroni, D. Cornelli, A. Pifferi, A. Torricelli, and R. Cubeddu, "Absorption of collagen: effects on the estimate of breast composition and related diagnostic implications" J. Biomed. Opt. 12(1), 014021 (2007).

65. P. Taroni, A. Bassi, D. Cornelli, A. Farina, R. Cubeddu, and A. Pifferi, "Diffuse optical spectroscopy of breast tissue extended to 1100 nm" J. Biomed. Opt. 14(5), 054030 (2009).

66. P. Taroni, A. Pifferi, G. Quarto, L. Spinelli, A. Torricelli, F. Abbate, A. Villa, N. Balestreri, S. Menna, E. Cassano, and R. Cubeddu, "Noninvasive assessment of breast cancer risk using time-resolved diffuse optical spectroscopy" J. Biomed. Opt. 15(6), 060501 (2010).

67. R. Nachabe, D. J. Evers, B. H. W. Hendriks, G. W. Lucassen, M. van der Voort, E. J. Rutgers, M. Vrancken Peeters, J. A. Van der Hage, H. S. Oldenburg, J. Wesseling, and T. J. M. Ruers, "Diagnosis of breast cancer using diffuse optical spectroscopy from 500 to 1600 nm: comparison of classification methods" J. Biomed. Opt. 16(8), 087010 (2011).

68. R. Reif, M. S. Amorosino, K. W. Calabro, O. A'Amar, S. K. Singh, and I. Bigio, "Analysis of changes in reflectance measurements on biological tissues subjected to different probe pressures" J. Biomed. Opt. 13(1), 010502 (2008).

69. S. McGee, J. Mirkovic, V. Mardirossian, A. Elackattu, C. Yu, S. Kabani, G. Gallagher, R. Pistey, L. Galindo, K. Badizadegan, Z. Wang, R. R. Dasari, and M.

S. Feld, "Model-based spectroscopic analysis of the oral cavity: impact of anatomy" J. Biomed. Opt. 13(6), 064034 (2008).

70. G. O. Angheloiu, A. S. Haka, I. Georgakoudi, J. Arendt, M. G. Muller, O. R. Scepanovic, S. P. Evanko, T. N. Wight, P. Mukherjee, D. H. Waldeck, R. R. Dasari, M. Fitzmaurice, J. R. Kramer, and M. S. Feld, "Detection of coronary atherosclerotic plaques with superficial proteoglycans and foam cells using real-time intrinsic fluorescence spectroscopy" Atherosclerosis 215, 96-102 (2011).

71. J. Mirkovic, C. Lau, S. McGee, C. Yu, J. Nazemi, L. Galindo, V. Feng, T. Darragh, A. de las Morenas, C. Crum, E. Stier, M. S. Feld, and K. Badizadegan, "Effect of anatomy on spectroscopic detection of cervical dysplasia" J. Biomed. Opt. 14(4), 044021 (2009).

72. P. R. Bargo, S. A. Prahl, T. T. Goodell, R. A. Sleven, G. Koval, G. Blair, and S. L. Jacques, "*In vivo* determination of optical properties of normal and tumor tissue with white light reflectance and an empirical light transport model during endoscopy" J. Biomed. Opt. 10(3), 034018 (2005).

73. D. S. Gareau, F. Truffer, K. Perry, T. Pham, C. K. Enestvedt, J. Dolan, J. G. Hunter, and S. L. Jacques, "Optical fiber probe spectroscopy for laparoscopic monitoring of tissue oxygenation during esophagectomies" J. Biomed. Opt. 15(6), 061712 (2010).

74. T. H. Pham, K. A. Perry, C. K. Enestvedt, D. Gareau, J. P. Dolan, B. C. Sheppard, S. L. Jacques, and J. G. Hunter, "Decreased conduit perfusion measured by spectroscopy is associated with anastomotic complications" Ann. Thorac. Surg. 91, 380-386 (2011).

75. J. P. Rathmell, A. E. Desjardins, M. van der Voort, B. H. W. Hendriks, R. Nachabe, S. Roggeveen, D. Babic, M. Soderman, M. Brynolf, and B. Holmstrom, "Identification of the epidral space with optical spectroscopy" Anesthesiology 113, 1406-1418 (2010).

76. A. E. Desjardins, B. H. W. Hendriks, M. van der Voort, R. Nachabe, W. Bierhoff, G. Braun, D. Babic, J. P. Rathmell, S. Holmin, M. Soderman, and B. Holmstrom, "Epidural needle with embedded optical fibers for spectroscopic differentiation of tissue: *ex vivo* feasibility study" Biomed. Opt. Exp. 2(6), 1452-1461 (2011).

77. C, Zhu, T. M. Breslin, J. Harter, and N. Ramanujam, "Model based and empirical spectral analysis for the diagnosis of breast cancer" Biomed. Opt. Exp. 16(19), 14961-14978 (2008).

78. L. G. Wilke, J. Q. Brown, T. M. Bydlon, S. A. Kennedy, L. M. Richards, M. K. Junker, J. Gallagher, W. T. Barry, J. Geradts, and N. Ramanujam, "Rapid noninvasive optical imaging of tissue composition in breast tumor margins" Am. J. Surg. 198, 566-574 (2009)

79. J. Q. Brown, T. M. Bydlon, L. M. Richards, B. Yu, S. A. Kennedy, J. Geradts, L. G. Wilke, M. K. Junker, J. Gallagher, W. T. Barry, and N. Ramanujam, "Optical assessment of tumor resection margins in the breast" IEEE 16(3), 530-544 (2010).

80. T. M. Bydlon, S. A. Kennedy, L. M. Richards, J. Q. Brown, B. Yu, M. K. Junker, J. Gallagher, J. Geradts, L. G. Wilke, and N. Ramanujam, "Performance metrics

of an optical spectral imaging system for intra-operative assessment of breast tumor margins" Opt. Exp. 18(8), 8058-8076 (2010).

81. S. Kennedy, J. Geradts, T. Bydlon, J. Q. Brown, J. Gallagher, M. Junker, W. Barry, N. Ramanujam, and L. Wilke, "Optical breast cancer margin assessment: an observational study of the effects of tissue heterogeneity on optical contrast" Breast Cancer Research 12, R91 (2010).

82. V. Chang, P. S. Cartwright, S. M. Bean, G. M. Palmer, R. C. Bentley, and N. Ramanujam, "Quantitative physiology of the precancerous cervix *in vivo* through optical spectroscopy" Neoplasia 11(4), 325-332 (2009).

83. V. Chang, S. M. Bean, P. S. Cartwright, and N. Ramanujam, "Visible light optical spectroscopy is sensitive to neovascularization in the dysplastic cervix" J. Biomed. Opt. 15(5), 057006 (2010).

84. K. Vishwanath, D. Klein, K. Chang, T. Schroeder, M. W. Dewhirst, and N. Ramanujam, "Quantitative optical spectroscopy can identify long-term local tumor control in irradiated murine head and neck xenografts" J. Biomed. Opt. 14(5), 054051 (2009).

85. H. W. Beumer, K. Vishwanath, L. Puscas, H. R. Afshari, N. Ramanujam, and W. T. Lee, "Detection of squamous cell carcinoma and corresponding biomarkers using optical spectroscopy" Otolaryngology Head and Neck Surgery 144(3), 390-394 (2011).

86. D. J. Robinson, M. B. Karakullukcu, B. Kruijt, S. C. Kanick, R. P. L. Van Veen, A. Amelink, H. J. C. M. Sterenborg, M. J. H. Witjes, and I. B. Tan, "Optical spectroscopy to guide photodynamic therapy of head and neck tumors" IEEE 16(4), 854-862 (2010).

87. J. G. J. V. Aerts, A. Amelink, C. van der Leest, J. P. J. J. Hegmens, A. Hemmes, B. Den Hamer, H. J. C. M. Sterenborg, H. C. Hoogsteden, and B. N. Lambrecht, "HIF1a expression in bronchial biopsies correlates with tumor microvascular saturation determined using optical spectroscopy" Lung Cancer 57, 317-321 (2007).

88. S. C. Kanick, C. van der Leest, R. S. Djamin, A. M. Janssens, H. C. Hoogsteden, H. J. C. M. Sterenborg, A. Amelink, and J. G. J. V. Aerts, "Characterization of mediastinal lymph node physiology *in vivo* by optical spectroscopy during endoscopic ultrasound-guided fine needle aspiration" J. Thora. Onco. 5(7), 981-987 (2010).

89. A. Amelink, O. P. Kaspers, H. J. C. M. Sterenborg, J. E. Van der Wal, J. L. N. Roodenburg, M. J. H. Witjes, "Non-invasive measurement of the morphology and physiology of oral mucosa by use of optical spectroscopy" Oral Oncol. 44, 65-71 (2008).

90. A. Amelink, H. J. C. M. Sterenborg, J. L. N. Roodenburg, M. J. H. Witjes, "Non-invasive measurement of the microvascular properties of non-dysplastic and dysplastic oral leukoplakias by use of optical spectroscopy" Oral Oncol. (2011).

91. A. Amelink, J. Haringsma, and H. J. C. M. Sterenborg, "Noninvasive measurement of oxygen saturation of the microvascular blood in Barrett's dysplasia by use of optical spectroscopy" Gastrointest. Endosc. 70(1), 1-6 (2009).

92. A. Amelink, D. J. Kok, H. J. C. M. Sterenborg, and J. R. Scheepe, "*In vivo* measurement of bladder wall oxygen saturation using optical spectroscopy" J. Biophotonics 4(10), 715-720 (2011).

93. A. E. Cerussi, A. J. Berger, F. Bevilacqua, N. Shah, D. Jakubolowski, J. Butler, R. F. Holocombe, and B. J. Tromberg, "Sources of absorption and scattering contrast for near-infrared optical mammography" Acad. Radiol. 8, 211-218 (2001).

94. A. E. Cerussi, D. Jakubolowski, N. Shah, F. Bevilacqua, R. Lanning, A. J. Berger, D. Hsiang, J. Butler, R. F. Holocombe, and B. J. Tromberg, "Spectroscopy enhances the information content of optical mammography" J. Biomed. Opt. 7(1), 60-71 (2002).

95. A. E. Cerussi, D. Hsiang, N. Shah, R. Mehta, A. Durkin, J. Butler, and B. J. Tromberg, "Predicting response to breast cancer neoadjuvant chemotherapy using diffuse optical spectroscopy" PNAS. 104(10), 4014-4019 (2007).

96. A. E. Cerussi, S. Siavoshi, A. Durkin, C. Chen, W. Tanamai, D. Hsiang, and B. J. Tromberg, "Effect of contact force on breast tissue optical property measurements using a broadband diffuse optical spectroscopy handheld probe" App. Opt. 48(21), 4270-4277 (2009).

97. N. Shah, A. Cerussi, C. Eker, J. Espinoza, J. Butler, J. Fishkin, R. Hornung, and B. J. Tromberg, "Noninvasive functional optical spectroscopy of human breast tissue" PNAS 98(8), 4420-4425 (2001).

98. N. Shah, A. E. Cerussi, D. Jakubolowski, D. Hsiang, J. Butler, and B. J. Tromberg, "Spatial variations in optical and physiological properties of healthy breast tissue" J. Biomed. Opt. 9(3), 534-540 (2004).

99. N. Shah, J. Gibbs, D. Wolverton, A. Cerussi, N. Hylton, and B. J. Tromberg, "Combined diffuse optical spectroscopy and contrast-enhanced magnetic resonance imaging for monitoring breast cancer neoadjuvant chemotherapy: a case study" J. Biomed. Opt. 10(5), 051503 (2005).

100. D. B. Jakubowski, A. E. Cerussi, F. Bevilacqua, N. Shah, D. Hsiang, J. Butler, and B. J. Tromberg, "Monitoring neoadjuvant chemotherapy in breast cancer using quantitative diffuse optical spectroscopy: a case study" J. Biomed. Opt. 9(1), 230-238 (2004).

101. S. Chung, A. Cerussi, C. Klifa, H. Baek, O. Birgul, G. Gulsen, S. Merritt, D. Hsiang, and B. Tromberg, "*In vivo* water state measurements in breast cancer using broadband diffuse optical spectroscopy" Phys. Med. Biol. 53, 6713-6727 (2008).

102. S. H. Chung, A. E. Cerrusi, S. I. Merrit, J. Ruth, and B. J. Tromberg, "Non-invasive tissue temperature measurements based on quantitative diffuse optical spectroscopy (DOS) of water" Phys. Med. Biol. 55, 3753-3765 (2010).

103. S. Kukreti, A. Cerussi, B. Tromberg, and E. Gratton, "Intrinsic near-infrared spectroscopic markers of breast tumors" Dis. Markers 25(6), 281-290 (2008).

104. S. Kukreti, A. Cerussi, W. Tanamal, D. Hsiang, B. J. Tromberg, and E. Gratton, "Characterization of metabolic differences between benign and malignant tumors: High-spectral-resolution diffuse optical spectroscopy" Radiology 254(1), 277-284 (2010).

105. W. Tanamai, C. Chen, S. Siavoshi, A. Cerussi, D. Hsiang, J. Butler, and B. Tromberg, "Diffuse optical spectroscopy measurements of healing in breast tissue after core biopsy: case study" J. Biomed. Opt. 9(1), 230-238 (2004).

106. N. Rajaram, J. S. Reichenberg, M. R. Migden, T. H. Nguyen, and J. W. Tunnell, "Pilot clinical study for quantitative spectral diagnosis of non-melanoma skin cancer" Lasers Med. Surg. 42, 716-727 (2010).

107. N. Rajaram, T. J. Aramil, K. Lee, J. S. Reichenberg, T. H. Nguyen, and J. W. Tunnell, "Design and validation of a clinical instrument for spectral diagnosis of cutaneous malignancy" Appl. Opt. 49(2), 142-152 (2010).

108. G. Zonios, and A. Dimou, "Modeling diffuse reflectance from semi-infinite turbid media: application to the study of skin optical properties" Opt. Exp. 14(9), 8661-8674 (2006).

109. G. Zonios, A. Dimou, M. Carrara, and R. Marchesini "*In vivo* optical properties of melanocytic skin lesions: common nevi, dysplastic nevi and malignant melanoma" Photochem. and Photobio. 86, 236-240 (2010).

110. G. Zonios, and A. Dimou, "Optical properties of human melanocytic nevi *in vivo*" Photochem. Photobio. 85, 298-303 (2009).

111. G. Zonios, A. Dimou, and D. Galaris, "Probing skin interaction with hydrogen peroxide using diffuse reflectance spectroscopy" Phys. Med. Biol. 53, 269-278 (2008).

112. H. Wang, J. Jiang, C. Lin, J. Lin, G. Huang, and J. Yu, "Diffuse reflectance spectroscopy detects increased hemoglobin concentration and decreased oxygenation during colon carcinogenesis from normal to malignant tumors" Opt. Exp. 17(4), 2805-2817 (2009).

113. B. J. Tromberg, A. Cerrusi, N. Shah, M. Compton, A. Durkin, D. Hsiang, J. Butler, and R. Mehta, "Diffuse optics in breast cancer: detecting tumors in pre-menopausal women and monitoring neoadjuvant chemotherapy" Breast Cancer Res. 7(6), 279-285 (2005).

Chapter 2

Estimation of lipid and water concentrations in scattering media withdiffuse reflectance spectroscopy from 900 to 1600 nm

Rami Nachabé

Benno H. W. Hendriks

Adrien E. Desjardins

Marjolein van der Voort

Martin B. van der Mark

Henricus J. C. M. Sterenborg

Abstract

We demonstrate a method to estimate the concentrations of water and lipid in scattering media such as biological tissues with diffuse optical spectra acquired over the range of 900 – 1600 nm. Estimations were performed by fitting the spectra to a model of light propagation in scattering media derived from diffusion theory. To validate the method, spectra were acquired from tissue phantoms consisting of lipid and water emulsions and swine tissues *ex vivo* with a two-fiber probe.

Estimation of lipid and water concentrations in scattering media withdiffuse reflectance spectroscopy from 900 to 1600 nmEstimation of lipid and water concentrations in scattering media with diffuse reflectance spectroscopy from 900 to 1600 nm

Chapter 2

1. Introduction

Diffuse optical spectroscopy (DOS) is a widely used technique that can provide a wealth of clinically-relevant information about the physiological composition of tissues [1-4]. DOS measurements can be obtained non-invasively with an optical fiber probe, making them well-suited for guiding tissue resections during open surgeries. In the field of biomedical spectroscopy, many studies have focused on the estimation of the concentrations of deoxy-hemoglobin (Hb) and oxy-hemoglobin (HbO_2). In the visible and near infrared wavelength ranges, these two chromophores are often the dominant absorbers in biological tissue [1-6]. However, lipid and water concentrations can also be of interest to discriminate between malignant and normal tissues in the breast [7] and to distinguish benign lesions from cysts in breast [8] in particular when employed in fiber-tissue probes.

The estimation of lipid and water concentrations with DOS in the 900-1000 nm wavelength range was addressed by several studies [9-10]. These studies focused on measurements on phantoms made of intralipid or emulsions made with different kinds of oils. However, very few studies have focused on the estimation of lipid and water concentrations in biological tissues with DOS with wavelengths above 1000 nm [11-13]. This wavelength region is potentially attractive from the standpoint of measuring concentrations of water and lipid because absorption features of these chromophores are more prominent than those in the 900-1000 nm range.

Several methods have been demonstrated for estimating optical properties and chromophore concentrations from DOS measurements. Several models have been widely used over the last decade such as analytical solutions derived from diffusion theory [1, 14], differential path length spectroscopy [6, 15], combined frequency-domain and continuous wave broadband diffuse optical spectroscopy [7, 10] and empirical models based on Monte Carlo simulations and experimental phantoms with known optical properties [14, 16-19]. However, these studies were only applied to wavelengths ranges below 1000 nm.

The model proposed in this study utilizes an analytical solution of a diffusion theory approximation to light propagation in scattering media. First described by Farrell *et al.* [14], it expresses the intensity of received light as a function of the optical properties of the medium, i.e. the absorption and the scattering, and the distance between the emitting source and location at the surface of the medium where it is received. To the authors' knowledge, this study represents the first application of the Farrell model to DOS measurements in the wavelength range of 900 to 1600 nm.

To validate the estimation method, DOS measurements were performed on tissue phantoms consisting of custom emulsions for which the lipid and water content were accurately known. Commercial food products, such as butters and margarine, were also utilized as phantoms. To investigate the accuracy of the algorithm with different scattering properties, the particle size distribution (PSD) was varied. To provide an indication of the relevance of this method for deriving concentrations from biological tissue, spectra were acquired from swine tissue *ex vivo*.

2. Materials and methods

2.1 Experimental setup

A 1.3 mm diameter optical probe was used for which the distal end was angled 70 degrees. The probe contains two optical fibers with axis of symmetry parallel to the axis of symmetry of the probe therefore the fibers were separated at the distal end by a distance of 2.48 mm (center to center). Figure 1 shows a sagittal cross-section of the probe where the two lines inside the probe correspond to the axis of symmetry of the two optical fibers. The optical fibers are low-OH fibers from Ocean Optics of 220 microns diameter with a core of 200 microns and an NA of 0.22. One fiber is connected to a Tungsten Halogen broadband light source with an integrated shutter (Ocean Optics, HL-2000-HP) and the second fiber is connected to a spectrometer with a spectral response from 800 to 1700 nm. The spectrometer has a holographic grating (150 grooves/mm and 1250 nm blaze) and an InGaAs sensor array of 512x1 pixels and a pixel size of 500x50 microns (Andor Technology, DU492A -1.7).
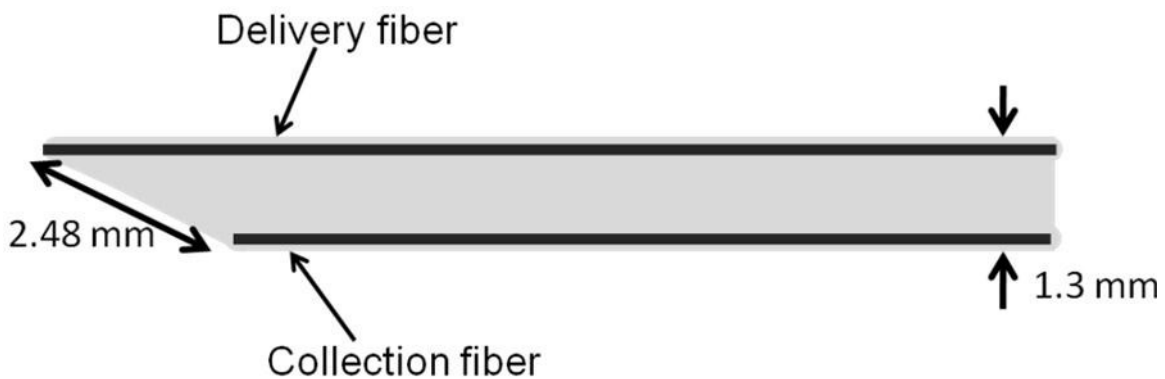

Figure 1. Schematic sketch of the sagittal cross-section of the probe. The distal end is on the left side and the two lines inside the probe correspond to the axis of symmetry of each of the two optical fibers.

2.2 Data pre-processing

The data was acquired via an interface where the integration time can be set between 1μs and several minutes. To suppress the dark current, the detector is thermoelectrically cooled to a temperature of -50ºC. A wavelength calibration was performed to assign a wavelength value to each pixel of the detector. This was done by fitting a second order polynomial to a set of atomic lines from an Argon light source with peaks at known wavelengths.

The spectra $S(\lambda_i)$ that were processed to estimate the amount of lipid and water were calibrated by first acquiring an intensity calibration spectrum $C(\lambda_i)$. To this aim, the reflectance of a white reflectance standard (LabSphere, WS-1-SL) was measured. A custom made probe-holder was made to hold the probe tightly and keep the surface of the optical fibers at the distal end parallel to the reflectance standard at a fixed distance of 2 mm. The white reflectance standard reflects the light uniformly over the probe surface and this spectrum was used as the system response to compensate for the spectral shape

of the light emitted by the lamp and the wavelength-dependent sensitivity of the detector as well as any wavelength-dependent sensitivity in the optics and gratings of the system. This calibration step was followed by a background measurement in order to minimize the impact of the ambient light, dark current and the electric offsets of the detector. As soon as the detector temperature was stable and the light output was stable (roughly 5 minutes after starting our setup), the calibration was performed before each set of measurements.

The spectrum of the tissue can be described as a function of wavelength with the following equation:

$$S(\lambda_i) = \frac{T(\lambda_i) - T_{bg}(\lambda_i)}{C(\lambda_i) - C_{bg}(\lambda_i)} \quad (1)$$

where $S(\lambda_i)$, $T(\lambda_i)$ and $C(\lambda_i)$ are the calibrated tissue spectrum, the effective measured tissue spectrum and the white reflectance standard measured spectrum, respectively. After each tissue measurement, a background measurement $T_{bg}(\lambda_i)$ is acquired by shuttering the light input and subtracted from $T(\lambda_i)$. A background measurement $C_{bg}(\lambda_i)$ is also acquired after the measurement of the white reflectance standard $C(\lambda_i)$.

All the measurements discussed throughout this paper were taken by placing the surface of the optical fibers at the distal end parallel and in contact with the phantoms and the tissues. Having polished fibers at an angle and the size of the optical fibers surface did not hamper our parameter estimation since the distance between the emitting and collecting fibers was sufficiently large (i.e. 2.48 mm) so that it did not influence our spectral fitting. For much shorter fiber distance separation, the effective radius of the optical fibers and the probe of the geometry influence the reflectance measurements and thus should be taken into account [17, 19].

2.3 DOS model and data analysis

Several models [14, 16-20] have been described in literature to express the intensity of light collected by a fiber after several scattering and absorption events in a diffuse medium. The model that is used in this paper is expressed in equation (2) and corresponds to the solution of the diffusion equation for a semi-infinite medium and is a widely accepted model in the field of biomedical photonics [14]. This analytical expression for the diffuse reflectance $R(\mu_a(\lambda), \mu_s'(\lambda), \rho)$ is a function of the distance ρ between the emitting and collecting fiber, the absorption coefficient $\mu_a(\lambda)$ and the reduced scattering coefficient $\mu_s'(\lambda)$ and is given by

$$R(\mu_a(\lambda), \mu_s'(\lambda), \rho)$$
$$= \frac{\mu_s'}{4\pi(\mu_s' + \mu_a)} \left[z_0 \left(\mu_{eff} + \frac{1}{\tilde{r}_1} \right) \frac{e^{-\mu_{eff}\tilde{r}_1}}{\tilde{r}_1{}^2} \right.$$
$$\left. + (z_0 + 2z_b) \left(\mu_{eff} + \frac{1}{\tilde{r}_2} \right) \frac{e^{-\mu_{eff}\tilde{r}_2}}{\tilde{r}_2{}^2} \right] \quad (2)$$

where $\mu_{eff} = (3\mu_a[\mu_a + \mu'_s])^{1/2}$ is the effective attenuation coefficient and $z_0 = (\mu_a + \mu'_s)^{-1}$ is the location of the virtual scattering source. The extrapolated boundary condition is expressed as $z_b = 2AD$ where A is a parameter that depends on the refractive index of the tissue and the surrounding medium. An analytical model for A was described in [14] which expresses A as a function of the relative refractive index and the critical angle. We made the assumptions that the difference in refractive index of tissue and the optical fibers is small and therefore considered that there were no refractive index mismatch which leads to set A=1. Furthermore, $D = (3[\mu_a + \mu'_s])^{-1}$ is the diffusion constant, $\tilde{r}_1 = (z_0^2 + \rho^2)^{1/2}$ is the distance between the single scattering source and the collecting fiber, and $\tilde{r}_2 = ((z_0 + 2z_b)^2 + \rho^2)^{1/2}$ is the distance between the image source and the collecting fiber. In this model, the reduced scattering coefficient $\mu'_s = \mu_s(1 - g)$ is a function of the scattering coefficient μ_s and the anisotropy parameter g. However, the reduced scattering parameter can be approximated by a power law function as $\mu'_s = a\left(\frac{\lambda}{\lambda_0}\right)^{-b}$ with amplitude a and where b is a parameter related to the particle size [4]. Here λ_0 is a normalization wavelength that is set to 1200 nm and thus a corresponds to the reduced scattering at this specific wavelength ($a = \mu'_s(\lambda_0 = 1200$ nm$)$). The absorption coefficient is expressed as:

$$\mu_a(\lambda) = f_{Water} \cdot \mu_a^{Water}(\lambda) + f_{Lipid} \cdot \mu_a^{lipid}(\lambda) \quad (3)$$

where f_{Water} and f_{Lipid} are the water and lipid volume fractions respectively and; $\mu_a^{Water}(\lambda)$ and $\mu_a^{Lipid}(\lambda)$ are the absorption coefficient of water and lipid, respectively.

Data were analyzed by fitting equation (2) to the processed measurement data obtained by equation (1) in order to estimate the optical properties of the probed samples. The parameter ρ that corresponds to the distance between the emitting and collecting fiber is a fixed input argument set at 2.48 mm. Equation (1) and (2) are related by a wavelength-independent constant. This constant corresponds to the ratio between the fraction of light from the calibration standard collected by the fiber and the light from the measured phantoms. The fitting locks onto the spectral shape of the measurements while the constant, which is also derived from the fitting, accounts for the absolute value of the fitting. The fitting procedure of the spectrum is a Levenberg-Marquardt minimization method available in Matlab, which produced an estimation of the parameters f_{Water}, f_{Fat}, a and b. The advantage of this way of fitting is that the absorption coefficients of pure water and pure lipid are input to the model that constrains the spectral shape. The following section describes in detail how we obtained, from measured spectra, these two wavelength dependent absorption coefficients that are essential for the fitting procedure. Moreover, the reduced scattering coefficient is defined by the amplitude parameter a and slope parameter b only. In contrast, refs [7, 10] fit equation (3) to pre-fitted absorption and reduced scattering or measured optical properties for a set of wavelengths.

In order to assess the reliability of the estimated parameters, the goodness of fit was assessed with the covariance matrix [21].

Estimation of lipid and water concentrations in scattering media withdiffuse reflectance spectroscopy from 900 to 1600 nmEstimation of lipid and water concentrations in scattering media with diffuse reflectance spectroscopy from 900 to 1600 nm

Chapter 2

The model holds when the reduced scattering is greater than the absorption and the distance between the optical fibers is greater than the scattering length. Moreover, the medium should be homogenous. In this paper, our phantoms and tissue measurements fulfill these assumptions to some extent.

2.4 Absorption measurement of lipid and water

It should be emphasized that accurate tables of extinction coefficients as a function of wavelength are required to estimate the exact amount of chromophores [15]. In order to ensure the optimization of the fits to the model, we decided to measure our own absorption spectra of water and lipid in the wavelength range of 900 to 1600 nm.

The absorption properties of lipid and water were computed based on transmission measurements at constant temperature of 30 degrees through cuvettes of 0.1, 0.2, 0.5 and 1 cm width with a 1-nm resolution spectrophotometer [Lambda 900 Spectrometer, Perkin Elmer]. These measurements were made at different temperatures ranging from 30 degrees up to 45 degrees to assess the dependence of the absorption values to temperature. It appeared that there were no changes in the absorption of lipid. In the case of water, the higher the temperature the more the 972 nm absorption peak of the water shifts to lower wavelengths (roughly 5 nm for an increase of temperature from 30 to 40 degrees) resulting in a higher absorption value (5% relative increase of the absolute value). Additionally, it appeared that the water absorption at 1192 nm decreases with negligible shift of the peak. Figure 2.a and 2.b show the absorption coefficient of water at 30, 34, 37 and 40 degrees Celsius for different wavelengths ranges (a linear scale was applied to the figure to highlight the differences).
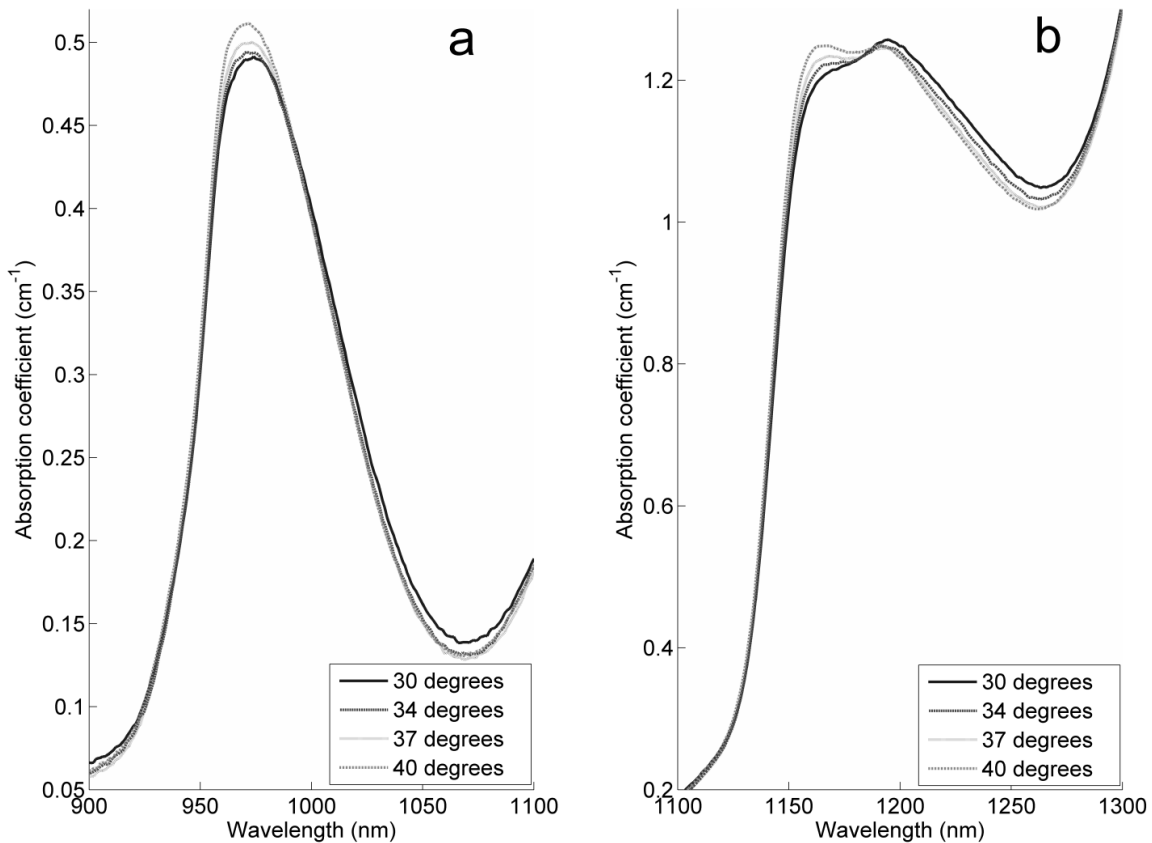
Figure 2. Absorption coefficient of water at different temperature for the wavelength range of 900 to 1100 nm (a) and 1100 to 1300 nm (b). Full line, dashed-line, dotted-line, dashed and dotted line correspond to measurement at 30, 34, 37 and 40 degrees respectively.

Figure 3 depicts the absorption coefficients of water $\mu_a^{Water}(\lambda)$ and lipid $\mu_a^{Fat}(\lambda)$ between 900 and 1600 nm at 30 degrees Celsisus. The type of lipid that was used was 100% beef fat. The absorption peaks at 930, 1040, 1211, 1392 and 1413 nm are in good agreement with measurements performed by Van Veen [22] in the visible-NIR range and Anderson in the NIR–Mid IR range [11]. The water absorption peaks at 972, 1192 and 1453 nm are also in good agreement with the measurments reported by Hale and Querry [23]. Besides, the absolute value of the measured absorption of the lipid and water is in good agreement with that published by Anderson [11].
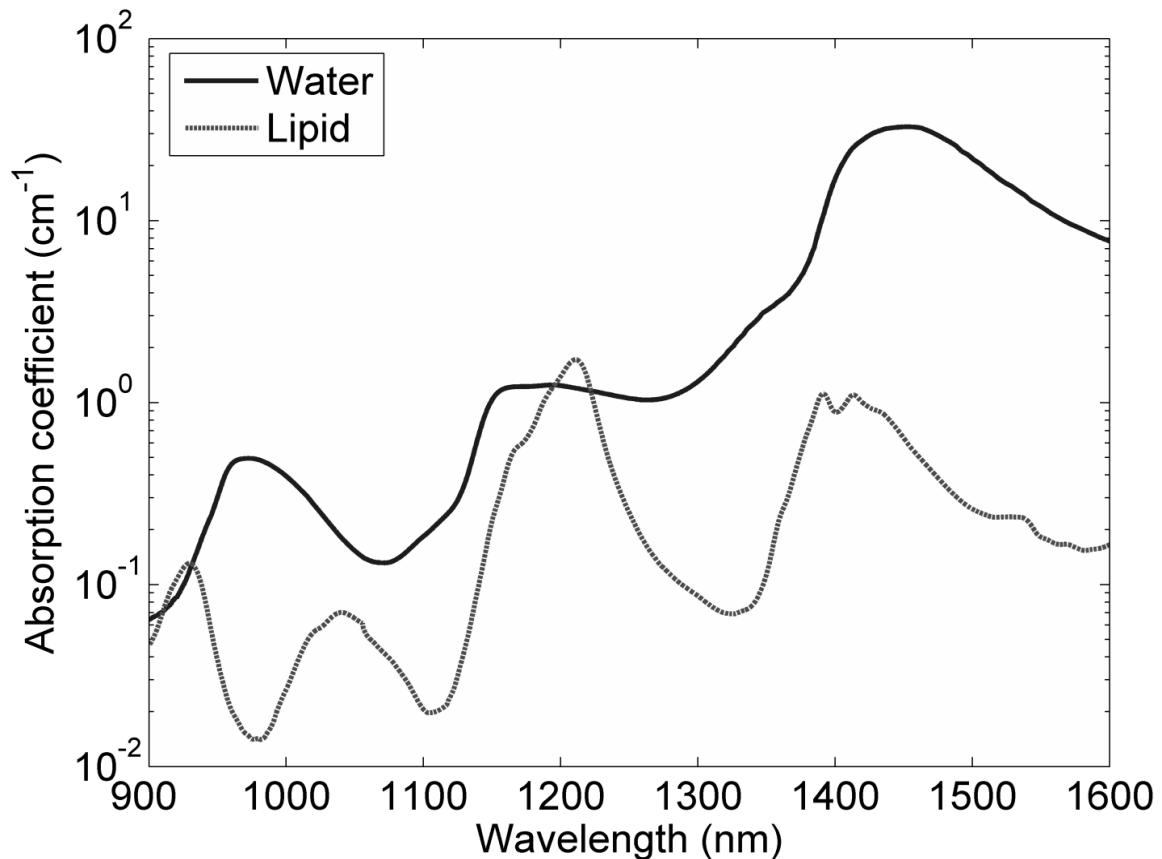
Figure 3. Absorption spectra of water and fat from 900 to 1600 nm.

2.5 Tissue phantom preparation

Phantoms were made by mixing three ingredients: 100% beef fat (commercial frying fat), water, and an emulsifier (Triton X-100 from Roche). According to the technical data sheet of the commercial frying fat, the solid fraction compositions (SFC) were respectively 37% at 20 degree Celsius, 20% at 30 degrees Celsius and 4% at 40 degrees Celsius. The beef fat was melted by heating it to a temperature such that the SFC is less than 1% to make it completely liquid and thus easy to mix with water. Taking this into consideration, the water, the lipid and the emulsifier were heated up to 50 degrees, below the cloud temperature of the Triton X-100 which is 65 degrees and high enough to get a liquid lipid. The amount of emulsifier comprised 4% of the total amount of lipid that was used to prepare the phantoms as suggested by Merritt *et al* [10]. The three ingredients were mixed together at the same temperature with a kitchen blender (Philips HR1363) at high speed for a minute. Samples of 40 ml with 10%, 30% and 60% lipid-to-water ratio were prepared. Half of each solution was poured in separate containers to ultrasonicate the content. An ultrasonication probe (IKA T25 digital Ultra-Turrax) was used to reduce the particle size and thereby to change the scattering properties of the emulsions. Thus six samples were prepared in total, with three different lipid-to-water ratios and different particle size distributions.

The particle size distribution (PSD) of each of the six samples was measured with an apparatus based on the coulter principle (Multisizer 3 coulter counter from Beckman

Coulter). This apparatus could not resolve submicron particle sizes due to the limited dynamic range of the system. The PSD of the six emulsions we prepared in the lab is shown in Figure 4. The first row of figures corresponds to the measurements performed on the samples that were mixed with the kitchen blender. The second row corresponds to the samples which were ultrasonicated. By comparing the PSD of the ultrasonicated with the non-ultrasonicated samples for each of the various lipid-to-water ratios, it appears that the maximum of the distribution shifts to the smaller particle size as expected. However, the standard deviation of the particles size is higher for lower lipid content so if one wants to obtain a more uniform PSD for low lipid content samples it is necessary to use other techniques.
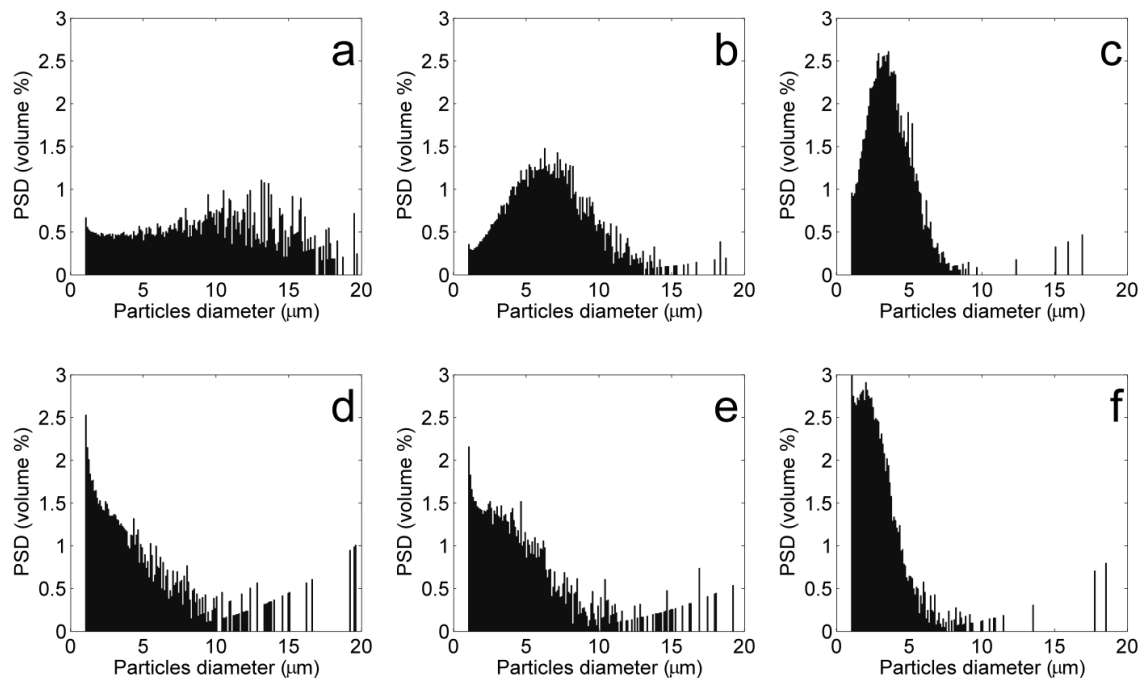
Figure 4. Particle size distribution measurements (PSD) of the emulsions. The top row graphs show the PSD of the emulsions that were blended with a kitchen blender for the 10% (a), 30% (b) and 60% (c) lipid-to-water ratio respectively. The bottom row shows the PSD of the same emulsions after applying an ultrasonic mixing for the 10% (d), 30% (e) and 60% (f) lipid-to-water ratio respectively.

3. Results and discussion

Figure 5 and 6 show the measured spectra at a temperature around 30 degrees of the different lipid and water emulsions (dashed line) and the corresponding best fits (solid line). The presence of lipid in the sample is correlated with the narrow peak at 1211 nm which is an absorption signature of lipid. Moreover, for the sample that contains more lipid than water, the 930 nm absorption peak of lipid is clearly visible in the measured spectrum. Above 1400 nm, the intensity is null and this is due to the very high absorption of water above this specific wavelength given the fiber distance separation.
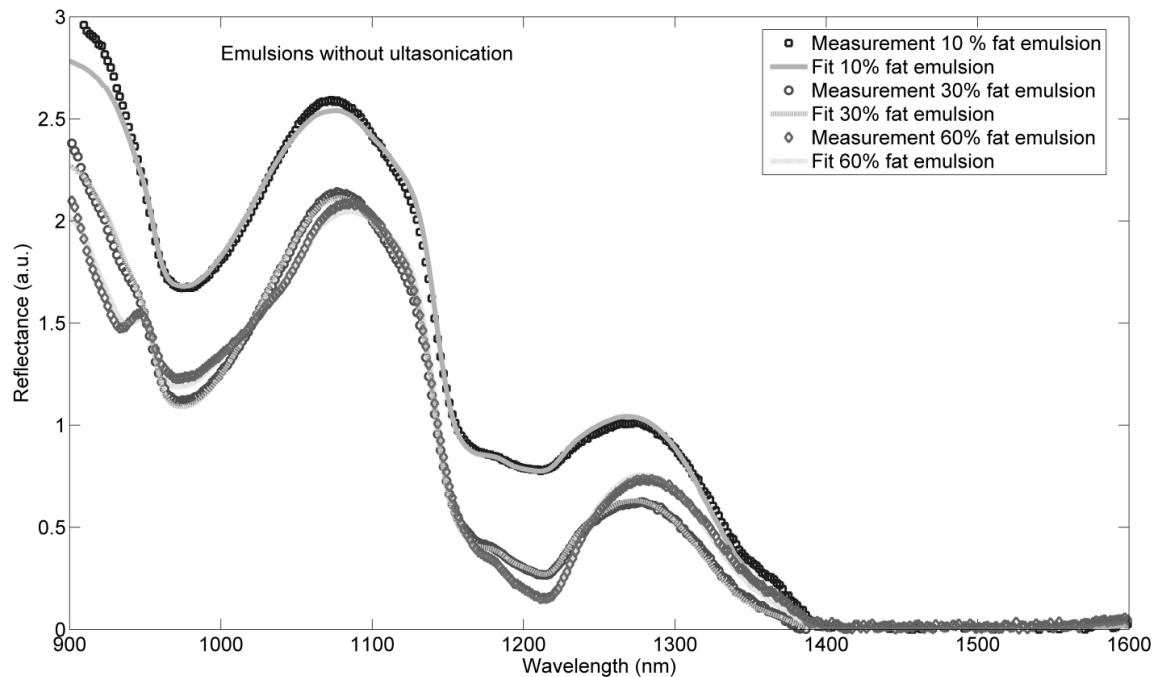
Figure 5. Results of the fitting (Line curves) on the measured spectra (Marker curves) of the different emulsions mixed with a blender.

The estimated parameters for each phantom emulsion are displayed in Table 1 and the variances of the fitted values derived from the calculation of the covariance matrix are displayed between brackets next to the estimated values. The estimation of the lipid-to-water ratio is within 5% error from the true value.

Table 1. Estimation of the optical properties of the custom emulsions without and with ultrasonication.

Lipid-to-water ratio	10 %		30 %		60 %	
Ultra-sonication	Yes	No	Yes	No	Yes	No
Water (%)	86.5 (±2.2)	86.7 (±2.6)	70.1 (±2.2)	69.3 (±1.6)	41.0 (±1.2)	41.7 (±1.0)
Lipid (%)	11.5 (±1.6)	10.8 (±1.9)	29.7 (±2.4)	30.0 (±1.8)	58.2 (±2.3)	57.8 (±1.8)
μ_s' (120 nm) (cm^{-1})	26.3 (±0.4)	29.5 (±0.5)	64.2 (±1.0)	72.3 (±0.8)	84.4 (±1.0)	87.1 (±0.9)
b	0.06 (±0.06)	0.29 (±0.07)	0.40 (±0.06)	0.70 (±0.04)	0.56 (±0.04)	0.87 (±0.04)

The scattering parameter increased with the amount of lipid in the sample. This was expected since the lipid is the only scatterer in the various samples. The estimated

slope value varied with respect to the scatterer size [4]. From the estimated parameters for the slope, it appeared that the slope for the ultrasonicated samples was greater than for the non-ultrasonicated samples. This observation correlates with the PSD measurements as discussed in the beginning of this section i.e. high slope values for samples with small average particles size.
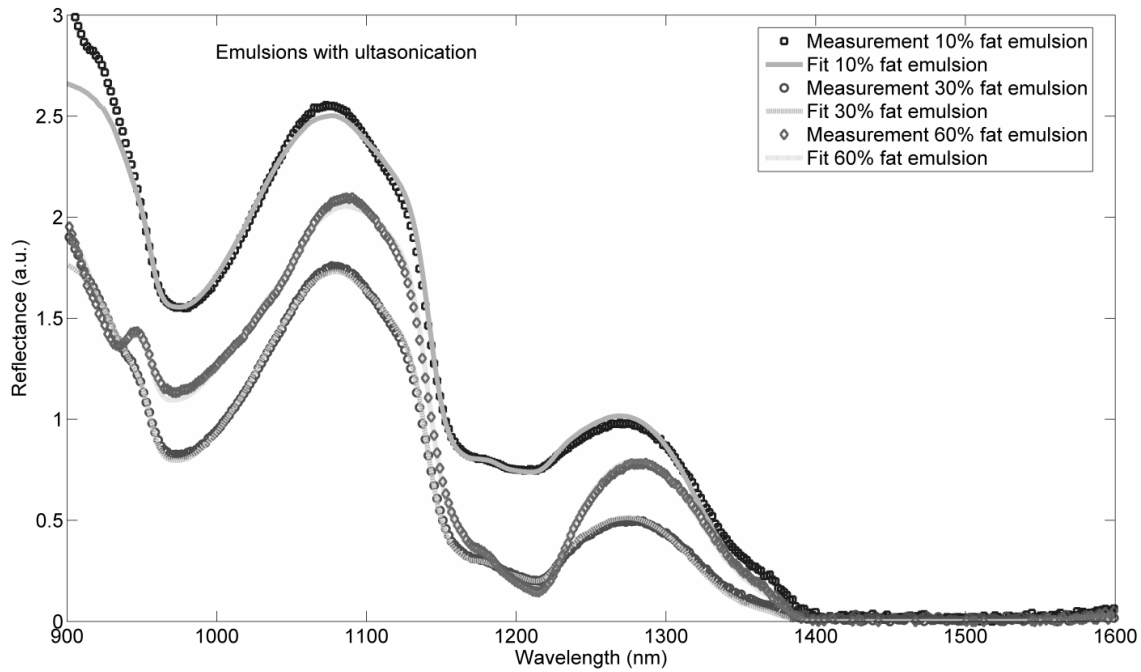
Figure 6. Results of the fitting (Line curves) on the measured spectra (Marker curves) of the different emulsions mixed with a blender and the sample preparation included an ultrasonication process.

In summary, we have shown with the set of custom made phantoms, that we could estimate the amount of water and lipid for different reduced scattering profiles from spectroscopic measurements with our optical probe using a fit to a diffusion approximation model. The following step was to complement the validation with a phantom study with a wider range of lipid-to-water ratios.

Measurements on commercial lipid-water samples such as butter and margarine were also performed at room temperature in order to further validate our method and to highlight the difference in the spectra for a wider range of lipid-to-water ratios. Butter samples with 25%, 35%, 60% and 83% lipid content, and a 40% lipid content margarine sample were also measured. A suspension of 320 mg of $BaSO_4$ in 20 ml of water was prepared so that we had a light scattering sample without lipid in order to mimic muscle-like tissue with 0% lipid.

Figure 7 depicts the different measurements of the commercial butters (dashed line) and the respective best fits (solid line). It is important to notice that the absorption spectra of lipid and water both have an absorption peak around 1200 nm wavelength, but that the widths of these peaks are different. The lipid peak is much narrower than the water peak. For increasing concentration of lipid with respect to water, the measurements

depicted in Figure 7 show a narrowing of the peak in the spectra in the vicinity of 1200 nm.
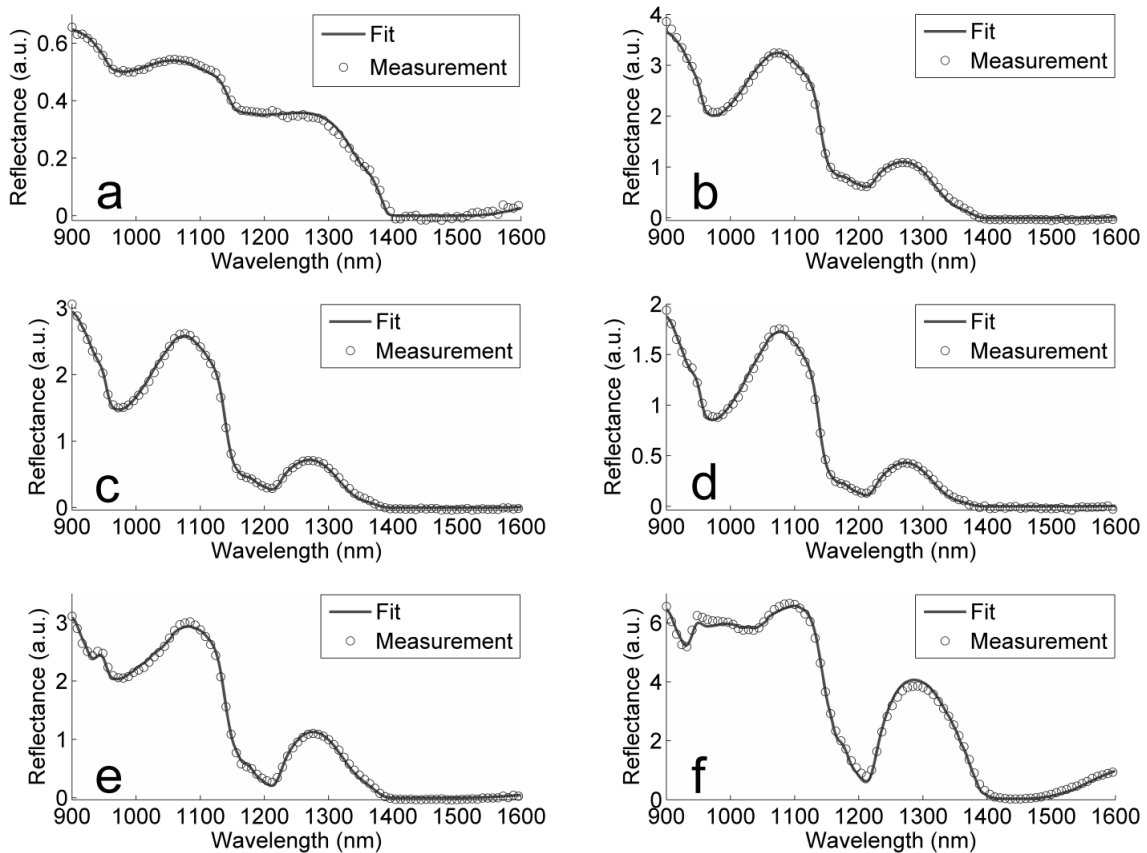

Figure 7. Fits (line curves) to the measured spectra (data points curves) of the solution of BaSO₄ in water (a) and the 25% (b), 35% (c), 40% (d), 60% (e) and 83% (f) lipid content commercial butters and margarine.

The fitting routine was performed on the measurements to estimate the amount of lipid and to compare it with the value written on the packages of the commercial samples. The results from the fits are summarized in Table 2 and reveal that with our method it is possible to retrieve the amount of lipid with a deviation below 5% in comparison with the amount of lipid indicated on the commercial packages.

Several reasons can explain the deviation that were encountered and also the wide range of scattering between the different commercial samples. The fact the absorption spectrum derived from beef fat was used as a reference absorption spectrum in the fitting routine is potentially a source of error since it is a different kind of fat than in butters. Butter, margarine and animal fats (e.g. lard) are known to be composed of different kind of fats which are divided into three families: saturated fat, monounsaturated fat and polyunsaturated fat. Butter is mainly composed of saturated fat (typically 66% saturated, 30% monounsaturated and 4% polyunsaturated fat) whereas margarine is mainly composed of monounsaturated and polyunsaturated fat (typically 21% saturated, 46% monounsaturated and 33% polyunsaturated fat) and animal fat of saturated and

monounsaturated fat (typically 41%, 47% and 12% of respectively saturated, monounsaturated and polyunsaturated fat).

Table 2. Estimation of the optical properties of the BaSO₄ in water (A), 25% lipid content butter (B), 35% lipid content butter (C), 40% lipid content margarine (D), 60% lipid content butter (E) and 83% lipid content butter (F).

	Sample					
	A	B	C	D	E	F
Water (%)	93.6 (±2.5)	74.6 (±1.5)	63.9 (±1.1)	57.3 (±1.1)	36.1 (±0.8)	13.8 (±0.5)
Lipid (%)	0 (±4.6)	25.2 (±1.7)	36.0 (±1.6)	42.7 (±1.8)	63.7 (±2.0)	85.4 (±2.5)
μ_s' (1200 nm) (cm⁻¹)	1.7 (±0.5)	43.7 (±0.4)	68.5 (±0.6)	94.9 (±0.9)	75.0 (±0.7)	53.7 (±0.6)
b	0.55 (±0.03)	0.01 (±0.03)	0.03 (±0.02)	0.33 (±0.02)	0.09 (±0.03)	0.01 (±0.03)

Figure 8 depicts the absorption coefficient of 100% lipid-content oil composed of 10% saturated, 30% monounsaturated and 60% polyunsaturated fat; and the beef fat. One major difference is the presence of an extra absorption peak at 1170 nm and slight difference in the absolute value of the absorption. The most optimal fit would be obtained by using the same type of fat of each commercial sample to estimate the amount of lipid in the various commercial samples. Therefore, we decided to just use the absorption coefficient from the beef fat as the reference for lipid in the fitting. The more unsaturated the fat is, the larger the molecule. As a result, the scattering can vary significantly from sample to sample depending on the distribution of the different types of fat in the butter (e.g. industrial margarine is composed of droplets of 5 to 10 microns diameter size).

In the case of the custom emulsions, it can clearly be seen that the fitting curve between 900 and 1000 nm is not accurate compared to the rest of the wavelength range. This is mainly due to the temperature of the sample. The PSD measurements were done just before the actual acquisition of the spectra and thus the temperature of the samples was not constant. Several studies, such as Ref. [24], showed that the absorption coefficient of water is sensitive to temperature. Thus, the effect of temperature on the absorption coefficient of water is important to take into consideration.

Estimation of lipid and water concentrations in scattering media withdiffuse reflectance spectroscopy from 900 to 1600 nmEstimation of lipid and water concentrations in scattering media with diffuse reflectance spectroscopy from 900 to 1600 nm
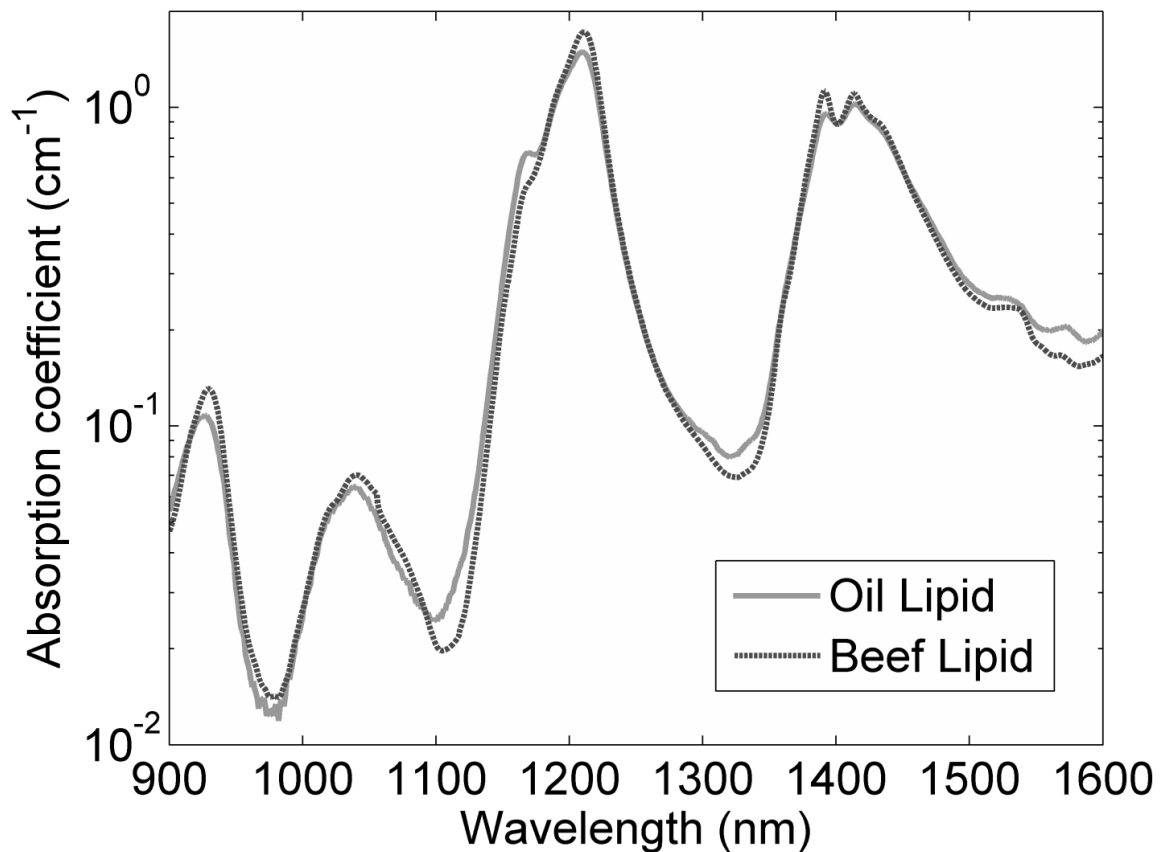
Chapter 2

Figure 8. Comparison between two types of lipids: the dashed line corresponds to the beef lipid whereas the full line curve corresponds to 100% lipid oil (sunflower oil).

Figure 9 shows *ex vivo* measurements (marker curves) of excised tissue from a pig and their respective fit curves (line curves). The measurements were performed on subcutaneous fat, muscle, visceral fat and white matter from the spinal cord by inserting the tip of the probe in the tissue. In Table 3, the estimated parameters for each tissue are summarized. Due to the fact that for the wavelength range of study, hemoglobin and oxygenated hemoglobin have their highest absorption values (roughly 2cm^{-1}) between 900 and 1000 nm, whereas water is the dominant absorber above 1000 nm as pinpointed in [25]; we did not include these two absorbers in the fitting routine. Our *ex vivo* tissue samples did not contain more than 1% of total blood volume fraction and thus hemoglobin did not have any influence on the fit parameters.
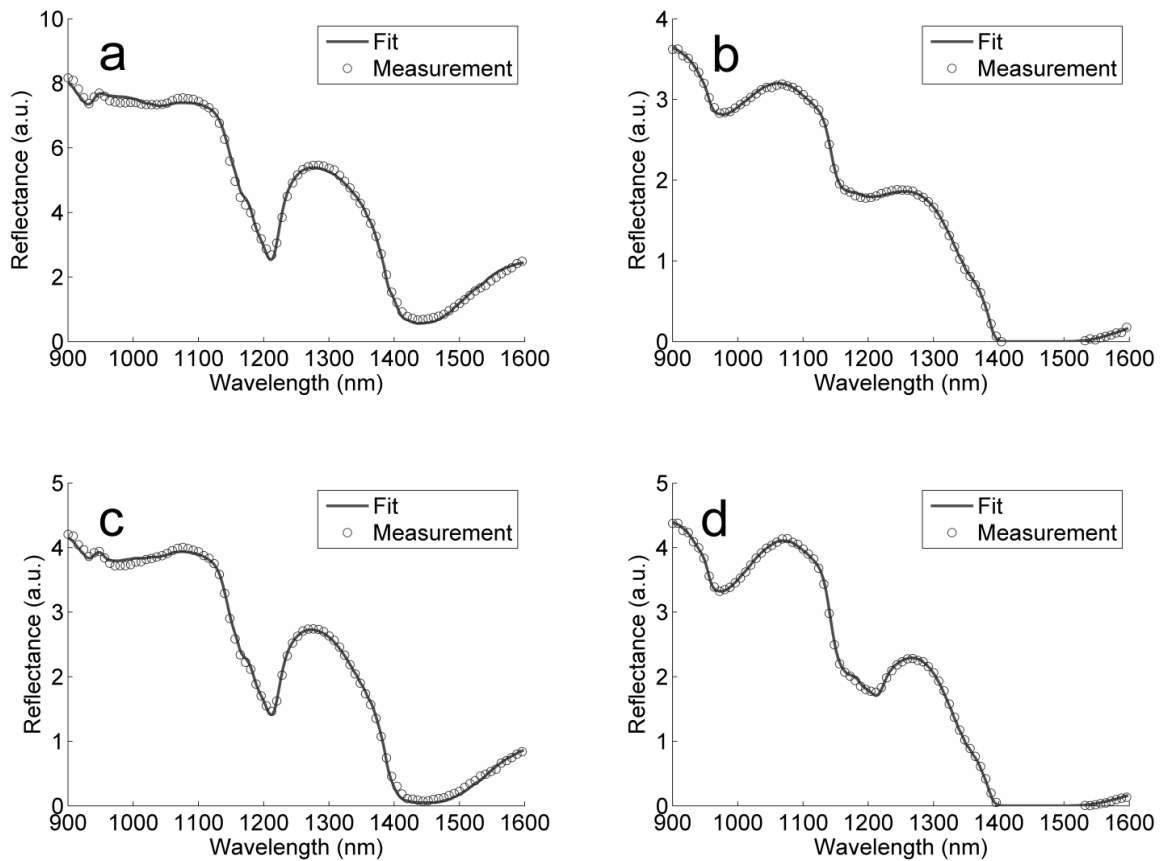
Figure 9. Fits (line curves) to the ex vivo tissue measurements (data point curves) of subcutaneous fat (a), muscle (b), visceral fat (c) and white matter (d).

The estimated values are in agreement with those published from previous studies [26-29]. The composition in lipid and water of the subcutaneous fat was defined in Ref. [28] as being of 14% water and 86% fat which is in perfect agreement with our reported result. The estimation of water and from the muscle measurement is around 75% which is within the range of 60% to 80% of water in muscle whereas the estimated lipid content is roughly 2% within the 0% to 8% range [29]. In visceral fat, the estimation of lipid is 74% within the lipid content range of 60% and 90% in adipose tissue [29]. White matter is mainly axons surrounded with myelin; this physiological property is also in agreement with our finding from the acquired spectrum. From the estimation of the optical properties, it follows that white matter contains about 25% of lipid and the rest is water which is slightly above the reported 20% [29]. The scattering amplitudes that are estimated from the measured tissues are within the range of values available in Ref. [27]. Ref. [6] and Ref. [26] respectively presents the scattering of different tissues and fatty breasts which are comparable to our results. The scattering slope values estimated are within the range of 0.18 to 2.84 described in Ref. [26].

The absorption and reduced scattering coefficient can be computed thanks to the relation described in equation (3) and the power law function, respectively. Figure 10 shows the optical properties for each of the *ex* vivo tissue measurements that were computed once the fit parameters in table 3 were obtained.
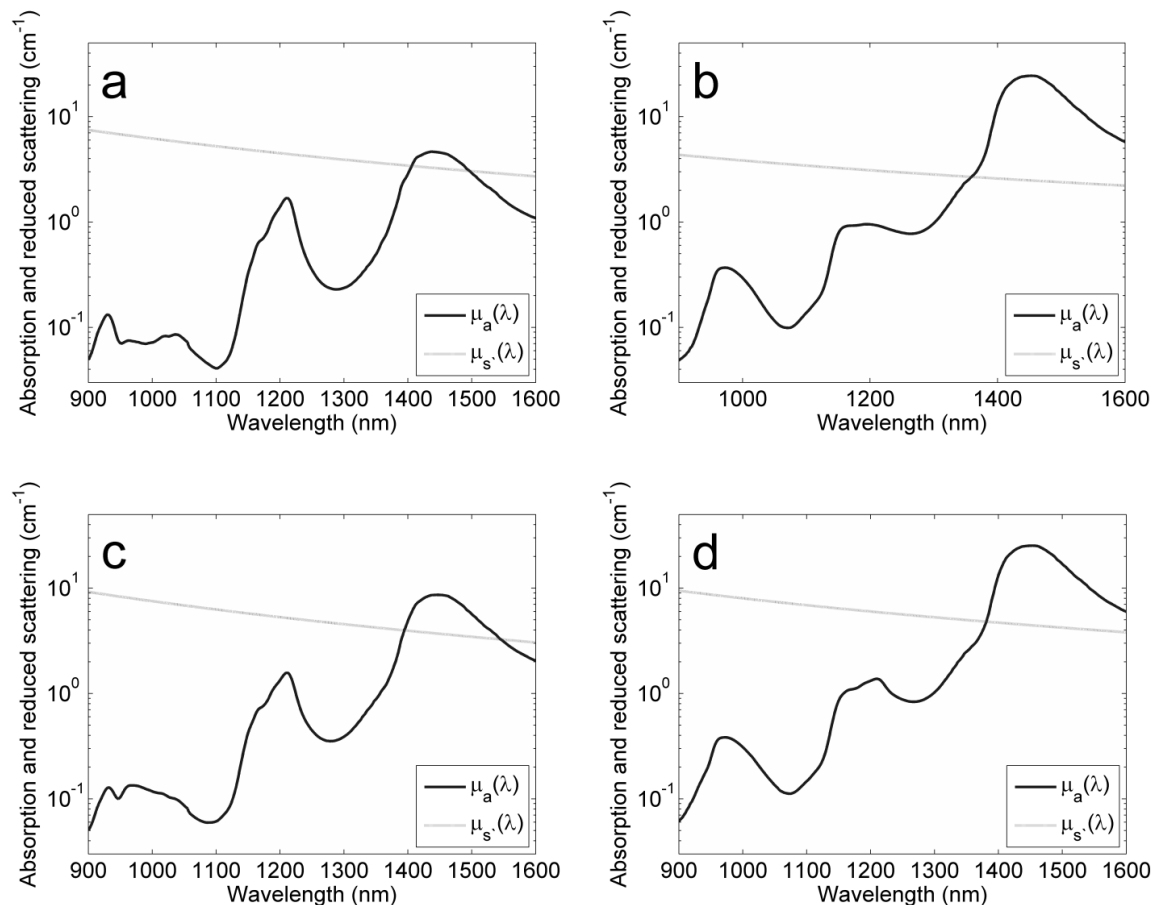
Estimation of lipid and water concentrations in scattering media withdiffuse reflectance spectroscopy from 900 to 1600 nmEstimation of lipid and water concentrations in scattering media with diffuse reflectance spectroscopy from 900 to 1600 nm

Chapter 2

Figure 10. Absorption and reduced scattering coefficients of the ex vivo tissue measurements of subcutaneous fat (a), muscle (b), visceral fat (c) and white matter (d).

Although the reduced scattering coefficient above 1350 nm is lower than the absorption coefficient, it is still possible to estimate the proper volume fraction of water and lipid. In particular, the fact that water and lipid have sharp peaks in the 900 to 1000 nm wavelength range and around 1200 nm makes the estimation of the amount of water and lipid in the full range of 900 to 1600 nm still possible. For wavelengths below 1350 nm, the reduced scattering coefficient is larger than the absorption coefficient. Since the reduced scattering coefficient is modeled by a power law for the whole wavelength range, the reduced scattering amplitude and slope constrained the fit and thus it is possible to evaluate the optical properties, despite the fact that absorption can be higher than the reduced scattering above 1350 nm. However, for low-lipid content tissues with low reduced scattering, care must be taken since the method may become inaccurate. If the fit deviates from the measurements for wavelengths above 1350 nm, this would be a sign that the applied model is no longer valid. For high-water content tissue, the signal can become null, given our fiber distance separation which also allows for a more stable fit. One can notice that around 1200 nm the absorption coefficient of water and lipid have roughly the same absolute values making this ratio less sensitive to errors in the fit model.

Table 3. Estimated optical properties of various swine tissues measured ex vivo.

	Subcutaneous fat	Muscle	Visceral fat	White matter
Water (%)	12.2 (±0.5)	74.6 (±2.2)	24.9 (±0.9)	76.8 (±1.5)
Lipid (%)	89.6 (±5.0)	1.9 (±1.2)	74.0 (±4.1)	26.4 (±1.3)
μ_s' (1200 nm) (cm^{-1})	4.5 (±0.6)	3.1 (±0.2)	5.3 (±0.7)	6.0 (±0.3)
b	1.76 (±0.21)	1.17(±0.08)	1.92 (±0.33)	1.58 (±0.24)

4. Conclusion

To accurately estimate water and lipid content in a small volume (e.g. a few mm^3), a higher extinction is preferable than that of the commonly used 900 to 1000 nm absorption peaks. In the wavelength range from 900 to 1600 nm, one finds more absorption peaks with higher absorption coefficients. We performed accurate measurements of the water and lipid extinction coefficient to allow us to obtain a reliable estimation of these two chromophores in mixtures.

We have demonstrated in this study that we can accurately estimate the amount of lipid and water with a diffuse optical spectroscopy technique in the near infrared for wavelengths in the range of 900 to 1600 nm. The phantom study proved that we can estimate, within less than 5% error, the amount of lipid and water in the various samples that were prepared. Furthermore, by applying ultrasonication to our phantoms to shrink the particle size, we have seen that the slope of the reduced scattering increased without effecting the estimation of water and lipid content. The validation of our method was completed with the estimation of the concentration of lipid in commercial food samples with known lipid content.

This phantom study is complemented by *ex vivo* measurements and analysis that provides information on the optical properties of different tissues. The amount of lipid and water will prove to be important for discriminating healthy and cancerous tissue. With our method, we could provide real-time clinical feedback to physicians on the amount of lipid and water of tissue with the goal to classify between normal, malignant and benign samples when acquiring spectra from fiber-tissue probes.

5. Acknowledgments

References

1. G. Zonios, L. T. Perelman, V. M. Backman, R, Manoharan, V. D. Fitzmaurice, Jacques Van Dam, and Michael S. Feld, "Diffuse reflectance spectroscopy of human adenomatus colon polyps *in vivo*", Appl. Opt. **38**, 6628-6637 (1999)

2. J. R. Mourant, I. J. Bigio, J. Boyer, T. M. Johnson and J. Lancey, "Elastic scattering spectroscopy as a diagnostic for differentiating pathologies in the gastrointestinal tract: preliminary testing", J. Biomed. Opt. **1** , 192-199 (1996)

3. M. P. L. Bard, A. Amelink, V. N. Hegt, W. J. Graveland, H. J. C. M. Sterenborg, H. C. Hoogsteden and J. G. J. V. Aerts, "Measurement of Hypoxia-related parameters in bronchial mucosa by use of optical spectroscopy", American Journal of respiratory and critical care medicine **171** (2005)

4. G. Zonios and A. Dimou, "Light scattering spectroscopy of human skin *in vivo*", Optics Express **17**, 1256-1267 (2009)

5. G. Zonios, J. Bykowski, and N. Kollias, "Skin melanin, hemoglobin, and light scattering properties can be quantitatively assessed *in vivo* using diffuse reflectance spectroscopy", J. Invest. Dermatol. **117**, 1452-1457 (2001)

6. A. Amelink, O.P. Kaspers, H. J. C. M. Sterenborg, J. E. Van der Wal, J. L. N. Roodenburg, M. J. H. Witjes, "Non-invasive measurement of the morphology and physiology of oral mucosa by use of optical spectroscopy" Oral Oncology **44**, 65-71 (2008)

7. A. E. Cerussi, N. Shah, D. Hsiang, A. Durkin, J. Butler and B. J. Tromberg, "*In vivo* absorption, scattering of 58 malignant breast tumors determined by broadband diffuse optical spectroscopy", J. Bio. Opt. **11**(4), 04 4005 (2006)

8. A. Pifferi, P. Taroni, A. Torricelli, F. Messina, R. Cubeddu, and G. Danesini, "Four wavelength time-resolved optical mammography in the 680-980 nm range", Opt Lett. **28**, 1138-1140 (2003)

9. R. Michels, F. Foschum, and A. Kienle, "Optical properties of fat emulsion", Optics Express **16**, 5907-5925 (2008)

10. S. Merritt, G. Gulsen, G. Chiou, Y. Chu, C. Deng, A. E. Cerussi, A. J. Durkin, B. J. Tromberg, O. Nalcioglu, "Comparison of water and lipid content measurements using diffuse optical spectroscopy and MRI in emulsion phantoms", Technology in cancer research and treatment **2**, 563-569, (2003)

11. R. R. Anderson, W. Farinelli, H. Laubach, D. Manstein, A. N. Yaroslavsky, J. Gubelli, K. Jordan, G. R. Neil, M. Shinn, W. Chandler, G. P. Williams, S. V. Benson, D. R. Douglas, and H. F. Dylla, "Selective photothermolysis of lipid-rich tissues: a free electron laser study", Lasers Surg. Med. **38**, 913-919 (2006)

12. A. N. Bashkatov, E. A. Genina, V. I. Kochubey, and V. V. Tuchin, "Optical properties of human skin, subcutaneous and mucous tissues in the wavelength range from 400 to 2000 nm", J. Phys. D: Appl. Phys. **38**, 2543-2555 (2005)

13. T. L. Roy, and S. N. Thennadil, "Optical properties of human skin in the near infrared wavelength range of 1000 to 2200 nm", J. Biomed. Optics **6**, 167-176 (2001)

14. T. J. Farrell, M. S. Patterson, and B. Wilson, "A diffusion theory model of spatially resolved, steady-state diffuse reflectance for the non-invasive determination of tissue optical properties", Med. Phys. **19**, 879-888 (1992)

15. A. Amelink, T. Christiaanse, and H. J. C. M. Sterenborg, "Effect of hemoglobin extinction coefficient spectra on optical spectroscopic measurements of blood oxygen saturation", Optics Letter **34**, No. 10, 1525-1527 (2009)

16. P. R. Bargo, S. A. Prahl, T. T. Goodell, R. A. Sleven, G. Koval, G. Blair, and S. L. Jacques, "*In vivo* determination of optical properties of normal and tumor tissue with white light reflectance and an empirical light transport model during endoscopy", J. Biomed. Opt. **10**, (2005)

17. G. Zonios, I. Bassukas, and A. Dimou, "Comparative evaluation of two simple diffuse reflectance models for biological tissue applications", Appl. Optics **47**, 4965-4973 (2008)

18. J. Sun, K. Fu, A. Wang, A. W. H. Lin, U. Utzinger, and R. Drezek, "Influence of fiber optic probe geometry on the applicability of inverse models of tissue reflectance spectroscopy: computation models and experimental measurements", Appl. Opt. **45**, 8152-8162 (2006)

19. R. Reif, O. A'Amar, and I. J. Bigio, "Analytical model of light reflectance for extraction of the optical properties in small volumes of turbid media", Appl. Opt. **46**, 7317-7328 (2007)

20. A. Amelink, H. J. C. M. Sterenborg, M. P. L. Bard, and S. A. Burgers, "*In vivo* measurement of the local optical properties of tissue by use of differential path-length spectroscopy", Opt. Lett. **29**, 1087-1089 (2004)

21. A. Amelink, D. J. Robinson, and H. J. C. M. Sterenborg, "Confidence interval on fit parameters derived from optical reflectance spectroscopy measurements", J. Biomed. Opt. **13**, (2008)

22. R. L. P. van Veen, H. J. C. M. Sterenborg, A. Pifferi, A. Torricelli, E. Chikoidze, and R. Cubeddu, "Determination of visible near-IR absorption coefficients of mammalian fat using time- and spatially resolved diffuse reflectance and transmission spectroscopy", J. Biomed. Optics **10**, (2005)

23. G. M. Hale and M. R. Querry, "Optical constants of water in the 200-nm to 200-micrometer wavelength region", Appl. Opt. **12**, 555-563 (1973)

24. K. Buijs, and G. R. Choppin, "Near-Infrared of the structure of water", J. Chem. Phy. **39**, 2035-2041, (1963)

25. A. Roggan, M. Friebel, K. Dorchel, A. Hahn, and G. Muller, "Optical properties of circulating human blood in the wavelength range of 400-2500 nm", J. Biomed. Optics **4**, (1999)

26. R. L. P. van Veen, W. Verkruysse, and H. J. C. M. Sterenborg, "Diffuse reflectance spectroscopy from 500 to 1060 nm by correction for inhomogenously distributed absorbers", Opt. Let. **27**, (2002)

27. V. V. Tuchin, "Tissue optics: light scattering methods and instruments for medical diagnosis" Second edition, SPIE tutorial text in optical engineering,170-191 (SPIE Press, Washington, 2007)

Estimation of lipid and water concentrations in scattering media withdiffuse reflectance spectroscopy from 900 to 1600 nmEstimation of lipid and water concentrations in scattering media with diffuse reflectance spectroscopy from 900 to 1600 nm

Chapter 2

28. J. Wang and R. N. Pierson, "Disparate hydration of adipose and lean tissue require a new model for body water distribution in man", Journal of Nutrition **106**, 1687-1693, (1976)

29. F. A. Duck, "Physical properties of tissue: a comprehensive reference book", Academic Press, Harcourt Brace Jovanovich, Publishers, (1990)

Chapter 3

Estimation of biological chromophores using diffuse reflectance spectroscopy: benefit of extending the UV-VIS wavelength range to include 1000 to 1600 nm

Rami Nachabé

Benno H. W. Hendriks

Marjolein van der Voort

Adrien E. Desjardins

Henricus J. C. M. Sterenborg

Abstract

With an optical fiber probe, we acquired spectra from swine tissue between 500 and 1600 nm by combining a silicon and an InGaAs spectrometer. The concentrations of the biological chromophores were estimated by fitting a mathematical model derived from diffusion theory. The advantage of our technique relative to those presented in previous studies is that we extended the commonly-used wavelength ranges of 500 and 1000 nm to include the range of 1000 to 1600 nm, where additional water and lipid absorption features exist. Hence, a more accurate estimation of these two chromophores is expected when spectra are fitted between 500 and 1600 nm than between 500 and 1000 nm. When extending the UV-VIS wavelength range, the estimated total amount of chromophores approached 100% of the total as present in the probed volume. The confidence levels of the water and lipid related parameters increases by a factor of four.

1. Introduction

Diffuse optical spectroscopy (DOS) has been widely used as a tool for determining optical properties of tissue. Such tools are investigated as an aid for detecting cancers [1-4], for monitoring changes in tissue optical properties that reflect morphological and physiological changes [5], and for monitoring therapy response for instance in photodynamic therapy [6]. Several methods exist to extract optical properties of tissue-like diffuse media such as time-resolved [7-8], frequency-domain [9], spatially-resolved continuous wave [10-11], combined frequency-domain and continuous wave broadband diffuse optical spectroscopy [3], and empirical models based on Monte-Carlo simulations and experimental phantoms of known optical properties [5, 12-13].

Most of the studies [2, 14-19] focused on the estimation of chromophore concentrations in the ultraviolet and visible wavelength range (typically between 350 and 800 nm) where deoxygenated and oxygenated hemoglobin are the main optical absorbers. Measurements in breast [2, 14-15] or on the skin [16] showed absorption from additional chromophores such as beta-carotene and melanin, respectively. Several studies used wavelength ranges extended up to 1000 nm [3, 17-18] in order to determine concentrations of water and lipid, which have distinct absorption peaks at 972 and 930 nm, respectively [18-19]. These studies [3, 17-19] used probes with fiber separations up to 1.7 cm. For probes with much shorter separation between the collecting and emitting fibers, the absorption dips in the reflectance due to lipid and water will also be much smaller since the transmitted light decays exponentially with the path length and the absorption coefficient (Beer's law). Thus, measurements of water and lipid content in this wavelength region using photon pathlengths of a few mm only will not be very accurate. Extending the commonly used wavelength range of 500 to 1000 nm up to 1600 nm enables the measurement of additional absorption peaks of water and lipid with absorption values that are an order of magnitude higher than those in the lower wavelength region. Although not extensively reported, not constraining the fitting parameters [17] often leads to an estimated summed volume of chromophores significantly different from a total of 100%. This could either mean that there is a biological entity within the probed volume that does not have optical absorption peaks (e.g. melanin) or that the model requires modifications. The present paper aims to investigate if the use of this extended wavelength region increases the accuracy of the measurement without constraining any of the fit parameters.

The applicability of an analytical solution that derives from diffusion theory to determine the optical properties was extensively studied and validated for wavelength ranges below 1000 nm [10-11]. In a former study [20], the absorption coefficients of water and lipid between 900 and 1600 nm ($I_{900 \to 1600}$) were measured and the applicability of the diffusion theory model to this wavelength range was validated for phantom measurements with known amounts of water and lipid.

To investigate whether having an additional spectrometer that can measure in the infrared up to 1600 nm can effectively improve the estimation of water and lipid concentrations, we compared the values of the parameters derived from the fits applied for two different wavelength ranges: the classical range from 500 to 1000 nm ($I_{500 \to 1000}$)

and the extended range from 500 to 1600 nm ($I_{500 \to 1600}$). Measurements on *in vivo* swine tissues were performed with combined silicon and InGaAs spectrometers and were analyzed by fitting an analytical model to the two wavelength ranges of interest. In order to assess the improvements to the fits when adding the InGaAs spectrometer, we compared the confidence intervals [21] of the estimated parameters obtained from both fits.

2. Methods
2.1 Instrumentation

A schematic diagram of the setup is shown in Fig. 1. The setup consists of an optical probe with three optical fibers with a NA of 0.22, a spectrometer with a silicon detector (Andor Technology, DU420A-BRDD), a spectrometer with an InGaAs detector (Andor Technology, DU492A-1.7) and a tungsten halogen broadband light source with an integrated shutter (Ocean Optics, HL-2000-HP). The optical probe has a diameter of 1.3 mm and its distal end is polished at an angle of 20 degrees in order to ease its insertion in the animals. The probe contains three 200 μm core diameter optical fibers with axis of symmetry parallel to the axis of symmetry of the probe. One optical fiber is connected to a light source. The second and third optical fibers are connected to the spectrometer with a silicon detector and the spectrometer with an InGaAs detector, respectively. The silicon detector is a matrix of 1024 by 255 pixels with pixel size of 26x26 microns whereas the InGaAs detector is a single array of 512 pixels with a pixel size of 500x50 microns. The spectral resolution for the silicon and InGaAs detectors are 4 and 10 nm, respectively. At the tip of the probe, the three optical fibers distal ends form an isosceles triangle in such a way that both collecting fibers were embedded side by side with a center-to-center distance of 370 microns and separated by a distance of 2.48 mm from the emitting fiber.
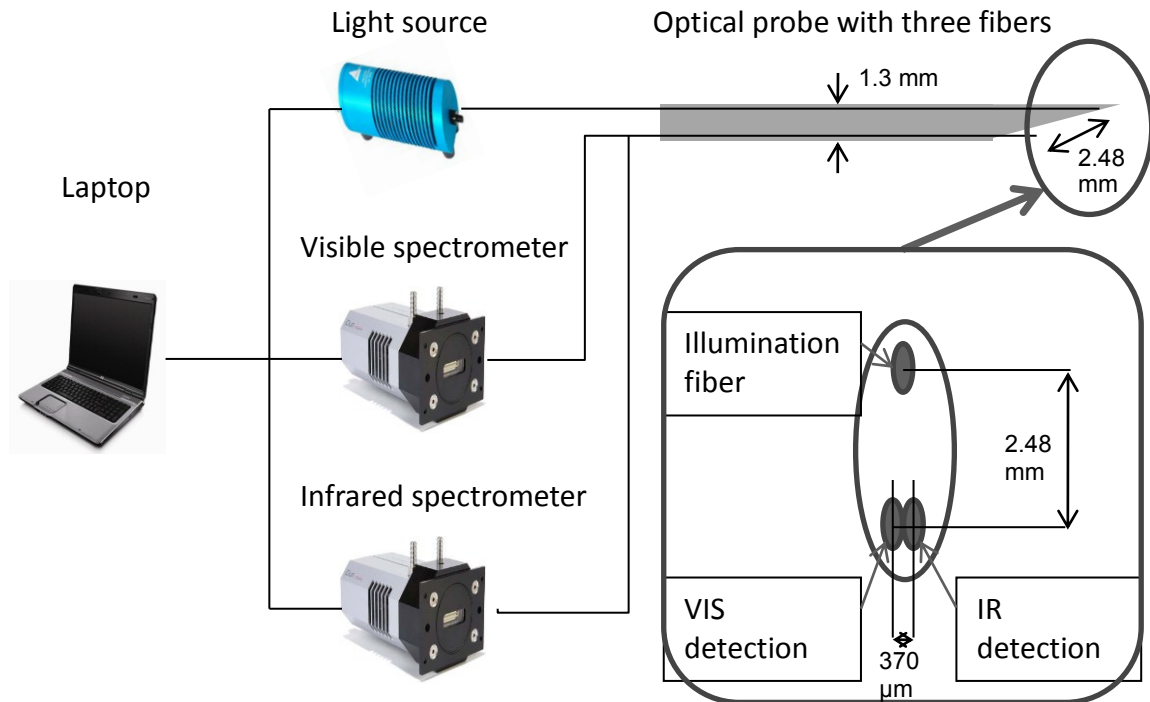
Figure 1. Sketch of the optical setup: it consists of a halogen lamp that is connected to a fiber and two spectrometers that are connected to two separate fibers that are located next to each other at the tip of the probe.

2.2 Data acquisition and pre-processing

The calibration and the generation of the spectra acquired with the InGaAs spectrometer was described elsewhere [20]. Briefly, the calibration procedure consisted of assigning a wavelength value to each pixel of the detector, then measuring a white reflectance standard to compensate for the spectral shape of the light emitted by the lamp and the wavelength-dependant sensitivity of the detector and the optics in the grating of the system; and a background measurement to compensate for the dark current and electric offsets of the detector. The tissue spectra are computed by dividing the measured spectra in tissue corrected for background by the calibration measurement of the white reflectance standard. We applied the same process for the spectra acquired with the silicon spectrometer. The spectra obtained from both spectrometers have an overlapping wavelength range between 900 and 1000 nm which was used to compute the matching factor to form continuous spectra from 500 and 1600 nm. For all the acquired spectra, the matching factor should be ideally equal to one but is on average 0.9±0.3. This is due to the fact that the light is collected via two separate fibers and in an inhomogeneous medium there might be a sampling error. To avoid this artifact, one single fiber should be connected to a fiber splitter in order to collect the light from the same sampling volume. However, using a fiber splitter will reduce the light transmission by more than 50% and thus longer integration times might be needed to achieve a good signal-to-noise ratio making real-time feedback impossible.

2.3 Tissue measurements

Measurements were performed on three anaesthetized swine after approval from the internal review board of the animal lab facility. The swine were originally dedicated for a different clinical study; however we were allowed to perform our measurements. Spectra were taken at different locations within the animals, where the position of the tip of the optical probe was confirmed by X-ray or ultrasound imaging. Tissue boundaries were avoided in order to measure in volumes as homogenous as possible.

The integration time for a single spectrum acquisition ranges from a quarter of a second to two seconds but most spectra were acquired with an integration time of one second yielding to a signal-to-noise ratio of 200:1 and 120:1 for the Silicon and InGaAs detector, respectively. However, all measurements on the white reflectance standard for calibration were made with an integration time of two seconds. For both spectrometers, the integration time was kept the same. In total, we obtained 296 spectra including 143 measurements on various fatty layer structures (from which 56 subcutaneous fat in the back of the pig and 87 visceral fat in the epidural space) and 153 muscle measurements in the back of the three animals.

2.4 Analytical model

The acquired spectra were fitted with the analytical model developed by Farrell *et al.* [10] which has the absorption coefficient $\mu_a(\lambda)$ and the reduced scattering coefficient $\mu_s'(\lambda)$, in cm^{-1}, as input arguments. In a previous work [20], this model was described and used to estimate water and lipid concentration and its validity was shown in the 900-1600 nm wavelength range.

A double power law function was used to describe the wavelength dependence of the reduced scattering (cf. Eq. (1)). The first law corresponds to the contribution of Mie scattering [22-24] whereas the second power law corresponds to the contribution of Rayleigh scattering which can be significant in the visible wavelength range [25]. The reduced scattering is expressed in cm^{-1} and is a function of wavelength:

$$\mu_s'(\lambda)=a\left(\rho_{MR}\left(\frac{\lambda}{\lambda_0}\right)^{-b}+(1-\rho_{MR})\left(\frac{\lambda}{\lambda_0}\right)^{-4}\right). \qquad (1)$$

In Eq. (1), λ_0 is a normalization wavelength set to 800 nm and the parameter *a* corresponds to the reduced scattering amplitude at this specific wavelength. The reduced scattering corresponds to the sum of Mie and Rayleigh scattering and, therefore, ρ_{MR} is defined as the Mie-to-Rayleigh fraction of the scattering. The reduced scattering slope of the Mie scattering is denoted *b* and is related to the particle size [26].

The main chromophores that absorb in the visible and near infrared are hemoglobin derivatives in the blood (deoxy-hemoglobin and oxy-hemoglobin) [27, 28], water and lipid [18, 20, 29]. Instead of modeling the absorption coefficient $\mu_a(\lambda)$ as the

sum of absorption coefficients weighted by the respective concentrations of the four chromophores of interest, we decided to express the absorption coefficient as:

$$\mu_a(\lambda) = C(\lambda) v_{BL} \mu_a^{Blood}(\lambda) + v_{WL}\left((1-\alpha_{WL})\mu_a^{Water}(\lambda) + \alpha_{WL}\mu_a^{Lipid}(\lambda)\right). \quad (2)$$

The absorption coefficients of hemoglobin in blood, water and lipid are $\mu_a^{Blood}(\lambda)$, $\mu_a^{Water}(\lambda)$ and $\mu_a^{Lipid}(\lambda)$, respectively; and are depicted in Fig. 2. The absorption coefficient of blood is multiplied by the blood volume fraction $v_{BL} = [Hb] + [HbO_2]$, where $[Hb]$ and $[HbO_2]$ correspond to the concentration of deoxygenated and oxygenated hemoglobin, respectively; and a correction factor $C(\lambda)$ that accounts for the effect of pigment packaging [30] and alters for the shape of the absorption spectrum. The correction factor is given by

$$C(\lambda) = \frac{1 - \exp\left(-2R\mu_a^{Blood}(\lambda)\right)}{2R\mu_a^{Blood}(\lambda)} \quad (3)$$

where R corresponds to the effective vessel radius. The absorption coefficient of hemoglobin in blood is given by

$$\mu_a^{Blood}(\lambda) = \alpha_{BL}\mu_a^{HbO_2}(\lambda) + (1-\alpha_{BL})\mu_a^{Hb}(\lambda). \quad (4)$$

Here $\mu_a^{HbO_2}(\lambda)$ and $\mu_a^{Hb}(\lambda)$ represent the basics extinction coefficient spectra of oxygenated and deoxygenated hemoglobin, respectively, assuming a blood hemoglobin content of 150 g/l (typical value for human blood). The oxygenated hemoglobin fraction in the total amount of hemoglobin is noted $\alpha_{BL} = [HbO_2]/([HbO_2] + [Hb])$ and is commonly known as the blood oxygen saturation. Similarly $v_{WL} = [H_2O] + [Lipid]$ and $\alpha_{WL} = [Lipid]/([Lipid] + [H_2O])$ where $[Lipid]$ and $[H_2O]$ correspond to the concentration of lipid (density of 0.86g/ml) and water, respectively. They correspond to the total amount of water and lipid in the probed volume and the lipid fraction within this volume, respectively. This way of relating the water and lipid parameters in the expression of the absorption coefficient defined in Eq. (2) rather than estimating separately the water and lipid volume fraction corresponds to a minimization of the covariance of the basis functions for fitting resulting in a more stable fit.

From the acquired spectra we derive eight parameters: a, b, ρ_{MR}, R, v_{BL}, α_{BL}, v_{WL} and α_{WL}. Hence three parameters define the reduced scattering coefficient, and five components the absorption coefficient, from which three are related to blood and the two other to water and lipid. Although not commonly used when fitting beyond 500 nm, a Rayleigh scattering term and the correction factor for pigment packaging were used [17]. According to an F-test with p<0.001 [31], the fit is improved for 64% and 89% of the data

when considering Rayleigh scattering and the pigment packaging factor in the model, respectively. The spectra were fitted over the 500-1000 nm and 500-1600 nm wavelength ranges using a non constrained nonlinear least-squares Levenberg-Marquardt fitting algorithm. The confidence intervals on the estimated parameters at a confidence level of 99% were assessed from the square roots of the diagonal elements of the covariance matrix [21].
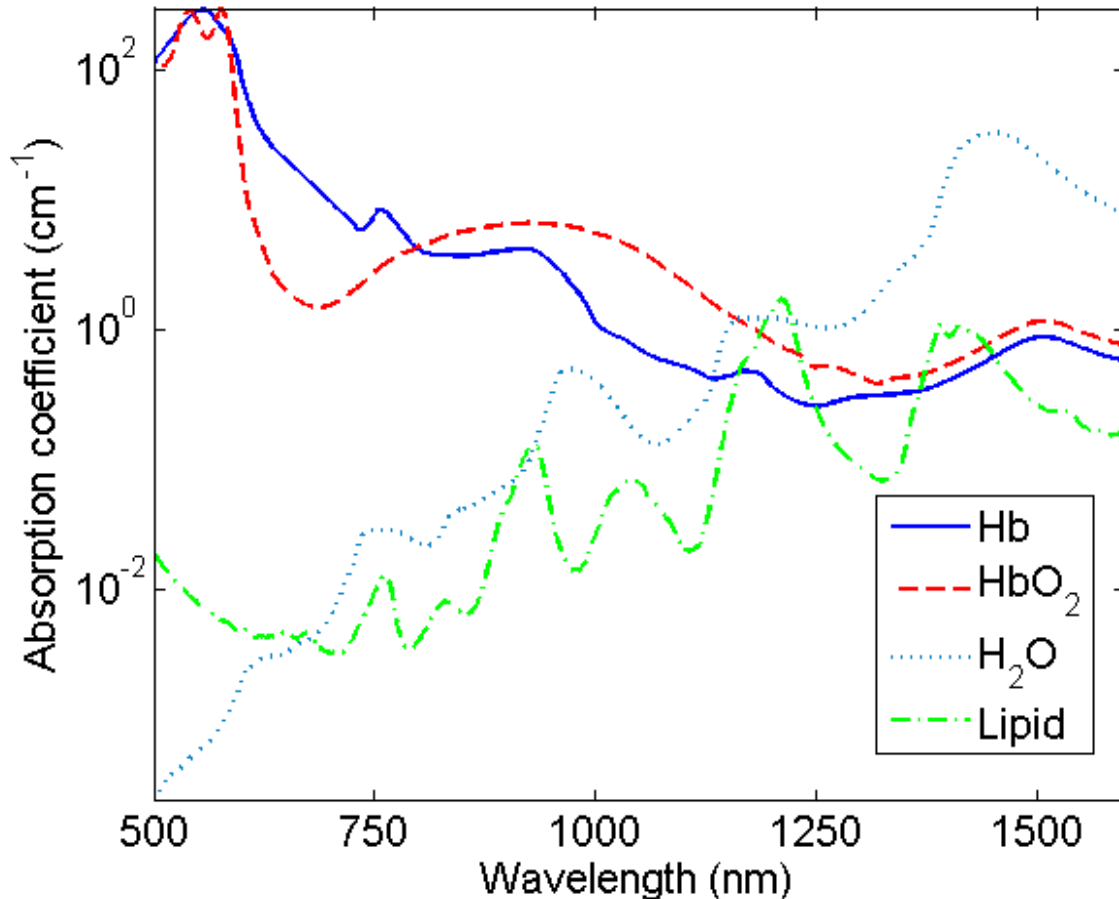

Figure 2. Absorption coefficient of deoxygenated hemoglobin (full line), oxygenated hemoglobin (dashed line), water (dotted line) and lipid (dashed-dotted line) from 500 to 1600 nm.

A detailed study on the validation and calibration of the model in the 900-1600 nm wavelength range was described in Ref. 20 based on phantom experiments. Given the extensive literature descriptions of the model validation in the 500-1000 nm wavelength range [10-11], only a validation comparable to the one in Ref. 10 was performed to make sure that the model estimates the correct blood volume faction with our setup. A set of phantoms that consist of human blood diluted in a scattering solution (80 mg of oil-free scattering powder in PBS) were prepared to obtain blood volume fractions of 0.5, 1, 5 and 10% of a total phantom volume of 10 ml for each dilution. As soon as the blood was extracted from the subject, a blood oxygen saturation of 98.9% was measured with a blood gas analyzer (RapidPoint 405) before the preparation of the phantoms. When

comparing the estimated blood volume fractions with the actual values, a linear regression of equation y=0.97x-0.01 was obtained (R^2=0.993). A blood oxygen saturation of 96.1±2.3% was estimated which is in good agreement with the value estimated by the blood gas analyzer.

3. Results and discussion

Fig. 3 shows typical diffuse optical spectra measured on a muscle and a fat layer respectively with the corresponding fit over $I_{500\to1600}$. Moreover, it also shows the residual.
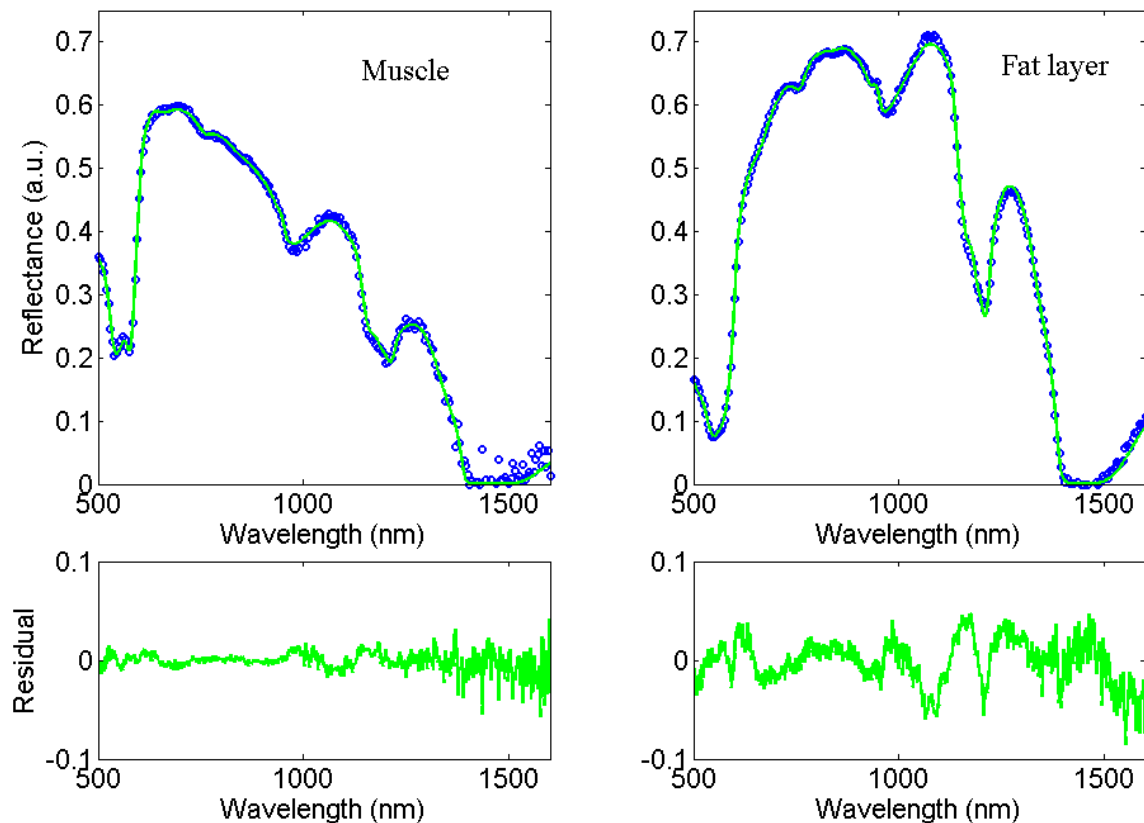

Figure 3. Typical measurement of muscle and fat layer (dotted line), and the corresponding fits and residuals between 500 and 1600 nm (full line).

When measuring with a silicon spectrometer, it is possible to estimate the amount of water and lipid due to the absorption peaks of these two chromophores that exist in the 900 to 1000 nm wavelength range. However it is interesting to investigate whether any advantages arise from adding an InGaAs spectrometer to accurately estimate the amount of water and lipid. Table 1 summarizes the average values that are estimated from fitting at $I_{500\to1000}$ (Fit 1) and $I_{500\to1600}$ (Fit 2) and their respective average confidence intervals. It is clear from Table 1 that the total amount of chromophores (i.e. $v_{BL}+v_{WL}$) is closer to 100% when the fit is applied over $I_{500\to1600}$. As a matter of comparison, there is a

significant difference (t-test, p<0.05) from a 100% total amount of chromophores for 67% of the spectra fitted over $I_{500 \rightarrow 1000}$ and only 28% when fitted over $I_{500 \rightarrow 1600}$.

Among the 28% of the spectra for which the t otal amount of chromophores is statistically different from 100%, a few spectra gave numbers statistically higher than 100% when fitting between 500 and 1600 nm. A number of effects might be the cause of this. The temperature of the animals decreased during the measurement sessions thus the water temperature in the body decreased. Therefore, the absorption coefficient of water which is temperature dependant need to be adapted in the fitting [20]. Moreover the type of lipid that is used in the fit is from beef fat and not from swine. As lipid is composed of different types of fat such as unsaturated, monosaturated and polysaturated fat; the beef fat can be chemically different from swine fat. This difference in fat provides differences in absorption coefficient of lipid [20]. As it can be seen in the residual curve of the fat layer measurement in Fig. 3, the largest deviations are around 1100 and 1200 nm where the main difference in absorption values of fat exists as presented in Fig. 8 of reference 20.

Table 1. Average estimated parameters and corresponding average confidence intervals for fat layers and muscle as derived from fitting over $I_{500 \rightarrow 1000}$ (Fit 1) and $I_{500 \rightarrow 1600}$ (Fit 2).

Parameters	Fat layers (n=143)		Muscle (n=153)	
	Fit 1	Fit 2	Fit 1	Fit 2
	500-1000	500-1600	500-1000	500-1600
a (cm^{-1})	5.2±1.7	6.3±0.7	4.0±1.0	4.6±0.4
b	0.7±0.3	0.8±0.1	0.7±0.3	0.6±0.1
ρ_{MR} (%)	98±8	98±6	93±10	87±6
R (µm)	23±9	15±5	27±8	19±4
v_{BL} (%)[*]	1.0±0.3	0.8±0.1	2.4±0.6	2.0±0.2
α_{BL} (%)	21±5	21±7	27±5	25±5
v_{WL} (%)[*]	112±30	95±5	114±42	89±5
α_{WL} (%)	60±5	68±1	10±13	18±3

[*]Significant difference from 100% of the sum with p<0.05 for 67% of all the spectra when Fit 1 is applied and 28% of the spectra when Fit 2 is applied.
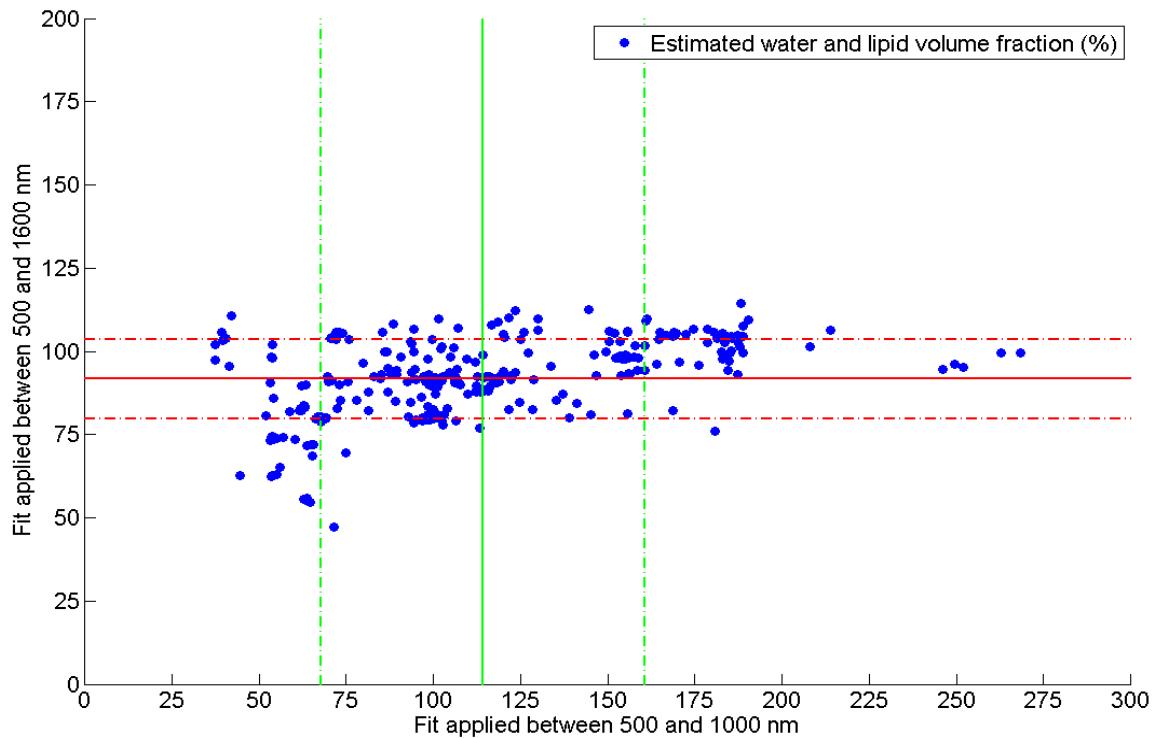
Figure 4. Estimated water and lipid volume fraction (dots) when fitting between 500 and 1000 nm versus 500 and 1000 nm and the respective mean and standard deviation.

Figure 5 shows in a log-log scale for each of the parameters v_{BL}, α_{BL}, v_{WL} and α_{WL} the comparison of the confidence intervals for the two wavelength ranges of interest. Computing the average of the ratio of the confidence intervals obtained for both fits shows that extending the wavelength range up to 1600 nm narrows the confidence intervals of the water and lipid related parameters on average by a factor of four and the total blood volume fraction of a factor of two whereas no improvements are seen for the blood saturation levels.

A Spearman's rank correlation test [17] is performed to assess the correlation between the values obtained for the two different wavelength ranges. Such a test determines whether strong correlation exists between the estimated parameters for both wavelength ranges. However, there could be high correlation despite a different dispersion (statistical variability) of the values and therefore a statistical test is required to determine whether the standard deviations of the estimated values are of the same order for both fits. The Levene's test [32] was applied to investigate whether there are significant differences between the dispersion of the estimated parameters from both fits.
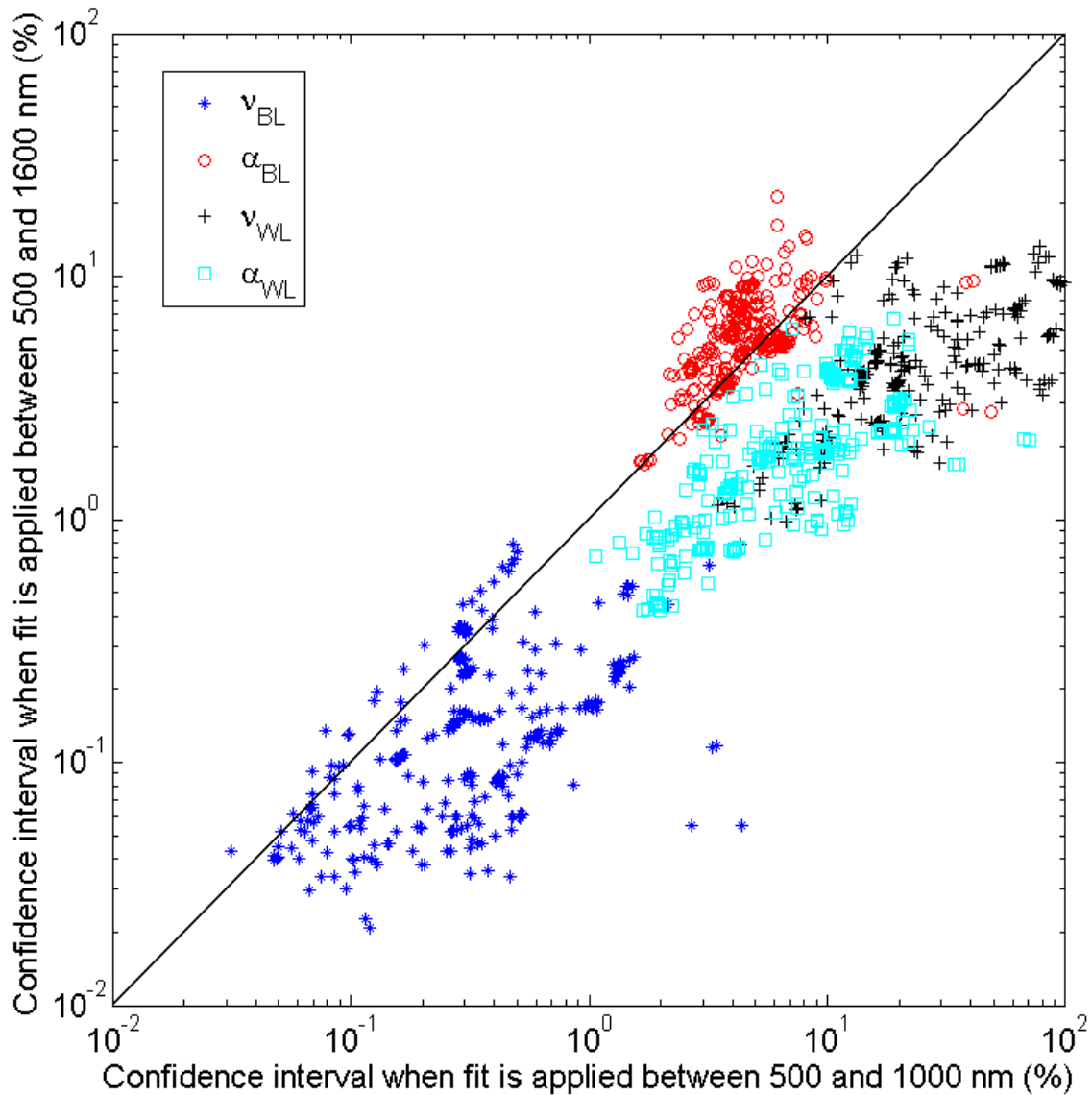
Figure 5. Comparison of confidence intervals obtained when fit is applied between 500 and 1000 nm and 500 and 1600 nm of the blood volume fraction (stars), blood saturation (circles), water and lipid volume fraction (crosses) and lipid fraction in the total volume (squares).

Table 2 provides the Spearman's rank correlation coefficient for each parameter and indicates which parameters have significant differences with respect to the values and the dispersion of the values based on the analysis of variance and Levene's tests. The confidence intervals of the Spearman's correlation coefficients were computed by using a Fisher's z-transformation [32] with $p < 0.05$. From Table 2, it is clear that adding the 900-1600 nm data induces statistical differences for ν_{WL} and α_{WL}. One can notice that the lipid fraction parameter is the only parameter that does show significant difference in values but not in dispersion. As seen in Table 1, the lipid fraction estimated over $I_{500 \rightarrow 1000}$ is smaller than when fitting over $I_{500 \rightarrow 1600}$. However the values do vary between 0 and

100% and therefore there is a non-significant difference in the dispersion of the estimated value for this parameter. From Table 2, the Spearman's correlation factors are considered to be high (above 0.8) except for the scattering related parameter and the water and lipid volume fraction.

Although there is a significant difference in the reduced scattering amplitude values a for both fits, their correlation factor is only as high as 0.75 and not more. It is thus interesting to know the cause of this effect. For this purpose, a t-test was performed for all the estimated values of reduced scattering to know which data points give significant differences with $p < 0.05$. Fig. 6.a. depicts the data points for which there is no significant difference in the estimated reduced scattering amplitude values for both fits (blue stars) and those for which there is difference (red diamonds) according to the t-test.

Table 2. Spearman's correlation rank for each estimated parameter and parameters that show significant differences in value and dispersion.

Parameters	Spearman's correlation factor of the estimated values	Significant difference of the estimated parameters values with $p < 0.05$ for the analysis of variance test	Significant difference of the dispersion of the estimated parameters with $p < 0.05$ for the Levene's test
a (cm^{-1})	0.75 ± 0.05	+	+
b	0.22 ± 0.10	-	-
ρ_{MR} (%)	0.55 ± 0.08	+	+
R (µm)	0.82 ± 0.03	-	-
v_{BL} (%)	0.81 ± 0.04	-	-
α_{BL} (%)	0.87 ± 0.02	-	-
v_{WL} (%)	0.50 ± 0.09	+	+
α_{WL} (%)	0.90 ± 0.02	+	-

From Fig. 6.a, it can be seen that the values which are different all have low reduced scattering amplitudes. By plotting the corresponding water and lipid volume fractions that were estimated (cf. Fig. 6.b.), we observe that the values that show significant differences in the reduced scattering amplitudes mainly corresponds to the spectra for which v_{WL} was estimated to be larger than 100% when the fit is applied between 500 and 1000 nm. When fitting up to 1600 nm, the estimated v_{WL} for these spectra approaches 100% and the reduced scattering amplitude becomes higher. Thus when the reduced scattering amplitude of the measured tissues is low (i.e. smaller than the inverse of the fiber distance separation of 5cm^{-1}), its covariance with v_{WL} is high which leads to an incorrect estimation of the latter parameter. Besides, a change in the estimated

reduced scattering amplitudes also induces a change in the estimation of the blood volume fraction (cf. Fig. 6.c.). The amount of blood is overestimated when fitting over the 500 to 1000 nm wavelength range in case of low reduced scattering samples. Otherwise, the blood volume fraction values are not altered whilst the amount of water and lipid volume fraction is improved.

By fitting up to 1600 nm where additional absorption features of water and lipid exist, the covariance with the reduced scattering as defined in Eq. (1) is smaller and still allows for a reliable fit when the reduced scattering coefficient is low. In case the fit is performed between 500 and 1000 nm, for small reduced scattering values, the scattering is underestimated whereas the absorption due to water, lipid and blood is overestimated.
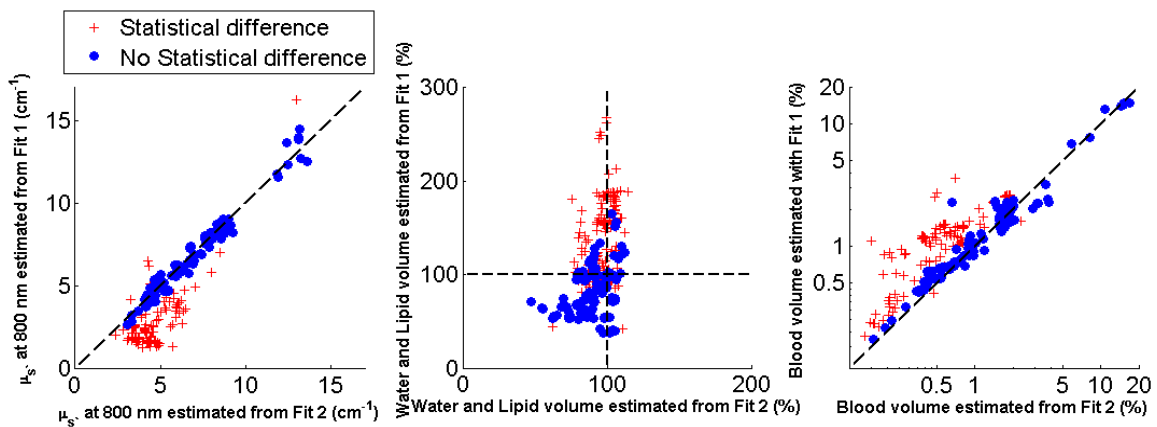

Figure 6. Comparison of the estimated reduced scattering amplitude when fit is applied between 500 and 1000 nm (Fit 1) and 500 and 1600 nm (Fit 2) where the circles correspond to no statistical difference in absolute values and the crosses with statistical differences (a). The corresponding water and lipid volume fractions shows larger deviation from 100% when Fit 1 is applied (b). The corresponding blood volume fraction shows overestimations of the values when Fit 1 is applied (c).

4. Conclusion

We have presented a comparison on the estimation of the absorption and reduced scattering related parameters when fits are applied to spectra measured in the commonly used wavelength range of 500 to 1000 nm acquired with a silicon detector and the wavelength range of 500 to 1600 nm obtained when adding an InGaAs spectrometer. The fitting procedure was deliberately performed without constraining the values. Judging on the confidence intervals computed for each estimated parameter, having an additional spectrometer to measure up to 1600 nm provides up to four time higher confidence on the estimation of the water and lipid related parameters due to the presence of additional absorption features above 1000 nm. The blood volume fraction showed a factor of two improvement in the confidence intervals when fitting up to 1600 nm. The covariance between the reduced scattering amplitude and the water and lipid volume fraction is high

for low reduced scattering amplitudes leading to errors in the estimation of absorbers if the fit is applied between 500 and 1000 nm.

5. Acknowledgments

References

1. B. M. L. Bard, A. Amelink, V. N. Hegt, W. J. Graveland, H. J. C. M. Sterenborg, H. C. Hoogsteden, and J. G. J. V. Aerts, "Measurement of hypoxia-related parameters in bronchial mucosa by use of optical spectroscopy", Am. J. Respir. Crit. Care Med. **171**, 1178-1184 (2005).

2. Z. Volynskaya, A. S. Haka, K. L. Bechtel, M. Fitzmaurice, R. Shenk, N. Wang, J. Mazemi, R. R. Dasari, and M. S. Feld, "Diagnosing breast cancer using diffuse reflectance spectroscopy and intrinsic fluorescence spectroscopy", J. Biomed. Opt. **13**, 024012 (2008).

3. A. E. Cerussi, N. Shah, D. Hsiang, A. Durkin, J. Butler, and B. J. Tromberg, "In vivo absorption , scattering of 58 malignant breast tumors determined by broadband diffuse optical spectroscopy", J. Biomed. Opt. **11**, 044005 (2006).

4. J. Q. Brown, L. G. Wilke, J. Geradts, S. A. Kennedy, G. M. Palmer, and N. Ramanujam, "Quantitative optical spectroscopy: a robust tool for direct measurement of breast cancer vascular oxygenation and total hemoglobin content in vivo", Cancer Res. **69**, 2919-2926 (2009).

5. A. Amelink, H. J. C. M. Sterenborg, M.P. L. Bard, and S. A. Burgers, "In vivo measurement of the local optical properties of tissue by use of differential path-length spectroscopy", Opt. Lett. **29**, 1087-1089 (2004).

6. A. Amelink, A. P. van den Heuvel, W. J. De Wolf, D. J. Robinson, and H. J. C. M. Sterenborg, "Monitoring PDT by means of superficial reflectance spectroscopy", J. Photochem. Photobio. **79**, 243-251 (2005).

7. S. Andersson-Engels, R. Berg, A. Persson, and S. Svanberg, "Multispectral tissue characterization with time-resolved detection of diffusely scattered white light", Opt. Lett. **18**, 1697-1699 (1993).

8. A. Pifferi, A. Torricelli, P. Taroni, A. Bassi, E. Chikoidze, E. Giambattistelli, and R. Cubeddu, "Optical biopsy of bone tissue: a step toward the diagnosis of bone pathologies", J. Biomed. Opt. **9**, 474-480 (2004).

9. S. Fantini, M. A. Francechini-Fantini, J. S. Maier, S. A. Walker, B. Barbieri, and E. Gratton, "Frequency-domain multichannel optical detector for noninvasive tissue spectroscopy and oximetry", Opt. Eng. **34**, 32-42 (1995).

10. T. J. Farrell, M. S. Patterson, and B. Wilson, "A diffusion theory model of spatially resolved, steady-state diffuse reflectance for the non-invasive determination of tissue optical properties", Med. Phys. **19**, 879-888 (1992).

11. G. Zonios, L. T. Perelman, V. M. Backman, R. Manoharan, V. D. Fritzmaurice, J. Van Dam, and M. S. Feld, "Diffuse reflectance spectroscopy of human adenomatus colon polyps in vivo", Appl. Opt. **38**, 6628-6637 (1999).

12. R. Reif, O. A'Amar, and I. J. Bigio, "Analytical model of light reflectance for extraction of the optical properties in small volumes of turbid media", Appl. Opt. **46**, 7317-7328 (2007).

13. G. Zonios, I. Bassukas, and A. Dimou, "Comparative evaluation of two simple diffuse reflectance models for biological tissue applications", Appl. Optics **47**, 4965-4973 (2008).

14. R. L. P. van Veen, A. Amelink, M. Menke-Plymers, C. Van der Pol, and H. J. C. M. Sterenborg, "Optical biopsy of breast tissue using differential path-length spectroscopy", Phys. Med. Biol. **50**, 2573-2581 (2005).

15. I. J. Bigio, S. G. Bown. G. Briggs, C. Kelley, S. Lakhani, D. Pickard, P. M. Ripley, I. G. Rose, and C. Saunders, "Diagnosis of breast cancer using elastic-scattering spectroscopy: preliminary clinical results", J. Biomed. Opt. **5**, 221-228 (2000).

16. G. Zonios, and A. Dimou, "Modeling diffuse reflectance from semi-infinite turbid media: application to the study of skin optical properties", Opt. Exp. **14**, 8661-8674 (2006).

17. R. L. P. van Veen, W. Verkruysse, and H. J. C. M. Sterenborg, "Diffuse-reflectance spectroscopy from 500 to 1060 nm by correction for inhomogeneously distributed absorbers", Opt. Lett. **27**, 040246-040248 (2002).

18. R. L. P. van Veen, H. J. C. M. Sterenborg, A. Pifferi, A. Torricelli, E. Chikoidze, and R. Cubeddu, "Determination of visible near-IR absorption coefficients of mammalian fat using time and spatially resolved diffuse reflectance and transmission spectroscopy", J. Biomed. Opt. **10**, 054004 (2005).

19. S. Merritt, G. Gulsen, G. Chiou, Y. Chu, C. Deng, A. E. Cerussi, A. J. Durkin, B. J. Tromberg, and O. Nalcioglu, "Comparison of water and lipid content measurements using diffuse optical spectroscopy and MRI in emulsion phantoms", Tech. in Cancer Res. Treat. **2**, 563-569 (2003).

20. R. Nachabé, B. H. W. Hendriks, A. E. Desjardins, M. van der Voort, M. B. van der Mark, and H. J. C. M. Sterenborg, "Estimation of lipid and water concentrations in scattering media with diffuse optical spectroscopy from 900 to 1600 nm", J. Biomed. Opt. **15**, 037015 (2010).

21. A. Amelink, D. J. Robinson, and H. J. C. M. Sterenborg, "Confidence intervals on fit parameters derived from optical reflectance spectroscopy measurements", J. Biomed. Opt. **13**, 054044 (2008).

22. H. J. van Staveren, C. J. M. Moes, J. Van Marle, S. A. Prahl, and M. J. C. Van Gemert, "Light scattering in Intralipid-10% in the wavelength range of 400-1100 nm", Appl. Opt. **30**, 4507-4514 (1991).

23. C. M. Gardner, S. L. Jacques, and A. J. Welch, "Light transport in tissue: accurate expressions for one-dimensional fluence rate and escape function based upon Monte Carlo simulation", Las. Surg. Med. **18**, 129-138 (1996).

24. P. R. Bargo, S. A. Prahl, T. T. Goodell, R. A. Sleven, G. Koval, G. Blair, and S. L. Jacques, "In vivo determination of optical properties of normal and tumor tissue with white light reflectance and an empirical light transport model during endoscopy", J. Biomed. Opt. **10**, 034018 (2005).

25. I. S. Saidi, S. L. Jacques, and F. K. Tittel, "Mie and Rayleigh modeling of visible-light scattering in neonatal skin", Appl. Opt. **34**, 7410-7418 (1995).

26. G. Zonios, and A. Dimou "Light scattering spectroscopy of human skin in vivo", Opt. Exp. **17**, 1256-1267 (2009).

27. W. G. Zijlstra, A. Buursma, and O. W. Van Assendelft, *Visible and near infrared absorption spectra of human and animal haemoglobin* (Utrecht, The Netherlands, VSP Publishing, 2000).

28. A. Roggan, M. Friebel, K. Dorchel, A. Hahn, and G. Muller, "Optical properties of circulating human blood in the wavelength range of 400-2500 nm", J. Biomed. Opt. **4**, 36-46 (1999).

29. G. M. Hale, and M. R. Querry, "Optical constants of water in the 200 nm to 200 micrometer wavelength region", Appl. Opt. **12**, 555-563 (1973).

30. W. Verkruysse, G. Lucassen, J. F. De Boer, D. J. Smithies, J. S. Nelson, and M. J. C. Van Gemert, "Modelling light distributions of homogenous versus discrete absorbers in light irradiated turbid media", Phys. Med. Biol. **42**, 51-65 (1997).

31. P. R. Bevington, and D. K. Robinson, *Data reduction and error analysis for the physical sciences* (McGraw-Hill, New York, 1969).

32. D. Sheskin, *Handbook of parametric and non parametric statistical procedures* (Chapman and Hall/CRC, 2007).

Chapter 4

Validation of interventional fiber optic spectroscopy with MR spectroscopy, MAS-NMR spectroscopy, high performance thin layer chromatography, and histopathology for accurate hepatic fat quantification

Rami Nachabé

José W. A. van der Hoorn

Roland van de Molengraaf

Rolf Lamerichs

Jeroen Pikkemaat

Charles F. Sio

Benno H. W. Hendriks

Henricus J. C. M. Sterenborg

Abstract

Objectives: To validate near infra-red (NIR) based optical spectroscopy measurements of hepatic fat content using a minimally invasive needle-like probe with integrated optical fibers enabling real-time feedback during percutaneous interventions. The results were compared with magnetic resonance spectroscopy (MRS) as validation and with histopathology, being the clinical golden standard. Additionally, *ex vivo* magic angle spinning nuclear magnetic resonance (MAS-NMR) spectroscopy and high performance thin layer chromatography (HPTLC) were performed for comparison.

Materials and Methods: Ten mice were used for the study of which half received a regular chow diet and the other half a high fat diet to induce obesity and hepatosteatosis. The mice were imaged with a clinical 3-Tesla MR to select a region of interest (ROI) within the right and left lobes of the liver, where MRS measurements were acquired *in vivo*. Subsequently, optical spectra were measured *ex vivo* at the surface of the liver at six different positions immediately after resection. Additionally, hepatic fat was determined by MAS-NMR spectroscopy and HPTLC. Histopathologic analyses were performed and used as the reference standard. Pearson's correlation and linear regression analysis were done to assess the correlation of the various techniques with NIR. A one-way analysis of variance including post hoc Tukey's multiple comparison tests were used to study the difference in fat estimation between the various techniques.

Results: For both of the mice groups, the estimated fat fractions by the various techniques were significantly similar, $P = 0.072$ and 0.627 for chow diet and high fat diet group, respectively. The Pearson's correlation value between NIR and the other techniques for fat determination showed the same strong linear correlation (P above 0.990, $P < 0.001$); whereas for histopathology which is a rather qualitative measure, the Pearson's correlation value was slightly lower (P = 0.925, $P < 0.001$). Linear regression coefficient computed to compare NIR to the other techniques resulted in values close to unity with MRS having the narrowest confidence interval (CI) (r = 0.935, 95% CI: [0.860–1.009]) demonstrating highly correlating results between NIR and MRS.

Conclusions: NIR spectroscopy measurements from a needle-like probe with integrated optical fibers for sensing at the tip of the needle can quickly and accurately determine hepatic fat content during an interventional procedure and might therefore be a promising novel diagnosing tool in the clinic.

Validation of interventional fiber optic spectroscopy with MR spectroscopy, MAS-NMR spectroscopy, high performance thin layer chromatography, and histopathology for accurate hepatic fat quantification

Chapter 4

1. Introduction

Hepatic steatosis as the most prevalent liver disorder is found in a broad spectrum of disease. It is characterized by an excessive accumulation of triglycerides in the cytoplasm of the hepatocytes, being the key histological feature. Besides alcoholic liver disease, the intrahepatic accumulation of lipids may also be associated with non-alcoholic fatty liver disease (NAFLD), a feature not only encompassing the rather benign hepatosteatosis, but also the more severe non-alcoholic steatohepatitis, which may lead to irreversible liver cirrhosis and hepatic failure. NAFLD is strongly associated with obesity, insulin resistance and hyperlipidemia, features of the metabolic syndrome.[1] As obesity and the metabolic syndrome are globally gaining prevalence in pandemic proportions, NAFLD may become a major disorder and should be detected in the early reversible stage.

Currently, the golden standard to determine intrahepatic fat is histological analysis of samples obtained from a liver biopsy, which might be prone to inter-observer variance[2] and to sampling errors.[3] Though, the invasiveness is its major drawback. Ultrasound (US) is a non-invasive technique that is the most widely used to detect fatty infiltration in liver by comparing the echogenicity in the liver and fat free organs such as the kidney cortex or spleen.[4] However, this technique is not quantitative, prone to inter-observer variance and not optimal in presence of morbid obesity. Another method is based on computer tomography (CT) imaging where the Hounsfield attenuation values in liver and spleen are compared knowing that fat has a lower X-ray absorption than water and blood.[5] Similarly to US, it is difficult to obtain accurate quantification of fat from CT images especially in the less severe cases of steatosis. Moreover, its ionizing radiation limits its use, particularly in children. Magnetic Resonance Imaging (MRI) is a widely used technique to estimate fat in liver by using commercially available algorithms such as in-phase/opposed-phase, the Dixon method[6] and its additional refinements[7] to quantify fat fractions in liver. However, these techniques are sensitive to field inhomogeneity which potentially yield large errors on the estimation of fat.[8] Nevertheless, a recent study conducted by Kühn *et al.* demonstrated that $T2^*$-corrected Dixon MRI for estimating hepatic fat content showed excellent correlation with liver biopsy without being limited by liver iron content and fibrosis or cirrhosis.[9] Magnetic resonance spectroscopy (MRS) enables measurements of water and fat proton signals and is generally considered as the most accurate non-invasive technique for hepatic fat quantification.[10] Still, MRS remains a research tool for clinical studies and is not yet used in daily routine liver examinations.

Optical spectroscopy measurements acquired with needle-like optical probes is a relatively new technique that is being developed over the last decade to estimate blood volume fractions and saturation in oxygen in the tissue by analyzing the spectra in the visible and near infra-red wavelengths range between 400 and 900 nm.[11-13] We recently developed an optical setup and needles with integrated optical fibers that allows spectral measurements in the infra-red wavelengths range up to 1600 nm where fat and water absorption bands exist that enable accurate fraction estimation of these substances in addition to blood.[14] The advantage of using such a broad wavelength range is that the error on the estimated fat fractions is below 3%.[15] A thorough study was performed in order to evaluate the accuracy and the reliability of the fat fraction estimation in phantoms

with a wide range of known fat content.[14] In addition to light absorption caused by the various biological chromophores, the light scattering in tissue correlated to the cellular structure and morphology is estimated as well. Recently, we have published a study discriminating tumors from healthy human liver tissue based on the difference in light scattering and the amount of bile in the liver estimated using a similar model as in the present study.[16] Compared to our previous studies[14-16], we extended the infra-red wavelength range of measurement from 1600 to 1800 nm where additional fat and water absorption bands exist; enabling higher accuracy in quantification of these biological chromophores.

Fatty liver disease requires diagnostic tools that can accurately estimate hepatic fat given the fact that it is positively diagnosed by histopathology for lipid accumulation as low as 5%.[17] Therefore, the goal of the study is to perform a validation of the NIR technique with MRS by estimating fat in the liver of two groups of mice under different dietary conditions. One group of mice was subjected to a regular chow diet, considered as healthy controls, whereas the second was subjected to a high fat diet inducing obesity and hepatosteatosis. Besides, *ex vivo* histopathology, the clinical golden standard, was performed for comparison as well as two other *ex vivo* techniques being magic angle spinning nuclear magnetic resonance (MAS-NMR)[18-22] and high performance thin layer chromatography (HPTLC).

2. Materials and methods

2.1. Animal model and measurement protocol

Ten male heterozygous APOE*3Leiden.CETP (cholesteryl ester transfer protein) transgenic mice,[23] 8-10 weeks of age, were matched on their body weight into a healthy control group, which received a regular chow diet (n = 5) or to a diet induced obese group (n = 5), supplemented a high fat diet containing 32% (w/w) lard (60 %kcal fat, D12492 Research Diets, NJ, USA). The mice remained on the dedicated diets for 16 weeks, resulting in obesity in the high fat fed group (body weight of 46.9 ± 2.2 g versus 29.0 ± 1.0 g in the chow group). The animals received food and water *ad libitum*. Body weight and food intake were monitored bi-weekly during the study.

The mice were anesthetized using a mixture of isoflurane (1-3%) and medical air. Liver fat was measured in the left and right lobe non-invasively by MRS. Subsequently, the mice were euthanizaed by CO_2 suffocation and livers were resected and immediately measured with NIR spectroscopy. After the NIR spectroscopy measurements, the livers were dissected, divided into several pieces and stored for further *ex vivo* analyses.

Animals were obtained from the SPF breeding stock at TNO Metabolic Health Research (Leiden the Netherlands). Animal experiments were approved by the Institutional Animal Care and Use Committee of The Netherlands Organization for Applied Research (TNO).

2.2. Near Infra-Red spectroscopy

We have recently built an optical setup that allows optical spectroscopy measurements of tissue to estimate physiological and morphological information such as

Validation of interventional fiber optic spectroscopy with MR spectroscopy, MAS-NMR spectroscopy, high performance thin layer chromatography, and histopathology for accurate hepatic fat quantification

Chapter 4

chromophores volume fractions (e.g. blood, water, lipid, bile, etc.), blood saturation in oxygen and light scattering due to tissue density using an optical tissue model.[14-16]

Briefly, the setup comprises a light source (Ocean Optics, Duiven, The Netherlands) and two optical spectrometers (Ocean Optics, Duiven, The Netherlands) that resolve light from 400 to 1200 nm and 900 to 2100 nm, respectively. A custom-made needle-like optical probe is connected to the light source and to both spectrometers via 200 micrometer diameter optical fibers.

The light that travels through the liver from the emitting to the collecting fibers is subject to optical absorption and scattering, properties that are related to the physiological and morphological properties of tissue. This tissue-light interaction is described by a model deriving from the diffusion theory and allows extraction of parameter of interest i.e. the fat fraction within the probed volume at the tip of the needle.[14-16] A non-linear least squares inversion of the model is applied to fit the measurement curves with the set of parameters that best describes the tissue optical properties. The absorption coefficients of light by the various chromophores in their pure state in liver tissue (i.e. oxygenated hemoglobin, deoxygenated hemoglobin, bile, water and lipid) are used as *a priori* knowledge in the model to estimate the corresponding volume fractions in the total volume probed with the needle.[14-16]

Figure 1 depicts the absorption of light by water and lipid from 400 to 2200 nm that we measured as described elsewhere.[14] Briefly, pure water and fat were inserted in separate cuvettes of different thickness and their optical transmission were measured with a 1 nm resolution high-end laboratory spectrophotograph (Perkin Elmer, Waltham, MA). From the transmission measurements, the absorption coefficients are computed and used as references for the analysis. These two chromophores have high absorption coefficients compared to other absorbers for wavelengths above 900 nm. Water has higher absorption coefficients than fat. However the fat absorption peaks at 930, 1211, 1720 and 1760 nm are of the same order of magnitude as the water absorption values altering the spectral shape of the measured spectra in case of presence of fat in the liver. The penetration depth depends on the optical properties of the probed tissue i.e. the absorption and reduced scattering coefficients. In average, it is roughly half the distance that separates the source and detection optical fibers. In our case the fiber separation distance is 2.5 mm yielding a penetration depth of approximately 1.25 mm.

NIR spectroscopy measurements were performed on the fresh excised livers immediately after sacrificing the mice. The optical probe was gently put in contact with the surface of the liver without pricking. In principle the needle can be inserted inside the liver, however, surface measurements were preferred to avoid damaging of the tissue that can hamper *ex vivo* analysis for HPTLC, MAS-NMR and histopathology. In total 30 NIR spectra were measured at 6 different positions: in the upper-left, lower-left, central-left, upper-right, lower-right and central-right of the liver.

The measurement acquisition time per spectrum is 500 ms and the analytical model was used to fit the measurement between 450 and 1800 nm to extract the fat volume fraction.[16] The percentage of fat is calculated as percentage over water and fat similarly to MRS and MAS-NMR. Per mouse, the hepatic fat content was the calculated average of all fat fractions derived from the 30 NIR measurements of the liver.
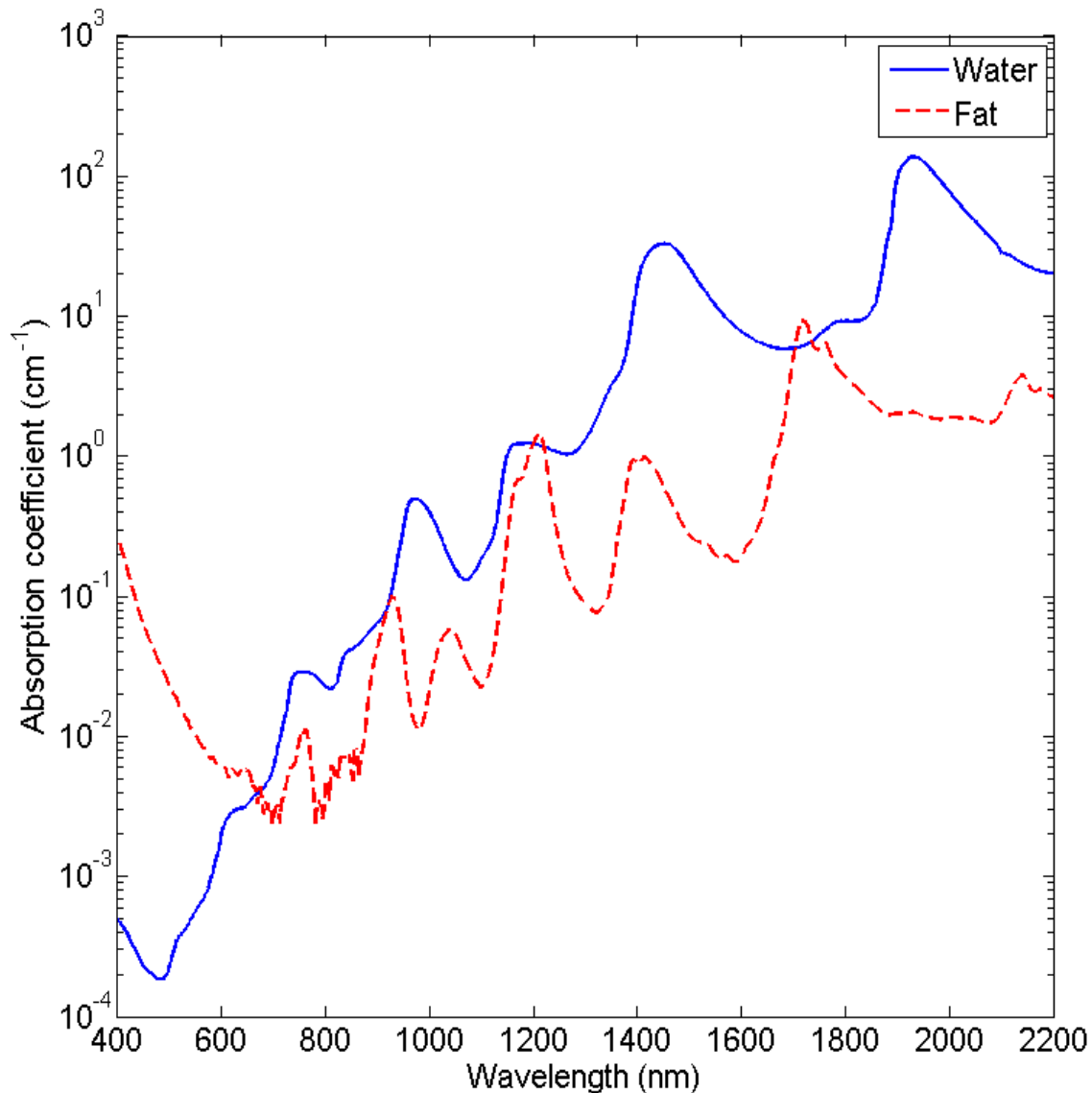
Figure 1: Optical absorption coefficient of water and fat.

2.3. Magnetic Resonance Imaging

After 16 weeks of dietary intervention (either chow or high fat diet), the mice were anaesthetized by isoflurane inhalation and placed in a dedicated small animal setup. Core body temperature and respiration rate were controlled and recorded during the measurements. The MRI experiments were performed using a 3T Philips Achieva MR scanner (Philips Healthcare, Best, the Netherlands) with a Quasar dual gradient system (amplitude 80mT/m, slew rate 200mT/m/ms). All experiments were performed under software release 2.5.3. For imaging the liver and acquiring the MRS spectra, a dedicated whole body mouse coil (solenoid receive only, Philips Research, Hamburg, Germany) was used. This solenoid coil was placed perpendicular to the main magnetic field of the MR scanner. To position the mouse inside the MR coil, a dedicated mouse cradle (Equipement Vétérinaire MINERVE, Esternay, France) equipped with an anesthesia breathing mask and heating pad (using air) for maintaining the body temperature of the anesthetized mouse. The cradle with the mouse was positioned in such a way that the

liver of the mouse is positioned at the center of the MR coil. **Figure 2** depicts from left to right the sagittal, transversal and coronal planes from a mouse MR image. Based on anatomical landmarks, a ROI of 27 mm^3 was placed at the left and the right lobes of the liver for MRS measurements.
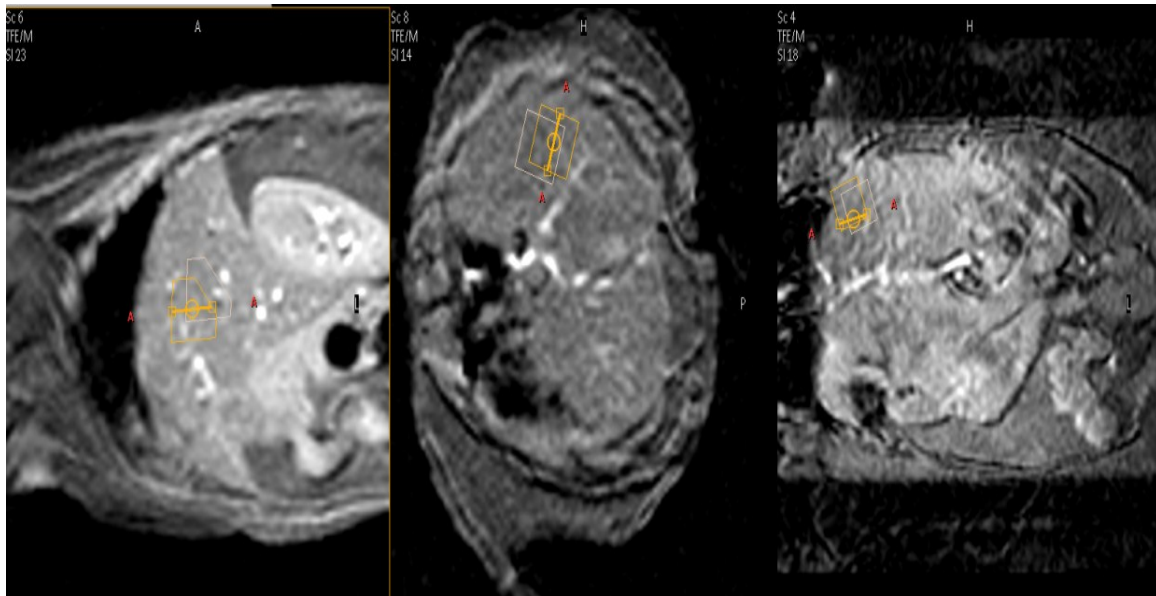

Figure 2: Sagittal, transversal, and coronal planes from a mouse MRI image. Based on anatomical landmarks, a ROI of 27 mm^3 was placed at the left and the right (shown) lobes of the liver for measuring a spectrum.

2.4. Magnetic Resonance Spectroscopy

All spectroscopy data were recorded with a Point RESsolved Spectroscopy (PRESS) sequence[24] which is a volume selective MRS sequence based on 3 orthogonal selection gradients in combination with 3 RF pulses. Spoiler gradients were used to suppress unwanted signals. This sequence results in a spectrum from the volume defined by the intersection of the three slice selective profiles.

Extra care was taken in planning of the volume in order to avoid chemical shift displacement errors as much as possible. Chemical shift displacement is caused by the difference in chemical shift in combination with a selection gradient. As a consequence, the actual physical volume from which the -CH$_2$ signals of the fat originate, will be different from the water volume. During planning both volumes were always shown on the image. Care was taken that both volumes were planned within the liver, avoiding major blood vessels.

After optimization of gradient shimming, three consecutive spectra were acquired: (a) TR/TE = 4000 ms/31 ms, voxel size of 5x5x5 mm^3 and without water suppression; (b) TR/TE = 4000 ms/31 ms, voxel size of 3x3x3 mm^3 and without water suppression; (c) TR/TE = 4000 ms/31 ms, voxel size of 3x3x3 mm^3 and with water suppression. Long TR was chosen for complete relaxation to ensure accurate quantifications. In principle, a single spectrum takes a couple of minutes however the combination of shimming and acquiring three consecutive spectra makes the total MRS scan time of 20 minutes. For all

three spectra, acquisition parameters included as well a number of signal averages of 32 with a readout of 1024 data points over 2000 Hz spectral bandwidth. The first acquisition was mainly used for the shim optimization; the second acquisition was used to estimate the fat fractions whereas the third acquisition was used to have an improved fit of the CH_2-signal for a more accurate quantification.

The data were processed using jMRUI v3.0 software. After phase correction of the spectra, quantitative analysis was performed using the Advanced Magnetic Resonance (AMARES) algorithm within jMRUI.[25] The amount of triglycerides can be quantified by integrating the triglyceride $C(H_2)_n$ signal (1.1 - 1.3 ppm) against H_2O signal. These values are T_2-corrected since both signals have a different T_2 relaxation time and thus undergo a different amount of signal decay at a chosen echo time. The corrected signal A_0 can be calculated as $A_0 = A_{TE}/\exp(-TE/T_2)$ where A_{TE} is the integral at the measured echo time and T_2 is the spin-spin relation time of the H_2O or the triglyceride $C(H_2)_n$ signal. The T_2 values used in this study are 34 ms for H_2O and 68 ms for $C(H_2)_n$ taken from literature.[26] The lipid-percentage F_{MRS} is calculated as $F_{MRS} = 100 \cdot A_{0\text{-triglyceride}}/(A_{0\text{-triglyceride}} + A_{0\text{-water}})$ with $A_{0\text{-triglyceride}}$ and $A_{0\text{-water}}$ corresponding to the corrected integral of the $C(H_2)_n$ and H_2O signals, respectively.[27]

2.5. HR-MAS 1H-NMR spectroscopy description to estimate fat in liver

After isolation of the whole liver, a piece of the left lobe was snap frozen in liquid nitrogen and stored below -70°C until the measurements by HR-MAS NMR. Shortly before the measurements, approximately 6 mg of frozen tissue was excised from the liver near the site that was previously selected for the *in-vivo* localized magnetic-resonance spectroscopy. The frozen tissue was rapidly transferred into a cooled zirconia 12 μL HR-MAS NMR rotor (CortecNet, product code HZ05537). Subsequently, 8 μL of cooled 99.95% D_2O was added to the tissue, a Kel-F spherical spacer (CortecNet, product code H8548) was inserted to restrict the sample volume to 12 μL,[21] the excess of D_2O was removed, and the rotor was sealed with a Kel-F cap (CortecNet, product code H6304). HR-MAS ^{1}H-NMR spectra were acquired on a Bruker AVANCE 600MHz NMR (Rheinstetten, Germany) spectrometer equipped with a Bruker 4mm ^{1}H/^{13}C HR-MAS probe at a spinning speed of 6000 Hz. The magnetic-field homogeneity was optimized by minimizing the line width of the H_2O resonance. The Free Induction Decay (FDI) sequence had the following parameters: number of averages is 64; spectral bandwidth of 24 kHz; number of data points is 64k; and a repetition time of 5 s. After apodization with a 0.1 Hz exponential window function and Fourier transform, the NMR signals of H_2O and the fatty-acid CH_3 group were manually selected and quantified using the Bruker TOPSPIN NMR software package.

2.6. HPTLC measurements to determine hepatic fat

After isolation of the whole liver, a piece of the left and right lobe were snap frozen in liquid nitrogen and stored below -70°C until the measurements of lipids by HPTLC as described previously.[28] In short the liver pieces were homogenized in PBS (phosphate-buffered saline). Protein content of all samples was determined and

Validation of interventional fiber optic spectroscopy with MR spectroscopy, MAS-NMR spectroscopy, high performance thin layer chromatography, and histopathology for accurate hepatic fat quantification

Chapter 4

subsequently lipids were extracted. Briefly, a solution of 200 µg protein in 800 µL of MilliQ was mixed with 3 ml Methanol/Chloroform (2:1), after which 500 µL Chloroform, 100 µL Internal Standard and 1 mL MilliQ water was added. All were mixed and centrifuged for 10 min at 300 rpm. After the centrifugation the chloroform layer was collected and dried under nitrogen. The pellets were dissolved in 50 µL chloroform and transferred to a HPTLC plate for separation of triacylglycerols (TG), free cholesterol (FC) and cholesterol esters (CE). The lipids were separated using HPTLC on silica gel plates and subsequent analysis was performed by TINA 2.09 software (Rayest Isotopen Meßgeräte GmbH, Straubenhardt, Germany). The hepatic fat content was calculated as mg TG/ mg protein from two samples per mouse.

2.7. Histopathology to determine hepatosteatosis

After isolation of the whole liver, a piece of the left lobe was formalin fixed and embedded in paraffin. Microscopic sections (5 µm thick) were used for histological analysis. Sections were stained with haematoxylin-phloxine-saffron. Hepatosteatosis was determined by the amount of hepatocellular microvacuolisation around the central vene (centrilobular). The severity was defined by estimating the percentage of affected cells: 1-Very slight (<5%), 2- Slight (5-50%) and 3- Moderate (>50%). The livers from the chow diet group were considered as the healthy reference and therefore this method might be considered semi-quantitative. For statistical analyses the estimated percentages of affected cells were used. All analyses were performed by one toxicological pathologist.

2.8. Statistical analysis

All the data obtained by each technique can be described by a normal distribution according to the Jarque-Bera test for normality.[29] Therefore, the estimated fat fractions are described as mean ± SD.

A one-way analysis of variance combined with a *post hoc* Tukey's procedure for multiple comparison correction was applied to evaluate whether a technique gives significant differences from the others.

Pairwise comparisons of the determined fat fraction by NIR with the different techniques were assessed using Pearson's correlation analysis. The Pearson's correlation coefficient provides an indication on the linearity of the estimated fat with NIR with respect to the values estimated by another technique.

Pairwise robust linear regression fits were performed to evaluate the relation in fat estimation between NIR and each of the other techniques. For each mouse, a mean and a standard deviation fat fraction value are computed from all the estimated fat fractions measured at the different positions within a single mouse. The SD values were taken as weighting factor in the robust linear regression fit. A linear regression coefficient close to unity would mean that NIR gives similar values than the technique for which it is compared. For each linear regression coefficient, a 95% CI was computed. The data are displayed as scatter plots including bars that represent SDs within each mouse along with their linear fits and corresponding 95% confidence bounds.

Histopathological results may be considered rather qualitative than quantitative as the chow group was defined as the healthy reference, with a disease score of '0'.

Therefore these are slightly different from each of the other techniques results and thus not included neither in the one-way analysis of variance test for the comparisons of means nor in the pairwise robust linear regression computational procedure.

3. Results

Sixteen weeks of high fat feeding clearly induced hepatosteatosis as compared to the chow diet as determined by NIR, MRS, MAS-NMR and HPTLC and as confirmed by histopathologic analysis. Indeed, for each of the methods, applying a one-way analysis of variance test to the determined fat fraction values showed that there is a significant difference between both groups of mice ($P < 0.002$).
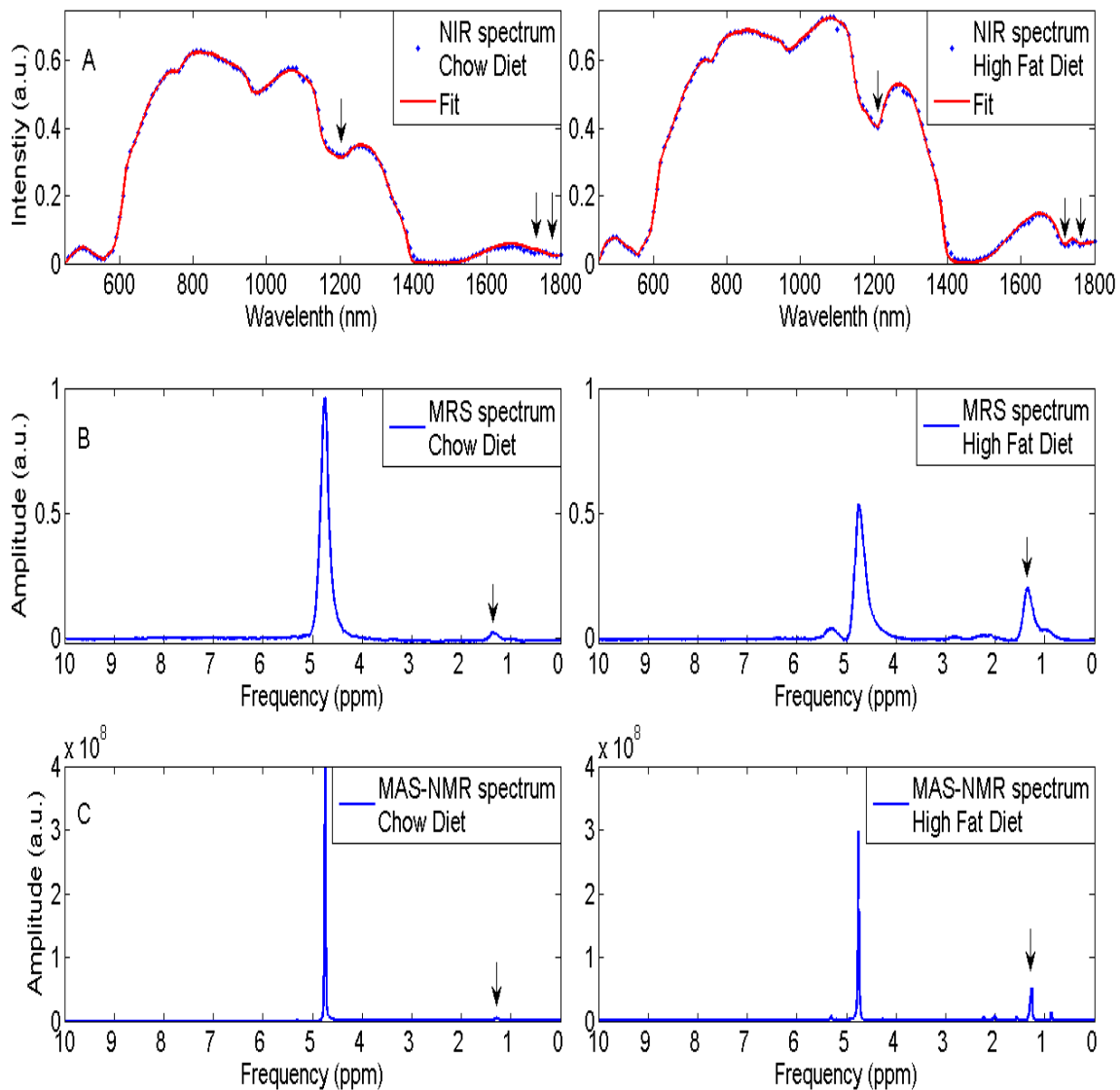
Figure 3: Representative spectra from (A) NIR, (B) MRS, and (C) MAS-NMR measurements of a mouse liver under chow diet (left) and high fat diet (right) conditions. The arrows indicate wavelengths and frequencies corresponding to fat signatures in the spectra.

Validation of interventional fiber optic spectroscopy with MR spectroscopy, MAS-NMR spectroscopy, high performance thin layer chromatography, and histopathology for accurate hepatic fat quantification

Chapter 4

Figure 3A depicts NIR spectra of a liver from a chow diet and a high fat diet mouse, respectively. Light absorption below 900 nm is mainly due to the presence of blood-derived chromophores such as oxygenated hemoglobin and deoxygenated hemoglobin, and bile;[16] whereas absorption above 900 nm is mainly due to water and fat in the tissue.[14] Besides, examples of MRS (**Figure 3B**) and MAS-NMR **(Figure 3C)** spectra acquired in a mouse under chow diet and a mouse under high fat diet are displayed, respectively. The peaks at a chemical shift of 4.7 ppm correspond to presence of water whereas the peaks at a chemical shift of 1.3 ppm to triglycerides fatty acids. The arrows in **Figure 3** indicate the wavelengths and frequencies for which fat signature exist. Representative histologic pictures from a liver from the chow diet group and from the high fat diet group are presented in **Figure 4**.
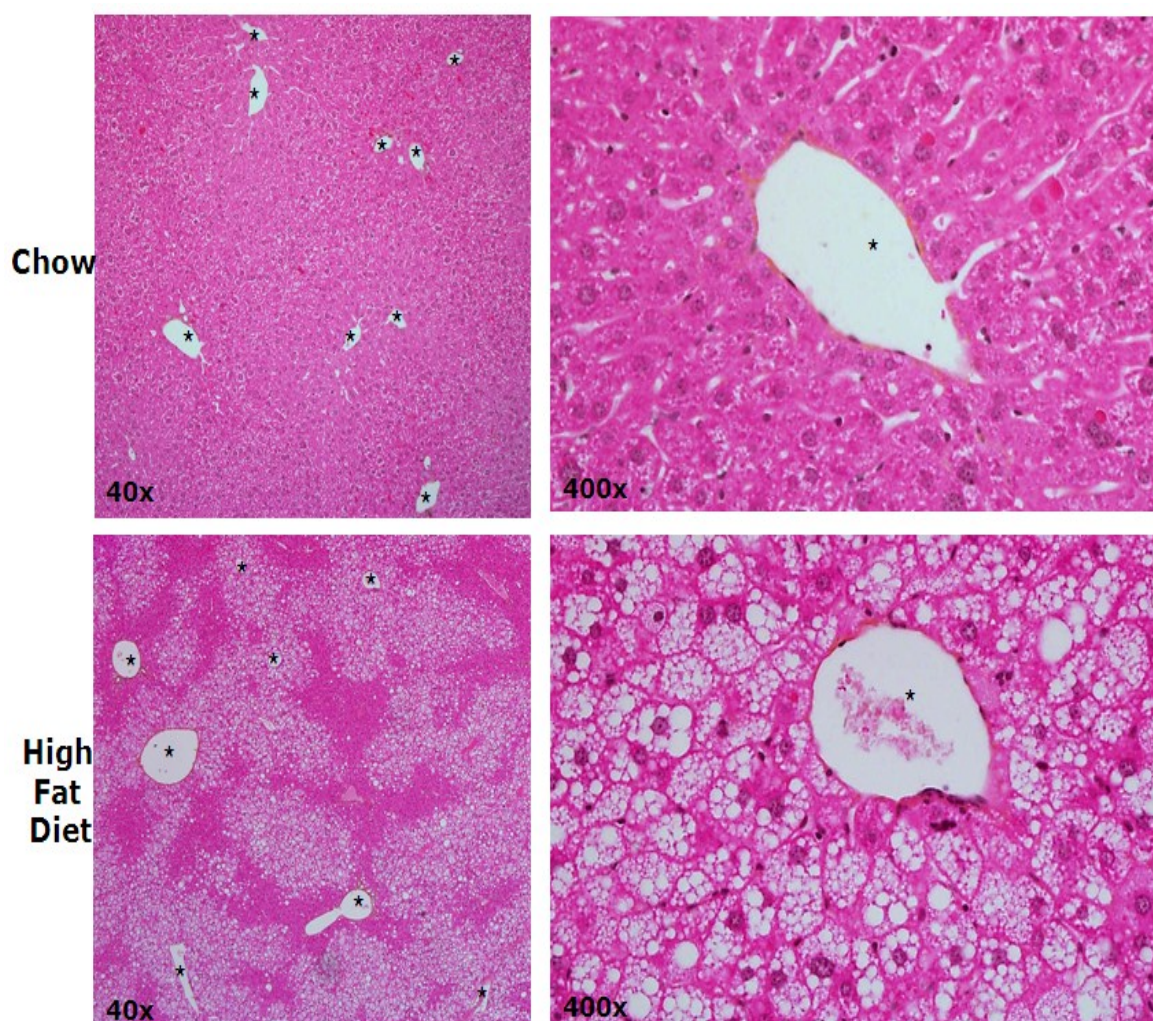
Figure 4: Representative histologic pictures from mouse livers after chow diet (top) and high fat diet (bottom) at different magnifications (left 40x and right panel 400x). As compared to the chow diet, livers from the high fat diet show histolofical features of hepatosteatosis, evidenced by lipid accumulation in the hepatocytes. Asterisk denotes adipose cells.

Quantitative fat estimation in the liver using the various techniques were statistically compared and found not different (**Table 1**). The *P*-value for the chow diet and high fat diet category are 0.072 and 0.627, respectively; therefore none of the methods showed significant difference from another method for hepatic fat quantification for any of the mice groups. With respect to the chow diet group, NIR and MRS showed the same average fat fraction within a difference of 0.4 percent point whereas a difference of 2.7 and 1.1 percent point was observed with MAS-NMR and HPTLC, respectively. However, no statistically significant difference was obtained according to Tukey's *post hoc* test. The different techniques to measure hepatic fat in the high fat group were very similar.

TABLE 1. Mean and standard deviation of the estimated fat in each mice group by the different techniques

Group	Fat (%) estimated by the various techniques (mean ± SD)				*P*-value[*]
	NIR	MRS	MAS-NMR	HPTLC	
Chow diet	4.5 ± 2.2	4.1 ± 1.4	7.2 ± 1.8	5.6 ± 1.0	0.072
High fat diet	23.6 ± 7.3	25.6 ± 9.3	20.2 ± 4.0	26.5 ± 7.3	0.627

[*]Computed with a multiple group one-way analysis of variance test. No significant differences observed between any pairwise comparison of the techniques after Tukey's post hoc multiple comparison tests.

After comparing the results on group level of the various methods, we calculated the correlations between the results obtained with the NIR technique and each of the other techniques. **Table 2** summarizes the Pearson's correlation coefficients with corresponding CI applied to the data from NIR spectroscopy and the other techniques. NIR showed very high correlation with Pearson's coefficient P above 0.990 ($P < 0.001$) with all other techniques. Histopathology as semi-quantitative analysis demonstrated a lower value (P = 0.925, $P < 0.001$). All compared techniques showed high Pearson's correlation coefficients meaning that a strong linearity exists between NIR and the different methods in determining the fat fraction in liver. Additionally, **Table 2** summarizes the linear regression coefficient and corresponding 95% confidence intervals when comparing the estimated fat with NIR with another method. NIR and MRS showed the linear regression coefficient with the narrowest CI comprising unity (r = 0.935, 95% CI: 0.860-1.009). Therefore NIR showed to be the most comparable to MRS for fat fractions quantification. Comparison with HPTLC showed as well a linear regression coefficient lower than unity whereas it was above unity when comparing with MAS-NMR. All the regression coefficients have CI comprising unity besides for HPTLC that has an upper bound of 0.993.

Validation of interventional fiber optic spectroscopy with MR spectroscopy, MAS-NMR spectroscopy, high performance thin layer chromatography, and histopathology for accurate hepatic fat quantification

Chapter 4

TABLE 2. Pearson's correlation P and linear regression r coefficients computed when comparing estimated fat fractions from NIR with respect to MRS, MAS-NMR, and HPTLC and to histopathological scores.

	MRS	MAS-NMR	HPTLC	Histopathology[*]
P coefficient	0.993 [0.970-0.998]	0.990 [0.955-0.998]	0.993 [0.969-0.998]	0.925 [0.845-0.991]
r coefficient	0.935 [0.860-1.009]	1.030 [0.781-1.279]	0.896 [0.799-0.993]	-

[*]Computed by comparing fat fractions determined with NIR versus the hepateastosis scores from histopathology. All P coefficients have $P < 0.001$. CI with $P < 0.05$ displayed between brackets.

Figure 5 depicts the average fat fractions and SD determined by NIR versus MRS (**Figure 5A**), MAS-NMR (**Figure 5B)** and HPTLC (**Figure 5C**), respectively. Additionally, **Figure 5** depicts the linear regression fits and the 95% confidence bounds. MRS, HPTLC, and MAS-NMR are the techniques with narrowest to widest confidence bounds. The SD of estimated fat fraction with NIR within each mouse is similar to the one of HPTLC but larger than MRS. As only a single MAS-NMR spectrum was acquired per mouse, no SDs are available for this method. Given the fact that histopathology is a semi-quantitative method, no linear regression was applied to compute the regression coefficient between NIR and this method.
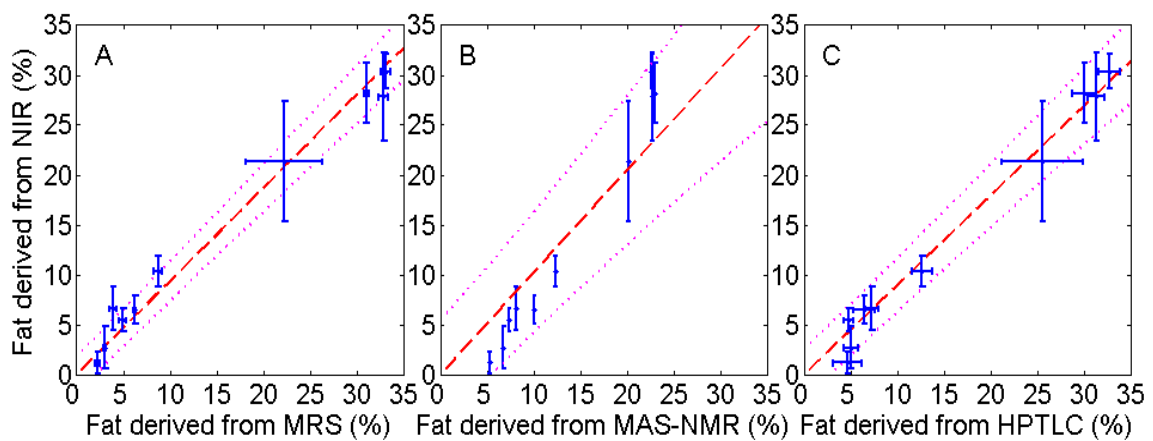

Figure 5: Mean and SD of fat fraction in each mouse determined by (A) NIR versus MRS, (B) MAS-NMR, (C) HPTLC. The dashed line corresponds to the linear regression and the dotted lines correspond to the 95% confidence bound.

4. Discussion

In the present study we evaluated the NIR based optical spectroscopy measurements of hepatic fat content using a minimally invasive needle-like probe as compared to *in vivo* MRS measurements as validation, to histopathology being the clinical golden standard, to MAS-NMR spectroscopy, and to HPTLC measurements.

NIR spectroscopy showed very good agreement in fat quantification as compared to MRS with a very high Pearson's correlation coefficient and a linear regression coefficient of 0.935 making NIR underestimating the fat in liver of 6.5% compared to MRS. Whereas the average fat determined in the chow diet mice category is similar for both techniques (difference of 0.4 percent point), it is in average 2% lower in the case of high fat diet mice liver measurements yielding to a regression coefficient lower than unity when comparing NIR to MRS. We have performed two previous studies where we investigated the necessity to measure above 1000 nm and the accuracy of fat estimation with NIR from phantom measurements with fat content ranging from 0 to 83% of the total volume yielding a regression coefficient of 1.02 (R^2 = 0.999).[14-15] These studies showed the importance of extending the commonly-used wavelength ranges (between 400 and 1000 nm) up to 1600 nm for a more accurate fat quantification. In this present study, we extended the wavelength range up to 1800 nm, where additional fat and water absorption bands exist. The local maxima of fat absorption at 1720 and 1760 nm are the only wavelength for which these maxima coincide with a local minimum of water absorption; adding more accuracy for fat quantification in comparison to what has already been published so far in literature. Bernard et al.[30] performed MRS measurements in phantoms with fat content ranging from 0% to 100% and the analysis yielded a regression of 1.06 (R^2 = 0.993). Consequently, based on the results from published phantoms study, MRS seems to be slightly overestimating fat fractions compared to NIR which can explain the regression coefficient of 0.935 when comparing NIR with MRS in this study. From **Figure 5A**, one can notice that the SD per mouse if smaller when the hepatic fat is estimated with MRS compared to NIR. This is due to the fact that only a single measurement per lobe is performed whereas three measurements per lobe are performed with NIR showing differences in fat content between the measurements performed close to the center of the liver compared to the other locations.

Computing a linear regression coefficient to compare the estimated fat fractions between NIR and histopathology is not applicable. This is mainly due to the fact that histopathology is a rather semi-quantitative method. Moreover, the chow group was defined as the healthy reference with measured fat fractions below 5%, hence the 'null' score for hepatosteatosis. Nevertheless, the correlation with NIR is still very high suggesting strong linearity.

MAS-NMR and HPTLC are two techniques enabling *ex vivo* fat quantification and were used for comparison with NIR. Good agreements are observed between NIR and each of both methods with roughly similar Pearson's correlation coefficient values. However, the linear regression coefficient comparing NIR to MAS-NMR is the only one to be above unity. Moreover, only a single measurement per liver was performed with MAS-NMR and therefore no standard deviations are available for enhanced comparisons. Fat fractions estimated with HPTLC showed slightly higher values than NIR however the standard deviations are comparable. A potential explanation for this difference is the fact that the determined fat fractions with NIR correspond to the percentage of fat over water and fat whereas the fat fractions derived from HPTLC corresponds to percentage of fat over protein in liver and not water.

Validation of interventional fiber optic spectroscopy with MR spectroscopy, MAS-NMR spectroscopy, high performance thin layer chromatography, and histopathology for accurate hepatic fat quantification

Chapter 4

NIR spectroscopy has been used so far to quantify hemoglobin derivatives, and few studies investigated fat quantification in breast by measuring the spectra up to 1000 nm only.[31-32] Kitai *et al.*[33] measured the optical properties such as the absorption and reduced scattering coefficients with time-resolved NIR spectroscopy on graft livers and showed correlation between the hepatic fat quantification and the ratio of reduced scattering to absorption however no quantitative fat is derived. The present study is the first to use a wavelength range up to 1800 for a very quick and a more accurate fat quantification.

As fatty liver disease is considered to be positively diagnosed by histopathology for lipid accumulation as low as 5%,[17] NIR seems to be a suitable technique for this purpose as demonstrated in this study. This suggests that NIR spectroscopy is a tool that performs as good as the other techniques that exists for hepatic fat quantification. NIR spectroscopy has the advantage of being very quick in acquiring and analyzing the spectra for fat quantification enabling real-time feedback for clinician compared to other techniques by only tipping the liver tissue. However optical fibers integrated in needles makes this technique invasive causing potential discomfort to patients.

With NIR measurements at the tip of a needle, only local fat distributions can be estimated and therefore mapping of fat accumulations in the liver is only possible along the needle path. Existing NIR based imaging tools for fat mapping exist for breast however the breast is compressed in order to minimize the thickness of the organ and be able to have light penetrating through the whole breast.[32]

Quantifying fat with NIR is a relatively new technique that has only been used so far in investigational studies whereas MRS is already a well-established technique that is used in the clinics. A number of NIR studies in the oncology field were performed which demonstrated that fat content appeared to be a reliable discriminator between tumors and the surrounding healthy tissue.[16, 34] Ongoing human *in vivo* studies carried out in the clinic will provide a better picture of the potential of this technique. With NIR sensing, it should be in principle possible to differentiate between microvesicular and macrovesicular fat content of liver cells. As a matter of fact, we have demonstrated that it is possible to distinguish with NIR between different sizes of lipid vesicles emulsified with water.[14] Phantoms with known fat content where measured before and after shrinking of the vesicles sizes in order to investigate the effect of the particles size on the NIR spectra. The results showed that the fat content could be accurately determined independently from the particles size and that one can correlate the particles size with the slope of the estimated reduced scattering. The smaller the particles size, the higher the scattering slope. It appeared from this study that the chow diet mice group has a statistically higher reduced scattering slope (1.27±0.28) in comparison to the high fat diet mice group (0.98±0.23) suggesting larger particles size in the liver of mice under high fat diet as compared as the mice under chow diet. This corroborates with what can be seen on the histopathology slices in **Figure 4** where the high fat diet liver slice shows larger adipose cells as compared to the chow diet liver slice. Therefore NIR can be an interesting tool to assess the suitability of a donor liver since one of the exclusion criteria is the extent of macrovesicular hepatic fat content.[35]

Table 3 summarizes the characteristics of the different methods. NIR spectroscopy has the advantage of being a fast method to measure and estimate the hepatic fat. The acquisition time of 20 minutes for MRS is higher than the average values reported in literature. This is mainly due to the fact that we added higher order shims to our shim procedure to obtain the most optimal results possible. In standard clinical settings, higher order shims are not used. In comparison to MRS, high accuracy of fat estimation is reached with NIR however it has the disadvantage of being invasive whereas MRS is non-invasive. Nevertheless, the measurements can be performed in the body and therefore no additional chemical processing of the tissue is required after its resection as compared to MAS-NMR and HPTLC.

TABLE 3. Characteristics of different methods for hepatic fat quantification

	Measure time	Invasiveness	Accuracy	Practice	Main disadvantage
NIR	Sub-second	Minimally	High	Research	Invasive
MRS	20 minutes	Non	High	Common	Time consuming
MAS-NMR	10 minutes	Resection	Average	Rare	Tissue excised
HPTLC	Days	Resection	Average	Rare	Tissue excised
Histopathology	Days	Biopsy	Qualitative	Very Common	Tissue excised

Histopathology is considered as golden standard in the clinic.

5. Conclusion

This study investigated the potential of NIR spectroscopy for hepatic fat quantification by validating this method with the most commonly-used techniques such as MRS and histopathology, as well as HPTLC and MAS-NMR. A paucity of NIR studies for fat determination in a wide wavelength range from 450 to 1800 nm makes this study the first to be benchmarked with state of the art methods. We hypothesize that optical fibers integrated in needles could have the potential of providing instantly relevant feedback on hepatic fat quantification during interventional procedures in relevant parts of the liver.

6. Acknowledgments

Validation of interventional fiber optic spectroscopy with MR spectroscopy, MAS-NMR spectroscopy, high performance thin layer chromatography, and histopathology for accurate hepatic fat quantification

Chapter 4

References

1. Marchesini G, Bugianesi E, Forlani G, et al. Nonalcoholic fatty liver, steatohepatitis, and the metabolic syndrome. Hepatology. 2003; 37: 917-923.
2. Kleiner DE, Brunt EM, Van Natta M, et al. Design and validation of a histological system for nonalcoholic fatty liver disease. Hepatology. 2005; 41: 1313-1321.
3. Adams LA, Angulo P, Lindor KD. Nonalcoholic fatty liver disease. CMAJ. 2005; 173: 734-735
4. Mehta SR, Thomas EL, Bell JD, et al. Non-invasive means of measuring hepatic fat content. World J. Gastroenterol. 2008; 14: 3476-3483.
5. Fischer MA, Gnannt R, Raptis D, et al. Quantification of liver fat in the presence of iron and iodine: an ex-vivo dual-energy CT study. Invest. Radiol. 2011; 46: 351-358.
6. Dixon WT. Simple proton spectroscopic imaging. Radiology. 1984; 153: 189-194
7. Fabbrini E, Conte C, Magkos F. Methods for assessing intrahepatic fat content and steatosis. Curr. Opin. Clin. Nutr. Metab. Care. 2009; 12: 474-481.
8. Springer F, Machann J, Claussen CD, et al. Liver fat content determined by magnetic resonance imaging and spectroscopy. 2010; 16: 1560-1566.
9. Kühn JP, Evert M, Friedrich N, et al. Noninvasive quantification of hepatic fat content using three-echo Dixon magnetic resonance imaging with correction for $T2^*$ relaxation effects. Invest. Radiol. 2011; 46.
10. Reeder SB, Robson PM, Yu H, et al. Quantification of hepatic steatosis with MRI: the effects of accurate fat spectral modeling. J. Magn. Reson. Imaging. 2009; 29: 1332-1339.
11. Bigio IJ, Bown SG, Briggs G, et al. Diagnosis of breast cancer using elastic-scattering spectroscopy: preliminary clinical results. J. Biomed. Opt. 2000; 5: 221-228.
12. Van Veen RL, Amelink A, Menke-Pluymers M, et al. Optical biopsy of breast tissue using differential path-length spectroscopy. Phys. Med. Biol. 2005; 50: 2573-2581.
13. Yu B, Burnside ES, Sisney GA, et al. Feasibility of near-infrared diffuse optical spectroscopy on patients undergoing image guided core-needle biopsy. Opt. Express. 2007; 15: 7335-7350.
14. Nachabé R, Hendriks BH, Desjardins AE, et al. Estimation of lipid and water concentrations in scattering media with diffuse optical spectroscopy from 900 to 1600 nm. J. Biomed. Opt. 2010; 15: 037015.
15. Nachabé R, Hendriks BH, Van Der Voort M, et al. Estimation of biological chromophores using diffuse optical spectroscopy: benefit of extending the UV-VIS wavelength range to include 1000 to 1600 nm. Biomed. Opt. Express. 2010; 1: 1432-1442.
16. Nachabé R, Evers DJ, Hendriks BH, et al. Effect of bile absorption coefficients on the estimation of liver tissue optical properties and related implications in discriminating healthy and tumorous samples. Biomed. Opt. Express. 2011; 2: 600-614.

Validation of interventional fiber optic spectroscopy with MR spectroscopy, MAS-NMR spectroscopy, high performance thin layer chromatography, and histopathology for accurate hepatic fat quantification

Chapter 4

17. Angulo P, Lindor KD. Non-alcoholic fatty liver disease. J. Gastroenterol. Hepatol. 2002; 17: 186-190.

18. Bollard ME,Garrod S, Holmes E, et al. High-resolution 1H and 1H-13C magic angle spinning NMR spectroscopy of rat liver. Magn. Reson. Med. 2000; 44: 201-207.

19. Garrod S, Humpher E, Connor SC, et al. High-resolution 1H NMR and magic angle spinning NMR spectroscopic investigation of the biochemical effects of 2-bromoethanamine in intact renal and hepatic tissue. Magn. Reson. Med. 2001; 45: 781-790.

20. Martínez-Granados B, Monleón D, Martínez-Bisbal MC, et al. Metabolite identification in human liver needle biopsies by high-resolution magic angle spinning 1H NMR spectroscopy. NMR Biomed. 2006; 19: 90-100.

21. Waters NJ, Garrod S, Farrant RD, et al. High-Resolution Magic Angle Spinning 1H NMR Spectroscopy of Intact Liver and Kidney: Optimization of Sample Preparation Procedures and Biochemical Stability of Tissue during Spectral Acquisition. Anal. Biochem. 2000; 282: 16-23.

22. Waters NJ, Holmes E, Waterfield CJ, et al. NMR and pattern recognition studies on liver extracts and intact livers from rats treated with alpha-naphthylisothiocyanate. Biochem. Pharmacol. 2002; 64: 67-77.

23. Westerterp M, Van der Hoogt CC, De Haan W, et al. Cholesteryl ester transfer protein decreases high-density lipoprotein and severly aggravates athersoclerosis in APOE*3-Leiden mice. Arterioscler. Thromb. Vasc. Biol. 2006; 26: 2552-2559.

24. Bottomley PA. Spatial localization in NMR spectroscopy in vivo. Ann. N. Y. Acad. Sci. 1987; 508: 333-348.

25. Naressi A, Couturien C, Devos JM, et al. Java-based graphical user interface for the MRUI quantitation package. Magma 2001; 12: 141-152.

26. De Bazelaire CM, Duhamel GD, Rofsky NM, et al. MR imaging relaxation times of abdominal and pelvic tissue measured in vivo at 2.0T: preliminary results. Radiology 2004; 230: 652-659.

27. Guiu B, Loffroy R, Petit JM, et al. Mapping of liver fat with triple-echo gradient echo imaging: validation against 3T proton MR spectroscopy. Eur. Radiol. 2009; 19: 1789-1793.

28. Van Ginneken V, Verhey E, Poelmann R, et al. Metabolics (liver and blood profiling) in a mouse model in response to fasting: a study of hepatic steatosis. Biochim. Biophys. Acta. 2007; 1771: 1637-1670.

29. Jarque CM, Bera AK. A test for normality of observations and regression residuals. Inter. Stat. Rev. 1987; 55: 163-172.

30. Bernard CP, Liney GP, Manton DJ, et al. Comparison of fat quantification methods: a phantom study at 3.0T. J. Magn. Reson. Imaging. 2008; 27: 192-197.

31. Tromberg BJ, Shah N, Lanning R, et al. Non-invasive in vivo characterization of breast tumors using photon migration spectroscopy. Neoplasia. 2000; 2: 26-40.

32. Spinelli L, Torricelli A, Pifferi A, et al. Bulk optical properties and tissue components in the female breast from multiwavelength time-resolved optical mammography. J. Biomed. Opt. 2004; 9: 1137-1142.

33. Kitai T, Beauvoit B, Chance B. Optical determination of fatty change of the graft liver with near-infrared time-resolved spectroscopy. 1996; 62: 642-647.
34. Nachabé R, Evers DJ, Hendriks BH, et al. Diagnosis of breast cancer using diffuse optical spectroscopy from 500 to 1600 nm: comparison of classification methods. J. Biomed. Opt. 2011; 16: 087010.
35. Fischer MA, Nanz D, Reiner CS, et al. Diagnostic performance and accuracy of 3-D spoiled Gradient-dual-Echo MRI with water- and fat-signal separation in liver-fat quantification: comparison to liver biopsy. Invest. Radiol. 2010; 45: 465-470.

Chapter 5

Effect of bile absorption coefficients on the estimation of liver tissue optical properties and related implications in discriminating healthy and tumorous samples

Rami Nachabé

Daniel J. Evers

Benno H. W. Hendriks

Gerald W. Lucassen

Marjolein van der Voort

Jelle Wesseling

Theo J. M. Ruers

Abstract

We investigated differences between healthy tissue and metastatic tumor from *ex vivo* human partial liver resections using diffuse optical spectroscopy with a fiber optic probe. We extracted various physiological and morphological parameters from the spectra. During evaluation of the residual between the measurements and a fit model based on diffusion theory, we found that bile is an additional chromophore absorbing in the visible wavelength range that was missing in our model. Consistency of the residual with the absorption spectrum of bile was noticed. An accurate measurement of the absorption coefficient of bile from various human bile samples was performed and implemented into the fit model. Having the absorption coefficient of bile as *a priori* knowledge in the model showed a clear improvement in terms of reducing the fitting discrepancies. The addition of this chromophore yields significantly different estimates of the amount of blood. Furthermore, the estimated bile volume fraction and reduced scattering amplitude turned out to be two main relevant discriminators between normal and metastatic liver tissues.

1. Introduction

Incidence and mortality rates of primary and secondary liver cancer have progressively increased worldwide over the last two decades [1]. In the western world, malignant lesions of the liver are generally metastases from other organs. Tumors of the gastro-intestinal tract, such as primary colorectal cancer, preferentially metastasize to the liver.

For liver metastases of colorectal origin, resection is the only accepted treatment with curative intent. However, radiofrequency ablation (RFA) is an increasingly practiced treatment modality for patients with liver malignancy that are not suitable for surgery [2-4].

The main negative prognostic factor for survival after liver surgery is a positive surgical margin [5, 6]. Histological analysis to determine the surgical margin is still considered to be the golden standard. However, intra-operative margin analysis would allow direct surgical intervention of a positive surgical margin, therefore reducing the chance of post-operative loco-regional recurrence.

Patients treated with RFA have demonstrated prolonged survival compared to patients treated with chemotherapy alone [7, 8]. Nevertheless, localization of the ablative needle and monitoring of the ablation process are important steps for optimal treatment of liver malignancies with RFA, since incidence of loco-regional disease recurrence due to ineffective ablation ranges from 3.6% to 60% [9]. Therefore, real-time intra-operative needle localization and ablation monitoring could improve ablation efficacy and disease-free survival.

Diffuse optical spectroscopy with fiber optic probes is a widely used technique to estimate the optical properties of tissue [10-15]. Concomitantly, several models have been developed to extract the absorption and reduced scattering coefficients from the measured spectra which are subsequently converted into physiological parameters. Such parameters are very useful to discriminate between healthy tissue and tumors in different organs. Indeed, several *ex vivo* and *in vivo* clinical studies were performed in the last decade showing the potential of optical spectroscopy to discriminate between healthy and tumor samples. However, only a few studies have focused on estimating tissue optical properties from spectroscopy measurements in liver [26-28] compared to other organs such as breast [11, 16-18], cervix [19, 20], lung [10, 21, 22] and skin [23-25].

In the present paper, we report on an *ex vivo* clinical study of healthy and metastatic human liver tissue where we measured the diffuse optical spectra in the 500-1600 nm wavelength range. From the acquired spectra, several physiological and morphological parameters of clinical relevance were extracted, using a widely accepted analytical model developed by Farrell *et al.* based on the diffusion theory [29]. Recently, we have shown the applicability of the model to wavelength ranges extended to 1600 nm where additional absorption features of water and lipids appear [30, 31]. Parameters that were also obtained by fitting the model to the measurements are blood, water, lipid volume fractions, average vessel radius, oxygen saturation level in blood and tissue scattering properties. Accurate analysis of the measured spectra suggested that bile is an important chromophore in the liver because it significantly absorbs in the visible wavelength range. This chromophore should therefore be included in the fitting model.

The difference between healthy and tumor *ex vivo* human liver tissue was investigated based upon the parameters extracted from these measurements.

2. Materials and methods

2.1 Patients and liver tissue handling

The presented pilot study on *ex vivo* liver was conducted at the Netherlands Cancer Institute in Amsterdam (NKI-AVL) under approval from the internal review board committee. Spectra were collected from liver surgical specimens after partial liver hepatectomy. Before resection of the specimen, the hepatic vessels that provide the blood supply to the part of the liver containing the tumor were clamped up to one hour before the resection started. Directly after resection, tissue was transported to the pathology department for further processing. After gross inspection by the pathologist, the optical spectra were collected from macroscopic normal and malignant tissue samples. Spectroscopy measurements were performed on freshly excised tissue before formalin fixation within two hours after the resection. In order to ensure that the measurements were at the tumor location, the samples were cut by the pathologist such that the tumor would be exposed in the most optimal way for measurements. All tumors were colorectal metastases and none were primary tumors. At the measurement sites, tissue was collected for conventional histopathology and the slides were analyzed at the pathology department. The pathological findings were correlated with the optical measurements.

Several spectra were measured on liver tissues from 14 enrolled patients. In average, 15 spectra at different sites were taken from each of the fourteen healthy and metastatic tumor samples, respectively. All the measurements taken from the 14 samples were included in the study and compiled with the results from the pathological report. All measurements were performed by the same operator and care was taken to ensure the same measuring conditions on all the samples.

2.2 Instrumentation and calibration

The spectra were collected from the different samples with an instrument which was used in our previous study [31]. The setup consists of a halogen broadband light source with an embedded shutter, an optical probe with three fibers and two spectrometers that can resolve light from 400 to 1100 nm (silicon detector) and 800 to 1700 nm (InGaAs detector), respectively. A filter that rejects light for wavelengths below 465 nm was mounted in front of the spectrometers to reject second order light at the detectors. The 1.3 mm diameter probe has a fiber connected to the light source and two other fibers each connected to a spectrometer. The center-to-center distance between the emitting and collecting fibers is 2.48 mm, where the tip of the probe has an angled bevel. All optical fibers are low-OH fibers of 200 microns core diameter. The spectrometers are controlled by custom-made software to acquire the data. Figure 1 depicts a schematic of the full setup.

The system was calibrated prior to each measurement on the tissue samples. The calibration consisted of several steps. First, the detectors were cooled down to -40°C. Once the temperature was stable, a wavelength calibration was performed to assign a wavelength value to each pixel of both detectors, fitting a second order polynomial to a

set of atomic lines from argon and mercury light sources with peaks at known wavelengths. The second steps consisted of calibrating the system with a white reflectance standard measurement to compensate for the spectral shape of the light emitted by the lamp and the wavelength-dependent sensitivity of the detectors. Subsequently, a background measurement was carried out. Each spectrum was acquired by measuring simultaneously with both spectrometers. The analyzed spectra corresponded to tissue measurements corrected for the spectral shape of the light source, and the spectral response of the detectors measured on a white standard reference measurement as described in detail in our previous studies [30, 31].

The simultaneously acquired spectra in the 400-1100 nm range and in the near-infrared 800-1700 nm range were combined to a single spectrum, using the 950-1000 nm range to scale the near-infrared spectrum to the visible spectrum. For the spectral analyses we have used the 500-1600 nm spectral range, where the 500 to 1000 nm and 1000 to 1600 nm correspond to the data collected with the silicon and InGaAs detectors, respectively [31].
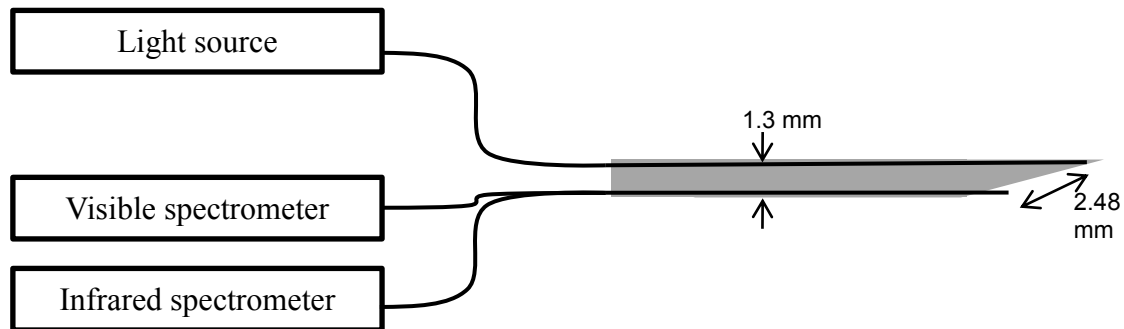

Figure 1. Schematic of the optical setup and the design of the optical probe.

2.3 Mathematical modeling of the diffuse optical spectra

The measured diffuse optical spectra were fitted, using the method of Farrell *et al.* [29] where the reduced scattering coefficient $\mu_s'(\lambda)$, the absorption coefficient $\mu_a(\lambda)$ and the center-to-center distance between the emitting and collecting fibers at the tip of the probe are input arguments for the model. The spectra were fitted over the wavelength range of 500-1600 nm, using a non-constrained linear least squares fitting algorithm. The validation of this method with the setup and optical probe described in section 2.2 was performed in our previous work based on an extensive phantom and *in vivo* animal studies [30-31]. Briefly, we demonstrated that the fiber distance separation that is used is large enough in order not to infringe the diffusion theory assumptions. An extensive phantom study with different absorption and reduced scattering properties was performed to investigate the robustness of the fit. It was also shown that the model is suitable to properly estimate chromophore concentrations independently from the reduced scattering profile which was varied by changing the particle size distribution in the phantoms. The confidence intervals of the estimated parameters that derive from the covariance matrix were also used to investigate the reliability of the fits from the phantom measurements. The wavelength dependant reduced scattering coefficient is expressed by a double power law

$$\mu_s^{'}(\lambda)=a\left(\rho_{MR}\left(\frac{\lambda}{\lambda_0}\right)^{-b}+\left(1-\rho_{MR}\right)\left(\frac{\lambda}{\lambda_0}\right)^{-4}\right) \quad [cm^{-1}], \quad (1)$$

where the wavelength λ is expressed in nm and is normalized to a wavelength value of $\lambda_0 = 800$ nm. The reduced scattering coefficient is expressed as the sum of a Mie and a Rayleigh scattering where ρ_{MR} is the Mie-to-total reduced scattering fraction and b corresponds to the slope of the Mie reduced scattering. The total reduced scattering amplitude at λ_0 is denoted by a .

We adopted the formulation of the absorption coefficient that is described in our previous study [31] where the absorption, due to chromophores present in the measured tissue, is expressed as

$$\mu_a^{Tissue}(\lambda)=\mu_a^{Blood}(\lambda)+\mu_a^{WL}(\lambda) \quad [cm^{-1}] \quad (2)$$

where $\mu_a^{Blood}(\lambda)$ corresponds to the absorption by blood and $\mu_a^{WL}(\lambda)$ corresponds to absorption by water and lipid in the probed tissue. The blood related absorption coefficient is given by

$$\mu_a^{Blood}(\lambda)=C(\lambda)\,v_{Blood}\left[S_tO_2\mu_a^{HbO_2}(\lambda)+\left(1-S_tO_2\right)\mu_a^{Hb}(\lambda)\right] \quad [cm^{-1}] \quad (3)$$

where $\mu_a^{HbO_2}$ and μ_a^{Hb} are the absorption coefficient of oxygenated hemoglobin HbO_2 and deoxygenated hemoglobin Hb, respectively. The parameter v_{Blood} corresponds to the blood volume fraction for a concentration of hemoglobin in whole blood of 150 mg/ml and S_tO_2 corresponds to the oxygen saturation of the blood in the probed volume. The factor C is a wavelength dependant correction factor known as a pigment packaging factor [32] and is given by

$$C(\lambda)=\frac{1-\exp\left(-2R\left[S_tO_2\mu_a^{HbO_2}(\lambda)+\left(1-S_tO_2\right)\mu_a^{Hb}(\lambda)\right]\right)}{2R\left[S_tO_2\mu_a^{HbO_2}(\lambda)+\left(1-S_tO_2\right)\mu_a^{Hb}(\lambda)\right]} \quad (4)$$

with R the average vessel radius expressed in cm; note however that its value is reported in microns throughout this paper. The absorption due to the presence of water and lipid in the measured tissue is defined as

$$\mu_a^{WL}(\lambda)=v_{WL}\left[f_{Lipid}\mu_a^{Lipid}(\lambda)+\left(1-f_{Lipid}\right)\mu_a^{H_2O}(\lambda)\right] \quad [cm^{-1}] \quad (5)$$

with $\mu_a^{H_2O}$ and μ_a^{Lipid} being the absorption coefficient of water and lipid (density of 0.86 g/ml [31]) , respectively. The parameters v_{WL} and f_{Lipid} correspond to the total volume fraction of water and lipid in the tissue and the lipid fraction within this volume, respectively. Describing the absorption due to water and lipid as in equation (5) has the advantage that the covariance between v_{WL} and f_{Lipid} is smaller compared to the sum of the absorption of water and lipid separately weighted by corresponding volume fractions [31]. However, throughout this paper v_{WL} and f_{Lipid} are converted to water and lipid fractions and reported as such because of their clinical relevance for interpretation.

When inspecting the measured spectra, it was observed that there was a missing absorber in the visible wavelength range i.e. between 500 and 750 nm. The assumption was that bile would be the missing absorber in the fit model, since it is an endogenous compound which is abundant in liver [33]. Absorption by bile was included by incorporating it into equation (2) so that the total absorption is expressed as

$$\mu_a^{Total}(\lambda)=\mu_a^{Tissue}(\lambda)+v_{Bile}\mu_a^{Bile}(\lambda) \quad [cm^{-1}] \quad (6)$$

where v_{Bile} and μ_a^{Bile} are the volume fraction and absorption coefficient of bile, respectively. The absorption coefficient was determined by measuring bile freshly obtained from the gallbladder of two patients who underwent a cholecystectomy as part of the liver resection operation. The bile was poured in cuvettes of different thickness (1, 2, 5 and 10 mm) and the optical transmission was measured in a spectrophotograph (Lambda 900 Spectrometer, Perkin Elmer) with a resolution of 1 nm. The bile absorption is depicted in figure 2 (circle-marked curve) and it corresponds to the measured absorption coefficients from 300 to 1600 nm. In the near-infrared, the bile absorption is similar to the water absorption coefficient [33]. This is due to the fact that bile is mainly composed of water. In the visible, bile has a local maximum at 409 nm, a local minimum at 350 nm and a large absorption peak centered at 605 nm. Additionally, figure 2 shows the absorption coefficient in a logarithmic scale of fully oxygenated hemoglobin [34], deoxygenated hemoglobin [34], lipid [30] and water [30] from 400 to 1600 nm.

In the model, we have used the bile absorption coefficient as the measured bile absorption coefficient from which the water absorption coefficient was retrieved. Figure 3 depicts the normalized absorption coefficients of bile, oxygenated and deoxygenated hemoglobin starting from 500 nm (starting wavelength of the fit). Bile has a large absorption peak at 605 nm of 5.4 cm^{-1} and its value does not change more than 5% between 550 and 650 nm. This large absorption peak can significantly change the spectral shape in the visible range of a measurement where bile is present in the tissue.
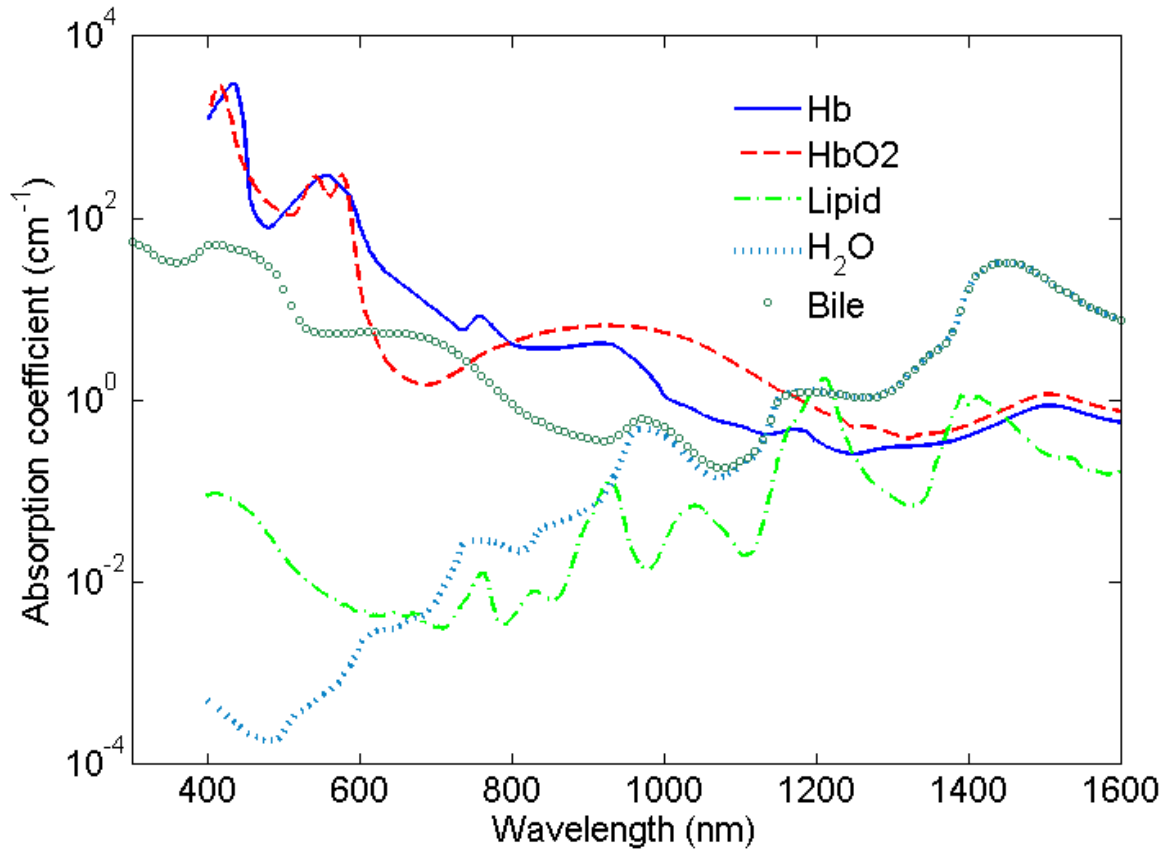
Figure 2. Absorption coefficients of deoxygenated hemoglobin (solid line), oxygenated hemoglobin (dashed line), lipid (dashed-dotted line) and water (dotted line) from 400 to 1600 nm .Absorption coefficient of bile (circle-marked line) from 300 to 1600 nm. The absorption coefficient axis is in a logarithmic scale.

From the acquired spectra the following parameters a, b, ρ_{MR}, R, ν_{Blood}, StO_2, ν_{WL}, f_{Lipid} and ν_{Bile} are determined. For each of these fit parameters, the confidence intervals were computed from the square root of the diagonal of the covariance matrix for a critical value of 0.05 [35]. A statistical F-test was performed to evaluate the improvement when bile is added to the model. The F-test is based on analyzing the difference between the sum-of-squares of the model with and without the bile absorption component. From the number of data points within the wavelength range where the fit was performed and the number of fit parameters for the models with and without the bile component, an F-ratio is computed from which a *p*-value can be extracted. If the *p*-value is smaller than the specific significance level chosen to be 0.05, the model with the bile component leads to a better description of the measured spectra. Statistical comparison of the parameters estimated from the healthy and metastatic tumor measurements was performed, using the Kruskal-Wallis non-parametric test with significance determined by computed *p*-values [36].
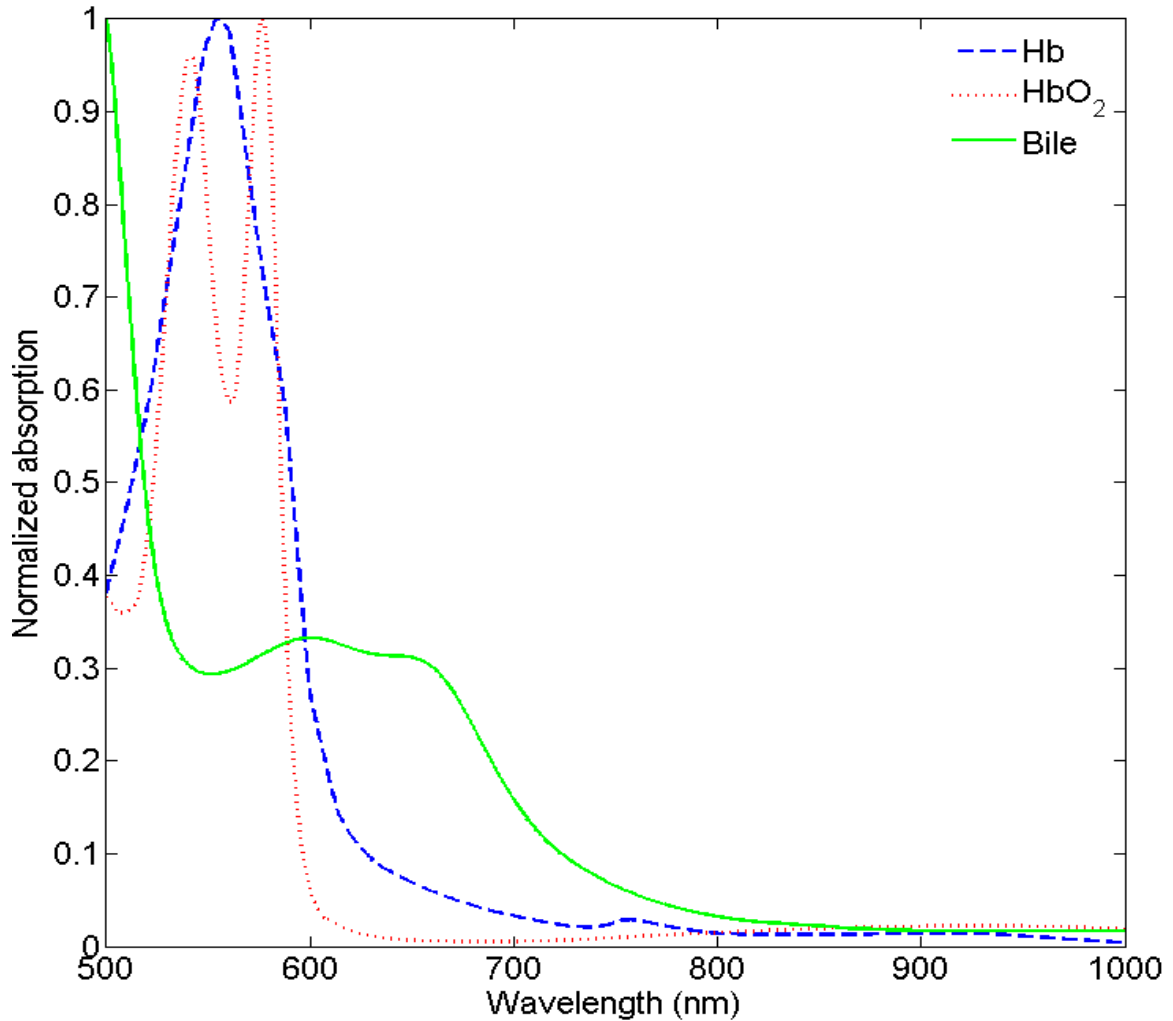
Figure 3. Normalized absorption coefficients of deoxygenated hemoglobin (dashed line), oxygenated hemoglobin (dotted line), and bile (solid line) between 500 and 1000 nm.

3.   Results and discussion

3.1 Mathematical model applied to the healthy liver tissue measurements

Figure 4 shows a measured spectrum from 500 to 1600 nm of a healthy liver sample (dotted line), the corresponding fit curve without the bile component added into the model (solid line) and the 95% confidence bounds (dashed lines) [37]. For the measurement shown in figure 4, the parameters and the corresponding confidence intervals obtained from the fit are v_{Blood} =4.4±0.3%, S_tO_2 =22±8%, R =76±13µm, v_{WL} =91±2%, f_{Lipid} =17±2%, and a reduced scattering amplitude of 14.2±0.3 cm^{-1} at 800 nm with a Mie-to-total reduced scattering fraction of 19±4%. When investigating the residual (χ^2=0.238) and the confidence bounds, a large deviation between the measurement and the fit curves was observed around the deoxygenated hemoglobin peak at 758 nm.
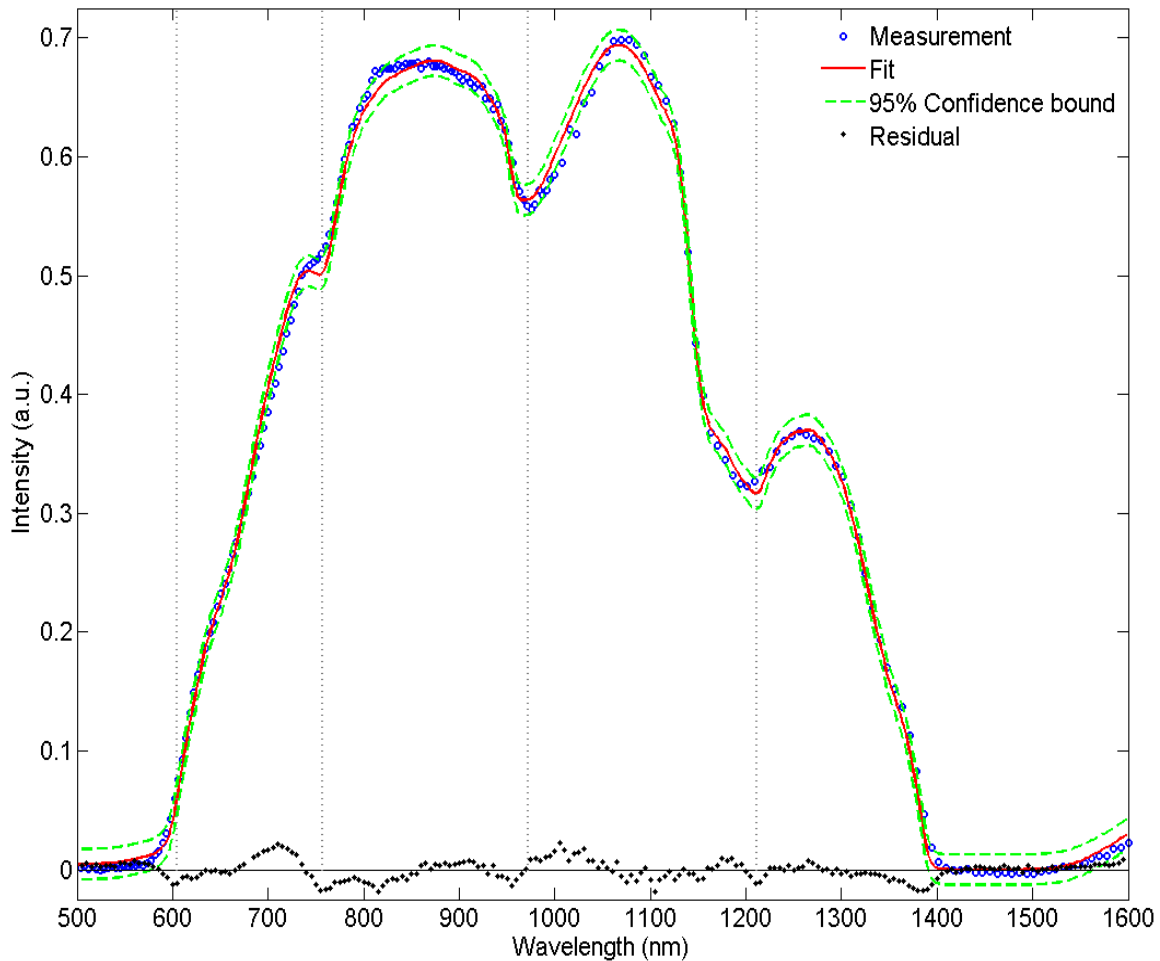
Figure 4. Reflectance measurement (dotted line) from a normal ex vivo tissue sample and its fit (solid line) without bile absorption coefficient implemented in the model and the corresponding 95% confidence bound (dashed lines). The vertical dotted lines at 605, 757, 972 and 1211 nm correspond to the absorption peaks location of bile, deoxygenated hemoglobin, water and lipid, respectively.

By adding the absorption coefficient of bile to the model, the large deviation around 758 nm significantly reduced while the confidence bounds narrowed towards the fit curve. The measurement curve in figure 5 is the same than the one depicted in figure 4 with a fit including the bile absorption coefficient in the model. For the measurement shown in figure 5, the estimated values and the corresponding confidence intervals are $\nu_{Bile} = 3.9 \pm 0.7\%$, $\nu_{Blood} = 3.5 \pm 0.3\%$, $S_t O_2 = 37 \pm 8\%$, $R = 56 \pm 13 \mu m$, $\nu_{WL} = 93 \pm 2\%$, $f_{Lipid} = 19 \pm 1\%$, and a reduced scattering amplitude of 14.5 ± 0.3 cm^{-1} at 800 nm with a Mie-to-total reduced scattering fraction of $25 \pm 7\%$ were found. The residual decreased to a value of $\chi^2 = 0.206$. In comparison to the outcome of the model without bile, the oxygen saturation level is higher, indicating that the bile absorption was compensated by deoxygenated hemoglobin. Similar results can be seen in table 1 which shows comparison of the mean and standard deviation of the parameters obtained from all the spectra measured on the 14 normal human liver tissue samples. Based on the confidence intervals, the model with bile showed for each sample that the parameters were estimated

more reliably compared to the model without bile. Another observation in figure 5 is that the 95% confidence bound is closer to the fit curve, especially in the wavelength range between 500 and 800 nm where a bile absorption peak is present.
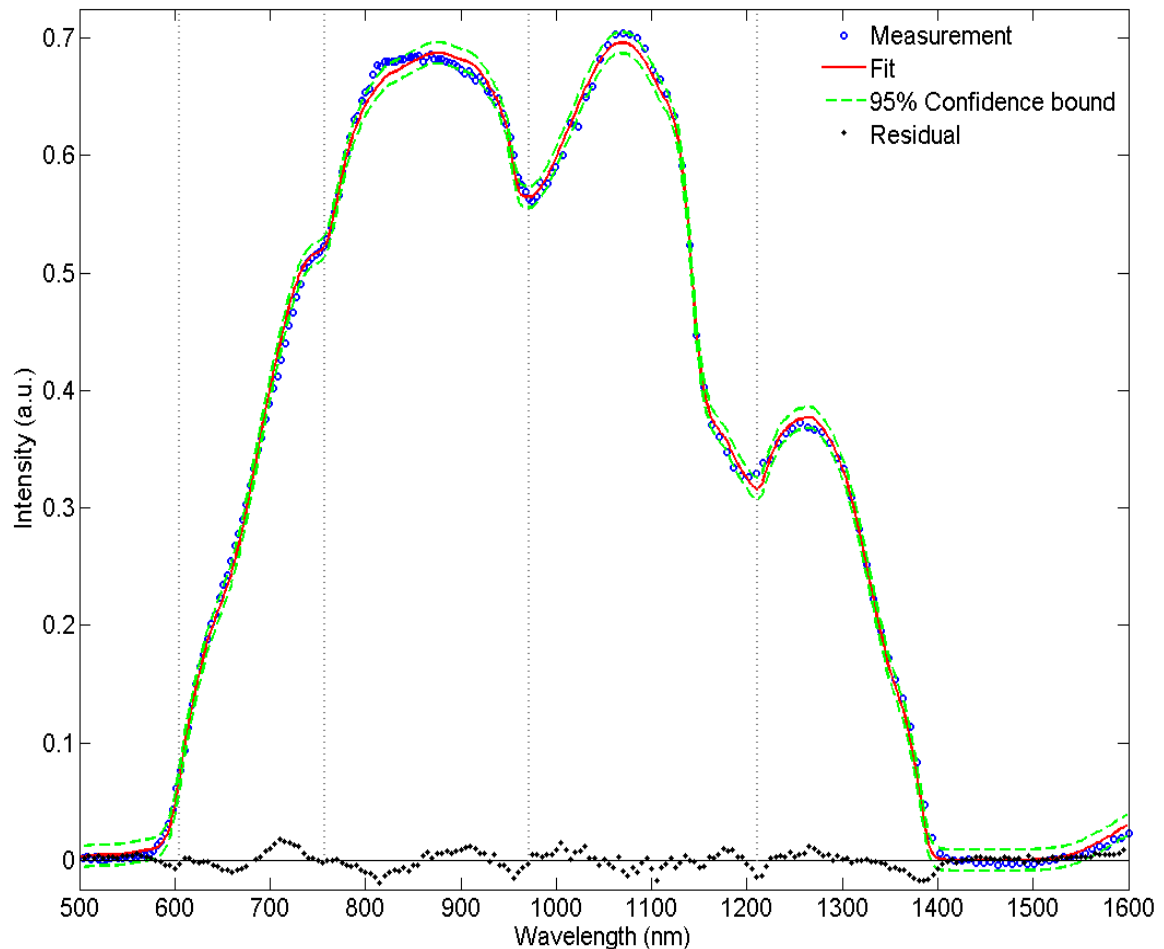

Figure 5. Reflectance measurement (dotted line) from a normal ex vivo tissue sample and its fit (solid line) with bile absorption implemented in the model and the corresponding 95% confidence bound (dashed line). The vertical dotted lines at 605, 757, 972 and 1211 nm correspond to absorption peaks location of bile, deoxygenated hemoglobin, water and lipid, respectively.

In order to depict the imprint of bile absorption on the measured spectra, a forward calculation of the spectrum with the estimated parameters can be computed by setting the bile volume fraction to 0%. Figure 6 shows another example of a healthy liver spectrum and the corresponding fits where the estimated bile volume fraction is 10.4%. Additionally, the forward computation of the spectrum by using the estimated parameters as input arguments and setting the bile volume fraction to 0% is plotted and the area comprised between the generated curves and the fitted curves is illustrated and highlights the spectral changes that result from bile absorption.

113

Table 1. Mean and standard deviation of the estimated values of the physiological and morphological parameters of healthy liver tissues obtained from the fitting model without and with bile absorption coefficient.

Parameters	Fit without bile	Fit with bile
Bile (%)	-	6.6±4.5
Blood volume fraction (%)	4.8±0.3	3.4±2.0
Blood oxygenation level (%)	6±8	8±14
Average vessel radius (microns)	67±28	50±22
Water volume fraction (%)	77±7	76±7
Lipid volume fraction (%)	17±11	19±11
Reduced scattering at 800 nm (cm^{-1})	17±2	17±3
Mie Slope	0.5±0.3	1.0±0.5
Mie-to-total scattering fraction (%)	19±10	37±19

According to a statistical F-test with $p<0.05$, 95% of the data showed improvement on the fitting when bile is added to the model.

In order to mathematically evaluate whether bile is the missing absorber in the model, a statistical F-test was applied to all the data acquired at healthy sites in the liver [37]. *P*-values were computed from the F-ratios to evaluate if the model with bile absorption improved the fits. In total, 95% of the data have shown that the model including bile described best the measured spectra with a *p*-value below 0.05.
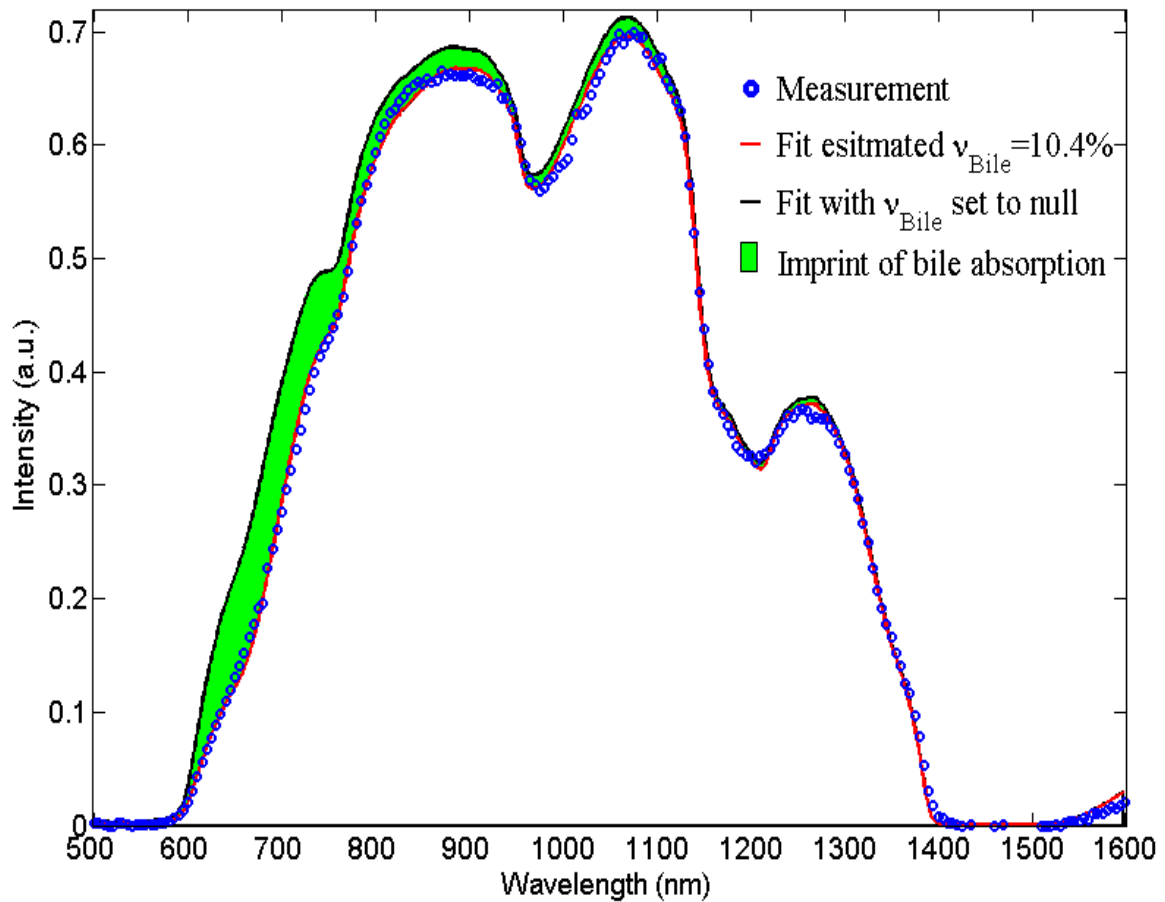
Figure 6. Tissue measurement from a normal tissue sample (dotted line) with an estimated bile volume fraction estimated from the fit (red solid line) of 10.4%. The colored area indicates the imprint of bile absorption obtained by comparison with a forward computation of the diffuse reflectance spectrum where the bile volume fraction is set to 0% (black solid line).

3.2 Comparison of healthy and metastatic tumor liver tissue

Figure 7 shows a typical spectrum (dotted line) from both healthy and metastatic tumor liver tissues with the corresponding fit curves (solid line) including bile. Major differences between the two typical spectra correlated with a difference in the estimated parameters.

From the typical metastatic tissue measurement depicted in figure 7, the estimated parameters and the corresponding confidence intervals are v_{Bile} =0±0%, v_{Blood} =1.5±0.1%, S_tO_2 =3±5%, R =31±3μm, v_{WL} =101±2%, f_{Lipid} =10±1%, and a reduced scattering amplitude of 9.8±0.3 cm^{-1} at 800 nm with a Mie-to-total reduced scattering fraction of 76±4%.
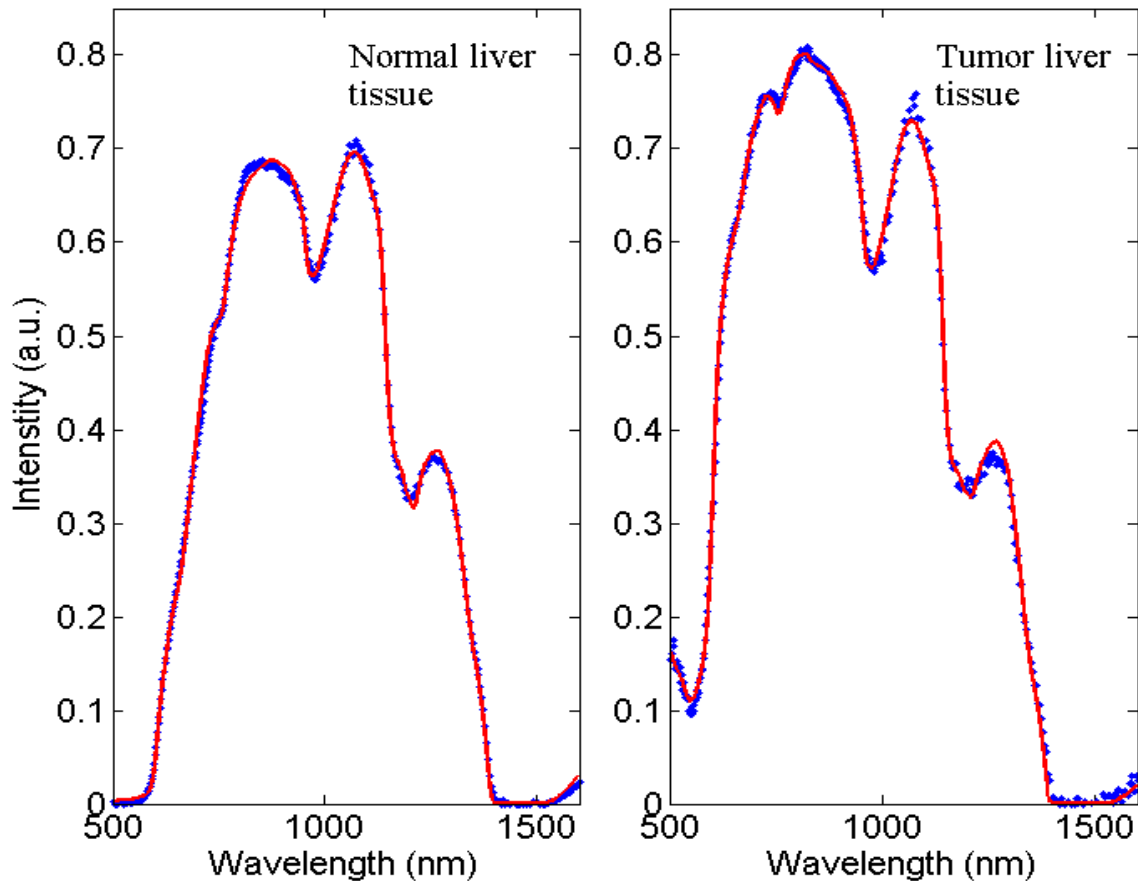
Figure 7. Reflectance measurement of healthy and metastatic tumor liver tissues (dotted line) and their corresponding fits (solid line).

Table 2 summarizes all the median and standard deviations derived from the interquartiles of the various fit parameters for all the measurements performed in the fourteen samples of healthy and metastatic liver tissues. The advantage of reporting the median and the standard deviation derived from interquartiles instead of the mean and standard deviation is that the data cannot be described by a parametric distribution, hence we used a non-parametric statistical Kruskal-Wallis test instead of a t-test to find which parameters show significant difference between the two types of tissue, as was also done in previous studies [10, 12, 13, 16, 17, 19, 21, 22]. The blood oxygenation was not reported, due to the fact that the study was conducted on *ex vivo* samples. Therefore this parameter does not reflect the actual oxygenation level as it would be *in vivo*. According to the Kruskal-Wallis statistical test, the values that showed most significant differences between healthy and metastatic tissues with $p < 0.01$ were bile, the reduced scattering amplitude and the water volume fraction.

Effect of bile absorption coefficients on the estimation of liver tissue optical properties and related implications in discriminating healthy and tumorous samples

Chapter 5

Table 2. Median and standard deviation of the various morphological parameters estimated from ex vivo measurements performed on normal and metastatic tumor tissues in liver.

Parameters	Normal liver (14 samples)	Metastatic Tumor (14 samples)
Bile (%)[a]	5.5±2.3	1.0±1.1
Blood volume fraction (%)	3.2±1.6	0.8±2.4
Blood oxygenation level (%)	8±14	45±44
Average vessel radius (microns)	53±20	67±82
Water volume fraction (%)[a]	76±4	93±17
Lipid volume fraction (%)	16±3	12±6
Reduced scattering at 800 nm (cm^{-1}) [a]	17±3	10±3
Mie Slope	1.2±0.7	0.5±0.5
Mie-to-total scattering fraction (%)	44±25	57±15

[a]Indicates significant differences with $p<0.01$ for the Kruskal-Wallis test.

Figure 8 shows a picture of a tumor and the surrounding healthy liver tissue. It is visually clear that the tumor is less rich in blood than the healthy liver tissue. All the measured tumors were at least a centimeter in diameter and rather white in appearance.
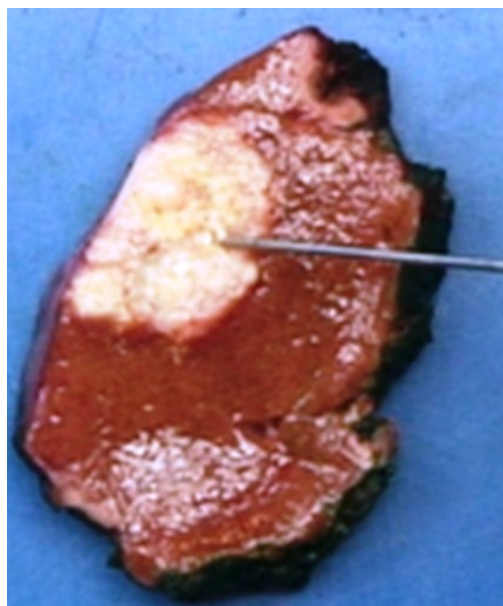

Figure.8. Picture of a tumor surrounded by healthy liver tissue. The optical probe is directed towards the tumor site.

4. Discussion

A paucity of studies has investigated the absorption coefficient of bile. Maitland *et al.* [33] measured the absorption coefficient of bile from 350 to 2450 nm and stated that bile has its main absorption peaks at 400, 1450 and 1900 nm. The latter two most likely correspond to absorption due to the presence of water in bile, whereas the peak at 400 nm corresponds to an actual absorption peak of bile. After measuring the absorption coefficient of bile, we observed a broad absorption peak between 550 and 650 nm with a local maximum of 5.4 cm^{-1} at 605 nm. Our measurement also suggests that there is a higher absorption peak at 409 nm, whereas the maximum reported by Maitland *et al.* is at 400 nm [33]. The presented bile absorption coefficients in this paper can therefore be considered as an updated measurement of the one reported by Maitland *et al.* [33].

This study demonstrated the necessity to incorporate the bile absorption coefficient into the model when fitting spectroscopic measurements in liver tissue. In 95% of the measured healthy tissue data, including bile in the fitting model provided a better fit according to a statistical F-test. The fit parameters that were mainly altered when the bile was not added to the model were the blood volume fraction and the average vessel radius. For the 14 measured normal samples, the blood volume fraction decreased on average from 4.8±1.7% to 3.4±2.0%, whereas no significant changes were observed for the oxygenation level of blood. Figure 2 and 3 illustrates a higher absorption for deoxygenated hemoglobin than for oxygenated hemoglobin between 550 and 750 nm. The main absorption of bile is between these wavelengths. The resulting fit model without bile compensates for the residual by overestimating the deoxygenated hemoglobin yielding higher blood volumes with unchanged oxygen saturation levels. Moreover, this discrepancy is observed between the measurement and the fit curves depicted at 758 nm in figure 4 where no bile was taken into account in the model. It is important to note that deoxygenated-hemoglobin has a distinct spectral absorption peak at 758 nm (cf. figure 2) resulting in an inflection point in the fits that is not present in the measured liver spectra. Furthermore, changes are observed in the Mie slope and Mie-to-total reduced scattering fractions, whereas the reduced scattering amplitude remains unchanged. Finally, no effects on the estimation of water and lipid fractions is seen when bile is not present in the model. This is expected since there are no overlapping absorption features between these two biological parameters.

It is important to note that the bile that was used to measure its absorption coefficients comes from patients suffering from metastatic colorectal cancer. Therefore the pigmentation concentration in the bile can vary from one person to another, resulting in slightly different absorption coefficients; hence the presence of a significant residual around 800 nm when bile is added in the model (cf. figure 5). However, this is not the case in all patients. Another remark with respect to the residual is the small deviation between the measurement and the fits around 1211 nm which is most probably due to changes in water absorption coefficients with temperature. Indeed, the tissue measurements were performed *ex vivo* after resection, and hence the temperature of the samples decreased from body temperature down to the room ambient temperature when brought to the pathology department. We have shown elsewhere [30] that water

Effect of bile absorption coefficients on the estimation of liver tissue optical properties and related implications in discriminating healthy and tumorous samples

Chapter 5

absorption coefficient is temperature dependant and that it is prone to significant variation in absorption in the vicinity of 1200 nm, hence the small residual around this wavelength.

The analysis of the diffuse optical spectra showed significant differences according to the Kruskal-Wallis non-parametric test with a critical value of 0.01 for bile and water volume fractions, as well as the reduced scattering amplitude and the oxygenation saturation of blood.

The study by Kitai *et al.* [26] measured the optical properties before and after clamping the left branches of the hepatic pedicle, including the portal vein and hepatic artery, during 60 minutes. Their study showed that the oxygenation level in blood equals 75% just before clamping the vessels and drops down to 8% one hour after clamping. The median oxygenation values in the healthy tissues and tumors presented in table 2 are 8% and 45%, respectively. In our study, the blood vessels of the resected specimens were clamped up to one hour before the resection was completed and the samples were transported within a time frame of two hours after resection to the pathology department. Therefore, there was no more blood flow and perfusion to the liver tissue in the *ex vivo* samples yielding to a decrease in oxygenation levels when the samples were delivered for measurements. It is therefore difficult to draw any conclusions by comparing the estimated oxygenation levels in healthy tissues and the tumors measured *ex vivo*.

The reduced scattering amplitude and the bile volume fraction showed the most significant differences (p<0.0001) between healthy and metastatic liver tissues. As shown in table 2, healthy tissue has more than five times more bile than tumors whereas the reduced scattering amplitude is almost twice as high. Healthy liver tissue is mainly constituted of hepatocytes which are cells that are arranged as very thin plates separated by fine vascular sinusoids where blood flows; allowing perfusion of the bile throughout the liver [38]. In the tumor, this structure is lost, causing a different perfusion of the bile and an alteration of the cell structures yielding to a different light scattering. This observation is consistent with the fact that the tumors in liver are metastases of colorectal cancer with different structural composition. The tumor consists therefore of abnormal colorectal tissue cells embedded in collagenous cellular stroma induced by the epithelial tumor cells. Such tumors are almost completely devoid of stroma. Therefore, hardly any bile is expected in the tumor cells from colorectal origin.

The reduced scattering amplitude is 1.7 times higher in healthy tissue than in tumors. Germer *et al.* measured the absorption coefficient, scattering and anisotropy of human liver tissues and colorectal liver metastases *in vitro* at 850, 980 and 1064 nm [39]. They found that scattering in human liver tissues is in average 1.7 times higher than in the metastases tissues. However, the large difference in anisotropy yields to reduced scattering of 9.5 and 11 cm^{-1} at 800 nm (extrapolated values) for normal and metastatic liver tissue, respectively [39]. Therefore, the reduced scattering amplitude of the metastatic tumor reported in table 2 is very comparable to the value reported in ref. [39] whereas the value in healthy liver tissue is much higher.

The water volume fraction showed significant difference between both types of tissue with higher water content in tumor. There is a multitude of factors that could explain this observation. In particular, the fact that water is attracted to necrotic tissue

which is also abundantly present in most colorectal liver metastases, the high water content of collagenous stroma in general, and tumor induced stroma could play a role.

From Table 2, one can observe a low Mie scattering contribution in liver compared to other organs. The reported Mie-to-total scattering fraction in healthy tissue and tumors are 44% and 57%, respectively. Optical properties such as the absorption coefficient, scattering coefficient and anisotropy of porcine liver were measured with a double integrating sphere setup by Fritz *et al.* [40] where it is clearly shown that the anisotropy of liver tissue steeply increases from 0.75 to 0.9 between 400 and 600 nm and is constant at a value of 0.93 beyond 600 nm up to 1600 nm. By applying the double power law for reduced scattering as expressed in Eq. (1) to the data of Fritz *et al.* up to 1600 nm, the Mie-to-total reduced scattering contribution is as low as 59% which is comparable to the values reported in table 2. This is a result of the high gradient of the anisotropy below 600 nm. Rayleigh scattering occurs due to the interaction of light with sub-micron structures, such as thin fibers, in tissue and it was proven that it is necessary to include a Rayleigh term in the reduced scattering model beyond 500 nm [41]. Liver is very rich in sub-micron reticular fibers in the perisinusoidal space separating hepatocytes from sinusoids, likely yielding high Rayleigh scattering [38].

Table 2 reports a median value of blood volume fraction in healthy and metastatic tissue of 3.2% and 0.8%, respectively. However, despite this large difference, there is statistically no significant difference ($p < 0.05$) between the two types of tissue because the standard deviation for tumor tissue is very large. The reason is that in two of the fourteen tumor samples, which were large necrotic samples, high amounts of blood were present. Indeed it is known that most tumors have a vascular network of higher density than most normal tissues. However, the opposite is true for colorectal liver metastases, as normal liver tissue is extremely well vascularized to fulfill its many functions related to metabolism, detoxification, bile production, etc. The absorption coefficient of the human liver measurements in ref. [39] was found to be higher in the liver than in the metastases for the wavelengths of interest which in fact means that more blood is present in healthy liver tissue than in metastatic tumors which corroborates with the estimated blood volume fraction in table 2.

Given the distance between the emitting and collecting fibers, the amount of light that is collected below 600 nm is in some cases close to the noise level because of the high blood amount (above roughly 5%) in the liver. The high amount of blood causes a decrease in the amount of light that is collected. In order to enhance the reliability of the estimated parameters of the blood and bile, one could measure below 500 nm where additional absorption peaks of these chromophores exist (cf. figure 2) by using a smaller distance separation between the emitting and collecting fibers.

5. Conclusion

In conclusion, this paper presents the first study in which bile, water and lipid are included in addition to oxygenated and deoxygenated hemoglobin in the discrimination between healthy and metastatic tumors tissues in human liver with diffuse optical spectroscopy. The absorption spectrum of bile was accurately measured and integrated in the model in order to estimate the concentration of this chromophore in the liver. We have

demonstrated that bile should be included when analyzing diffuse optical spectroscopy data, because of its presence in the liver bile ducts. Our results illustrate that discrimination between healthy and metastatic liver cancer tissues seems possible based on the estimated bile volume fraction and reduced scattering amplitude obtained from diffuse optical spectra measured on both types of tissue. Compared to healthy tissue, tumors have around five and two times lower bile and reduced scattering amplitude values, respectively. This method can also be applied during real-time intra-operative needle localization and ablation monitoring to improve ablation efficacy and hence disease-free survival.

6. Acknowledgments

References

1. Am. Canc. Org. 2010 official stats website: http://www.who.int/mediacentre/factsheets/fs297/en/index.html

2. N. C. Tsim, A. E. Frampton, N. A. Habib, and L. R. Jiao, "Surgical treatment for liver cancer", World J. Gastroenterol. **16**, 927-933 (2010).

3. N. Kemeny, "The management of resectable and unresctable liver metastases from colorectal cancer", Curr. Opin. Oncol. **22**, 364-373 (2010).

4. H. Shimada, K. Tanaka, I. Endou, and Y. Ichikawa, "Treatment for colorectal liver metastases: a review", Langenbeck's Arch. Surg. **394**, 973-983 (2009).

5. A. Muratore, D. Ribero, G. Zimmitti, A. Mellano, S. Langella, and L. Capussotti, "Resection margin and recurrence-free survival after liver resection of colorectal metastases", Ann. Surg. Oncol. **17**, 1324-1329 (2010).

6. T. M. Pawlik, C. R. Scoggins, D. Zorzi, E. K. Abdalla, A. Andres, C. Eng, S. A. Curley, E. M. Loyer, A. Muratore, G. Mentha, L. Capussotti, and J. N. Vauthey, "Effect of surgical margin status on survival and site of recurrence after hepatic resection for colorectal metastases", Ann. Surg. **241**, 715-722 (2005).

7. N. Bhardwaj, A. D. Strickland, F. Ahmad, A. R. Dennison, and D. M. Lloyd, "Liver ablation techniques: a review", Surg. Endosc. **24**, 254-265 (2010).

8. T. J. Ruers, J. J. Joosten, B. Wiering, B. S. Langenhoff, H. M. Dekker, T. Wobbes, W. J. Oyen, P. F. Krabbe, and C. J. Punt, "Comparison between local ablative therapy and chemotherapy for non-resectable colorectal liver metastases: a prospective study", Ann. Surg. Oncol. **14**, 1161-1169 (2007).

9. S. L. Wong, P. B. Mangu, M. A. Choti, T. S. Crocenzi, G. Dodd, G. S. Dorfman, C. Eng, Y. Fong, A. F. Giusti, D. Lu, T. A. Marsland, R. Michelson, G. J. Poston, D. Schrag, J. Seidenfeld, and A. Benson, "American society of clinical oncology 2009 clinical evidence review on radiofrequency ablation of hepatic metastases from colorectal cancer", J. Clin. Oncol. **28**, 493-508 (2010).

10. M. L. Bard, A. Amelink, V. N. Hegt, W. J. Graveland, H. J. C. M. Sterenborg, H. C. Hoogsteden, and J. G. J. V. Aerts, "Measurement of hypoxia-related parameters in bronchial mucosa by use of optical spectroscopy", Am. J. Respir. Crit. Care Med. **171**, 1178-1184 (2005).

11. Z. Volynskaya, A. S. Haka, K. L. Bechtel, M. Fitzmaurice, R. Shenk, N. Wang, J. Mazemi, R. R. Dasari, and M. S. Feld, "Diagnosing breast cancer using diffuse reflectance spectroscopy and intrinsic fluorescence spectroscopy", J. Biomed. Opt. **13**, 024012 (2008).

12. A. E. Cerussi, N. Shah, D. Hsiang, A. Durkin, J. Butler, and B. J. Tromberg, "In vivo absorption , scattering of 58 malignant breast tumors determined by broadband diffuse optical spectroscopy", J. Biomed. Opt. **11**, 044005 (2006).

13. J. Q. Brown, L. G. Wilke, J. Geradts, S. A. Kennedy, G. M. Palmer, and N. Ramanujam, "Quantitative optical spectroscopy: a robust tool for direct measurement of breast cancer vascular oxygenation and total hemoglobin content in vivo", Cancer Res. **69**, 2919-2926 (2009).

Effect of bile absorption coefficients on the estimation of liver tissue optical properties and related implications in discriminating healthy and tumorous samples

Chapter 5

14. G. Zonios, L. T. Perelman, V. M. Backman, R. Manoharan, V. D. Fritzmaurice, J. Van Dam, and M. S. Feld, "Diffuse reflectance spectroscopy of human adenomatus colon polyps in vivo", Appl. Opt. **38**, 6628-6637 (1999).

15. R. Reif, O. A'Amar, and I. J. Bigio, "Analytical model of light reflectance for extraction of the optical properties in small volumes of turbid media", Appl. Opt. **46**, 7317-7328 (2007).

16. R. L. P. van Veen, A. Amelink, M. Menke-Plymers, C. Van der Pol, and H. J. C. M. Sterenborg, "Optical biopsy of breast tissue using differential path-length spectroscopy", Phys. Med. Biol. **50**, 2573-2581 (2005).

17. C. Zhu, T. M. Breslin, J. Harter, and N. Ramanujam, "Model based and empirical spectral analysis for the diagnosis of breast cancer", Opt. Exp. **16**, 14961-12978 (2008).

18. I. J. Bigio, S. G. Bown, G. Briggs, C. Kelley, S. Lakhani, D. Pickard, P. M. Ripley, I. G. Rose, and C. Saunders, "Diagnosis of breast cancer using elastic-scattering spectroscopy: preliminary clinical results", J. Biomed. Opt. **5**, 221-228 (2000).

19. V. Chang, P. S. Cartwright, S. M. Bean, G. M. Palmer, R. C. Bentley, and N. Ramanujam, "Quantitative physiology of the precancerous cervix *in vivo* through optical spectroscopy", Neoplasia **11**, 325-332 (2009).

20. J. R. Mourant, T. J. Bocklage, T. M. Powers, H. M. Greene, K. L. Bullock, L. R. Marr-Lyon, M. H. Dorin, A. G. Waxman, M. M. Zsemlye, and H. O. Smith, "*In vivo* light scattering measurements for detection of precancerous conditions of the cervix", Gyneco. Onc. **105**, 439-445 (2007).

21. S. C. Kanick, C. van der Leest, R. S. Djamin, A. M. Janssens, H. C. Hoogsteden, H. J. C. M. Sterenborg, A. Amelink, and J. G. J. V. Aerts, "Characterization of mediastinal lymph node physiology *in vivo* by optical spectroscopy during endoscopic ultrasound-guided fine needle aspiration", J. Thoracic. Onc. **5**, 981-987 (2010).

22. S. C. Kanick, C. van der Leest, J. G. J. V. Aerts, H. C. Hoogsteden, S. Kascakova, H. J. C. M. Sterenborg, and A. Amelink, "Integration of single-fiber reflectance spectroscopy into ultasound-guided endoscopic lung cancer staging of mediastinal lymph nodes", J. Biomed. Opt. **15**, 017004 (2010).

23. G. Zonios, and A. Dimou, "Modeling diffuse reflectance from semi-infinite turbid media: application to the study of skin optical properties", Opt. Exp. **14**, 8661-8674 (2006).

24. G. Zonios, I. Bassukas, and A. Dimou, "Comparative evaluation of two simple diffuse reflectance models for biological tissue applications", Appl. Optics **47**, 4965-4973 (2008).

25. G. Zonios, and A. Dimou "Light scattering spectroscopy of human skin in vivo", Opt. Exp. **17**, 1256-1267 (2009).

26. T. Kitai, M. Miwa, H. Liu, B. Beauvoit, B. Chance, and Y. Yamaoka, "Application of near-infrared time-resolved spectroscopy to rat liver, a preliminary report for surgical application", Phys. Med. Biol. **44**, 2049-2061 (1999).

27. T. Kitai, T. Nishio, M. Miwa, and Y. Yamaoka, "Optical analysis of the cirrhotic liver by near-infrared time-resolved spectroscopy", Surg. Today **34**, 424-428 (2004).

28. C. P. Hsu, M. K. Razavi, S. K. So, I. H. Parachikov, and D. A. Benaron, "Liver tumor gross margin identification and ablation monitoring during liver radiofrequency treatment", J. Vasc, Inter. Radiol. **16**, 1473-1478 (2005).

29. T. J. Farrell, M. S. Patterson, and B. Wilson, "A diffusion theory model of spatially resolved, steady-state diffuse reflectance for the non-invasive determination of tissue optical properties", Med. Phys. **19**, 879-888 (1992).

30. R. Nachabé, B. H. W. Hendriks, A. E. Desjardins, M. van der Voort, M. B. van der Mark, and H. J. C. M. Sterenborg, "Estimation of lipid and water concentrations in scattering media with diffuse optical spectroscopy from 900 to 1600 nm", J. Biomed. Opt. **15**, 037015 (2010).

31. R. Nachabé, B. H. W. Hendriks, M. van der Voort, A. E. Desjardins, and H. J. C. M. Sterenborg, "Estimation of biological chromophores using diffuse optical spectroscopy: benefit of extending the UV-VIS wavelength range to include 1000 to 1600 nm", Biomed. Opt. Exp. **18**, 1432-1442 (2010).

32. W. Verkruysse, G. Lucassen, J. F. De Boer, D. J. Smithies, J. S. Nelson, and M. J. C. Van Gemert, "Modelling light distributions of homogenous versus discrete absorbers in light irradiated turbid media", Phys. Med. Biol. **42**, 51-65 (1997).

33. D. J. Maitland, J. T. Walsh, and J. B. Prystowsky, "Optical properties of human gallbladder tissue and bile", App. Opt. **32**, 586-591 (1993).

34. W. G. Zijlstra, A. Buursma, and O. W. Van Assendelft, *Visible and near infrared absorption spectra of human and animal haemoglobin* (Utrecht, The Netherlands, VSP Publishing, 2000).

35. A. Amelink, D. J. Robinson, and H. J. C. M. Sterenborg, "Confidence intervals on fit parameters derived from optical reflectance spectroscopy measurements", J. Biomed. Opt. **13**, 054044 (2008).

36. W. H. Kruskal, and W. A. Wallis, "Use of ranks in one-criterion variance analysis", J. Am. Stat. Association **47**, 583-621 (1952)

37. H. Motulsky, *Intuitive biostatistics* (Oxford University Press, 1995).

38. B.Young, J. Lowe, A. Stevens, and J. Heath, *Wheater's functional histology* (Churchill Livingstone, 2006).

39. C. Germer, A. Roggan, J. Ritz, C. Isbert, D. Albrecht, G. Müller, and H. Buhr, "Optical properties of native and coagulated human liver tissue and liver matastases in the near infrared range", Lasers in Surg. and Med. **23**, 194-203 (1998).

40. J. Ritz, A. Roggan, C. Isbert, G. Müller, H. Buhr, and C. Germer, "Optical properties of native and coagulated porcine liver tissue between 400 and 2400 nm", Lasers in Surg, and Med. **29**, 205-212 (2001).

41. I. S. Saidi, S. L. Jacques, and F. K. Tittel, "Mie and Rayleigh modeling of visible-light scattering in neonatal skin", Appl. Opt. **34**, 7410-7418 (1995).

Chapter 6

Optical sensing for tumor detection in the liver

Daniel J. Evers

Rami Nachabé

Daphne Hompes

Frits van Coevorden

Gerald W. Lucassen

Benno H. W. Hendriks

Loes van Velthuizen

Jelle Wesseling

Theo J. M. Ruers

Abstract

Introduction. There is an increasing trend for optical guidance techniques in surgery. Optical imaging using Diffuse Reflectance Spectroscopy (DRS) can distinguish different tissue types through a specific "optical fingerprint". We aim to evaluate whether DRS could discriminate metastatic tumor tissue from normal liver tissue and in this way would be a potential technology for further implementation into surgical or radiological intervention tools.

Methods. A miniaturized optical needle was developed able to collect DRS spectra between 500 and 1600 nm. Liver specimen of 24 patients operated for colorectal liver metastases were analyzed with DRS immediately after resection. Multiple measurements were performed and DRS results were compared to the histology analysis of the measurement locations. In addition, normal liver tissue was scored for the presence or absence of steatosis.

Results. A total of 780 out of the 828 optical measurements were correctly classified into either normal or tumor tissue. The resulting sensitivity and specificity were both 94%. The results of the analysis for each patient *individually* showed an accuracy of 100%. The Spearman's rank correlation of DRS estimated percentages of hepatic steatosis in normal liver tissue compared to that of the pathologist was 0.86.

Conclusion. DRS demonstrates a high accuracy in discriminating normal liver tissue from colorectal liver metastases. DRS can also predict the degree of hepatic steatosis with high accuracy. The technique, here demonstrated in a needle like probe, may as such be incorporated into surgical tools for optical guided surgery or percutaneous needles for radiological interventions.

1. Introduction

In the last decade, optical sensing by means of diffuse reflectance spectroscopy (DRS) has developed into a promising technique that could make a significant contribution to the diagnosis and treatment monitoring of cancer [1, 2]. DRS is an optical measurement technique that records changes in the spectral distribution of light after its interaction with the molecules of the tissue. Main changes in the reflected spectra are a result of a combination of absorption and scattering of light. By illuminating tissue with a selected spectral band of light and subsequent analysis of the characteristic scattering and absorption patterns, it is possible to obtain an 'optical fingerprint' of the tissue. Such an optical fingerprint represents specific quantitative biochemical en morphological information from the examined tissue and may depend on metabolic rate, vascularity, intra-vascular oxygenation and alterations in tissue morphology. By allowing specific differentiation between tissues, this technique has the potential to be incorporated into optical tools for cancer diagnosis and therapy. As such, DRS is progressively being explored for sole use as well as for combined use with conventional imaging techniques. It has been performed for tissue surface analysis during endoscopical procedures but also for analysis of tissue abnormalities in solid organs [3-8]. Within breast cancer, several groups have investigated the improvement of tissue biopsy and surgical margin analysis with DRS, demonstrating promising results in the discrimination of malignant lesions from normal breast tissue [9-11].

Also in patients with primary liver malignancy or metastatic disease to the liver, DRS could contribute to daily clinical care. For example, DRS can be incorporated into surgical tools or percutaneous intervention needles enabling direct optical guidance by real time tissue information at the tip of the instrument. Such an approach would result in guided surgery by optical sensing and could improve surgical outcome by predicting resection planes, especially in deep seated smaller tumors or those lesions that are difficult assessable. In addition, DRS has shown to identify irreversible cell damage during RFA procedures in animal experiments, opening the potential to monitor the efficacy during percutaneous RFA ablations in liver tumors [12]. Finally, DRS could be of additional value by predicting severe steatosis hepatis and therefore preventing too extensive resections in these high risk patients [13-16].

Despite the potential application of DRS in patients with liver malignancies, studies on the use of DRS in human liver tissue are scarce [12, 17-20]. Recently, we described bile to be an important liver tissue chromophore, enabling DRS analysis to overall discriminate normal liver tissue from metastatic tumor tissue [21]. However, in that study a method for tissue prediction in individual patients was still missing. To proceed to further clinical implementation we now aim to investigate whether DRS is able to discriminate tumor tissue from normal liver tissue in individual patients. Moreover, we are interested whether the technique could judge the presence of hepatic steatosis, an important limiting factor for extensive liver resections after prolonged chemotherapy.

2. Materials and methods

2.1 Clinical study design

This study was conducted at The Netherlands Cancer Institute (NKI-AVL) under approval of the internal review board. Liver tissue was obtained from 24 patients undergoing partial liver resection for metastatic colorectal cancer. Shortly after resection, tissue was transported to the pathology department for optical spectroscopy analysis. After gross inspection by the pathologist, the optical spectra were collected from macroscopic normal liver tissue and tumor tissue. From both tissue classes, multiple measurements were performed, in total 393 DRS measurements in normal liver parenchyma and 435 in metastatic liver lesions. After data acquisition, the measurement sites were marked and specimens were fixed in formalin. After fixation, the marked tissue measurement locations were selected for cutting and processed for standard Hematoxylin and Eosin (H&E) staining. An experienced pathologist, who was blinded for the outcome of the spectroscopy analysis, examined the histological slides and visually determined if the measurements location was either tumor or normal liver tissue. In addition, for normal liver tissue the degree of steatosis was determined. The quantitative assessment of steatosis was determined by estimating the percentage of hepatocytes containing lipid droplets (both micro- and macrosteatotic droplets). The pathologic degree of steatosis was estimated with 5% steps.

2.2 Instrumentation

The instrumentation and calibration procedure of our optical spectroscopy system has recently been described elsewhere by Nachabé *et al.* [21-24]

The system consists of a console comprising a Tungsten/Halogen broadband light source, two spectrometers and an optical probe with three optical fibers. The two spectrometers resolve light in the visible wavelength range between 400 nm and 1100 nm (Andor Technology, DU420A-BRDD) and in the near infrared wavelength range from 800 up to 1700 nm (Andor Technology, DU492A-1.7), respectively. The developed miniaturized optical probe contains three optical fibers: one fiber is connected to the light source, while the other two fibers are connected to the spectrometers to capture the diffusely scattered light from the tissue (Figure 1). The average tissue volume that is illuminated is roughly 5 mm^3. The acquisition time of each spectrum was on average one second.
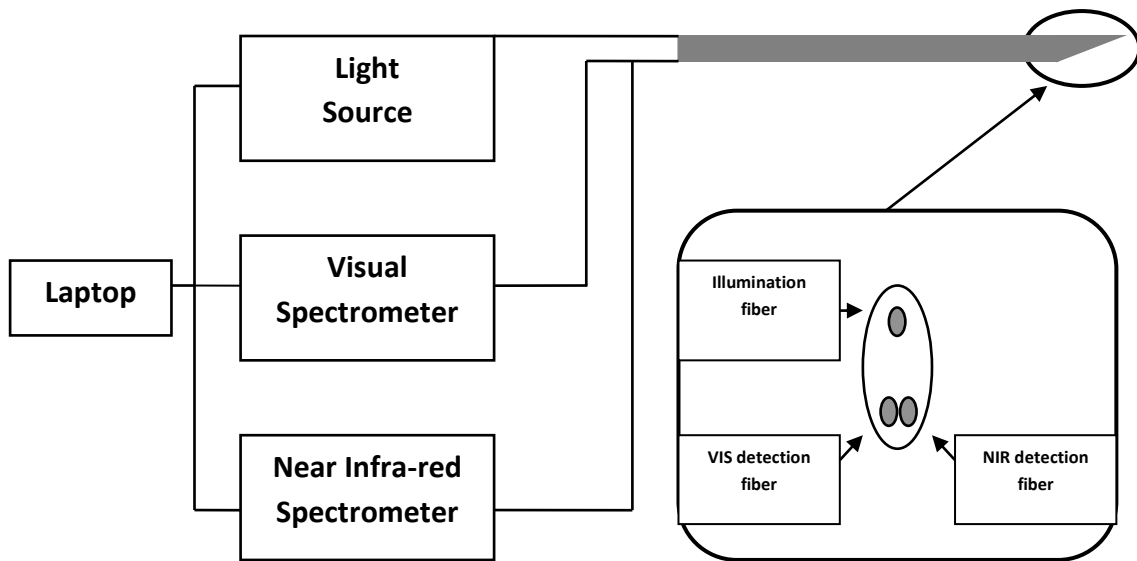
Figure 1. Schematic overview of the diffuse reflectance spectroscopy system.

2.3 Spectral data processing

The light delivered by the illumination optical fiber is subject to optical absorption and scattering. Each biological substance in the probed tissue has its intrinsic optical absorption property as a function of wavelength. In the wavelength range between 500 and 900 nm the dominant chromophores are hemoglobin (oxygenated and deoxygenated) [25], bile [21] and β-carotene [9]. In the wavelength range between 900 and 1600 nm, the dominant chromophores are water, fat and collagen [24]. Each of these chromophores has a well determined optical absorption spectrum available in literature [22]. The total absorption coefficient corresponds to the sum of each of these chromophore-specific absorption coefficient weighted by the respective volume fraction that it occupies within the total probed volume. In addition to absorption, light is also subject to optical scattering in tissue due to its morphological irregularity. Optical scattering is defined by a reduced scattering amplitude at an arbitrarily given wavelength (e.g. at 800 nm) and a slope. The scattering characteristics are dependent on the cellular structure of the target tissue and are sensitive to size and density of cellular and subcellular structures. Total scattering is composed of *Mie* scattering (scattering of cellular particles which have a diameter of the same or higher order of magnitude than the wavelength) and *Rayleigh* scattering (scattering of cellular particles which have a diameter smaller than the wavelength).

An analytical model was used to estimate the various chromophore volume fractions and scattering coefficients from all the acquired spectroscopy measurements. This model was first described by Farrell *et al.* [26] The measurements are fitted with the analytical model by applying a non-linear Levenberg-Marquardt inversion algorithm. Diffuse reflectance spectra acquired from the tissue were fitted and analyzed over the wavelength range from 500 to 1600 nm. Spectral characteristics analysis was performed with a Matlab software package (MathWorks Inc., Natick, MA). Quantified mean values for each tissue parameter were calculated and displayed in boxplots.

2.4 Tissue classification analysis

A *Classification And Regression Tree* (CART) algorithm was used to automatically classify each collected tissue into either of the two defined tissue types based on the parameters (i.e. volume fractions of the various chromophores and the reduced scattering properties) derived from the measurements [25]. With the CART algorithm, a decision tree is created based on the five most significantly different tissue chromophores and scattering parameters using a leave-one-out (LOO) cross validation scheme. Each spectrum is separately classified as either normal or tumor tissue based on the calculated thresholds in the decision tree and subsequently compared to the histology analysis and presented in terms of sensitivity and specificity. An advantage of the CART method is that the results can easily be interpreted and correlated to clinical details, since the input parameters are thresholds of the calculated values of the main tissue parameters. The CART analysis was performed for all acquired data collectively and also for each included patient individually. For the individual analysis, all measurements in each defined tissue class were analyzed and compared to the corresponding histological diagnosis. We chose an arbitrary threshold of an 80% agreement between all DRS measurements at a marked tissue site and the histopathological diagnosis of that site to either determine the DRS measurements as correct (≥80%) or define the measurements as uncertain (<80%).

2.5 Statistical analysis

The DRS-estimated quantification of each parameter in the liver tissues cannot be described by a parametric distribution such as the Gaussian distribution. The statistical differences between normal liver tissue and tumor tissue were therefore determined using the non-parametric Kruskal-Wallis test [27]. P-levels smaller than 0.05 were considered statistically significant.

The lipid fraction scored by the pathologist was the area fraction (L_{area}) of the slide containing lipid, while with the DRS method we determine the volume of lipid fraction. Assuming a homogeneous volume distribution this area fraction can be translated in a volume lipid fraction (L_{volume}) according to $L_{volume} = (L_{area})^{3/2}$. For the correlation between the DRS and pathologists quantification of steatosis, we used Spearman's rank correlation test. Analysis was performed using SPSS (Statistical Package for the Social Sciences, version 16.0).

3. Results

The characteristics of all 24 patients who were included in this study are displayed in Table 1.

Figure 2 shows the typical tissue spectra of both normal liver parenchyma and incised liver tumor tissue (colorectal liver metastases) from one of these patients. Notable spectral differences between the two tissue types are apparent. Photos of the corresponding tissue measurements and H&E stained tissue samples of the measurement locations are displayed on the right.

Table 1. Patient and tumor characteristics of all included patients.

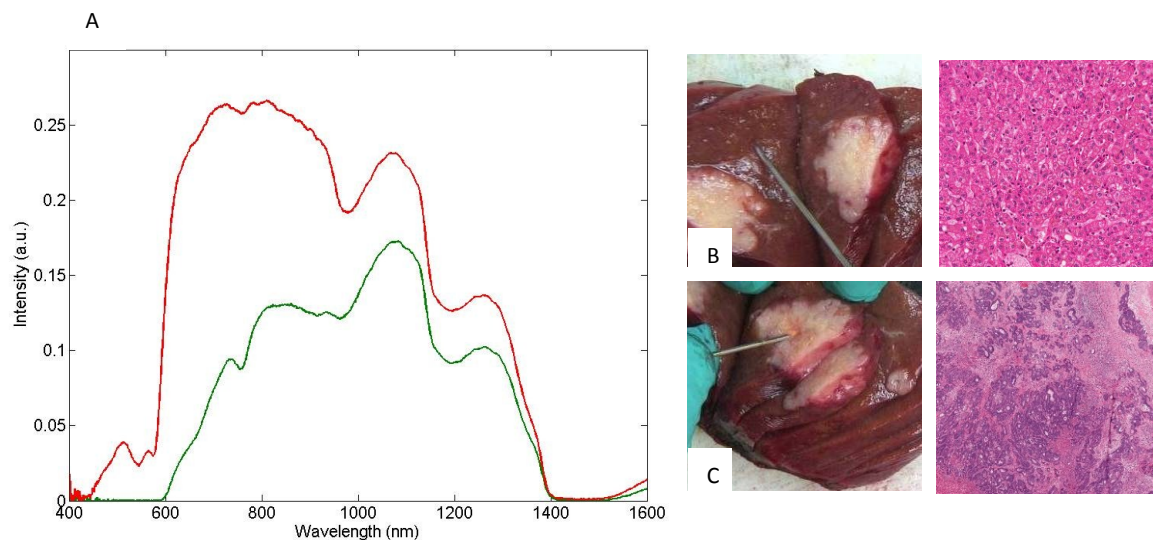|		
Number of patients	Male	14
	Female	10
Median age	Year	64
	Range	41-83
Tumor Origin	Colon	17
	Rectum	7

Figure 2. Comparison of two tissue spectra of normal liver tissue (green) and metastatic liver tumor (red). The optical spectra indicate the intensity of light received by the optical needle as a function of the wavelength for both tissue types (A). Displayed on the right is an incised resection specimen showing the typical white metastasis in the middle and the different positions of the optical probe in normal liver tissue (B) and tumor tissue (C) and the corresponding pathology slides of normal and tumor tissue (H&E staining).

3.1 Tissue classification analysis

Figure 3 displays boxplots of the five most significant tissue parameters as determined by spectral analysis. All of these parameters displayed P-values < 0.0001 when distinguishing normal liver tissue from liver tumor tissue. The most significant tissue chromophores were total hemoglobin, fat and bile content. The most significant scattering parameters were the scattering at 800 nm and the ratio between the *Mie* scattering and the total scattering.
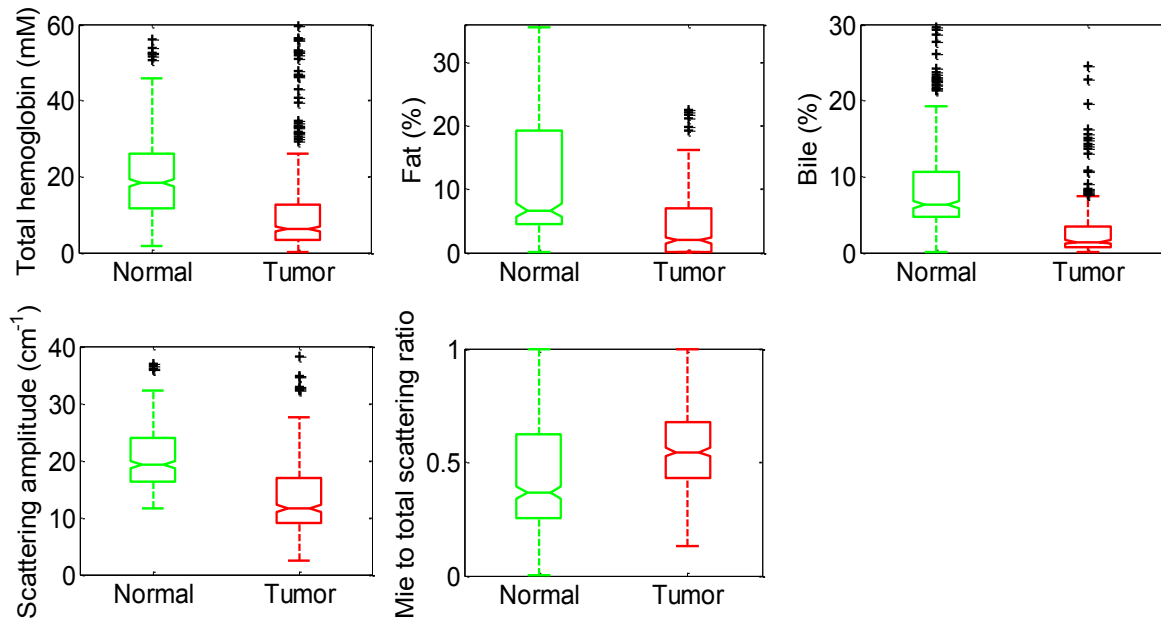
Figure 2. Boxplots of relevant tissue parameters derived from the spectral analysis. N=828 optical measurements. All P-values are below 0.0001.

Based on these five tissue parameters a decision tree was created using the CART algorithm. Table 2 displays the classification accuracy of this decision tree for all optical DRS measurements when compared to the histology analysis. A total of 780 out of the 828 optical measurements were correctly classified in either normal liver tissue or liver tumor. This resulted in a sensitivity and specificity of both 94%.

Table 2. Comparison of each optical spectrum classified by CART analysis into either normal liver tissue or tumor with the pathological diagnosis.

Pathology\Model based analysis	Tumor tissue	Normal liver tissue
Tumor tissue (N = 435)	410	25
Normal liver tissue (N = 393)	23	370

The result of the analysis for each patient *individually* is displayed in Table 3. For each patient, the ratio of the number of correctly classified tissue measurements for both normal liver tissue and liver tumor tissue is illustrated. The data shows that for each individual patient the defined tissue class on the basis of DRS measurements corresponds to the ultimate histological diagnosis. Therefore, the accuracy of DRS to predict either tissue class (normal tissue or tumor tissue) was 100%.

Table 3. Analysis of all performed optical measurements per patient. Fraction of the amount of measurements correctly classified out of the total number of measurements performed in either normal liver tissue of liver tumor.

Patient number	Neoadjuvant chemotherapy	Fraction of correctly classified measurements in normal tissue	Fraction of correctly classified measurements in tumor tissue
1	Yes	5/5	5/5
2	No	23/24	33/35
3	Yes	19/19	18/18
4	Yes	20/20	23/24
5	Yes	10/10	10/10
6	No	10/10	15/15
7	No	10/10	15/15
8	No	10/10	15/15
9	Yes	9/9	23/23
10	Yes	16/16	18/18
11	Yes	20/21	20/20
12	Yes	15/15	4/4
13	Yes	16/16	15/15
14	No	27/27	12/13
15	Yes	15/15	20/20
16	Yes	15/15	20/20
17	No	15/15	15/15
18	No	15/15	19/19
19	Yes	14/15	9/10
20	Yes	19/20	39/40
21	Yes	15/15	15/15
22	Yes	25/26	24/25
23	No	20/20	21/21
24	No	25/25	20/20

3.2 Hepatic steatosis

Figure 4a represents the correlation of the estimated percentage of steatosis in normal liver tissue as scored by the pathologist to the quantification of fat by the DRS analysis. The Spearman's rank correlation coefficient is 0.86. Figures 4b, c and d display examples of the optical spectra and corresponding histology specimen of three patients

with different levels of steatosis in the normal liver parenchyma. The spectrum at the vicinity of 1211 nm is mainly dominated by absorption of light by lipid cells. Alteration of the spectra in this wavelength band is observed with increasing lipid content [27].
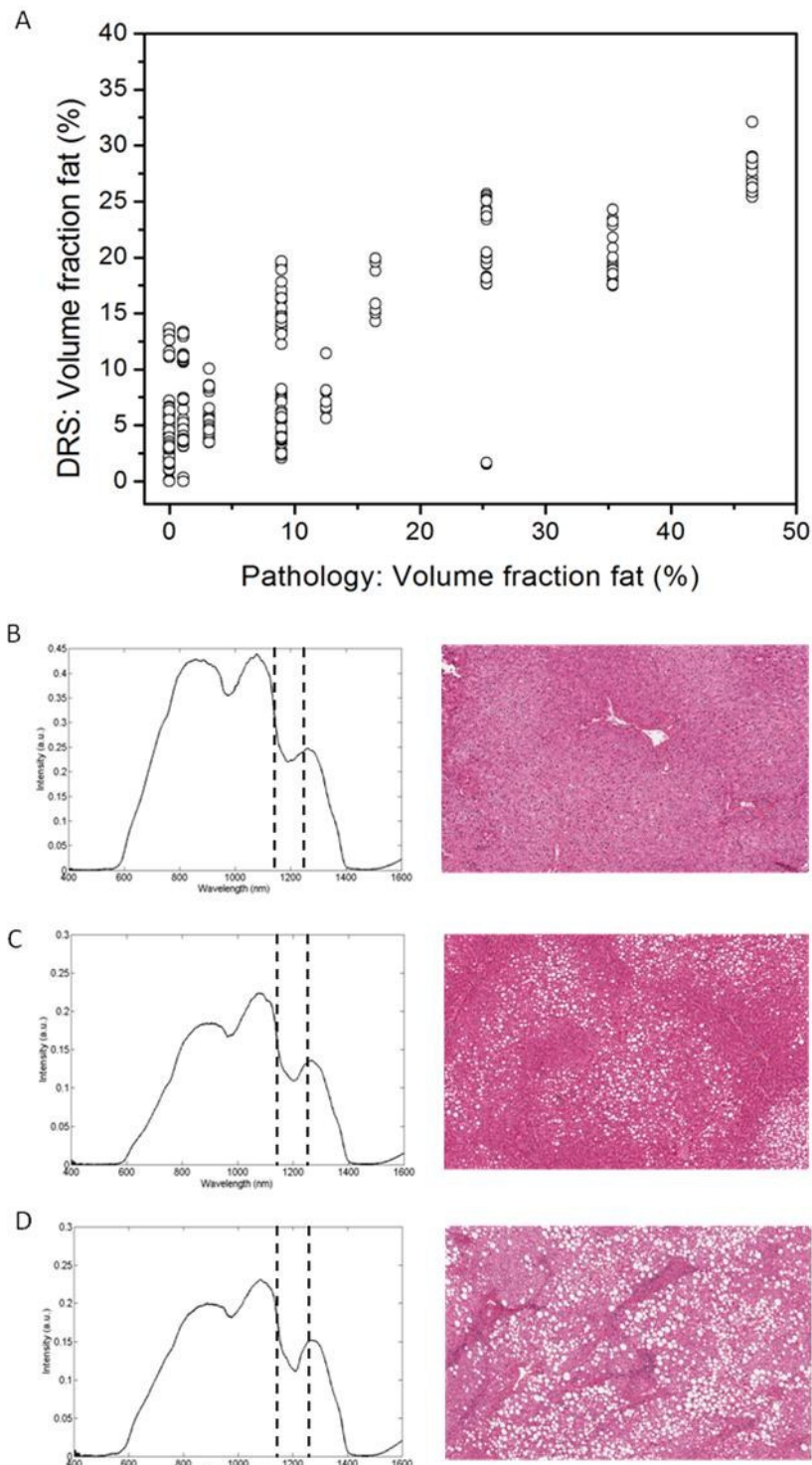
Figure 4. Comparison of the quantification of the total steatosis by DRS compared to the histological analysis (A). Example of optical spectra taken in healthy tissue and the corresponding histological slides (B, C, and D). The dashed lines correspond to the wavelength bad for which the spectra are altered by the presence of lipid in the probed volume.

4. Discussion

DRS has been demonstrated to be a promising new optical technique for tumor diagnosis by multiple studies for over a decade [3, 6, 28-35]. For several human tissue types, such as breast and oral cavity, an accuracy of up to 90% and 100% respectively were described for discrimination between normal tissue and tumor tissue. A limited number of studies investigated the application of DRS in human liver tissue, mainly focussing on spectroscopic assessment of thermal ablation [16-20]. In a recent paper, however, we demonstrated that the quantification of bile by DRS analysis offers the opportunity for more specific tissue discrimination in liver, such as between normal liver tissue and metastatic tumor tissue [21]. In continuation on these results we hypothesized that also in liver DRS is able to reach a high accuracy for the detection of tumor tissue. In the collective analysis of 828 optical measurements of 24 liver specimens, we indeed observed a sensitivity and specificity of the DRS of 94% when compared to the pathology analysis.

The performance of this tissue discrimination was based on the estimated hemoglobin, lipid and bile content as well as the reduced scattering amplitude and the Mie to total scattering ratio. From these derived parameters, it can be seen that normal tissue contains more blood, bile and fat than the tumor tissues. The finding with respect to blood correlates with the macroscopic observations (cf. Figure 2B and 2C) as normal liver is much more abundant in red blood cells compared to metastatic tumor tissue. An interesting observation compared to previous studies in other organs is the decreased total haemoglobin content in liver tumor compared to normal liver parenchyma. Previous studies have all detected higher total haemoglobin content in cancer lesions compared to normal tissue [6, 8, 9, 32, 36]. An explanation for this difference could be that previous papers all studied primary tumors, while in this paper all tumors were colorectal metastases that typically show a solid less vascularised whitish appearance. As notable in figure 2 these metastatic lesions do not all consist of vital tumor cells, but also show significant necrotic areas due to poor vascularity. Bile was less present in tumors as it concerns metastases from colorectal cancer and therefore very little bile is expected at these tumor sites. Another finding is that hardly any fat is present in tumors according to the derived fat content from the optical measurements. In general, hepatic metastases do not contain fat although rare cases with foci of fat in the metastases exist. Furthermore, normal tissue is found to have higher reduced scattering amplitude with a lower Mie scattering contribution as compared to tumor. This suggests that normal tissue has a larger density of small particles than tumors. This observation collaborates with the fact that healthy liver tissue is very rich in small hepatic cells compared to the metastases as can be seen in the histological slides in Figure 2. It must be noted that the present study was conducted in *ex-vivo* liver tissue. It remains to be determined whether specific tissue parameters, such as total haemoglobin count and bile content that contributed to the tissue discrimination in this study, will be of comparable significance in human tissue *in-vivo*. The effect of small haemorrhages, which could occur during in vivo measurements, remains to be seen. Oxygenation of tissue could significantly change after resection. For this reason we excluded this parameter form the analysis. The scattering and fat content parameters are unlikely to change significantly after resection since they are strongly

linked to the morphology of the tissue. Also for bile a significant differences between *ex vivo* and *in vivo* measurements are unlikely.

The presented figures of 94% accuracy for tissue discrimination are promising, but with regards to the diagnostic accuracy of any medical instrument used in clinical practice, the main interest will be the discriminative accuracy within any *individual* patient. In Table 3 we presented an overview of the discriminative accuracy of the DRS measurements for all patients individually. DRS measurements predicted the correct diagnosis for both normal and tumor tissue for each patient, indicating the potential of this technology for image guided surgery. The fact that the optical probe we used in this study is already needle sized shows that further development of specific surgical or interventional tools is within technical reach. Such a tools would be feasible for open and laparoscopic surgical procedures as well as for interventional procedures in the radiology department. It should be stressed that the results of DRS measurements including the analysis are available almost real time. The present measurement and analysis time at one tissue location is of the order of a few hundred milliseconds but can be further reduced in future.

In addtion, we have demonstrated a high correlation between the estimated fat content of the liver by DRS and the presence of steathosis in the histopathological specimen.

This would be most relevant when major liver surgery is considered, especially in those patients treated extensivly with pre-operative chemotherapy. In these patients steatosis is often induced by prolonged chemotherapy and has been releated to higher morbidity scores [37-40]. The presented results suggest that DRS could play a role in intra-operative decision-making concerning the extent of liver resection in these patients.

Although our results are promising towards the use of DRS in the clinical setting, several steps remain to be taken. First, our conclusions are based on *ex-vivo* data. The next step would be to reconfirm these conclusions in an *in-vivo* analysis. Furthermore, no primary liver malignancy was included in this study and the feasibility of DRS in primary liver cancer remains to be studied. This is stressed by the fact that bile is demonstrated to be an important discriminative chromophore between normal liver tissue and metastatic liver disease. In contrast to metastatic disease to the liver, primary liver cancer cells can produce bile. Therefore, the discrimination with DRS based on bile concentration might not be as significant for this tumor type as the results for colorectal liver metastases presented in this paper. Further studies are needed to investigate these possible differences.

5. Conclusion

In conclusion, we have demonstrated that DRS discriminates metastatic liver tissue from normal liver tissue with a high accuracy. Moreover, DRS proves able to determine the extent of steatosis, identifying those patients at risk for extented resections. These features illustrate the potential of DRS to be incorporated into image guided surgery tools. A prospective *in-vivo* analysis of DRS in liver and tumor tissue is underway to confirm the clinical application of this new technology for real time imaging

of surgical procedures as well as for minimally invasive procedures in the radiology department.

6. Acknowledgments

References

1. Brown J, Vishwanath K, Palmer G, Ramanujam N. Advances in quantitative UV-visible spectroscopy for clinical and pre-clinical application in cancer. Curr Opin Biotechnol 2009; 20 119-131.

2. Sćepanović O, Volynskaya Z, Kong C et al. A multimodal spectroscopy system for real-time disease diagnosis. Rev Sci Instrum 2009; 80: 043103.

3. Bard M, Amelink A, Hegt V et al. Measurement of hypoxia-related parameters in bronchial mucosa by use of optical spectroscopy. Am J Respir Crit Care Med 2005; 171 1178-1184.

4. Bensalah K, Peswani D, Tuncel A et al. Optical reflectance spectroscopy to differentiate benign from malignant renal tumors at surgery. Urology 2009; 73 178-181.

5. Dhar A, Johnson K, Novelli M et al. Elastic scattering spectroscopy for the diagnosis of colonic lesions: initial results of a novel optical biopsy technique. Gastrointest Endosc 2006; 63 257-261.

6. Fawzy Y, Petek M, Tercelj M, Zeng H. In vivo assessment and evaluation of lung tissue morphologic and physiological changes from non-contact endoscopic reflectance spectroscopy for improving lung cancer detection. J Biomed Opt 2006; 11 044003.

7. Mourant J, Bocklage T, Powers T et al. In vivo light scattering measurements for detection of precancerous conditions of the cervix. Gynecol Oncol 2007; 105 439-445.

8. Wang H, Jiang J, Lin C et al. Diffuse reflectance spectroscopy detects increased hemoglobin concentration and decreased oxygenation during colon carcinogenesis from normal to malignant tumors. Biomed Opt Express 2009; 17 2805-2817.

9. Kennedy S, Geradts J, Bydlon T et al. Optical breast cancer margin assessment: an observational study of the effects of tissue heterogeneity on optical contrast. Breast Cancer Res Treat 2010; 12: R91.

10. Keller M, Majumder S, Kelley M et al. Autofluorescence and diffuse reflectance spectroscopy and spectral imaging for breast surgical margin analysis. Lasers Surg Med 2010; 42 15-23.

11. Brown J, Wilke L, Geradts J et al. Quantitative optical spectroscopy: a robust tool for direct measurement of breast cancer vascular oxygenation and total hemoglobin content in vivo. Cancer Res 2009; 69 2919-2926.

12. Hsu C, Razavi M, So S et al. Liver tumor gross margin identification and ablation monitoring during liver radiofrequency treatment. J Vasc Interv Radiol 2005; 16 1473-1478.

13. Wong S, Mangu P, Choti M et al. American Society of Clinical Oncology 2009 clinical evidence review on radiofrequency ablation of hepatic metastases from colorectal cancer. J Clin Oncol. 2010; 28: 493-508.

14. Pawlik TM, Scoggins CR, Zorzi D et al. Effect of surgical margin status on survival and site of recurrence after hepatic resection for colorectal metastases. Ann Surg 2005; 241: 715-722, discussion 722-714.

15. Nordlinger B, Sorbye H, Glimelius B et al. Perioperative chemotherapy with FOLFOX4 and surgery versus surgery alone for resectable liver metastases from

colorectal cancer (EORTC Intergroup trial 40983): a randomised controlled trial. Lancet 2008; 371: 1007-1016.

16. Muratore A, Ribero D, Zimmitti G et al. Resection margin and recurrence-free survival after liver resection of colorectal metastases. Ann Surg Oncol. 2009; 17: 1324-1329.

17. Anderson C, Lin W, Beckham J et al. Fluorescence spectroscopy accurately detects irreversible cell damage during hepatic radiofrequency ablation. Surgery 2004; 136 524-531.

18. Anderson C, Lin W, Buttemere C et al. Real-time spectroscopic assessment of thermal damage: implications for radiofrequency ablation. J Gastrointest Surg 2004; 8 660-669.

19. Buttemere C, Chari R, Anderson C et al. In vivo assessment of thermal damage in the liver using optical spectroscopy. J Biomed Opt 2004; 9 1018-1027.

20. Doornbos R, Lang R, Aalders M et al. The determination of in vivo human tissue optical properties and absolute chromophore concentrations using spatially resolved steady-state diffuse reflectance spectroscopy. Phys Med Biol 1999; 44: 967-981.

21. Nachabé R, Evers D, Hendriks B et al. Effect of bile absorption coefficients on the estimation of liver tissue optical properties and related complications in discriminating healthy and tumorous samples. Biomed Optics Express 2011; 2: 600-614.

22. Nachabé R, Hendriks B, Desjardins A et al. Estimation of lipid and water concentrations in scattering media with diffuse optical spectroscopy from 900 to 1,600 nm. J Biomed Opt 2010; 15 037015.

23. Nachabé R, Hendriks B, van der Voort M et al. Estimation of bilogical chromophores using diffuse optical spectroscopy - benefit of extending the UV-VIS wavelength range to include 1000 to 1600nm. Optics Express 2010; 18: 1432-1442.

24. Nachabé R, Evers D, Hendriks B et al. Diagnosis of breast cancer using diffuse optical spectroscopy from 500 to 1600 nm: a comparison of classification methods. J Biomed Opt 2011; 16: 087010.

25. Breiman L, Friedman J, Olshen R, Stone C. Classification and Regression Trees. Belmont, CA. : Wadsworth Publishing Company 1984.

26. Farrell T, Patterson M, Wilson B. A diffusion theory model of spatially resolved, steady-state diffuse reflectance for the noninvasive determination of tissue optical properties in vivo. Med Phys 1992; 19: 879-888.

27. Kruskal W, Wallis W. Use of Ranks in One-Criterion Variance Analysis. Journal of the American Statistical Association 1952; 47: 583-621.

28. Zhu C, Palmer G, Breslin T et al. Diagnosis of breast cancer using fluorescence and diffuse reflectance spectroscopy: a Monte-Carlo-model-based approach. J Biomed Opt 2008; 13: 034015.

29. Zhu C, Breslin T, Harter J, Ramanujam N. Model based and empirical spectral analysis for the diagnosis of breast cancer. Biomed Opt Express 2008; 16: 14961-14978.

30. Breslin T, Xu F, Palmer G et al. Autofluorescence and diffuse reflectance properties of malignant and benign breast tissues. Ann Surg Oncol 2004; 11 65-70.

31. Mallia R, Narayanan S, Madhavan J et al. Diffuse reflection spectroscopy: an alternative to autofluorescence spectroscopy in tongue cancer detection. Appl Spectrosc 2010; 64 409-418.

32. Amelink A, Kaspers O, Sterenborg H et al. Non-invasive measurement of the morphology and physiology of oral mucosa by use of optical spectroscopy. Oral Oncol 2008; 44 65-71.

33. Bigio I, Bown S, Briggs G et al. Diagnosis of breast cancer using elastic-scattering spectroscopy: preliminary clinical results. J Biomed Opt 2000; 5 221-228.

34. van Veen R, Amelink A, Menke-Pluymers M et al. Optical biopsy of breast tissue using differential path-length spectroscopy. Phys Med Biol 2005; 50 2573-2581.

35. Volynskaya Z, Haka A, Bechtel K et al. Diagnosing breast cancer using diffuse reflectance spectroscopy and intrinsic fluorescence spectroscopy. J Biomed Opt 2008; 13 024012.

36. Zhu C, Palmer G, Breslin T et al. Diagnosis of breast cancer using diffuse reflectance spectroscopy: Comparison of a Monte Carlo versus partial least squares analysis based feature extraction technique. Lasers Surg Med 2006; 38 714-724.

37. Pessaux P, Chenard M, Bachellier P, Jaeck D. Consequences of chemotherapy on resection of colorectal liver metastases. J Visc Surg 2010; 147: 193-201.

38. Morris-Stiff G, Tan Y, Vauthey J. Hepatic complications following preoperative chemotherapy with oxaliplatin or irinotecan for hepatic colorectal metastases. Eur J Surg Oncol 2008; 34: 609-614.

39. McCormack L, Petrowsky H, Jochum W et al. Hepatic steatosis is a risk factor for postoperative complications after major hepatectomy: a matched case-control study. Ann Surg 2007; 245: 923-930.

40. de Meijer V, Kalish B, Puder M, Ijzermans J. Systematic review and meta-analysis of steatosis as a risk factor in major hepatic resection. Br J Surg 2010; 97: 1331-1339.

Chapter 7

Diffuse reflectance spectroscopy: a new guidance tool for improvement of biopsy procedures in lung malignancies

Daniel J. Evers

Rami Nachabé

Houke K. Klomp

Johanna W. van Sandick

Michel W. Wouters

Gerald W. Lucassen

Benno H. W. Hendriks

Jelle Wesseling

Theo J. M. Ruers

Abstract

Background. A significant number of percutaneous intra-thoracic biopsy procedures result in indeterminate cytological or histological diagnosis in clinical practice. Diffuse Reflectance Spectroscopy (DRS) is an imaging technique that can distinguish different tissue types on a microscopic level. DRS may improve needle localization accuracy during biopsy procedures. The objective of this study was to assess the ability of DRS to enhance diagnosis of malignant lung disease in human lung tissue.

Methods. *Ex-vivo* analysis with a DRS system was performed on lung tissue from 10 patients after pulmonary resection for malignant disease. Tissue spectra measured from 500 to 1600 nm were analyzed using two analysis methods; a model-based analysis that derives clinical and optical properties from the measurements and a partial least squares discriminant analysis (PLS-DA) which classifies measured spectra with respect to the histological nature of the measured tissue.

Results. Sensitivity and specificity for discrimination of tumor from normal lung tissue were 89% and 79% respectively based on the model-based analysis. Overall accuracy was 84%. The PLS-DA analysis yielded a sensitivity of 78%, a specificity of 86% and an overall accuracy of 81%.

Conclusions. The presented results demonstrate that DRS has the potential to enhance diagnostic accuracy in minimal invasive biopsy procedures of the lungs in combination with conventional imaging techniques.

1. Introduction

Essential first steps in the diagnostic work-up after detection of a suspected lung mass include describing the anatomical extent as well as the cellular origin of the tumor. Biopsy or fine needle aspiration of the lesion for further analysis is a crucial step in this process. For intra-thoracic lesions, this is often performed percutaneously. Correct localization of the biopsy needle within the target lesion is essential for success of this procedure and is frequently performed under image-guidance of computed tomography (CT).

Recent studies have reported varying figures of overall accuracy for thoracic biopsies, which respectively range between 67% and 96% [1-5]. Main factors influencing the biopsy accuracy are location and size of the intra-thoracic lesions as well as respiratory motion during the biopsy procedure. Moreover, even correct localization of the biopsy needle within the target lesion can still result in indefinite pathology diagnosis when the biopsy only consists of necrotic cell debris. Hence, a considerable number of patients undergoing percutaneous biopsies will subsequently require a repeated biopsy or even surgical intervention to obtain tissue material for diagnosis before an individualized treatment plan can be initiated.

In recent years, promising achievements in specific tissue discrimination have been made in the field of diffuse reflectance spectroscopy (DRS) that may allow improved accuracy in cancer diagnostics [6-8]. With this optical technique changes in the spectral distribution of light, as a result of either absorption or scattering of light, are recorded after the light has interacted with molecules in tissue. Subsequently, the collected spectral information is translated into morphological and physiological information. Changes in human tissue associated with malignant transformation include alterations in cellular composition, metabolic rate, vascularity, intra-vascular oxygenation and tissue morphology. DRS is sensitive to such changes in tissue, enabling discrimination between normal tissue and tumor. Ultimately, incorporation of this technology into biopsy needles may improve tip localization of the biopsy needle within the tissue compared to image-guided localization.

Many human tissue types have been subjected to optical spectroscopy with promising results for clinical application of this technique. Only a few studies involving optical spectroscopy have focused on the characterization of human lung tissue. Those published mainly involved the incorporation of DRS or Fluorescence spectroscopy (FS) into bronchoscopy tools [9-13]. Detection of superficial abnormalities during bronchoscopy procedures was proven to be enhanced with use of spectroscopy techniques within this setting. Sensitivity of DRS and FS ranged between 70 and 86%, specificity ranged between 68 and 82%.

Recently, we have developed and validated a novel DRS system combining detection of visual (VIS) and near-infrared light (NIR) spectrum [14-17]. Contrary to most previous studies with DRS that focus on the VIS part of the spectrum, we included the NIR (1000-1600 nm) spectrum.

The aim of this report is to assess the discrimination accuracy of our DRS system between normal lung tissue and tumor in an ex-vivo analysis.

2. Materials and methods
2.1 Clinical study design

This study was conducted at The Netherlands Cancer Institute (NKI-AVL) under approval of the internal review board committee. Lung tissue was obtained from 10 patients who had undergone a pulmonary resection (lobectomy or segmental resection) for primary non-small cell lung cancer or pulmonary metastases.

Directly after resection, tissue was transported to the pathology department for optical spectroscopy analysis. After gross inspection by the pathologist, the optical spectra were collected from macroscopic normal tissue and tumor samples. Spectroscopy measurements were performed on freshly excised tissue within two hours after the resection. Each specific measurement location was digitally photographed during the procedure. Figure 1(A) depicts a photograph of a resected lung sample with a cut through the tumor. A total of 330 optical measurements were performed on 67 tissue locations of both normal lung tissue and tumor. Resection specimens were then fixed in formalin. The measurement locations were subsequently selected and excised according to the measurement locations on the photos. These tissue samples were paraffin-embedded, cut in 2- to 3-μm-thick sections and stained with standard hematoxylin/eosin staining. An experienced pathologist, who was blinded for the outcome of the spectroscopy analysis, examined the histological slides. Examples of a pathology slide of normal lung tissue as well as tumor lung tissue are shown in Figure 1.
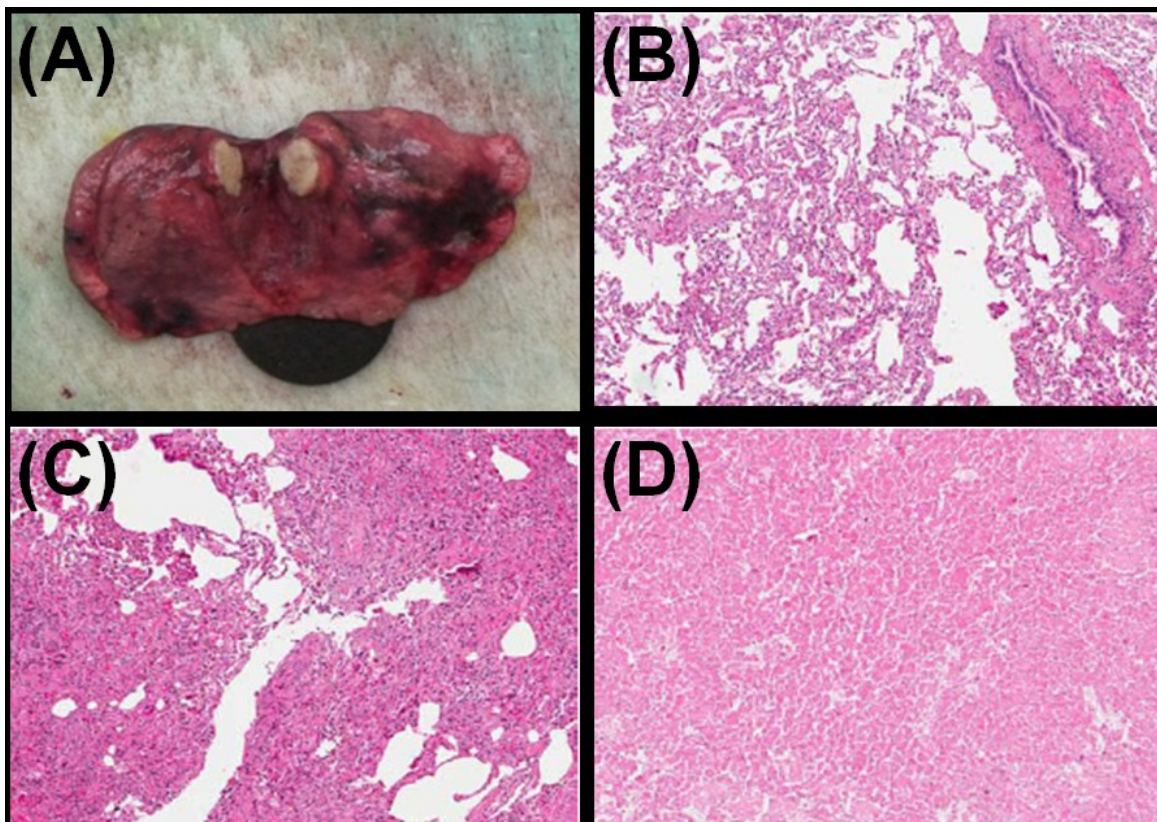
Figure 1. Photograph of a resected lung sample showing a cut through the tumor. An example of a pathology slide of normal lung tissue with pink appearance (B) and dark appearance (C) as well as lung tumor (D).

2.2 Instrumentation

The instrumentation and calibration procedure of our optical spectroscopy model have been described recently by Nachabé *et al* [14-17].

In short, *ex-vivo* diffuse reflectance spectra were measured with a portable spectroscopic system as described earlier [17]. The system consists of a console comprising a Tungsten/Halogen broadband light source and two spectrometers. The spectrometers resolve light either between 400 nm and 1100 nm (Andor Technology, DU420A-BRDD) or from 800 up to 1700 nm (Andor Technology, DU492A-1.7). An optical probe containing three optical fibers was connected to the optical setup. As depicted in Figure 2, one fiber is connected to the light source and the two other fibers are connected to the spectrometers to collect diffusely scattered light from the tissue. The optical probe has a diameter of 1.3 mm and its distal end is polished at an angle of 20 degrees. The illumination optical fiber is located at a distance of 2.48 mm from the two side-by-side optical fibers that are used to collect the diffused light (Figure 2). Such a setup enables spectral acquisition in the range between 500 to 1600 nm via an optical fiber with its distal end placed against the samples.
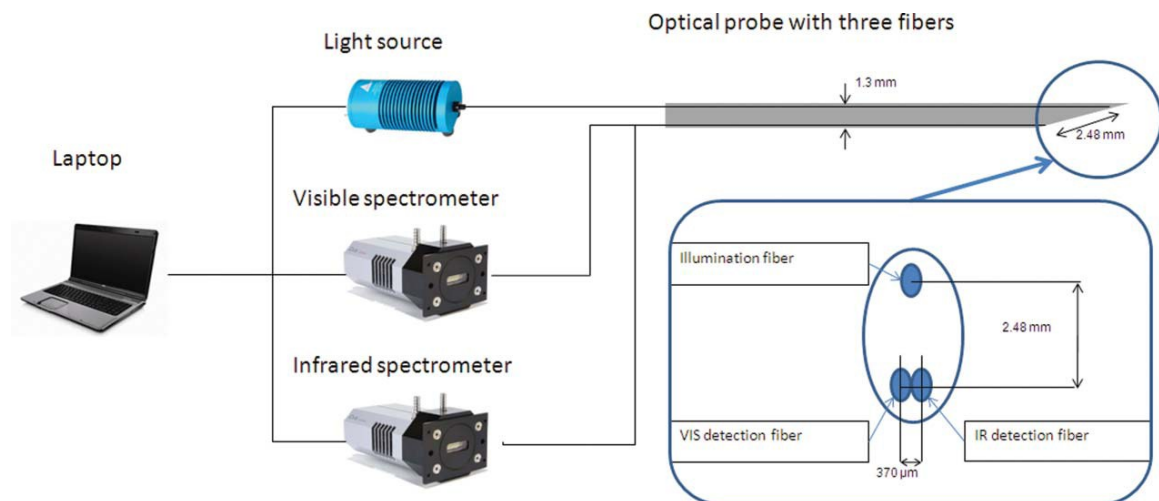

Figure 2. Schematic of the DRS optical setup.

2.3 Light-tissue interaction and optical spectroscopy

The light delivered by the illumination optical fiber is subject to optical absorption and scattering. Each biological substance in the probed tissue has its intrinsic optical absorption property as a function of wavelength. The most common biological substances that absorb light are blood-derived chromophores such as oxygenated and deoxygenated hemoglobin, water and lipid [15]. Oxygenated and deoxygenated hemoglobin have the most dominant absorption coefficients in the wavelength range below 900 nm whereas water and lipid have the most dominant absorption coefficient above 900 nm [15]. Each of these chromophores has a well determined optical absorption spectrum available in literature [15]. The total absorption coefficient corresponds to the sum of each of these chromophore-specific absorption coefficient weighted by the respective volume fraction that it occupies within the total probed volume. This is known as the Beer-Lambert law that applies in non-turbid media. However, in addition to absorption, light is also subject to optical

scattering in tissue due to its morphological irregularities at a structural level yielding deflection of the light rays after interaction with the different substances present in tissue. The optical scattering is mathematically defined as a monotonic decreasing power-law function over wavelength. Therefore the optical scattering is defined by a reduced scattering amplitude at an arbitrarily given wavelength (e.g. at 800 nm) and a slope. The diffused light that is collected at the detection optical fibers correspond to a non-linear mathematical relation of the wavelength-dependent absorption and scattering properties [18]. The volume of the probed diffused light in tissue is mainly dependent on the absorption and scattering properties as well as the distance between the illumination and collection fibers. Given the specification of the optical probe that was used in this study and the range of tissue absorption and scattering properties over the wavelength range of interest (i.e. 500 to 1600 nm), the average probed volume is roughly 5 mm^3.

2.4 Spectral data processing

Two different lung tissue types were classified in the spectral data processing: normal lung tissue and tumor. Furthermore, measured spectra from all included measurement locations were separated into either the *training* data set (N = 171 optical measurements from 35 tissue locations) or the *validation* data set (N = 159 optical measurements from 32 tissue locations). This was accomplished by randomly dividing measurement sets from different tissue locations of both normal lung tissue and tumor from each included patient between the two data sets. The histological breakdown of the optical measurements performed in these patients is displayed in table 1.

Table 1. Histological breakdown of tissue samples used for data analysis. N = 10 patients.

Measured tissue types	Optical measurement locations (training and validation sets) N= 67	Optical measurements (training and validation sets) N= 330	Optical measurement locations (and validation set) N= 32	Optical measurements (validation set) N= 159
Normal lung tissue	30	145	14	66
Tumor	37	185	18	93

Finally, all acquired spectra were analyzed in two ways: First, an analytical model derived from the diffusion theory was used to estimate the various chromophore volume fractions and scattering coefficients [18]. Second, a statistical classification of the tissue spectra was performed using partial least squares discriminant analysis (PLS-DA) [19].

Model-based analysis. Validation of the analytical model that was used to recover the chromophore volume fractions and scattering coefficients from the measurements has

recently been described [14-17]. Diffuse reflectance spectra measured from the tissue were fitted over the wavelength range from 500 to 1600 nm. A non-linear Levenberg-Marquardt inversion algorithm was used to estimate the various unknown chromophores volume fractions from the spectra within the analysis wavelength range. This inversion consists of determining the optimum volume fractions of the four chromophores of interest as well as the reduced scattering amplitude (which we arbitrarily defined at 800 nm) and slope which minimizes best the residual between the model and the measurement [15]. A total blood volume fraction is computed as the sum of the estimated oxygenated and deoxygenated haemoglobin volume fraction by considering a total haemoglobin concentration of 150 mg per ml of blood; oxygenation level in tissue computed as the ratio of oxygenated hemoglobin to the total blood volume fraction, water volume fraction and adipose tissue volume fraction. The absorption coefficient of each of these chromophores in its pure state is used as *a priori* knowledge during the fitting procedure. An example of a spectral measurement on a normal lung sample and a tumor with the corresponding fitting curve are shown in Figure 3. The spectral characteristics analysis was performed with Matlab software package (MathWorks Inc., Natick, MA). Quantified mean values for tissue parameters were calculated based on all tissue measurements and were displayed in boxplots.

Subsequently, we used the data from the *training* data set to design a decision tree for automated discrimination between normal lung tissue and tumor. This was performed using the *Gini index maximisation* and has recently been described by Nachabé *et al* [17]. By applying this evaluation method, thresholds of the most significantly discriminating tissue parameters are yielded from which all included tissue measurements could be differentiated into either tissue class with the least number of evaluation steps. The calculated thresholds were depicted as a decision tree.

PLS-DA analysis. Partial least squares (PLS) analysis is a regression method to find a linear relationship between a response variable *Y* (tissue type class) and the independent variables *X* (spectra). The method is based on finding a number of principal components (PC) that represent as much of the variance in *X* as possible and are relevant to the response variable *Y*. The PLS model is generated using part of the data, the *training* data set. A discriminant analysis (DA) method is subsequently performed to obtain thresholds for discriminating the different responses (tissue classes). Prediction of class (tissue type) on the remaining data (the *validation* data set) is obtained by comparing the predicted PLS scores with the DA thresholds. The measured tissue type is assigned to one of the two predefined tissue classes depending on the PLS scores. The PLS-DA algorithm scripts were implemented in MATLAB 7.2 using PLS Toolbox 5.8.
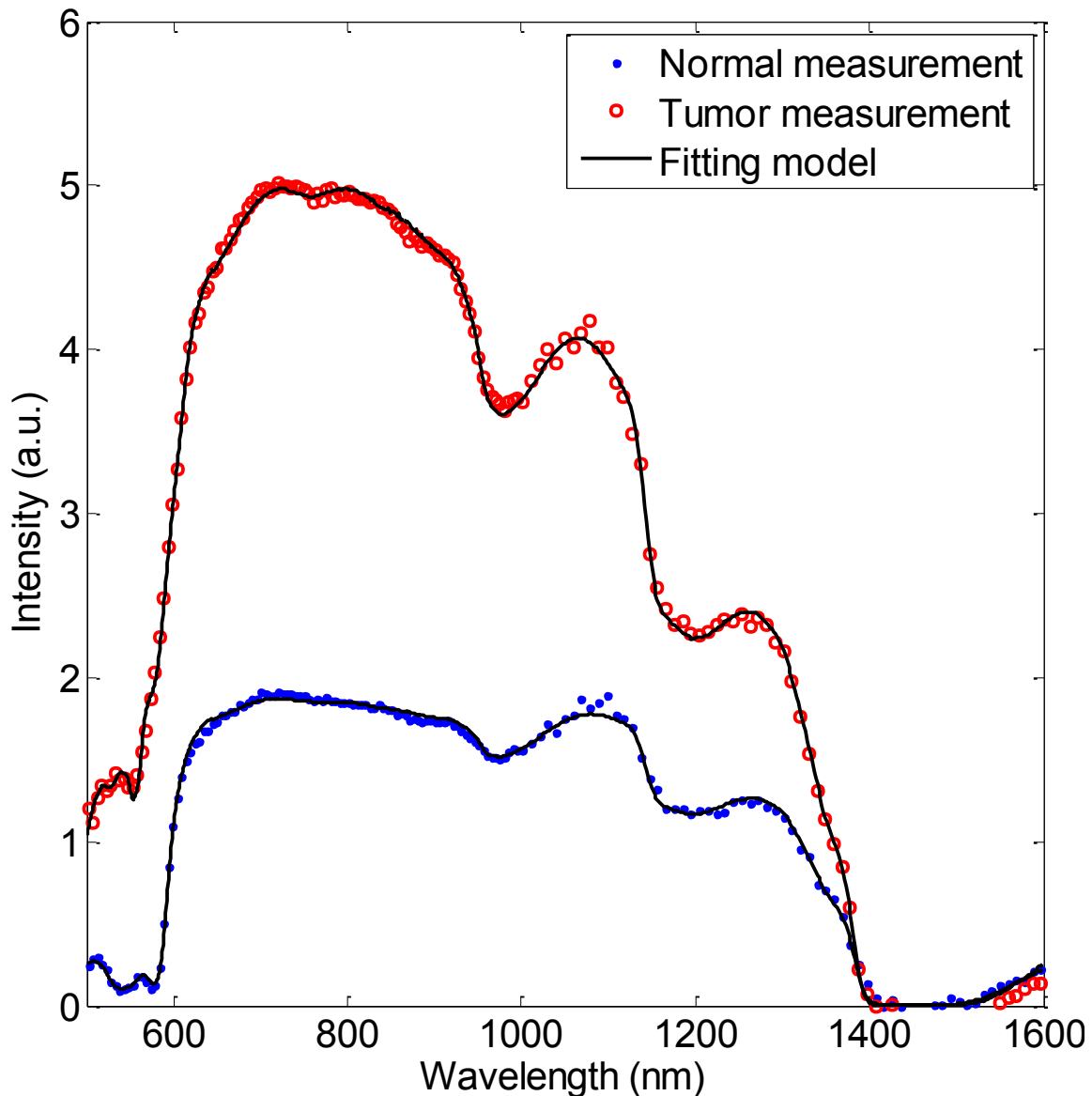
Figure 3. Example of spectral measurements in normal (point-marked curve) and tumor tissue (circle-marked curve) as well as the corresponding fit (solid line curve).

2.5 Statistical analysis

The DRS-estimated quantification of each parameter in the lung tissue cannot be described by a parametric distribution such as the Gaussian distribution. The statistical differences between the two distinguished lung tissues were therefore determined using a non-parametric Kruskal-Wallis test [20]. P-values smaller than 0.05 were considered statistically significant.

Discriminative accuracy for both the model-based and PLS-DA analysis were determined by comparing the means of all tissue spectra from each measurement location of the *validation* data set to the yielded thresholds from each analysis method and assigning each collected tissue spectrum to either defined tissue class. These results were then compared to the histology analysis and were subsequently presented in terms of sensitivity, specificity and overall accuracy.

3. Results

3.1 Study characteristics

Five of the included patients were male and five were female. All patients were smokers and the average age was 61 years old (range 38 to 74 years). Six of the patients had undergone neo-adjuvant treatment. Eight of the measured tumors were primary lung tumors and the remaining two measured tumors were metastases from the colon and from a melanoma.

3.2 Tissue parameter analysis

Tissue parameter quantification was performed as part of the model-based data analysis using all of the 330 collected optical spectra. Quantification was primarily performed on all relevant tissue parameters as well as on the reduced scattering coefficient at three different wavelengths. The tissue parameters with the most discriminative relevance were total hemoglobin volume fraction, water volume fraction, adipose tissue volume fraction and reduced scattering coefficient at 800 nm (Figure 4). Significant statistical differences were demonstrated for hemoglobin volume fraction ($P < 0.001$) and reduced scattering coefficient at 800 nm ($P < 0.01$).
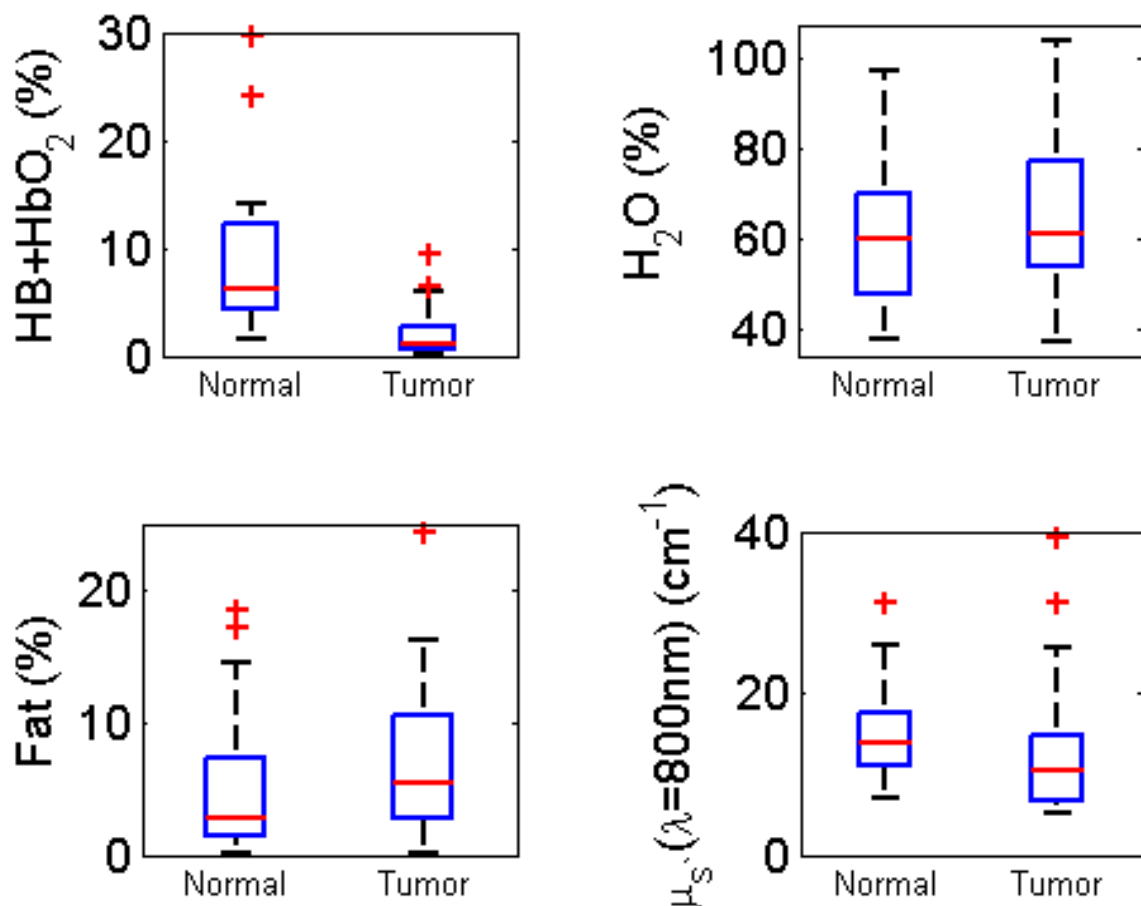

Figure 4. Boxplots of diagnostically relevant tissue parameters. N= 330 tissue measurements from 67 measurement locations. Hb+HbO$_2$ = total hemoglobin volume fraction, H$_2$O = water volume fraction; Fat = adipose tissue volume fraction; μ_s = reduced scattering coefficient at 800 nm.

149

3.3 Classification accuracy

Model-based analysis. The computed decision tree based on tissue parameter thresholds is demonstrated in Figure 5. The means of all collected tissue spectra from each measurement location could be assigned to either tissue class based on thresholds yielded from *hemoglobin volume fraction* and *reduced scattering coefficient* in a two-step analysis. Results from the tissue parameter quantification of the validation data set were analysed according to the defined thresholds. Compared to the histology analysis overall discriminative accuracy of the model-based analysis was 84% (Table 2).
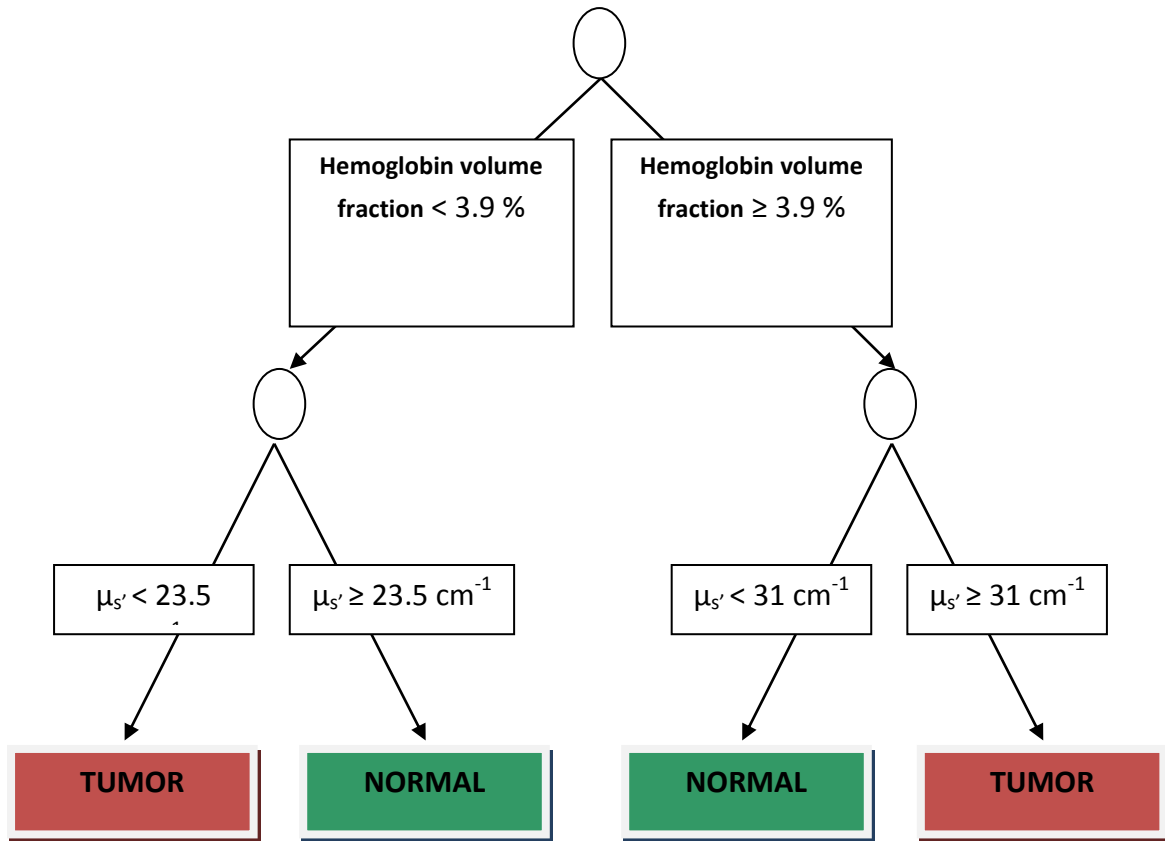

Figure 5. Discriminative thresholds for automated discrimination between normal lung tissue and tumor depicted in a decision tree. Thresholds were calculated based on quantification of tissue spectra from the training data set. N = 37 measurements locations.

Table 2. Model based classification accuracy of DRS measurements of lung tissue divided into 2 classes compared to the pathology analysis. N = 32 measurement locations.

Pathology\Model based analysis	Tumor tissue	Normal lung tissue
Tumor (N = 18)	16	2
Normal lung tissue (N = 14)	3	11

Sensitivity = 89%; Specificity = 79%; Overall accuracy = 84%.

PLS-DA analysis. Results from the PLS-DA classification analysis of the spectra are displayed in Figure 6. For several measurements difficulty discriminating between normal lung tissue and tumor was apparent. Overall discriminative accuracy of the PLS-DA analysis was 81% (Table 3).
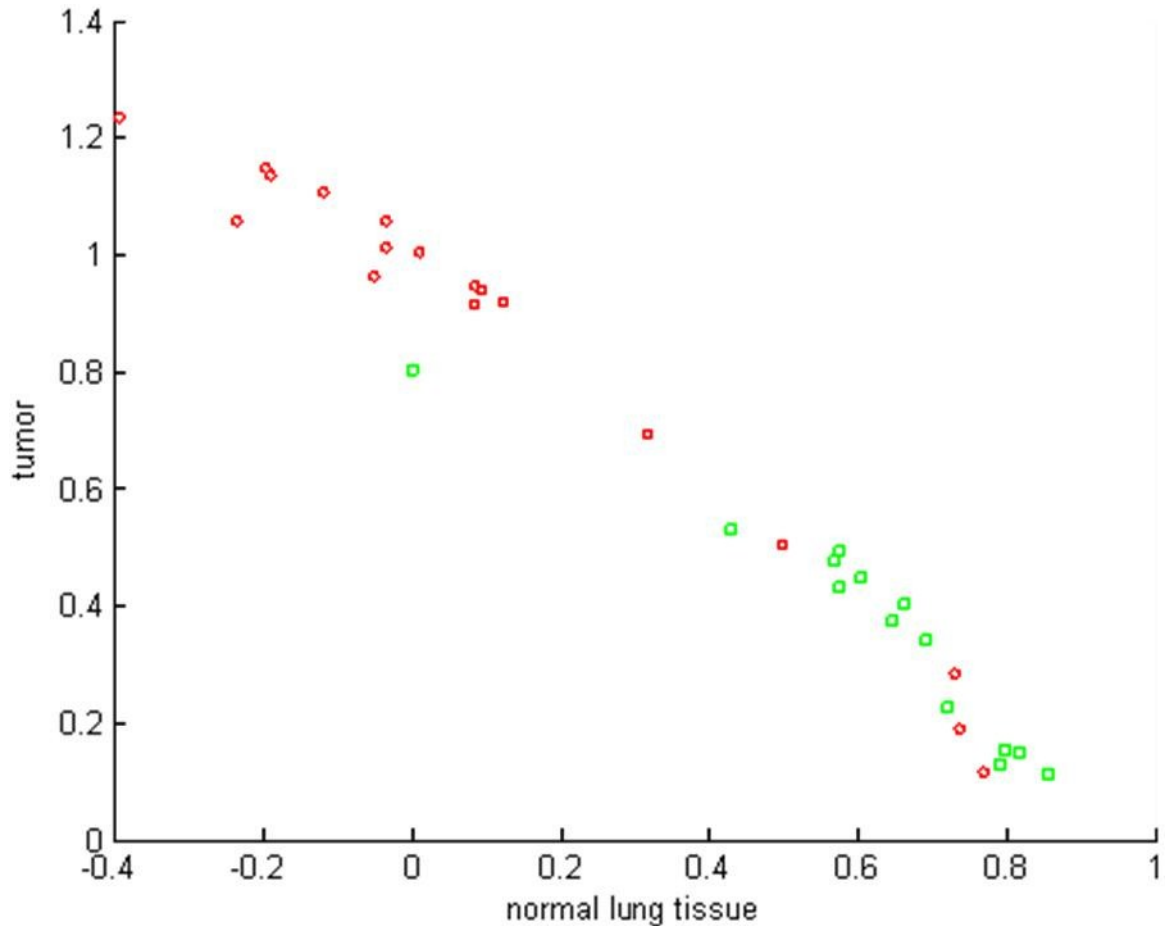

Figure 6. PLS-DA classification of the spectra of DRS measurements comparing benign to malignant tissue. Each square represents a tissue measurement from which the spectrum is compared to the spectral thresholds acquired from the training data set analysis. N= 32 measurement locations. Red circles represent the histological diagnosis tumor and green squares normal lung tissue.

Table 3. PLS-DA classification accuracy of DRS measurements of lung tissue divided into two classes compared to the pathology analysis. N = 32 measurement locations.

Pathology\PLS-DA	Tumor tissue	Normal lung tissue
Tumor tissue (N = 18)	14	4
Normal lung tissue (N = 14)	2	12

Sensitivity = 78%; Specificity = 86%; Overall accuracy = 81%.

4. Discussion

This report demonstrates first published results of a novel Diffuse Reflectance Spectroscopy system, combining the analysis of spectral results after *ex-vivo* lung tissue illumination with both visual and near infra-red light. Research with DRS on other human tissue has proven the potential of this technique for tissue discrimination. As yet, this was never performed including near-infrared spectra beyond 1000 nm [21-25]. The advantage of having an additional spectrometer that resolves light above 900 nm is the possibility to measure spectra in a range where water and lipid have high absorption coefficients [14]. Therefore accurate volume fractions of these biological substances can be determined and used for classification on top of the commonly used blood derived chromophores and scattering parameters [9-10]. Although no significant differences was observed between normal and tumor in water, Figure 4 shows that estimated water distribution is skewed to higher values in tumor than normal lung tissue. We expected that the water volume fraction would be higher in tumor tissue compared to normal because normal tissue consists of air filled alveoli compared to more solid, no air containing, tumor tissue. Probably due to the resection these alveoli are partly collapsed resulting in a more dark appearance of the normal lung tissue. This is supported by pathology findings showing collapsed alveoli in the normal lung tissue with darker appearance (Figure 1(C)). These results indicate that accurate determination of the water volume fraction might play a role in discriminating normal and tumor an *in vivo* setting where the above effect is not expected. As a result having a spectrometer to resolve light for wavelengths beyond 900 nm, being able to determine accurately the water volume fraction, might then turn out to be useful. From the boxplots, one can further notice that normal lung samples have significantly higher blood volume fraction than in tumors. This can be seen in Figure 1(A) with the tumor being the white part surrounded by the pink normal lung tissue. The scattering of tissue in normal is higher in normal than in tumor samples according to the boxplots. This is due to the fact that normal lung tissue has a multitude of alveolus filled with air that yields to greater light scattering (related to refractive index changes in tissue) as opposed to the solid tumors.

Using two different data analysis methods our DRS system yielded a promising overall discriminative accuracy of 84% for the model-based data analysis and 81% for the PLS-DA analysis compared to the pathology analysis. These results indicate that DRS has the potential to enhance diagnostic accuracy during minimal invasive thoracic procedures in combination with conventional imaging techniques.

In clinical practice, the main objective for correct localization of the needle within the target lesion is accurate identification of the tumor itself. High specificity of an imaging modality is therefore the most important parameter. Hence, the higher the specificity, the lesser indeterminate results can be expected. In previously published papers specificity for thoracic biopsies mainly with CT guidance ranges from 83 to 97%, resulting in indeterminate biopsies in 3 to 17% of the patients [1-5]. An indeterminate biopsy is defined as a biopsy which was thought to be taken from the target lesion, but cannot be characterized as malignant tissue by the pathologist. The best specificity result displayed in the current paper was 86% with the PLS-DA data analysis. This would result in an expected indeterminate test results of 14% of patients. Because the two diagnostic

tests can be considered independent when performed together, the test accuracy from both tests may be multiplied to calculate the suspected combined discriminative accuracy. A combination of biopsy with CT imaging and displayed DRS incorporated in a biopsy needle could in theory therefore improve biopsy specificity to 98%. It can be concluded that DRS has the potential to enhance diagnostic accuracy during minimal invasive thoracic procedures in comparison with conventional imaging techniques. This hypothesis will have to be proven in future *in-vivo* experiments.

Additional arguments can be given towards the expected feasibility of DRS in an *in-vivo* analysis. First; we would expect tissue scattering to have a more significant discriminative effect in an *in-vivo* analysis. Hence, in the *in-vivo* setting the alveoli will be air-filled. The expected scattering will therefore be higher compared to the *ex-vivo* collapsed alveoli due to the larger refraction index mismatch between air and human tissue. Thus, the expected difference in the scattering coefficient compared to solid tumor will be larger. Second; we expect the water volume fraction to show more difference between the normal and tumor tissue due to the air filled alveoli. Third; we expect a greater number of significant discriminative tissue parameters in *in-vivo* measurements. The main discriminative tissue parameters in this study were total hemoglobin volume fraction and the reduced scattering coefficient at 800 nm. Fawzy *et al.* and Bard *et al.* both demonstrated similar results with these tissue parameters in their *in-vivo* analysis of bronchial mucosa [9, 12]. Another important distinguishing parameter in their studies was tissue oxygen saturation. Both studies demonstrated tissue oxygen saturation to be diminished in cancerous lesions in comparison to normal lung tissue. In our DRS analysis, no significant differences in tissue saturation were displayed between normal lung tissue and tumor. Overall fitting results of our optical measurements revealed an average oxygenation in normal lung tissue of 31% (SD ±22%) compared to 24% (SD ±22%) in measured tumor tissue (data not displayed). This is most likely due to the nature of this analysis and the *ex-vivo* optical measurements. Moreover, during the operation the target tissue specimen is progressively impaired from blood circulation before final resection is performed.

Furthermore, for future analysis we plan to combine DRS with Fluorescence spectroscopy. Discriminative accuracy of such a combined spectroscopy system has been proven to be superior to each spectroscopy technique alone in two recent studies of human breast tissue [26, 27]. Thus, an overall improvement of our discriminative accuracy is to be expected in future *in-vivo* experiments of lung tissue.

Although our results are promising, a critical assessment must be noted. First, although analyses were performed on a significant number of measured spectra which are comparable to quantities in previously published studies, a restricted number of patients (N=10) and tissue specimens were utilized. Heterogeneity between patients could have a negative effect on the discriminative accuracy. Second, total hemoglobin volume fraction was demonstrated to be the main discriminative parameter. It is unclear what the discriminative value of a comparable analysis of lung tissue in an *in-vivo* setting would be in case of local hemorrhage caused by the optical needle. Hence, located hemorrhage during minimal invasive spectroscopy measurement could have a negative effect on

optical measurement due to the absorption properties of hemoglobin in the visual spectrum.

In conclusion, a novel Diffuse Reflectance Spectroscopy system was presented for analysis of human lung tissue. Overall discriminative accuracy of the DRS system compared to the pathology analysis was 84% and 81% for model-based and PLS-DA analysis, respectively. Based on the presented results, we conclude that DRS has the potential to enhance diagnostic accuracy in minimal invasive procedures of the lungs. *In-vivo* experiments are currently being performed by our group to confirm these results as a next step towards before clinical application.

5. Acknowledgments

References

1. Gong Y, Sneige N, Guo M, Hicks M, Moran C. Transthoracic fine-needle aspiration vs concurrent core needle biopsy in diagnosis of intrathoracic lesions: a retrospective comparison of diagnostic accuracy. *Am J Clin Pathol* 2006; 125:438-444.

2. Rivera M, Detterbeck F, Mehta A. Diagnosis of lung cancer: the guidelines. *Chest* 2003; 123:129S-136S.

3. Priola A, Priola S, Cataldi A, Di Franco M, Pazè F, Marci V, et al. Diagnostic accuracy and complication rate of CT-guided fine needle aspiration biopsy of lung lesions: a study based on the experience of the cytopathologist. *Acta Radiol.* 2010; 51(5):527-533.

4. Kothary N, Lock L, Sze D, Hofmann L. Computed tomography-guided percutaneous needle biopsy of pulmonary nodules: impact of nodule size on diagnostic accuracy. *Clin Lung Cancer* 2009; 10(5):360-363.

5. Aviram G, Greif J, Man A, Schwarz Y, Marmor S, Graif M, et al. Diagnosis of intrathoracic lesions: are sequential fine-needle aspiration (FNA) and core needle biopsy (CNB) combined better than either investigation alone? *Clin Radiol.* 2007; 62(3): 221-226.

6. Sćepanović O, Volynskaya Z, Kong C, Galindo L, Dasari R, Feld M. A multimodal spectroscopy system for real-time disease diagnosis. *Rev Sci Instrum* 2009; 80(4):043103.

7. Frangioni J. New technologies for human cancer imaging. *J Clin Oncol* 2008; 26(24):4012-4021.

8. Brown J, Vishwanath K, Palmer G, Ramanujam N. Advances in quantitative UV-visible spectroscopy for clinical and pre-clinical application in cancer. *Curr Opin Biotechnol* 2009; 20: 119-131.

9. Bard M, Amelink A, Hegt V, Graveland W, Sterenborg HJ, Hoogsteden H, et al. Measurement of hypoxia-related parameters in bronchial mucosa by use of optical spectroscopy. *Am J Respir Crit Care Med* 2005; 171: 1178-1184.

10. Bard M, Amelink A, Skurichina M, Noordhoek Hegt V, Duin R, Sterenborg H, et al. Optical spectroscopy for the classification of malignant lesions of the bronchial tree. *Chest* 2006; 129:995-1001.

11. Fawzy Y, Zeng H. Intrinsic fluorescence spectroscopy for endoscopic detection and localization of the endobronchial cancerous lesions. *J Biomed Opt* 2008; 13(6): 064022.

12. Fawzy Y, Petek M, Tercelj M, Zeng H. In vivo assessment and evaluation of lung tissue morphologic and physiological changes from non-contact endoscopic reflectance spectroscopy for improving lung cancer detection. *J Biomed Opt* 2006; 11(4):044003.

13. Hirsch F, Prindiville S, Miller Y, Franklin W, Dempsey E, Murphy J, et al. Fluorescence versus white-light bronchoscopy for detection of preneoplastic lesions: a randomized study. *J Natl Cancer Inst* 2001; 93(18):1385-1391.

14. Nachabé R, Hendriks BH, Desjardins A, van der Voort M, van der Mark M, Sterenborg HJ. Estimation of lipid and water concentrations in scattering media with diffuse optical spectroscopy from 900 to 1,600 nm. *J Biomed Opt* 2010; 15(3):037015.

15. Nachabé R, Hendriks BH, van der Voort M, Desjardins A, Sterenborg HJ. Estimation of bilogical chromophores using diffuse optical spectroscopy - benefit of extending the UV-VIS wavelength range to include 1000 to 1600nm. *Optics Express* 2010; 18(24): 1432-1442.

16. Nachabé R, Evers DJ, Hendriks BH, Lucassen G, van der Voort M, Wesseling J, et al. Effect of bile absorption coefficients on the estimation of liver tissue optical properties and related complications in discriminating healthy and tumorous samples. *Optics Express* 2011; 2(3): 600-614.

17. Nachabé R, Evers DJ, Hendriks BH, Lucassen G, van der Voort M, Rutgers EJ, et al. Diagnosis of breast cancer using diffuse optical spectroscopy from 500 to 1600 nm: a comparison of classification methods. *J Biomed Opt* 2011; 16(8): 087010.

18. Farrell T, Patterson M, Wilson B. A diffusion theory model of spatially resolved, steady-state diffuse reflectance for the noninvasive determination of tissue optical properties in vivo. *Med Phys.* 1992; 19(4):879-888.

19. Barker M, Rayens W. Partial least squares of discrimination. *J Chemometrics* 2003; 17(3):166-173.

20. Kruskal W, Wallis W. Use of Ranks in One-Criterion Variance Analysis. *J American Statistical Association* 1952; 47(260): 583-621.

21. Bigio I, Bown S, Briggs G, Kelley C, Lakhani S, Pickard D, et al. Diagnosis of breast cancer using elastic-scattering spectroscopy: preliminary clinical results. *J Biomed Opt.* 2000; 5(2):221-228.

22. Zhu C, Palmer G, Breslin T, Harter J, Ramanujam N. Diagnosis of breast cancer using diffuse reflectance spectroscopy: Comparison of a Monte Carlo versus partial least squares analysis based feature extraction technique. *Lasers Surg Med.* 2006; 38:714-724.

23. Brown J, Wilke L, Geradts J, Kennedy S, Palmer G, Ramanujam N. Quantitative optical spectroscopy: a robust tool for direct measurement of breast cancer vascular oxygenation and total hemoglobin content in vivo. *Cancer Res.* 2009; 69(7):2919-2926.

24. Chang V, Cartwright P, Bean S, Palmer G, Bentley R, Ramanujam N. Quantitative physiology of the precancerous cervix in vivo through optical spectroscopy. *Neoplasia* 2009; 11(4):325-332.

25. Wang H, Jiang J, Lin C, Lin J, Huang G, Yu J. Diffuse reflectance spectroscopy detects increased hemoglobin concentration and decreased oxygenation during colon carcinogenesis from normal to malignant tumors. *Opt Express* 2009; 17(4):2805-2817.

26. Volynskaya Z, Haka A, Bechtel K, Fitzmaurice M, Shenk R, Wang N, et al. Diagnosing breast cancer using diffuse reflectance spectroscopy and intrinsic fluorescence spectroscopy. *J Biomed Opt* 2008; 13(2):024012.

27. Majumder S, Keller M, Boulos F, Kelley M, Mahadevan-Jansen A. Comparison of autofluorescence, diffuse reflectance, and Raman spectroscopy for breast tissue discrimination. *J Biomed Opt* 2008; 13(5):054009.

Chapter 8

Diagnosis of breast cancer using optical spectroscopy from 500 to 1600 nm: a comparison of classification methods

Rami Nachabé

Daniel J. Evers

Benno H. W. Hendriks

Gerald W. Lucassen

Marjolein van der Voort

Emiel J. Rutgers

Marie-Jeanne Vrancken Peeters

Jos A. van der Hage

Hesters S. Oldenburg

Jelle Wesseling

Theo J. M. Ruers

Abstract

We report on the use of diffuse optical spectroscopy analysis of breast spectra acquired in the wavelength range from 500 to 1600 nm with a fiber optic probe. A total of 102 *ex vivo* samples of five different breast tissue types, namely adipose, glandular, fibroadenoma, invasive carcinoma and ductal carcinoma *in situ* from 52 patients were measured. A model deriving from the diffusion theory was applied to the measured spectra in order to extract clinically relevant parameters such as blood, water, lipid, and collagen volume fractions, β-carotene concentration, average vessels radius, reduced scattering amplitude, Mie slope and Mie-to-total scattering fraction. Based on a classification and regression tree algorithm applied to the derived parameters, a sensitivity-specificity of 98%-99%, 84%-95%, 81%-98%, 91%-95%, and 83%-99% were obtained for discrimination of adipose, glandular, fibroadenoma, invasive carcinoma, and ductal carcinoma *in situ*, respectively; and a multiple classes overall diagnostic performance of 94%. Sensitivity-specificity values obtained for discriminating malignant from non-malignant tissue were compared to existing reported studies by applying the different classification methods that were used in each of these studies. Furthermore, in these reported studies, either lipid or β-carotene was considered as adipose tissue precursors. We estimate both chromophore concentrations and demonstrate that lipid is a better discriminator for adipose tissue than β-carotene.

1. Introduction

Within present-day strategy of human breast cancer treatment, diagnostic biopsy and surgical margin assessment are two elements in which procedural accuracy could significantly be enhanced.

Missed diagnoses of cancer by false-negative biopsies have been reported ranging from 4.3 to 17.9%, despite ongoing advance in imaging technologies. Moreover, indeterminate pathology analysis will result in need of repeat biopsies in between 4 to 32% of patients [1-6].

Breast conservative therapy aimed at conserving as much breast tissue as possible, is the treatment of choice in patients with T1-T2 breast tumors. However, the rate of irradical resection and the need for a secondary surgical procedure is often over 10%, depending on the specific definition [7, 8].

Over the last decade, new tools have been developed to classify breast tissue and assess breast tissue margins based on optical spectroscopy techniques [9-22]. Bigio *et al.* performed *in vivo* elastic scattering spectroscopy measurements between 350 and 750 nm to discriminate between 13 malignant and 59 non-malignant breast tissue samples by applying artificial neural network (ANN) and hierarchical cluster analysis (HCA) on the spectra yielding sensitivity-specificity of 69%-85% and 67%-79%, respectively [9]. This study also showed that the spectral features between 400 and 500 nm in adipose tissue are mainly dominated by β-carotene light absorption, however optical properties were not derived from the measured spectra. The biomedical group at Duke University has performed several studies where optical properties were derived from measurements performed between 350 and 600 nm by using an inverse Monte-Carlo technique to extract hemoglobin and β-carotene concentrations as well as hemoglobin saturation and the reduced scattering amplitude [10-13]. Classification based on linear support vector machine (SVM) learning was performed to classify malignant (35 samples) from non-malignant samples (50 samples including adipose and fibrous tissue types) with a sensitivity-specificity of 83%-80% [10]. A more recent study from the same group showed that it is possible to discriminate 54 malignant samples from 70 non-malignant samples with a sensitivity-specificity of 83%-87% based on the extracted parameters from diffuse reflectance measurements [11]. Volynskaya *et al.* conducted an *ex vivo* breast (104 samples) study where a classification between four types of breast tissue was performed from diffuse reflectance spectra acquired from 350 to 750 nm [14]. Classification of 31 normal, 55 fibrocystic change, 9 fibroadenoma, and 9 infiltrating ductal carcinoma was achieved with a sensitivity-specificity of 100%-100% by using a logistic regression algorithm (LR). An *ex vivo* breast study by Majumder *et al.* showed that sparse multinomial logistic regression classification of 134 normal (adipose and glandular), 86 invasive ductal carcinoma, 18 ductal carcinoma *in situ* and 55 fibroadenoma spectra can be achieved with sensitivity-specificity ranging from 28%-86% to 86%-97% when only analyzing diffuse reflectance spectra acquired between 400 and 800 nm [15]. A more recent study showed sensitivity-specificity of 85%-96% when discriminating 145 normal from 34 tumor (invasive ductal carcinoma and ductal carcinoma *in situ*) samples [16]. Laughney *et al.* presented *ex vivo* non-contact optical properties estimations from spectra acquired between 510 and 785 nm from 29 breast

samples and a k-nearest neighbor (KNN) classification method was used to discriminate between different tissue types [17]. They have shown an interesting comparison of classifying the different types of tissue according to their pathology identity and by grouping them into subgroups such as adipose (7021 spectra), non-malignant (533 inflammation, 4110 benign epithelia, and 31226 normal epithelia spectra), and malignant (194 ductal carcinoma *in situ*, 479 invasive lobular carcinoma, and 22547 invasive ductal carcinoma spectra). Their results showed sensitivity-specificity of 87%-99%, 90%-82%, and 77%-90% for adipose, non-malignant and malignant, respectively. However, a sensitivity-specificity of 87%-99%, 74%-74%, 9%-91%, 0%-100%, 77%-90%, 0%-100%, and 0%-100% was reached for adipose, normal epithelia, benign, inflammation, invasive ductal carcinoma, ductal carcinoma *in situ*, and invasive lobular carcinoma, respectively.

Other studies [18-21] investigated wavelength ranges between 600 and 1100 nm where water and lipid were estimated in addition to hemoglobin. Therefore adipose tissue could be discriminated based on the amount of estimated lipid and not β-carotene, since this chromophore has negligible absorption above 600 nm. However these investigators did not perform classification on their data.

In our study, we have conducted an *ex vivo* trial to estimate optical properties from 102 samples of five different types of breast tissue: adipose, glandular, invasive carcinoma (IC), fibroadenoma (FA), and ductal carcinoma *in situ* (DCIS) measured in 52 patients. Optical spectra were taken with a setup that can resolve light from 500 nm up to 1600 nm and a model based on diffusion theory was applied to the measurements to estimate the optical properties by determining several parameters such as blood, water, and lipid volume fractions, reduced scattering amplitude, Mie slope, Mie scattering fraction, and pigment packaging factor [23, 24]. Besides, β-carotene was also included in our model since it has significant absorption up to 500 nm as demonstrated by other groups [9-11, 14]. Recent findings by Taroni *et al.* showed that collagen is an important absorber to include in the model for fitting the measured spectra as it has distinct absorption features above 900 nm [19-21]. Therefore, we measured the absorption coefficient of collagen up to 1600 nm and included it in our model.

We present the first study using DRS measurements on a 500-1600 nm wavelength range to estimate physiological, morphological and optical properties parameters of *ex vivo* breast tissue. The classification and regression tree (CART) algorithm, a probabilistic discriminative classification method, was applied to the derived parameters to evaluate the performance of diagnosis of the five measured types of tissues. Sensitivity-specificity computation and receiver operating characteristic (ROC) curves analysis were performed to quantify the overall performance of the diagnosis by using the Provost and Domingos measure (PDM) [25].

In addition, several classification methods that were used in literature to discriminate malignant from non-malignant tissues were applied to our data in order to compare our results with those reported in existing literature studies. Additional classification methods were also applied for comparison.

Finally, classification of adipose tissue based on either β-carotene or lipid only was compared as no existing breast studies in literature made a comparison on classifying adipose tissue based on only one of these two adipose tissue precursors.

2. Materials and methods
2.1. Ex vivo breast sample collection

The human breast samples were obtained under approval by the internal review board committee of the Dutch Cancer Institute in Amsterdam, The Netherlands (NKI-AVL) where this study was conducted. The breast samples that were measured corresponded to resection specimens of either to mastectomies or lumpectomies. Breast samples of patients subject to mastectomy were sliced with a thickness of roughly 0.5 to 1 cm whereas the sample sizes of the patients who were subject to lumpectomy (e.g. fibroadenoma) corresponded to the size of the excised tissue which was in average several millimeters in diameter. After surgical resection, resection samples were transferred to the pathology department within 2 hours where they were inked at the surface before slicing them for histological processing. All optical measurements were performed before formalin fixation and tissue preparations by the pathologists in order to limit as much as possible changes in the optical properties from the tissue conditions when excised. Five different types of tissue were measured based on the macroscopical indication by the pathologist: adipose, glandular, fibroadenoma (FA), invasive carcinoma (IC) and ductal carcinoma *in situ* (DCIS). A total number of 102 samples from 52 patients were investigated from which a total number of 980 spectra were acquired and co-registered with the pathological findings. The pathological diagnosis performance was very high for all the cases that we have tested. The cancerous cases were all macroscopically clear cut carcinomas; and in case of doubt we were reluctant to include such cases in this study. Table 1 summarizes the histological breakdown of the breast tissue samples including the amount of acquired spectra in this study.

Table 1. Histological description of breast tissue types and the corresponding amount of samples and spectra that were measured.

Type of breast tissue (abbreviation)	Number of samples	Number of spectra
Non-Malignant	**73**	**643**
Adipose	43	327
Glandular	23	189
Fibroadenoma (FA)	7	127
Malignant	**29**	**337**
Invasive Carcinoma (IC)	21	241
Ductal Carcinoma *In Situ* (DCIS)	8	96
Total	**102**	**980**

2.2. Instrumentation and spectral calibration

Ex vivo diffuse reflectance spectra were taken using a portable spectroscopic system as illustrated in Fig. 1 and used in previous studies [23, 24, 26]. A tungsten halogen broadband light source with an integrated shutter (Ocean Optics, HL-2000-HP) was used to deliver light into tissue. Delivery of light to the tissue and its collection were achieved with a 1.3 mm diameter fiber-optic probe with a distal end polished at an angle of 20 degrees. The probe comprises three 200-μm core diameter optical fibers with one fiber connected to the light source that is located 2.48 mm from the two side-by-side optical fibers that are used to collect the diffused light. The optical fibers used for the collection of light are connected to a spectrometer with a silicon detector (Andor Technology, DU420A-BRDD) and a spectrometer with an InGaAs detector (Andor Technology, DU492A-1.7), respectively. After thermoelectrically cooling the detectors to -40°C, wavelength values were assigned to each pixel of the detector by fitting a second-order polynomial to a set of atomic lines from an argon source with peaks at known wavelength. Subsequently, the spectral response of a white reflectance standard (Spectralon) with known reflectivity was measured by placing the distal end of the probe at a fixed distance of roughly 2 mm and followed by a background measurement in order to minimize the impact of ambient light. This step is necessary as it allows correcting for the system response (e.g. spectral shape of the light source and wavelength-dependent sensitivity in the optics and gratings and the detectors). This white reference measurement is used to divide each spectral measurement on the tissue samples for which a background measurement is subtracted yielding to the final reflectance measurement. The integration time for each measurement is in average 0.5 second. The reflectance spectra obtained with both spectra are combined together to form one single reflectance spectrum ranging from 500 to 1600 nm and is used in order to apply the mathematical modeling for the data analysis.
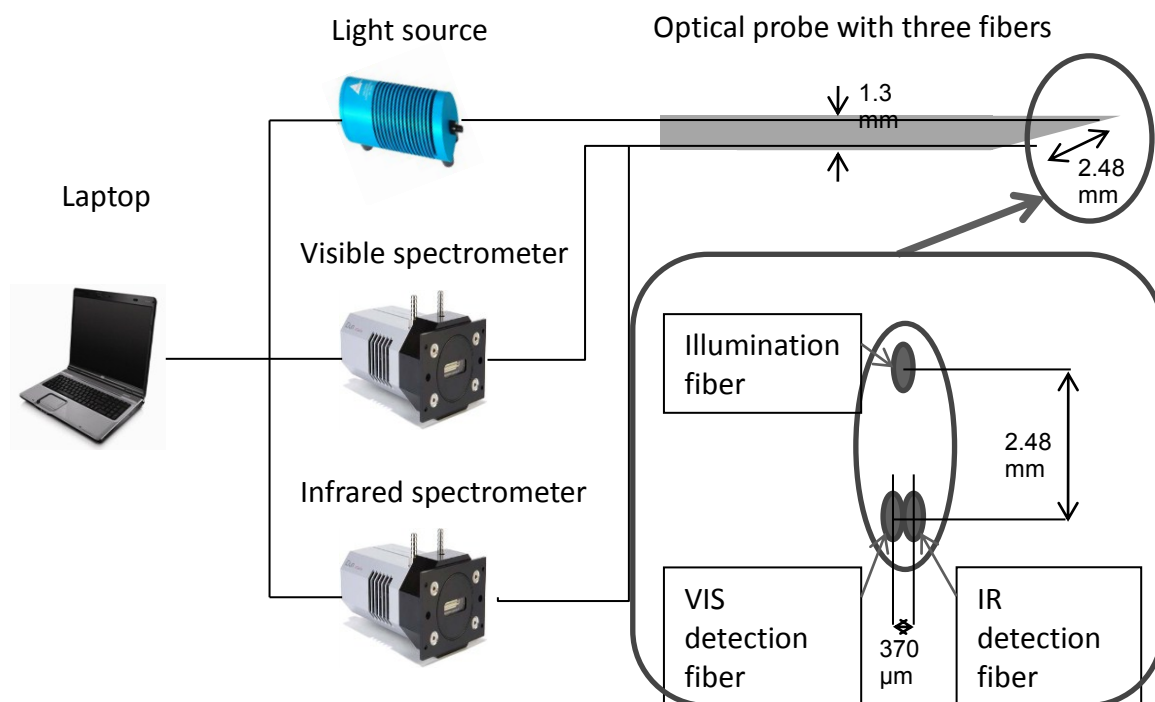

Figure 1. Schematic of the optical setup and the design of the optical probe.

2.3. Spectral data modeling

The measured spectra were fitted from 500 to 1600 nm with the model of Farrell *et al.* [27] that is derived from diffusion theory using a Levenberg-Marquardt non-linear inversion algorithm in order to determine the absorption coefficient $\mu_a(\lambda)$ and the reduced scattering coefficient $\mu_s'(\lambda)$ expressed in cm^{-1}. The validation of the model based on a phantom study, including spectral calibration procedures, and its application to *in vivo* and *ex vivo* tissues were justified in detail elsewhere [23, 24].

The model requires the distance between the emitting and collecting fibers as well as the wavelength-dependent absorption coefficients of the chromophores of interest as input arguments. Additionally, the reduced scattering coefficient was empirically modeled as:

$$\mu_s'(\lambda) = \alpha \left[\rho \left(\frac{\lambda}{\lambda_0} \right)^{-b} + (1 - \rho) \left(\frac{\lambda}{\lambda_0} \right)^{-4} \right] \quad (1)$$

where $\lambda_0 = 800$ nm corresponds to a wavelength normalization value, α is the reduced scatteringamplitude at λ_0, the Mie scattering slope is b, and ρ denotes the Mie-to-total reduced scattering fraction assuming Mie and Rayleigh scattering as the two types of scattering in tissue.

The absorption coefficient is expressed as a term that corresponds to vascular absorption $\mu_a^{Blood}(\lambda)$, of the light due to blood-derived chromophores and a second term $\mu_a^{Other}(\lambda)$ due to absorption of light by other chromophores present in breast tissue. The blood related absorbers are deoxygenated-hemoglobin (Hb) and oxygenated-Hemoglobin (HbO$_2$) and define the absorption coefficient due to blood as:

$$\mu_a^{Blood}(\lambda) = C(\lambda)v\left[StO_2\mu_a^{HbO_2}(\lambda) + (1 - StO_2)\mu_a^{Hb}(\lambda)\right] \quad (2)$$

where $\mu_a^{Hb}(\lambda)$ and $\mu_a^{HbO_2}(\lambda)$ correspond to absorption coefficients of pure Hb and HbO$_2$ given an average hemoglobin concentration in blood of 150 mg/ml, respectively. The parameters v and StO_2 correspond to the blood volume fraction and the level of hemoglobin saturation by oxygen, respectively. The parameter $C(\lambda)$ was used to account for inhomogenous distribution of hemoglobin in vessels and is known as pigment packaging factor [28] expressed as:

$$C(\lambda) = \frac{1 - \exp\left(-2R\left[StO_2\mu_a^{HbO_2}(\lambda) + (1 - StO_2)\mu_a^{Hb}(\lambda)\right]\right)}{2R\left[StO_2\mu_a^{HbO_2}(\lambda) + (1 - StO_2)\mu_a^{Hb}(\lambda)\right]} \quad (3)$$

where R corresponds to the average vessel radius. Studies that were performed on breast tissue [11, 14] showed that it is important to have β-carotene (βc) as an absorber in the model when recording spectra in the visible range. Indeed, these studies demonstrated that βc is an essential discriminator for adipose tissue in breast. Other studies that investigated optical properties of breast in the near infrared range [18, 20] discriminate

adipose tissue from other types of tissue based on light absorption by lipids. However, no studies so far used both βc and lipid. In our study we included both absorbers in the model and investigated the advantage of measuring up to 1600 nm where additional water and lipid absorption features exist [23] which enables more accurate estimation of lipid volume fraction [24].

Taroni *et al.* showed that collagen is an abundant absorber in several breast tissue types when recording optical spectra up to 1100 nm [19-21]. Therefore, we have measured collagen Type I (Sigma-Aldrich C9879) absorption coefficients from 500 to 1600 nm by tightly inserting the collagen fibers in cuvettes of 0.5, 1 and 2 mm thickness and measuring its absorption with a spectrophotograph with a 150 mm diameter integrating sphere (Lambda 900 Spectrometer, Perkin Elmer). The absorption measurements were separated from the scattering by mounting the cuvettes inside the integrating sphere far away from the detector. When a sample is mounted inside the sphere, the loss of light is mainly due to absorption by the sample related to the absorption coefficient. Because of the turbidity of the sample, scattering occurs. Therefore, an additional measurement was performed by allowing the forward transmitted light to escape out of an exit port in the back end of the sphere in order to measure scattering. The scattered light from the sample mounted inside the sphere is therefore measured, and subsequently the absorption coefficient can be determined by subtracting the measurement with the opened exit port from the measurement with closed exit port.

The absorption coefficient due to non-blood derived chromophores is expressed as:

$$\mu_a^{Other} = \psi \left[f_{Lipid} \mu_a^{Lipid}(\lambda) + \left(1 - f_{Lipid}\right) \mu_a^{H_2O}(\lambda) \right] + f_{Collagen} \mu_a^{Collagen}(\lambda)$$
$$+ c_{\beta c} \varepsilon_{\beta c}(\lambda) \quad (4)$$

where $\mu_a^{Lipid}(\lambda)$, $\mu_a^{H_2O}(\lambda)$, $\mu_a^{Collagen}(\lambda)$ and $\varepsilon_{\beta c}(\lambda)$ correspond to the absorption coefficients of lipid, water, collagen and the extinction coefficient (in cm^{-1}.M^{-1}) of β-carotene, respectively. The parameter ψ represents the water and lipid volume fraction, and f_{Lipid} represents the lipid fraction within the volume probed by the light. However, $f_{Collagen}$ corresponds to the collagen volume fraction in the probed tissue whereas $c_{\beta c}$ corresponds to the molar concentration of β-carotene. The absorption coefficients of the various chromophores of interest are depicted in Fig. 2. The absorption coefficient at unit concentration of Hb and HbO$_2$ that is used as *a priori* knowledge for the model are from Zijlstra *et al.* [29] whereas the extinction coefficient of β-carotene in human adipose cells is from van de Poll *et al.* [30]. Water and lipid absorption coefficients that are used in the presented study are from previous published work [23]. The collagen absorption coefficient presented in this study has a local maximum at 1200 nm of 1.54 cm^{-1} which is of the same order of magnitude as the water and lipid absorption coefficient in the vicinity of 1200 nm. It is important to note that collagen has a wider maximum than fat but narrower than water. Other local maxima at 911, 1030 and 1510 nm are observed with absorption coefficients of 0.21, 0.34, and 5.22 cm^{-1}. The presented absorption coefficient

of collagen is about an order of magnitude higher than the one presented by Taroni *et al.* [20], however it matches very well with the coefficients reported by Tsai *et al.* [31] and by Nunez [32]. The difference in collagen absorption values with Taroni *et al.* could be due to the fact that the density of our measured sample is different from the density used by Taroni *et al.*
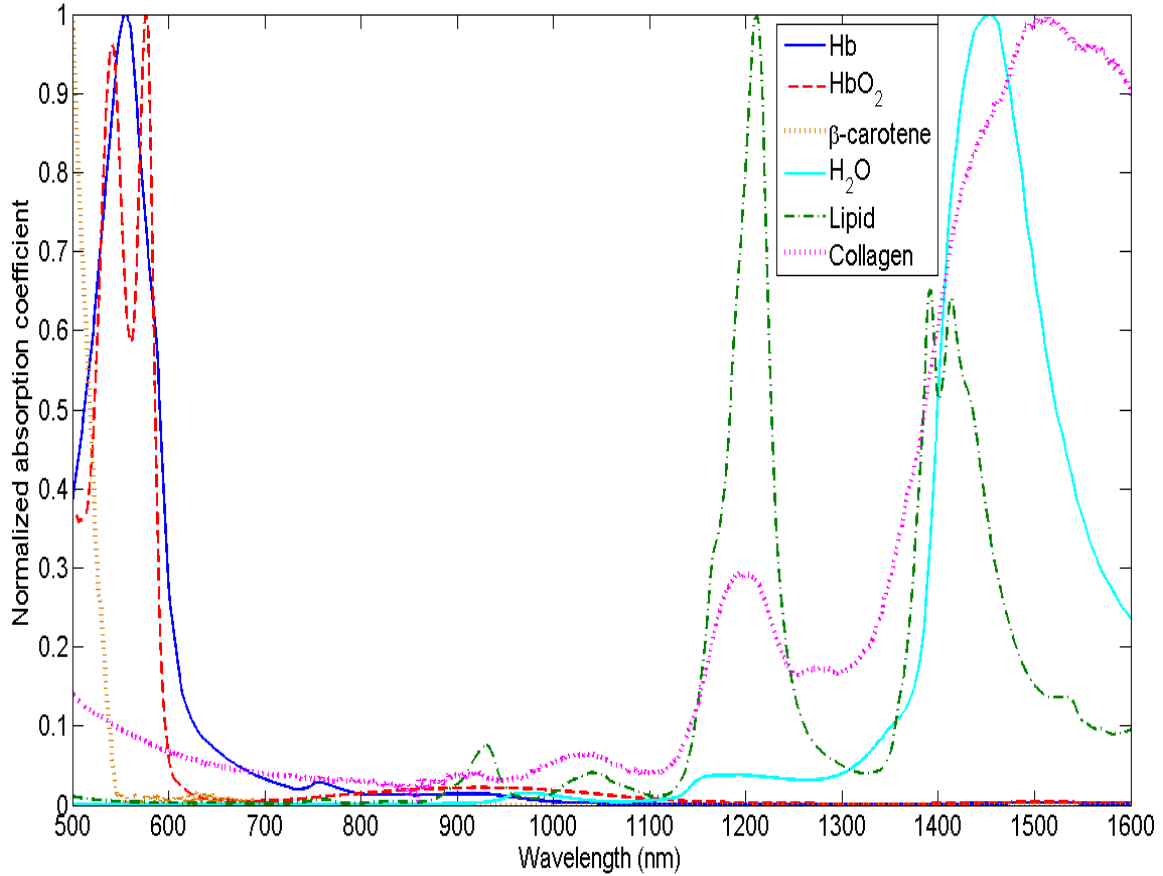

Figure 2. Normalized absorption coefficients of deoxygenated-hemoglobin (Hb), oxygenated-hemoglobin (HbO₂), β-carotene, water (H₂O), lipid and collagen.

In few cases, the ink used by the pathologist before cutting was spread into the tissue when slicing the breast samples, influencing the measured spectral shapes. In order to correct for this, the absorption coefficients of these inks were measured and added to the fitting. Given the large number of free parameters, two separate fits on different wavelength ranges were performed: the first fit was performed between 500 and 900 nm with $\mu_a^{Blood}(\lambda) + c_{\beta c}.\varepsilon_{\beta c}(\lambda)$ and $\mu_{s'}(\lambda)$ only in the model and the second fit was performed between 900 and 1600 nm with $\mu_a^{Other}(\lambda) - c_{\beta c}.\varepsilon_{\beta c}(\lambda)$ and $\mu_{s'}(\lambda)$ only in the model. The extracted values from both fits were used as initial guess for the fit applied over the full wavelength range between 500 and 1600 nm in order to ensure stability of the fit.

From fits to the spectra between 500 and 1600 nm, the following fit parameters were obtained: ν, StO_2, R, ψ, f_{Lipid}, $f_{Collagen}$, $c_{\beta c}$, α, b and ρ. For each estimated value, a

confidence interval computed from the covariance matrix was used to assess the reliability for each fit parameter [33].

2.4 Statistical analysis

A non-parametric Kruskal-Wallis statistical test was conducted to evaluate significant differences of the estimated parameters between the various types of breast tissue for a significance level of 5% (i.e. $p < 0.05$). The test examines if the medians of the various groups are not all equal; meaning that if the p-value is below the significance level, at least one type of tissue can be discriminated from the others. Therefore an additional *post hoc* test is required to account for multiple comparisons, as well as for the fact that comparisons can be interrelated. In this study, Tukey's *post hoc* test was applied at a significance level of 5%. This statistical procedure is a restricted pairwise comparison that follows the Kruskal-Wallis test which had indicated the significance of the differences [34].

2.5 Classification algorithms

The classification and regression tree (CART) algorithm was used to classify between the five types of tissue. The CART algorithm starts from a central node that discriminates the largest class, adipose tissue in our case, based on the best classifier. From this root node, a split is performed to discriminate the largest class from the other tissue classes. From the split, daughter partial trees are generated and other parameters are used for further splits. The purity of each node is assessed with the Gini's maximization index algorithm which corresponds to unity minus the sum of squares of the proportions of target classes at a specific node [35]. The advantage of CART is that it is a non-parametric method whereas other methods such as (linear discriminant analysis) LDA, LR, and KNN assume functional relations between dependent and predictor variables. Moreover, one of the advantages of CART is that it is easy to interpret since the input parameters for classification are used whereas other methods post-process the parameters into scores that might not be intuitively related to the input parameters. The performance of the diagnosis was evaluated by carrying out an ROC analysis. From the sensitivity-specificity values and the area under the ROC curves (AUC), the Provost and Domingos measure (PDM) for total AUC is computed to assess the accuracy of the diagnostic algorithms [25]. The PDM value corresponds to the sum of AUC of each class weighted by the class size fraction.

Classifications were carried out on the estimated parameters from the fit model using a leave-one-out (LOO) cross validation scheme. Additionally, a hold-out (HO) cross validation scheme with a 70%-30% training-testing split of the data was carried out. The split was performed by random selection of the data before splitting and classification. This partition procedure and classification was reproduced 20 times and the computed sensitivity-specificity values were averaged.

Several techniques were used in literature to classify parameters based on diffuse reflectance spectroscopy measurements or directly applied to the spectra as mentioned in the introduction section. The following classification algorithms were applied to our data: ANN [9], linear SVM [11], LR [14-16] and KNN employing Mahalabonis distance to

account for parameters intercorrelation [17], in order to evaluate the sensitivity-specificity of discriminating malignant and non-malignant types of breast tissue. Besides, other classification methods were also tested such as CART, LDA with Mahalanobis distance stratified covariance, and non-linear SVM to discriminate malignant from non-malignant breast tissues. However, the classification was performed by taking the amount of samples that corresponds to the lowest sample size within the malignant and non-malignant category respectively. This means that within the non-malignant category, 127 spectra from adipose and from glandular tissues were randomly selected and added to the FA spectra to form the non-malignant database whereas 96 spectra from IC were randomly selected and added to the DCIS spectra to form the malignant database. The purpose of such categorization is to avoid higher representation of one type of tissue over the others within the same category. Otherwise, discriminating malignant from non-malignant tissue would be comparable to classification of adipose versus IC given the fact that the total adipose and IC spectra represent 51% and 72% of the non-malignant and malignant samples size, respectively.

Furthermore, this study is the first that estimates both β-carotene and lipid from breast tissue measurements. A classification of adipose tissue was performed from all the parameters except lipid, water and collagen and another classification without β-carotene to evaluate which adipose precursor is the most accurate for adipose breast tissue classification using the CART algorithm.

3. Results

Fig. 3 depicts typical examples of spectra measured on adipose (Fig. 3.a), glandular (Fig. 3.b), FA (Fig. 3.c), IC (Fig. 3.d) and DCIS (Fig. 3.e) tissues and their corresponding fits. From the measurement of adipose breast tissue, one can notice the effect of β-carotene absorption on the spectra below 550 nm and the lipid absorption peaks at 930 and 1211 nm.
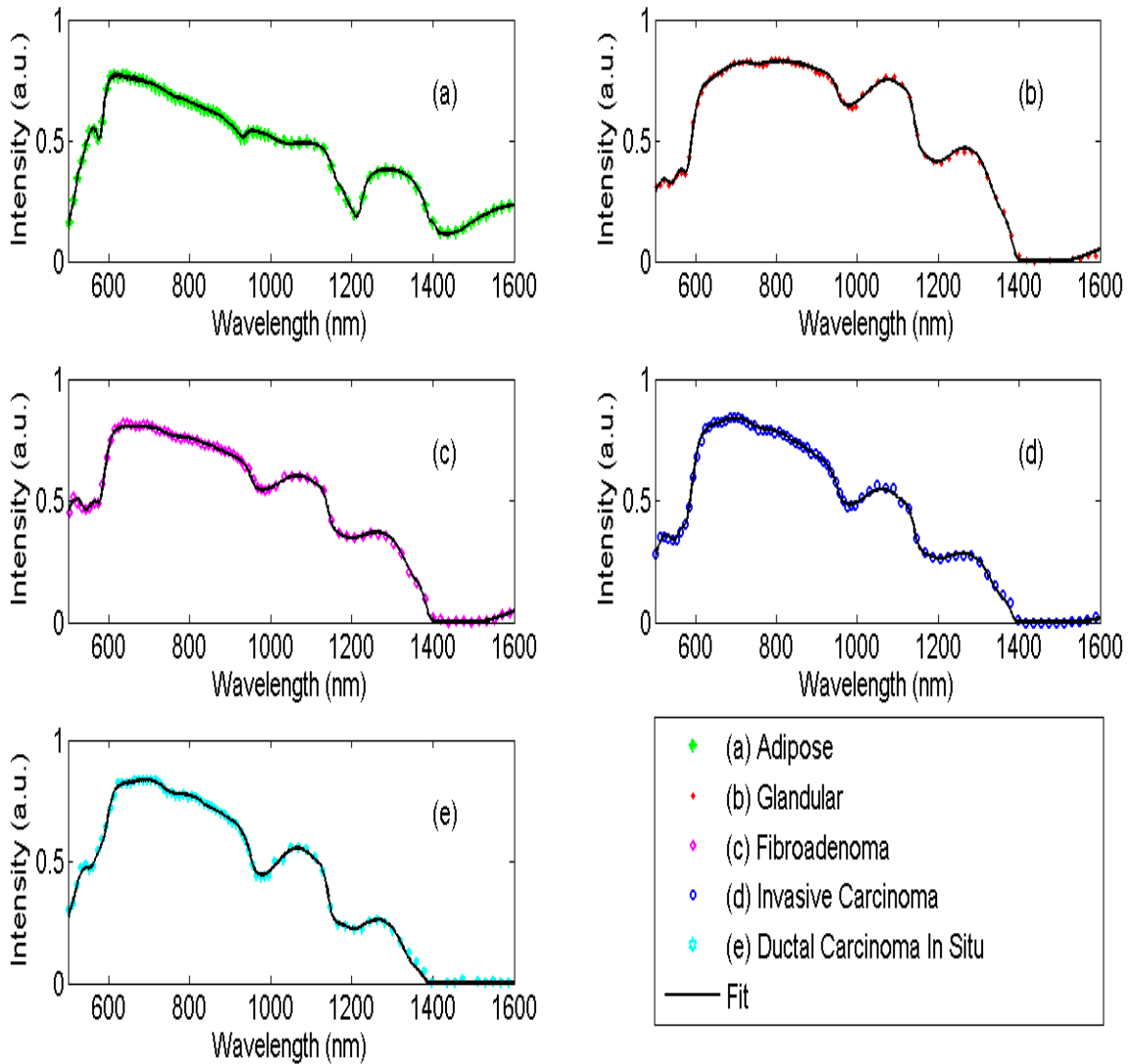
Figure 3. Typical measurement of adipose (a), glandular (b), FA (c), IC (d), and DCIS (e) and their corresponding fit curves.

Fig. 4 depicts the histograms of the median and standard deviation for each of the parameters derived from the fit per category of tissue type. Complementary to Fig.4, Table 2 displays the parameters that show significant differences ($p<0.05$) for pairwise types of tissue comparison according to a Kruskal-Wallis test followed by a *post hoc* multiple comparison Tukey's test.
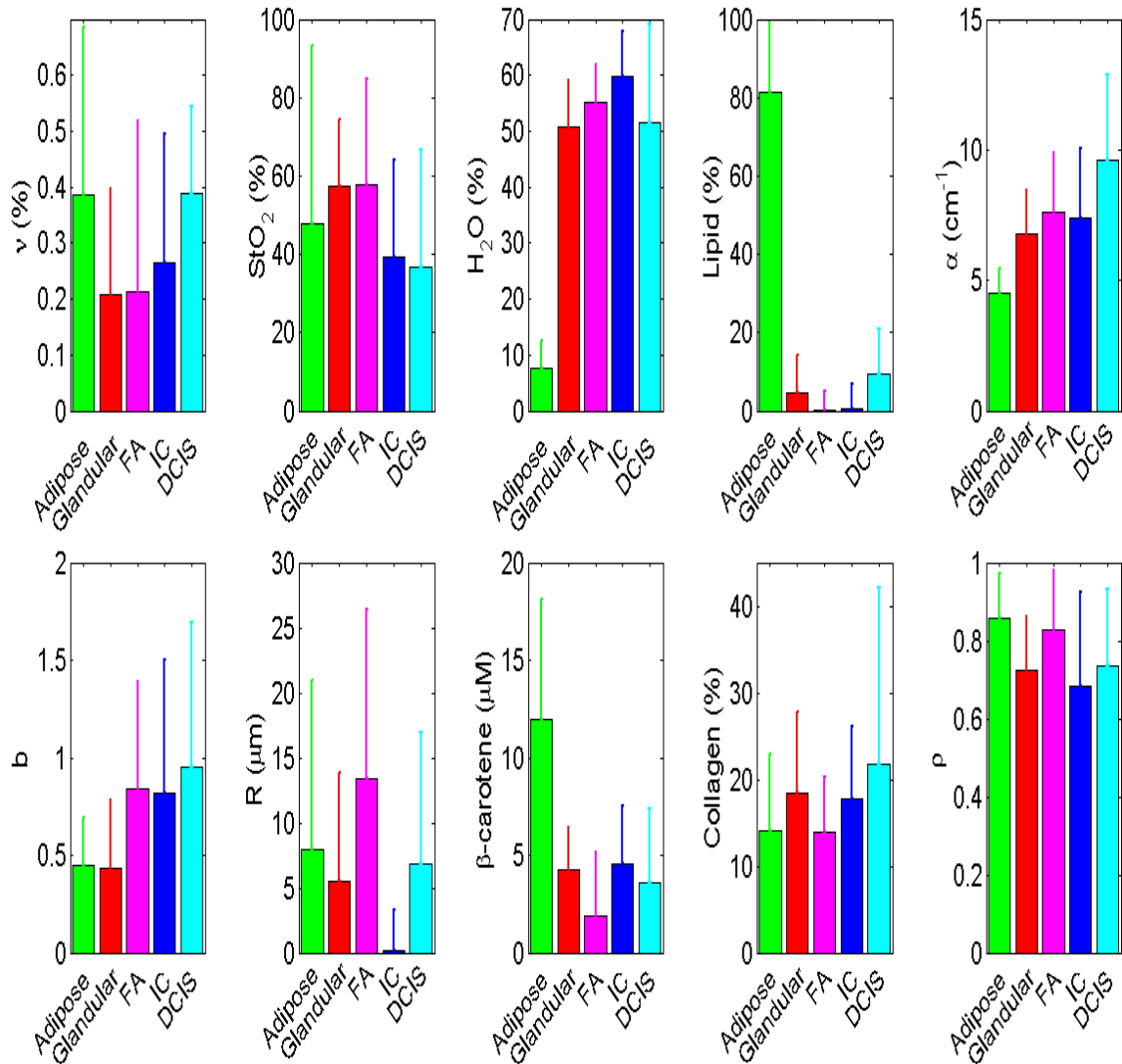
Figure 4. Average and standard deviation of the estimated blood volume fraction (v), oxygenation level (S_tO_2), water (H_2O), lipid, reduced scattering amplitude (α), scattering slope (b), vessel radius (R), β-carotene, collagen, and the Mie-to-total reduced scattering fraction (ρ) for each of the various types of breast tissues: adipose, glandular, FA, IC, and DCIS.

It can be seen that adipose and DCIS tissue contains almost twice as much blood as the other types of tissue whilst the blood oxygenation level is lower in malignant tissue ($StO_2 < 40\%$) compared to non-malignant tissue. Adipose tissue can clearly be distinguished from the other tissue types by its high lipid average volume fraction and β-carotene concentration of 80% and 12 μM, respectively. FA has the lowest β-carotene concentration and is significantly different from the other tissue types except for DCIS. The reduced scattering amplitude is the lowest for adipose tissue (roughly 5 cm^{-1}) and the highest for DCIS (roughly 10 cm^{-1}), whereas it is rather similar for the other tissues (around 7 cm^{-1}). A clear distinction can be observed for the Mie slope where it is almost 2-fold smaller for non-malignant compared to malignant samples. Apart from adipose tissue, IC showed significant differences based on the water content with the highest

amount among all tissues. Adipose and FA have the lowest collagen volume fraction of roughly 14%, whereas glandular and IC are about 18% and DCIS has the highest value with 22%. Although adipose and FA have similar collagen volume fractions, this parameter showed significant difference between DCIS and adipose tissue and not with FA due to the higher standard deviation in collagen in adipose tissue compared to FA. It can be seen that the trends in collagen are correlated with the estimated Mie scattering fractions: a lower collagen volume fraction corresponds to a higher Rayleigh scattering contribution.

Table 2. Parameters that show significant difference for the pairwise comparisons of the different tissue types after Kruskal-Wallis statistical test with post hoc Tukey's multiple comparison test (p<0.05).

Type of breast tissue	Type of breast tissue			
	Glandular	FA	IC	DCIS
Adipose	v, StO_2, H_2O, Lipid, α, βC, Collagen, ρ	v, StO_2, H_2O, Lipid, α, b, R, βC	v, StO_2, H_2O, Lipid, α, b, R, βC, Collagen, ρ	H_2O, Lipid, α, b, βC, Collagen, ρ
Glandular	-	b, R, βC, Collagen, ρ	StO_2, H_2O, α, b, R	v, StO_2, α, b
FA		-	StO_2, H_2O, R, βC, Collagen, ρ	v, StO_2, Lipid, α, R, ρ
IC			-	v, Lipid, α, R

Multiple class classification was performed with the CART method, on the five categories of breast tissue i.e. adipose, glandular, FA, IC, and DCIS in order to evaluate the performance of such a diagnosis. Fig. 5 depicts a decision tree that classifies all tissues based on a specific threshold value for each parameter. As can be seen, the first node allows discrimination of adipose tissue based on the lipid content. If the lipid volume fraction is above 40%, an acquired spectrum is considered to be taken in adipose tissue otherwise it is another type of tissue.
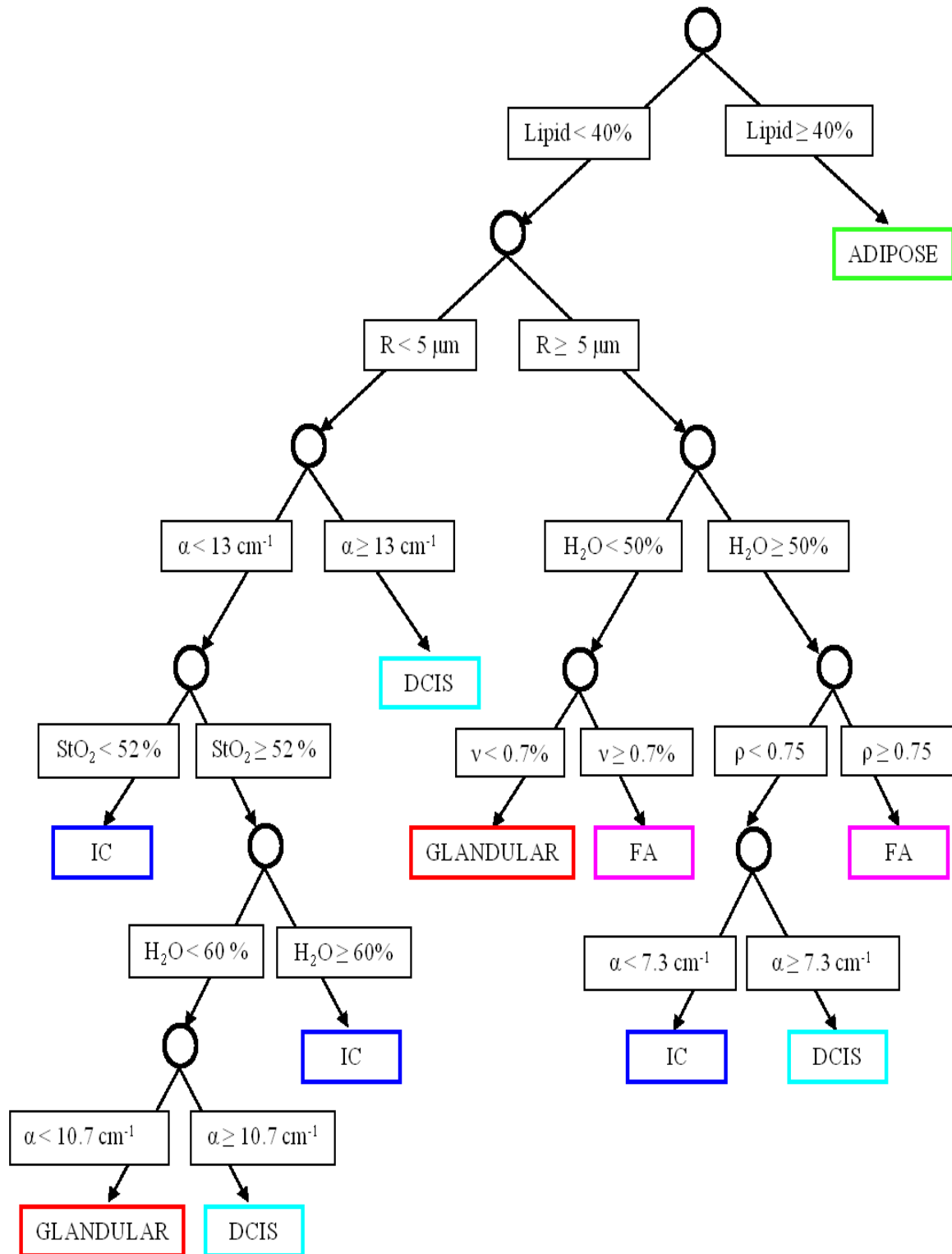
Figure 5. Classification decision tree of the different breast types based on parameter threshold values.

Table 3 corresponds to the confusion matrix displaying the diagnostic performance by comparing with the pathological diagnosis being the reference standard.

Table 3. Confusion matrix displaying classification of breast tissues using the CART algorithm for classification.

| Type of breast tissue (number of samples) | DRS classification diagnosis | | | | |
| | Non-Malignant | | | Malignant | |
	Adipose	Glandular	FA	IC	DCIS
Adipose (327)	**319**	6	2	0	0
Glandular (189)	7	**158**	8	15	1
FA (127)	0	11	**103**	11	2
IC (241)	0	15	4	**219**	3
DCIS (96)	0	5	1	10	**80**

Table 4 compares the sensitivity-specificity rates for each type of tissue when a LOO and HO cross validation were applied. The overall classification accuracy computed from the confusion matrix is 90% (879 out of 980). The type of tissue with the lowest sensitivity rate is FA whereas adipose tissue has the highest specificity rate.

Table 4. Sensitivity and specificity of CART classification of each type of tissue using leave-one-out (LOO) and 20-fold hold-out (HO) cross validation.

| Type of breast tissue | Sensitivity (%) - Specificity (%) | |
	Leave-one-out cross validation	Hold-out cross validation
Adipose	98 – 99	98±1 – 99±1
Glandular	84 – 95	80±6 – 95±2
FA	81 – 98	75±9 – 97±1
IC	91 – 95	86±6 – 94±2
DCIS	83 – 99	81±10 – 98±2

The receiver operating characteristic (ROC) curves for classification of each tissue are depicted in Fig. 6 including confidence intervals.
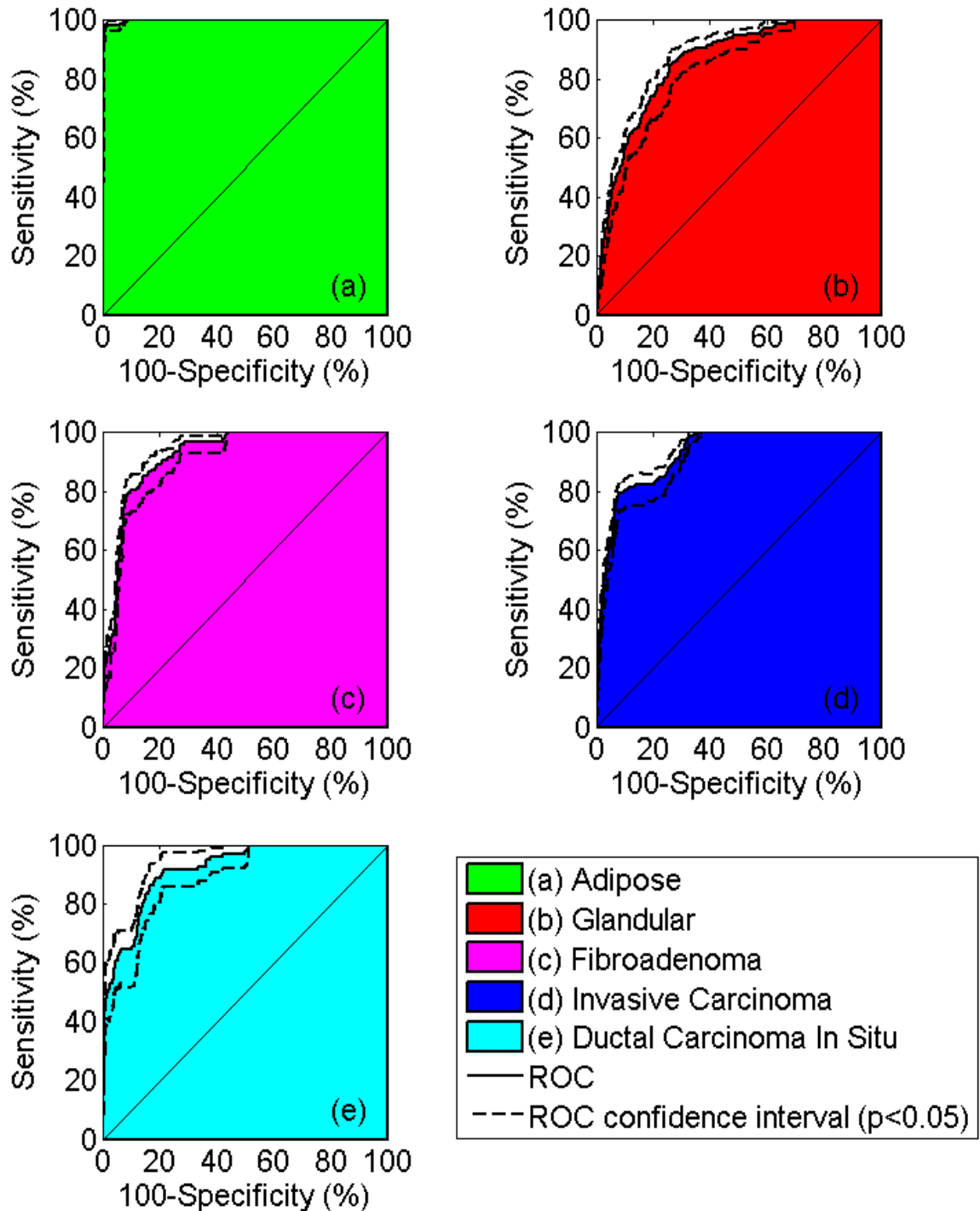

Figure 6. ROC curves (solid line) for classification of adipose (a), glandular (b), FA (c), IC (d), and DCIS (e) tissues including confidence intervals (dashed line) and corresponding AUC.

Corresponding area under curve (AUC) and PDM measures are summarized in Table 5. From the AUC values, the performance of the diagnosis can be classified into three categories with adipose as the best performance (AUC almost 100%), glandular as

the worst performance with AUC of 86% and FA, IC and DCIS as the median performance with comparable AUC values of roughly 92%. The PDM multiple classes overall performance of the diagnostic is 93.6%.

Table 5. AUC values of ROC curves for the five tissue types and PDM value.

Type of breast tissue	AUC	Confidence Interval
Adipose	99.8%	99.7%-99.9%
Glandular	85.9%	81.9%-87.9%
FA	92.3%	90.4%-94.1%
IC	92.5%	90.9%-94.0%
DCIS	91.8%	88.7%-93.4%
PDM for total AUC	93.6%	91.9%-94.9%

Table 6 summarizes the sensitivity-specificity obtained for classification of malignant versus non-malignant tissues by using various algorithms for classification. The obtained numbers are compared to what has already been reported by other studies from different research groups. The best algorithm performance applied to the data was reached with KNN classification whereas the poorest performance was reached with LDA classification.

Classification based on the CART method showed that discriminating adipose tissue based on the β-carotene values only yields to a sensitivity-specificity of 68%-92% whereas classification based on the lipid parameters yields to a sensitivity-specificity of 98%-99%. Using both parameters yielded a sensitivity-specificity of 99%-99%.

Table 6. Literature overview of diagnostic performance in discriminating malignant from non-malignant tissue and comparison of different classification algorithms applied to the data in the presented study.

Classification algorithm	Reference	Sens. (%)-Spec. (%)	Sens.-Spec. of this study (LOO)	Sens.-Spec. of this study (HO)
Artificial Neural Network	Bigio *et al.* [a]	69 – 85	89 – 98	91±2 – 96±4
K-Nearest Neighbor	Laughney *et al.*	90 – 77	96 – 99	94±4 – 98±2
Logistic Regression	Volynskaya *et al.*	100 – 100[b]	82 – 94	82±3 – 94±6
Logistic Regression	Keller *et al.* [a]	85 – 96[b]	82 – 94	82±3 – 94±6
Linear Support Vector Machine	Zhu *et al.*	83 – 87[b]	79 – 93	81±4 – 93±2
Non-Linear Support Vector Machine	-	-	90 – 97	88±4 – 97±2
Linear Discriminant Analysis	-	-	78 – 95	74±6 – 96±2
Classification And Regression Tree	-	-	88 – 93	85±6 – 92±3

[a] Sensitivity and specificity computed after classification of the spectra and not from the parameters derived from a fit-model.
[b] Fluorescence was also measured in these studies however the reported sensitivity-specificity corresponds to classification of parameters derived from diffuse optical spectroscopy only except for Keller *et al.*

4. Discussion

This study corresponds to the first in its kind that evaluates the classification of different types of breast tissue based on several parameters derived from spectroscopic data acquired from a wide wavelength range from 500 to 1600 nm. From Table 2, it is clear that adipose tissue is the easiest tissue that can be discriminated from the other types of tissue. More than seven parameters showed significant differences with lipid, water and β-carotene as main discriminators, as supported by other studies as well [9-22]. Glandular and DCIS tissues have the lowest amount of parameters that showed significant differences with other tissues. It is important to note that the use of *post hoc* Tukey's test is essential for reliable statistical test for significance of differences. If not used, additional parameters become significantly different between types of tissue. For example, lipid becomes significantly different between glandular and FA as well as IC if no *post hoc* test is performed. Moreover, glandular tissue has on average 5% lipid whereas FA and DCIS have below 0.5% lipid while still no significant differences are observed according to Tukey's test despite an order of magnitude difference in lipid content. Similarly to *ex vivo* [10, 11, 14] and *in vivo* [18, 22, 36] existing studies, we also observed a lower blood oxygenation level in malignant tissue compared to non-malignant tissue with significant differences (cf. Table 2 and Fig. 4). This is expected because malignant tissues are known to exhibit regions of hypoxia [36]. Although this observation corroborates with other existing *ex vivo* studies, this should be validated *in vivo* because the oxygenation level of the tissue can significantly change during and after tissue excision. Another interesting finding is that we observed comparable amounts of blood (0.3%) in malignant and non-malignant tissue similar to reported studies in literature. Yet on the contrary, Van Veen *et al.* [22] have reported a higher blood volume fraction in malignant tissue similarly to optical mammography studies that were conducted *in vivo* by Spinelli *et al.* on 190 patients from which 32 had cancer [37] and by Grosenick *et al.* on 154 patients with 87 carcinoma cases [38] (In Ref. 38, table 4 provides an overview on blood volume, oxygenation level, and reduced scattering properties of healthy and malignant tissue from various optical mammography studies available in literature). Among the malignant types of tissue, only DCIS exhibited larger amount of blood than the average value of blood in non-malignant tissues. An increase in blood volume fractions is a potential marker for angiogenesis. Yet again, the current study was performed *ex vivo* and an *in vivo* study is required to confirm this observation as shown by Van Veen *et al.* Furthermore, our data corroborates with the observation from other studies with respect to the reduced scattering amplitude. Indeed, the reduced scattering amplitude is higher in malignant tissue (8.1 cm^{-1}) than in non-malignant tissue (5.6 cm^{-1}). As expected, we observed that collagen volume fractions correlate with ρ. This is in agreements with findings of Saidi *et al.* [39] that the Rayleigh scattering in tissue is mainly due to sub-micron collagen fibers in the connective tissue suggesting a stronger Rayleigh contribution in glandular, IC and DCIS that contain the highest collagen volume fractions as depicted in Fig 4. Water content is the most prominent in IC and is significantly different from the other tissues (cf. Table 2). The lowest water volume fraction is obviously observed for adipose tissue since lipid contains almost no water. However collagen-rich stroma contains quite a lot of water as collagen fibers are

hydrophilic. Thus if a tumor induces a lot of stroma, the water content in the tumor will be relatively high as the fibers are loosely arranged leaving a lot of space for water molecules to intervene in the tumor. In breast tissue with benign sclerotic changes in which collagen gets cross-linked to a great extent, hardly any space is left for water molecules. Necrosis can also play a role in water increase but only a very small minority of all breast cancer contains necrotic areas in general. When investigating the differences in values of the different parameters within each patient instead of comparing tissue types from all the patients together, the *p*-values for discriminating a tissue from another becomes even smaller. Results of the spectral differences between different patients are to be presented in a future publication.

Multiple class classification with the CART algorithm demonstrated a very high overall diagnostic performance of 94% with the highest AUC value for adipose tissue and the lowest for glandular tissue as can be seen in the ROC curves in Fig. 6. In the study by Majumder *et al.*, glandular and adipose tissues were both classified as normal and discriminated with FA, IC and DCIS and obtained an overall classification performance of 88% using sparse multinomial LR on the diffuse reflectance spectra [15]. Our data showed better sensitivity-specificity for IC and DCIS (cf. Table 4) whereas FA showed similar performance. It is important to note that the amount of DCIS samples by Majumder *et al.* is rather small compared to the other tissues and therefore a low performance can be expected. Moreover, DCIS is not a common tissue measured by other groups (6, 2, and 1 samples measured by Majumder *et al.* [15], Zhu *et al.* [11], and Laughney *et al.* [17], respectively). It is recommended to acquire more spectra from a sample and to perform classification on the spectra in order not to bias the diagnosis by low numbers compared to other tissues.

For a better comparison of our results with existing literature studies, we have performed classification on our data using the techniques suggested in literature. Table 6 summarizes the classification algorithm used to discriminate malignant tissue (i.e. IC and DCIS) from non-malignant tissue (i.e. adipose, glandular and FA) and the table compares the reported sensitivity-specificity values as reported in literature with those obtained in our study. The sensitivity-specificity obtained with the same method for all categories of breast classification, i.e. the CART method, is 88%-93%. Compared to the results by Bigio *et al.*, ANN classification applied to our data showed better sensitivity-specificity. However, it is important to note that our classification was performed on the parameters derived from the spectra and not by applying the ANN classification to the spectra as done by Bigio *et al.* The KNN classification employing Mahalanobis distance metric to account for parameter intercorrelations, as used by Laughney *et al.*, showed the highest diagnostic performance. The sensitivity-specificity obtained with this method corresponds to a very high performance. One might question the classification method because the KNN algorithm can be biased since it is very sensitive to redundant or similar features because all features contribute to the similarity principle and thus to the classification. Using an LR based classification method showed a sensitivity-specificity of 82%-94% which is outperformed by the sensitivity-specificity of 100%-100% obtained by Volynskaya *et al.* However, it is important to note that the study by Volynskaya *et al.* did not include the 6 DCIS samples they measured because they considered it was a very

small number compared to the 9 IC, 9 FA, 31 normal and 55 fibrocystic change (FCC) samples they had measured. Keller *et al.* obtained a lower sensitivity but higher specificity compared to our result. It should be noted that they classified the spectra and not the parameters that were derived from the spectra. Moreover, they included fluorescence spectra to their classification scheme. Zhu *et al.* achieved a sensitivity-specificity of 83%-87% and 82±5%-89±5% using SVM classification with a LOO and HO cross-validation scheme, respectively. In our study, the sensitivity-specificity with linear SVM classification is 79%-93% and 81±4%-93±2% with a LOO and HO cross validation scheme, respectively. The data used for classification by Zhu *et al.* correspond to 89% of adipose tissue within the non-malignant category and 74% of IC among the malignant category. Therefore, the weight of classification is mainly dominated by adipose and IC for malignant and non-malignant tissue, respectively. In our study, 51% of the non-malignant samples correspond to adipose tissue and 71% of the malignant tissue samples correspond to IC. However, we have performed the classification by taking the same amount of spectra for each type of tissue within the malignant and non-malignant category in order to avoid an overrepresentation of adipose and IC within the non-malignant and malignant category, respectively. This can explain the fact that we observe a lower sensitivity than Zhu *et al.* However, we obtain a higher specificity suggesting that we can classify non-malignant tissue better thanks to the additional parameters derived from the fit-model. In case of non-linear SVM, i.e. using a Gaussian radial basis kernel function instead of a linear kernel, the performance of discriminating malignant tissue increased to a sensitivity-specificity of 82%-94%. As mentioned by Zhu *et al.* in a previous study [10], a classification based on linear algorithms could underperform in the diagnosis since the optical properties are non-linearly related in the description of the measured spectra, hence the better performance of the non-linear compared to the linear SVM algorithm applied to our data. Besides, for comparison with another non-linear classification method, a sensitivity-specificity of 78%-95% reached with LDA employing Mahalanobis distance yielded the lowest performance among the other classification methods with respect to specificity. From the various classification methods, large variations in sensitivity-specificity can be achieved and therefore care should be taken when comparing one's results with existing results in literature. The choice of the classification algorithm is very important and the sample sizes, the methods, and the linearity of the problem should be carefully taken into consideration. As a matter of fact, for classification problems with small sample size LDA is not suitable, as it is a parametric method assuming normal distribution of the data in each class. Other methods have the advantage of being non-parametric methods. However, KNN is very sensitive to redundant and similar features for classification. On the other hand, linear SVM finds linear separation of two classes in the training set with a hyperplane that has maximal distance from the two classes. If the groups are not linearly separable, non-linear SVM can be applied [40]. The LR algorithm is a probabilistic method that has the advantage of using few or no statistical assumptions but the drawback is that the complete data is needed for each class to calculate the probabilities. Hence large variations in sample sizes can bias the classification.

Among the studies quoted in Table 6, the study by Keller *et al.*, Majumder *et al.*, Zhu *et al.* and Volynskaya *et al.* performed fluorescence measurements. The latter two derived collagen and NADH concentrations from fitting the fluorescence spectra. Both studies showed a significant increase in collagen in malignant tissue compared to non-malignant tissue which correlates with our finding where we estimated collagen with diffuse reflectance spectroscopy measurements. Adding fluorescence to diffuse optical spectroscopy did not result in the same conclusions for the different studies. Volynskaya *et al.* showed a decrease in specificity from 100% to 96%, whereas Zhu *et al.* did not observe any differences in performance. Majumder *et al.* showed a tremendous improvement in discriminating the tumor types of tissue when adding fluorescence measurements to the classification routine increasing the overall diagnosis performance from 88% without fluorescence to 95% with fluorescence. Apart from fluorescence, Majumder *et al.* performed Raman spectroscopy measurements and showed that this optical tissue measurement technique yields to the best overall performance (99%). The group of biomedical photonics at MIT presented several Raman studies [41-44] showing that they can reach sensitivity-specificity of 83%-93% by classifying estimated parameters similar to those extracted from the measurements presented in this paper such as β-carotene, lipid, collagen as well as additional biological substances such as calcium, cholesterol, and cell nucleus. Interestingly, in comparison with the Raman results of the study conducted by the MIT group, the average collagen and fat fractions are reasonably similar for the different types of tissue except for adipose tissue where we estimate an average collagen content of 15%. In the latest study from the MIT group [42] the 20 spectra acquired from DCIS samples were not classified because this type of tissue was not encountered in the calibration data set they used for their diagnostic algorithm development. They do discuss nevertheless that applying their algorithm to the DCIS samples would result into 5 samples out of 20 to be classified as malignant based on classification of their estimated fat and collagen fractions derived from the fitted Raman spectra.

One final point of discussion concerns adipose tissue discrimination. Both lipid and β-carotene are adipose tissue precursors and only one of them was used in previous studies. In this paper, we estimate both chromophores and from classifying adipose tissue based on only one of the chromophores, it turned out that lipid is the best discriminator for adipose tissue with sensitivity-specificity of 98%-99% versus 68%-92% for β-carotene. It is known that β-carotene is significantly lower in smokers than non-smokers [45]. Thus, it can bias the discrimination of adipose tissue in breast depending whether a patient is a smoker or not, making lipid a more suitable discriminator.

5. Conclusion

We present the first breast diagnosis study based on estimating morphological, physiological and optical parameters derived from diffuse reflectance spectroscopy measurements on a 500 to 1600 nm wavelength range. Based on a classification and regression tree algorithm applied to the derived parameters, a sensitivity-specificity of 98%-99%, 84%-95%, 81%-98%, 91%-95%, and 83%-99% was obtained for discrimination of adipose, glandular, fibroadenoma, invasive carcinoma, and ductal

carcinoma *in situ*, respectively; and a multiple classes overall diagnostic performance of 94%. A comparison of different classification techniques to discriminate malignant and non-malignant tissue showed varying performance that can highly depend on the classification algorithm. Finally, to the best of our knowledge, given the fact this is the only study that estimates both β-carotene and lipid as adipose tissue precursor; we show that lipid is a much better discriminator with sensitivity–specificity of 98%-99% for lipid versus 68%-92% for β-carotene.

6. Acknowledgments

References

1. R. Ariga, K. Bloom, V. Reddy, L. Kluskens, D. Francescatti, K. Dowlat, P. Siziopikou, P. Gattuso, "Fine-needle aspiration of clinically suspicious palpable breast masses with histopathological correction", Am. J. Surg. **184**, 410-413 (2002)

2. R. Burns, J. Brown, S. Roe, L. Sprouse, A. Yancey, L. Whitherspoon, "Stereotactic core-needle breast biopsy by surgeons: minimum 2-year follow-up of benign lesions", Ann. Surg. **232**, 542-548 (2000)

3. B. Chaiwun, J. Settakorn, C. Ya-In, W. Wisedmongkol, S. Randaeng, P. Thorner, "Effectiveness of fine-needle aspiration cytology of breast: analysis of 2375 cases from northern Thaïland", Diagn. Cytopathol. **26**, 201-205 (2002)

4. R. Dameron, D. de Long, A. Fisher, D. de Long, L. Dodd, R. Nelson, "Indeterminate findings on imaging-guided biopsy: should additional intervention be pursued?", Am. J. Roentgenol. **173**, 461-464 (1999)

5. J. youk, E. Kim, L. Lee, and K. Oh, "Missed breast cancer at US-guided core needle biopsy: how to reduce them", Radiographics **27**, 79-94 (2007)

6. S. Willis, and I. Ramzy, "Analysis of false results in a series of 835 fine needle aspirates of breast lesions" Acta. Cytol. **39**, 858-864 (1995)

7. R. G. Pleijhuis, M. Graafland, J. De Vries, J. Bart, J. S. De Jong, and G. M. Van Dam, "Obtaining adequate surgical margins in breast-conserving therapy for patients with early-stage breast cancer: current modalities and future directions", Ann. Surg. Oncol. **16**, 2717-2730 (2009)

8. E. D. Kumiawan, M. H. Wong, I. Windle, A. Rose, A. Mou, M. Buchanan, J. P. Collins, J. A. Miller, R. L. Gruen, G. B. Mann, "Predictors of surgical margin status in breast-conserving surgery within a breast screening program", Ann. Surg. Oncol. **15**, 2542-2549 (2008)

9. I. J. Bigio, S. G. Bown, G. Briggs, C. Kelley, S. Lakhani, D. Pickard, P. M. Ripley, I. G. Rose, and C. Saunders, "Diagnosis of breast cancer using elastic-scattering spectroscopy: preliminary clinical results", J. Biomed. Opt. **5**, 221-228 (2000)

10. C. Zhu, G. Palmer, T. Breslin, J. Harter, and N. Ramanujam, "Diagnosis of breast cancer using diffuse reflectance spectroscopy: comparison of a Monte Carlo versus partial least squares analysis based feature extraction technique", Las. Surg. Med. **38**, 714-724 (2006)

11. C. Zhu, G. M. Palmer, T. M. Breslin, J. Harter, and N. Ramanujam, "Diagnosis of breast cancer using fluorescence and diffuse reflectance spectroscopy: a Monte-Carlo-modeled-based approach", J. Biomed. Opt. **13,** 034015 (2008)

12. C. Zhu, T. M. Breslin, J. Harter, and N. Ramanujam, "Model based and empirical spectral analysis for the diagnosis of breast cancer", Opt. Exp. **16,** 14961-14978 (2008)

13. T. M. Byldon, S. A. Kennedy, L. M. Richards, J. Q. Brown, B. Yu, M. K. Junker, J. Callagher, J. Geradts, L. G. Wilke, and N. Ramanujam, "Performance metrics

of an optical spectral imaging system for intra-operative assessment of breast tumor margins", Opt. Exp. **18**, 8058-8076 (2010)

14. Z. Volynskaya, A. S. Haka, K. L. Betchel, M. Fitzmaurice, R. Schenk, N. Wang, J. Nazemi, R. R. Dasari, and M. S. Feld, "Diagnosing breast cancer using diffuse reflectance spectroscopy and intrinsic fluorescence spectroscopy", J. Biomed. Opt. **13**, 024012 (2008)

15. S. K. Majumder, M. D. Keller, F. I. Boulos, M. C. Kelley, and A. Mahadevan-Jansen, "Comparison of autofluorescence, diffuse reflectance, and Raman spectroscopy for breast tissue discrimination", J. Biomed. Opt. **13**, 054009 (2008)

16. M. D. Keller, S. K. Majumder, M. C. Kelley, I. M. Meszoely, F. I. Boulos, G. M. Olivares, and A. Mahadevan-Jansen, "Autofluorescence and diffuse reflectance spectroscopy and spectral imaging for breast surgical margin analysis", Las. Surg. Med. **42**, 15-23 (2010)

17. A. M. Laughney, V. Krishnaswamy, P. B. Garcia-Allende, O. M. Conde, W. A. Wells, K. D. Paulsen, B. W. Pogue, "Automated classification of breast pathology using local measures of broadband light", J. Biomed. Opt. **15**, 066019 (2010)

18. A. E. Cerussi, N. Shah, D. Hsiang, A. Durkin, J. Butler and B. J. Tromberg, "*In vivo* absorption, scattering of 58 malignant breast tumors determined by broadband diffuse optical spectroscopy", J. Bio. Opt. **11**(4), 044005 (2006)

19. P. Taroni, D. Comelli, A. Pifferi, A. Torricelli, and R. Cubeddu, "Absorption of collagen: effects on the estimate of breast composition and related diagnostic implications", J. Biomed. Opt. **12**, 014021 (2007)

20. P. Taroni, A. Bassi, D. Comelli, A. Farina, R. Cubeddu, and A. Pifferi, "Diffuse optical spectroscopy of breast tissue extended to 1100 nm", J. Biomed. Opt. **14**, 054030 (2009)

21. P. Taroni, A. Pifferi, G. Quarto, L. Spinelli, A. Torricelli, F. Abbate, A. Villa, N. Balestreri, S. Menna, E. Cassano, and R. Cubeddu, "Noninvasive assessment of breast cancer risk using time-resolved diffuse optical spectroscopy", J. Biomed. Opt. **15**, 060501 (2010)

22. R. L. P. van Veen, A. Amelink, M. Menke-Pluymers, C. van der Pol, and H. J. C. M. Sterenborg, "Optical biopsy of breast tissue using differential path-length spectroscopy", Phys. Med. Biol. **50**, 2573-2581 (2005)

23. R. Nachabe, B. H. W. Hendriks, A. E. Desjardins, M. van der Voort, and H. J. C. M. Sterenborg, "Estimation of lipid and water concentrations in scattering media with diffuse optical spectroscopy from 900 to 1600 nm", J. biomed. Opt. **15**, 037015 (2010)

24. R. Nachabe, B. H. W. Hendriks, M. van der Voort, A. E. Desjardins, and H. J. C. M. Sterenborg, "Estimation of biological chromophores using diffuse optical spectroscopy: benefit of extending the UV-VIS wavelength range to include 1000 to 1600 nm", Biomed. Opt. Exp. **1**, 1432-1442 (2010)

25. F. Provost and P. Domingos, "Well-trained PETs: improving probability estimation trees", CeDER Working Paper #IS-00-04, Stern School of Business, New York University, NY, NY 10012 (2000)

26. R. Nachabe, D. Evers, B. H. W. Hendriks, G. W. Lucassen, M. Van der Voort, J. Wesseling, and T. J. Ruers, "Effect of bile absorption coefficients on the estimation of liver tissue optical properties and related implications in discriminating healthy from tumorous samples", Biomed. Opt. Exp. **2**, 600-614 (2011)

27. T. J. Farrell, M. S. Patterson, and B. Wilson, "A diffusion theory model of spatially resolved, steady-state diffuse reflectance for the non-invasive determination of tissue optical properties", Med. Phys. **19**, 879-888 (1992)

28. W. Verkruysse, G. W. Lucassen, J. F. de Boer, D. J. Smithies, J. S. Nelson, and M. J. C. van Gemert, "Modeling light distributions of homogenous versus discrete absorbers in light irradiated turbid media", Phys. Med. Biol. **42**, 51-65 (1997)

29. W. G. Zijlstra, A. Buursma, and O. W. van Assendelft, *Visible and near infrared absorption spectra of human and animal haemoglobin*, VSP Publishing, Utrecht, The Netherlands (2000)

30. S. W. van de Poll, *Raman spectroscopy of atherosclerosis PhD thesis,* University of Leiden, ISBN 90-9016109-0 (2003)

31. C. L. Tsai, J. C. Chen, and W. J. Wang, "Near-infrared absorption property of biological soft tissue constituents", J. Med. Bio. Eng. **21**, 7-14 (2001)

32. A. S. Nunez, *A physical model of human skin and its application for search and rescue,* Air Force Institute of Technology, Ohio, USA (2009)

33. A. Amelink, D. J. Robinson, and H. J. C. M. Sterenborg, "Confidence interval on fit parameters derived from optical reflectance spectroscopy measurements", J. Biomed. Opt. **13**, 054044 (2008)

34. H. Motulsky. *Intuitive biostatistics: a nonmathematical guide to statistical thinking.* Oxford University Press, USA (2010)

35. L. Breiman. *Classification and regression trees.* Wadsworth International group, Belmont, USA (1984)

36. J. Q. Brown, L. G. Wilke, J. Geradts, S. A. Kennedy, G. M. Palmer, and N. Ramanujam, "Quantitative optical spectroscopy: a robust tool for direct measurement of breast cancer vascular oxygenation and total hemoglobin content *in vivo*", Cancer Res. **69**, 2919-2926 (2009)

37. L. Spinelli, A. Torricelli, A. Pifferi, P. Taroni, G. Danesini, and R. Cubeddu, "Characterization of female breast lesions from multi-wavelength time-resolved optical mammography", Phys. Med. Biol. **50**, 2489-2502 (2005).

38. D. Grosenick, H. Wabnitz, K. T. Moesta, J. Mucke, P. M. Schlag, and H. Rinneberg, "Time-Domain scanning optical mammography: II. Optical properties and tissue parameters of 87 carcinomas". Phys. Med. Biol. **50**, 2451-2468 (2005).

39. I. S. Saidi, S. L. Jacques, and F. K. Tittel, "Mie and Rayleigh modeling of visible-light scattering in neonatal skin", Appl. Opt. **34**, 7410-7418 (1995)

40. T. Hastie, R. Tibshirani, and J. H. Friedman. *The elements of statistical learning: data mining, inference, and prediction.* Springer, New York (2001)

41. K. E. Shafer-Peltier, A. S. Haka, M. Fitzmaurice, J. Crowe, J. Myles, R. R. Dasari, and M. S. Feld, "Raman microspectroscopic model of human breast tissue:

implications for breast cancer diagnosis *in vivo*", J. Raman Spectroscopy **33**, 552-563 (2002)

42. A. S. Haka, K. E. Shafer-Peltier, M. Fitzmaurice, J. Crowe, R. R. Dasari, and M. S. Feld, "Diagnosing breast cancer by using Raman spectroscopy", Pro. Nat. Acad. Sci. **102**, 3317-3322 (2005)

43. A. S. Haka, Z. Volynskaya, J. A. Gardecki, J. Nazemi, J. Lyons, D. Hicks, M. Fitzmaurice, R. R. Dasari, J. P. Crowe, and M. S. Feld, "*In vivo* margin assessment during partial mastectomy breast surgery using Raman spectroscopy", Cancer Res. **66**, 12371-12376 (2006)

44. A. S. Haka, Z. Volynskaya, J. A. Gardecki, J. Nazemi, R. Shenk, N. Wang, R. R. Dasari, M. Fitzmaurice, and M. S. Feld, "Diagnosing breast cancer using Raman spectroscopy: prospective analysis", J. Biomed. Opt. **14**, 054023 (2009)

45. R. M. Russel, "Beta-carotene and lung cancer", Pure Appl. Chem. **74**, 1461-1467 (2002)

Chapter 9

Accurate tissue analysis of the breast with diffuse reflectance spectroscopy through an individualized approach

Daniel J. Evers

Rami Nachabé

Marie-Jeanne Vrancken Peeters

Jos A. van der Hage

Hesters S. Oldenburg

Emiel J. Rutgers

Gerald W. Lucassen

Benno H. W. Hendriks

Jelle Wesseling

Theo J. M. Ruers

Abstract

Background. Optical spectroscopy is increasingly used in breast tissue analysis. Despite years of research, final steps towards clinical application of optical spectroscopy are yet to be taken. One of the reasons for current inability for clinical application could be the continuously executed collective data analysis methods in combination with significant inter-patient breast tissue variations. An individualised approach for optical spectroscopy analysis in breast tissue could improve discrimination accuracy towards a future clinical application of this technique.

Methods. Breast tissue from 47 patients was included for an *ex-vivo* analysis with Diffuse Reflectance Spectroscopy (DRS). The measured optical spectra from all patients collectively and individually were analyzed.

Results. Collective patient data analysis for discrimination between normal and malignant breast tissue yielded sensitivity and specificity of 90% and 88%, respectively whereas individual patient data analysis improved discrimination accuracy to 100% for 31patients.

Conclusions. Individual patient discrimination of tumor tissue from normal tissue displayed improved accuracy between normal and malignant breast tissue. These results support further validation on an individual patient analysis and direct towards *in-vivo* application of DRS in clinical practice for diagnostic procedures in breast tissue.

1. Introduction

In the last decade new optical guidance techniques are increasingly being implemented into medical practice of cancer, rapidly evolving standard protocol and treatment strategies [1, 2]. One of these new optical techniques is *Diffuse Reflectance Spectroscopy* (DRS) [3-5]. DRS has the potential of differentiating biological structures and compositions by their intrinsic light absorption characteristics which varies with wavelength. It can provide detailed information of the underlying biological composition of tissue. DRS consists of recording the spectral response of tissue illuminated with light which is partially absorbed by endogenous chromophores as well as scattered by the various cells and fibers along its path towards a detection unit. Depending on the tissue composition and its structure, a specific spectral pattern is acquired from which the biological composition related to light absorption and tissue density related to light scattering are both recovered via well-established mathematical model that describes the spectral measurement [4]. By allowing specific differentiation between tissues, the technique has the potential to be incorporated into optical tools for cancer diagnosis and therapy.

One considered application for DRS that could improve clinical practice of breast cancer in the near future are the optical guided tissue biopsy. Current figures on repeated breast tissue biopsies due to indeterminate pathology analysis range from 5 to 30% [6-9].

Breast tissue can arguably be considered one of the most challenging human tissue types due to the general inhomogeneity of the morphology within both normal and malignant breast tissue [10]. Normal breast tissue composition is largely influenced by due age and hormonal status of the individual. Therefore, tissue analysis with DRS to discriminate tissue types based on the derived parameters from the measurements can be expected to be hampered by this diversity of tissue and inter-patient variation. Several groups have focussed on breast tissue discrimination with DRS [5, 11-17]. Presented results of discriminative accuracy based on analysis between normal and malignant breast tissue in these papers ranged between 65% and 90%. These results have not yet resulted in the development of optical spectroscopic guided instruments for use in clinical practice.

We believe that inter-patient variation within breast morphology hampers the discriminative accuracy as currently used and an important next step towards the application of optical techniques like DRS within clinical cancer is to focus on the development and optimization of individual patient analysis methods. Hence, with regards to the diagnostic accuracy between different tissues of any medical instrument used in clinical practice, the main interest of any physician will be the discriminative accuracy within any individual patient. Such an approach is already common practice in various imaging modalities like X-ray, CT, MRI or Ultrasound where malignant tissue is compared to normal tissue within an individual patient. This should also be considered as an important requirement for the introduction of any optical spectroscopy system for clinical use.

In a previous study, we published results of the development and validation of a novel Diffuse Reflectance Spectroscopy system combining detection of visible (VIS) and near-infrared (NIR) light spectra that enables DRS measurements on a very wide

wavelength range from 500 to 1600 nm [18, 19]. The aim of this present study is to confirm the hypothesis that the discriminative value of an individual analysis approach of breast tissue using DRS is an important step towards the development of intelligent medical tools such as an optical biopsy needle.

2. Materials and methods
2.1 Clinical study design

This study was conducted at The Netherlands Cancer Institute (NKI-AVL) under approval of the internal review board committee. Breast tissue was obtained from 47 female patients who had undergone either a local excision or total mastectomy of the breast due to the presence of a fibroadenoma or (pre)-malignant disease. Shortly after surgical resection, tissue was transported to the pathology department for optical spectroscopy analysis. After gross inspection by the pathologist, the spectroscopy measurements were performed on freshly excised tissue within two hours after resection. The optical spectra were collected from macroscopic normal fat, glandular tissue samples and fibroadenoma lesions as well as from (pre)-malignant tissue samples. On average, five optical measurements were performed at each measurement location. Subsequently, a biopsy of the measured tissue location was performed. These tissue samples were then fixated in formalin, paraffin-embedded, cut in 2- to 3-μm-thick sections and stained with standard hematoxylin/eosin staining. An experienced pathologist, who was blinded for the outcome of the spectroscopy analysis, examined the histological slides. For each measurement location, the percentages of adipose, glandular and fibroadenomatous tissue as well as ductal carcinoma in-situ (DCIS) and invasive carcinoma were respectively scored if present in the two dimensional image of the slide. Within the 47 resected tissue specimen, 160 measurements were performed in 11 fibroadenomatous lesions, 121 measurements in 11 areas of DCIS and 314 measurements in 35 lesions of Invasive carcinoma. Five of these lesions were lobular carcinomas and 30 were ductal carcinomas. A total of 294 measurements in adipose tissue of the breast specimen and 184 measurements in glandular tissue were performed. In total, 1073 DRS measurements were acquired.

2.2 Instrumentation

The instrumentation and calibration procedure of our optical spectroscopy system has been described in recent papers [18-20].

The system consists of a console comprising a Tungsten/Halogen broadband light source, two spectrometers and an optical probe with three optical fibers. The two spectrometers resolve light in the visible wavelength range between 400 nm and 1100 nm (Andor Technology, DU420A-BRDD) and in the near infrared wavelength range from 800 up to 1700 nm (Andor Technology, DU492A-1.7), respectively. The optical probe contains three optical fibers: one fiber is connected to the light source, while the other two fibers are connected to the spectrometers to capture the diffusely scattered light from the tissue. The average tissue volume that is illuminated is roughly 5 mm^3. The acquisition time of each spectrum was on average one second.

2.3 Spectral data processing

Five different breast tissue classes were distinguished in the spectral data processing: adipose tissue, glandular tissue, fibroadenoma, DCIS and invasive carcinoma. Additionally, we distinguished *normal breast tissue* (all tissue locations of adipose, glandular and fibroadenomatous tissue) from *malignant breast tissue* (DCIS and invasive carcinoma). An analytical model was used to estimate the various chromophore volume fractions and scattering coefficients from all the acquired spectroscopy measurements. This model was first described by Farrell *et al.* [21] The model has been further modified and validated to be applicable to human tissue samples [12, 19, 20, 22, 23]. Diffuse reflectance spectra acquired from the tissue were fitted and analyzed over the wavelength range from 500 to 1600 nm. The measurements are fitted with the analytical model by applying a non-linear Levenberg-Marquardt inversion algorithm. By fitting the model to the measured spectra, several parameters are derived such as total hemoglobin concentration (the sum of oxygenated and deoxygenated hemoglobin), water, lipid, collagen volume fractions, and β-carotene as well as the scattering amplitude at 800 nm wavelength. Light in the wavelength range between 500 and 1000 nm is mainly subject to absorption due to presence of hemoglobin and β-carotene in the probed volume; whereas for higher wavelength range it is due to presence of water, lipid and collagen [20]. The scattering of light is dependent on the cellular structure of the target tissue and is sensitive to the size and the density of cellular and subcellular structures. Spectral characteristics analysis was performed with a Matlab software package (MathWorks Inc., Natick, MA). The distribution of the quantified values of each tissue parameter was displayed in boxplots.
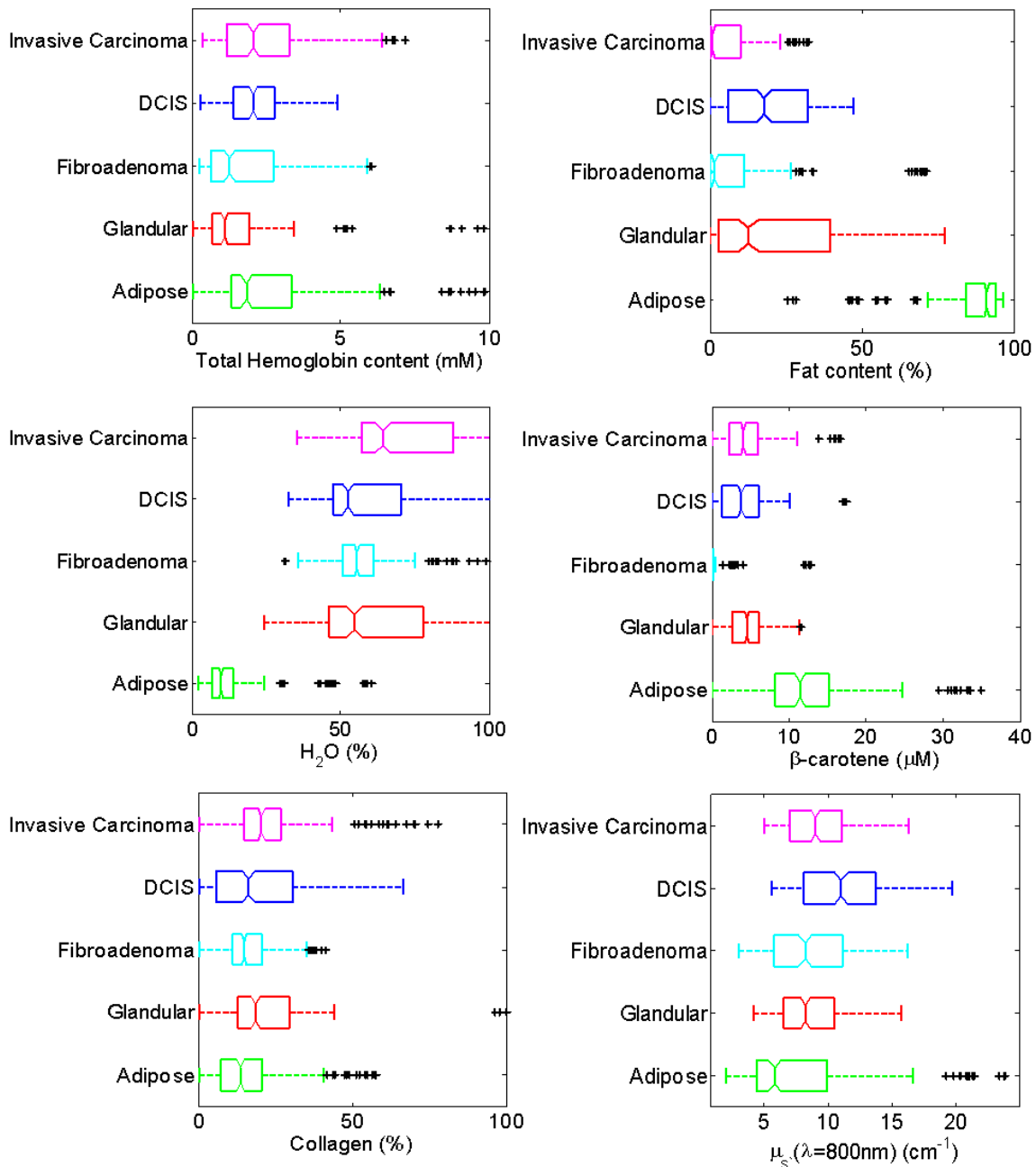
Figure 1. Boxplots of most significantly different tissue parameters. DCIS = ductal carcinoma in-situ; $\mu_{s'}$ = scattering at 800nm.

2.4 Tissue classification analysis

In the spectral data processing, breast tissue was categorized into the five defined tissue classes and also as two groups either as normal liver tissue or as tumor tissue. A Classification And Regression Tree (CART) algorithm was used to automatically classify each collected tissue into one of the defined breast tissue types based on the parameters derived from the measurements [24]. With the CART algorithm, a decision tree is created based on the five most significantly different tissue chromophores and scattering parameters using a leave-one-out (LOO) cross validation scheme. Each spectrum is separately classified based on the calculated thresholds in the decision tree and

subsequently compared to the histology analysis and presented in terms of sensitivity and specificity. The CART analysis was performed for all acquired data collectively and also for each included patient individually in which both normal breast tissue and (pre)malignant tissue was measured. It must be noted that the classification between normal breast tissue and malignant breast tissue was performed taking the amount of samples that corresponds to the tissue class with the lowest sample size in both groups. This was done to avoid overestimation of the discrimination accuracy due to the higher representation of one of the tissue classes over the other within either the normal or malignant tissue group. Within the normal breast tissue group, 160 tissue measurements of both adipose and glandular tissue were randomly selected and added to the corresponding to the number of fibroadenomatous tissue measurements. For the malignant tissue measurements, 120 invasive carcinoma tissue measurements were randomly selected.

Previously, the CART analysis with LOO cross validation scheme was studied by Nachabé *et al.* in the only published comparison to other generally used spectral classification algorithms [20]. The main advantage of the CART method is that the results can easily be interpreted and correlated to clinical details, since the input parameters are thresholds of the calculated values of the main tissue parameters.

2.5 Statistical analysis

The DRS-estimated quantification of each parameter in the breast tissue classes cannot be described by a parametric distribution such as the Gaussian distribution. The statistical differences of each parameter in the defined tissue classes were therefore determined using the non-parametric Kruskal-Wallis test [25]. P-values smaller than 0.05 were considered statistically significant.

3. Results

A total of 47 breast tissue specimens from female patients were included into this study. The mean age at time of operation was 52 years (range 20 – 74 years).

3.1 Cohort data analysis

Chromophore volume fractions and scattering coefficients from each of the tissue parameters were calculated from each tissue measurement using the analytical model. The distributions of each of the six most significantly different tissue parameters for each of the five distinguished tissue classes are depicted in Figure 1. Adipose tissue is best distinguished from the other tissue classes by fat,water , and β-carotene content, as well as by the scattering coefficient at 800 nm. Fibroadenomatous tissue is best discriminated from the other five tissue classes based fat and β-carotene. Each measurement was diagnosed using the CART algorithm to predict for each measurement to which of the five defined tissue classes it belongs and to classify it either as normal breast tissue or malignant breast tissue after comparison with the histology diagnosis. The results of the five class distribution of the analysis results are displayed in Table 1.

Table 1. Diagnosis for each tissue measurement generated by the DRS analysis compared to the histology diagnosis of the measurement location with the calculated sensitivity and specificity of all the measurements in each tissue class.

| Type of breast tissue (number of samples) | DRS classification diagnosis | | | | |
| | Malignant | | | Non-Malignant | |
	Invasive carcinoma	DCIS	FA	Glandular tissue	Adipose tissue
Invasive carcinoma (314)	**268**	17	6	23	0
DCIS (121)	22	**86**	1	12	0
FA (160)	13	5	**132**	10	0
Glandular tissue (184)	24	12	7	**141**	0
Adipose tissue (294)	9	6	0	10	**269**
Sensitivity(%)-Specificity (%)	85-90	71-95	83-98	77-93	91-100

A high specificity (≥90%) for all tissue classes was noted. Adipose tissue is the best distinguishable tissue from the rest and there is a notable overlap in diagnosis between glandular tissue and DCIS resulting in the lowest sensitivity rates. The result of discrimination between normal and malignant breast tissue samples is displayed in Table 2. After random selection of the tissue classes within both groups to fit the amount of measurements of the tissue class with the lowest sample size, the comparison of DRS to the pathology diagnosis yielded a sensitivity of 90% and a specificity of 88%.

Table 2. Classification of tissue measurements defined as normal or as malignant breast tissue.

Pathology (number of samples)	Malignant tissue	Normal tissue
Malignant tissue (N=242)	219	23
Normal tissue (N=480)	59	421
Sensitivity of 90% and specificity of 88%		

The microscopic heterogeneity of the various tissue samples is illustrated in Figure 2. Three examples of invasive carcinoma are displayed with different percentages of malignant tissue within the specimen, respectively classified by the pathologist as 20%, 50% and >90% invasive carcinoma within the tissue sample. The corresponding measured spectrum for each sample displays notable differences when compared. It is to be expected that these differences in histology and corresponding spectra will contribute to the difficulties distinguishing mainly glandular tissue from DCIS and invasive carcinoma, which were noted in Figure 1. We therefore divided all of the 314 measurements of invasive carcinoma into <50% or >50% malignant cells within the tissue specimen based on the individual pathology reports and compared these two groups to all measurements of glandular tissue.
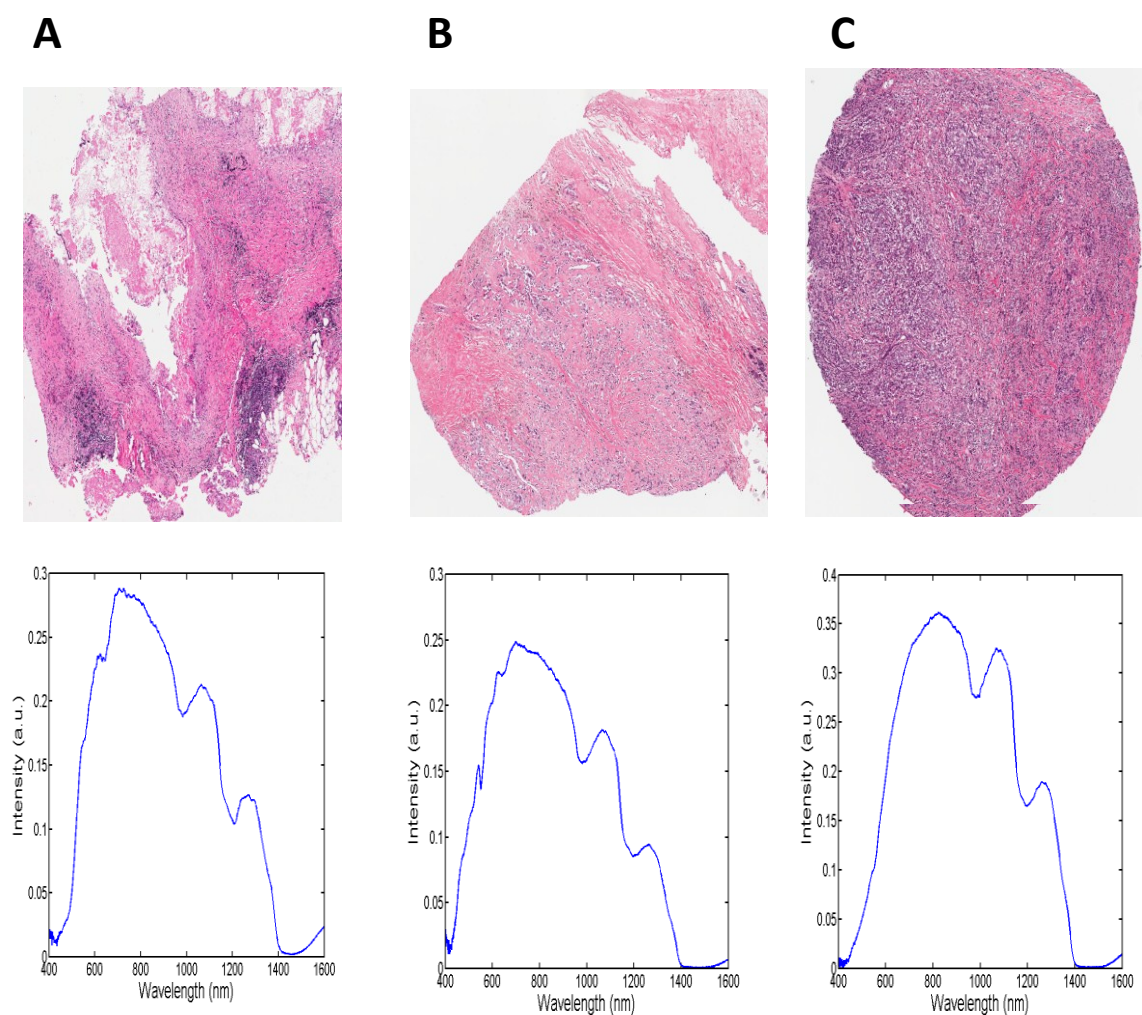

Figure 2. Example of the pathological heterogeneity within several tissue samples defined as 20% (A), 50% (B), and 90% (C) invasive carcinoma, respectively.

The results of the differences in significance of the quantification of most notable tissue parameters in the two malignant groups compared to glandular tissue are displayed in table 3. Both malignant groups can be discriminated from glandular tissue based on the parameters THC and fat. For the parameters scattering at 800nm, β-carotene and collagen

no significant differences are illustrated when the percentage of invasive carcinoma within the tissue specimen is < 50%, but are apparent for ratios of invasive carcinoma > 50%.

Table 3. Significant differences of the quantification of the most notable tissue parameters of all invasive carcinoma measurements with either <50% or >50% malignant cells within each tissue specimen compared to glandular tissue measurements. ~: Tissue parameter not significantly different when comparing glandular tissue with invasive carcinoma; ↑/↓ : tissue parameter respectively higher and lower in the invasive carcinoma compared to glandular tissue with a P-value < 0.05; ↑↑/↓↓ : tissue parameter respectively higher and lower in the invasive carcinoma compared to glandular tissue with a P-value < 0.0005.

Parameter	Invasive carcinoma 0-50%	Invasive carcinoma 50-100%
Total hemoglobin	↑↑	↑↑
Fat	↓↓	↓↓
β-carotene	~	↓
Collagen	~	↑↑
Scattering amplitude	~	↑↑

3.2 Individual data analysis

Discrimination between the classified tissue classes was also performed for each patient individually, with emphasis on the discrimination between normal and malignant breast tissue. In one of the 47 tissue specimen, all five defined tissue classes were present and could be examined. Results of the tissue and spectral analysis are displayed in Figure 3.
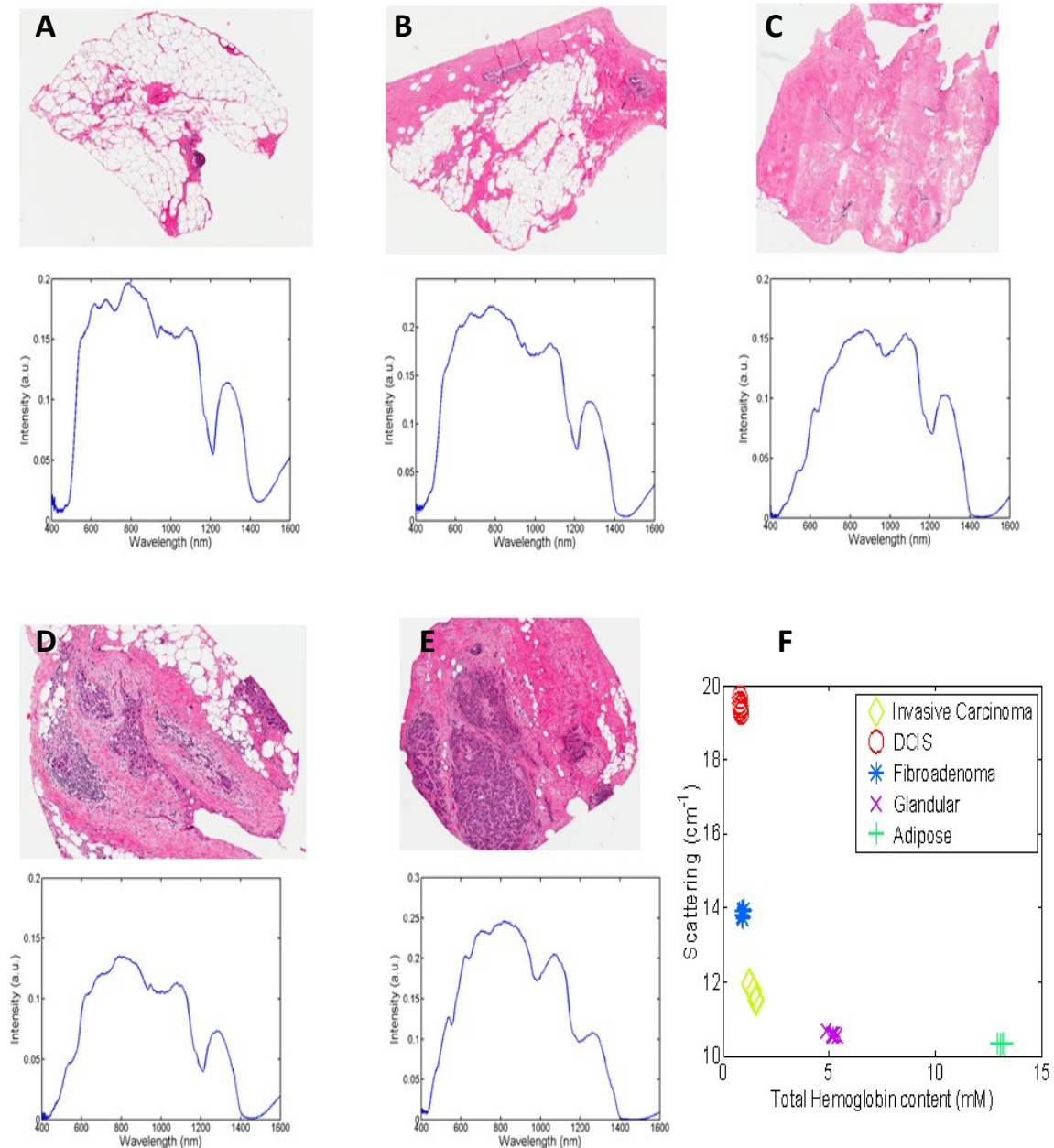
Figure 3. H&E staining of the five different tissue classes within one single patient specimen i.e. adipose tissue (A), glandular tissue (B), fibroadenomatous tissue (C), DCIS (D), and invasive carcinoma (e) including the corresponding spectra. The distribution of all the measurements for each defined tissue class based on the quantification of scattering at 800nm and total hemoglobin content is also illustrated (F).

For each tissue sample, a marked heterogeneity of the histology is notable. These variations can be expected to contribute to difficulty in the classification when a cohort of patients is examined. For each tissue class, the acquired optical spectrum is displayed as well as the scattering coefficient at 800nm wavelength versus the total haemoglobin content (THC) is plotted. When comparing the five tissue classes for this individual patient based on these two parameters (Figure 3F), the five classes can simply be discriminated from each other. Results of all performed measurements and the

discriminative accuracy between normal and malignant breast tissue on an individual basis are displayed in Table 4.

Table 4. Results of the discriminative accuracy between normal and malignant tissue measurements for each patient in which both groups were present.

Patient	Adipose	Glandular	FA	DCIS	Invasive	Sens.	Spec.
1	10	-	-	5	-	100	100
2	-	-	10	-	-	-	-
3	5	4	-	10	10	100	96
4	5	-	20	-	-	-	-
5	5	9	-	-	9	100	100
6	-	10	-	8	-	86	100
7	-	4	-	-	20	100	100
8	-	10	-	-	5	76	100
9	5	4	-	-	10	100	100
10	5	-	-	-	10	100	100
11	-	-	28	-	-	-	-
12	8	-	25	-	-	-	-
13	5	-	-	21	-	100	100
14	4	-	-	-	20	100	100
15	5	-	-	-	10	100	100
16	8	5	-	-	19	100	100
17	10	-	-	-	7	100	100
18	5	9	-	-	10	100	100
19	10	-	-	-	10	100	100
20	9	-	10	-	-	-	-
21	-	-	24	-	-	-	-
22	10	-	-	14	-	100	100
23	5	-	-	-	10	100	100
24	9	9	-	-	19	100	100
25	10	5	-	14	-	100	100
26	10	-	-	4	10	100	100
27	10	10	-	20	-	92	100
28	10	10	-	-	10	100	100
29	10	-	-	-	10	100	100
30	4	-	10	-	-	-	-
31	5	-	-	-	15	100	100
32	10	10	-	-	10	100	100
33	5	10	-	-	5	100	100
34	6	5	5	5	5	100	100
35	4	10	-	-	5	100	100
36	10	10	-	10	10	100	100
37	5	5	-	-	-	-	-
38	5	-	-	10	10	100	100
39	5	4	8	-	-	-	-
40	5	-	5	-	-	-	-
41	5	5	-	-	5	100	100
42	5	5	-	-	5	100	100
43	10	-	-	-	10	100	100
44	5	5	-	-	10	100	100
45	10	7	-	-	10	90	94
46	8	9	-	-	15	100	100
47	14	10	15	-	-	-	-
Total	**294**	**184**	**160**	**121**	**314**	**-**	**-**

4. Discussion

The implementation of optical technologies within clinical cancer is increasingly being explored [1-5]. For the approach to the clinical application of these new technologies within the diagnosis and treatment of breast malignancies, the heterogeneity of this human tissue must be considered. This heterogeneity is apparent on the histological slides of the tissue measurement locations displayed in Figures 2 and 3. Moreover, one must keep in mind that with DRS, one is comparing the optical characteristics of a tissue volume of several mm^3 to the histological characteristics of a tissue sample of 5 μm thickness typically. In this study of *ex-vivo* breast tissue we examined 47 specimens exploring the hypothesis that an individual approach to breast tissue analysis would enhance the discriminative accuracy between normal and malignant tissue and could therefore be an important step towards incorporation of DRS within clinical practice of breast cancer.

The histological heterogeneity depicted in Figures 2 and 3 is also apparent in the results of the quantification of several tissue parameters illustrated in Figure 1. When we distinguished between five different tissue classes, the boxplots clearly displayed a notable distribution range of most of the measurable optical parameters within the different tissue classes for measurements in multiple breast tissue locations. Adipose and fibroadenomatous tissue can be well differentiated from the other three tissue classes, yet the discrimination of glandular tissue from DCIS and invasive carcinoma is not so straightforward. The overall discrimination accuracy of DRS distinguishing 5 tissue classes was 82%. Sensitivity and specificity for each of the tissue classes ranged between 71% and 91% and between 90% and 100%, respectively. When we compared the combined measurements of normal and benign breast tissue to both malignant breast tissue classes the sensitivity was 90% and specificity 88%. These figures are conform best published figures in previous papers of DRS analysis in breast tissue [5, 13, 15, 16, 26, 27].

A more detailed analysis of the results in Figure 1 and Table 1 reveals the main discriminating difficulty between glandular tissue, DCIS and invasive carcinoma with a notable overlap in the quantification of the tissue parameters. This has been reported by Volynskaya *et al.* [12] with no significant differences in collagen and β-carotene in these tissue classes and by Zhu *et al.* [5] with similar concentrations in β-carotene and THC. We demonstrated a main discriminative factor to be the scattering at 800nm. Overall scattering has been previously published to be an important discriminative factor [5, 10].

These results can be explained when taking into mind that primary malignant degeneration in the breast is generally a gradual evolution of glandular tissue to carcinoma *in-situ* to an invasive carcinoma and that an important part of the composition of all three tissue classes will be fibro-vascular matrix with possible adipose component, it is not surprising that these tissues are not easily discriminated. Moreover, the presence of micro-calcifications in carcinoma *in-situ* areas and irregularly shaped and ordered cancerous cells in invasive carcinoma lesions is expected to cause notable scattering variations. The differences in composition between various cancerous lesions are displayed in Figure 2 and depending on the proportion of malignant cells within the measured specimen the different tissue parameters will be more or less significantly

different from normal glandular tissue as is demonstrated in Table 3. Finally, the age of the patients included into this study ranged from 20 to 74. The differences in menopausal status and composition of the normal breast structure between these patients would be expected to differ remarkably.

Notable improvement in the discrimination accuracy is displayed in the Figure 3 and Table 4. In one of the tissue specimen included in this study, all five distinguished tissue classes could be examined (Figure 3 and patient 34 in Table 4). Within the tissue samples of this single patient an inhomogeneous histology is apparent with various percentages of normal and malignant tissue types within each sample. From the DRS spectrum we selectively extracted the scattering coefficient at 800nm and THC. We subsequently compared the five different tissue classes based on these two tissue parameters (Figure 3F) and demonstrated in this analysis that each of the five tissue classes can easily be distinguished from the others. Moreover, the figures display a notably small variation of the two parameters within each tissue class. The discriminative accuracy of this individual analysis was 100% as displayed in Table 4. For each patient in which both normal breast tissue as malignant tissue was measured (N=36 patients), we performed a comparable individual discriminative analysis (Table 4). For 31 of these patients the discriminative accuracy of this individual analysis was 100%. The analysis of two of the patients revealed a sensitivity which was inferior to the collective analysis.

When we translate these results on individual analysis to clinical practice of tissue biopsy the main objective for correct localisation of the needle within the target lesion is accurate identification of malignant tissue from normal tissue. High specificity of the optical modality is therefore the most important parameter. Hence, the higher the specificity, the lesser indeterminate results can be expected. An indeterminate biopsy is defined as a biopsy which was thought to be taken from the target lesion, but cannot be characterized as malignant tissue by the pathologist. With an individual patient tissue analysis we displayed a specificity which was minimally 94% and in all but two patients was 100%. We therefore conclude that individual tissue analysis with DRS is superior to a collective data analysis and could enhance the accuracy in breast tissue biopsy when included into a biopsy needle.

5. Conclusion

Diffuse reflectance spectroscopy is considered as an important new optical sensing technique that could improve on various aspects of clinical practice in cancer in the near future. Based on the results presented in this paper, we conclude that the analysis of optical characteristics of different tissue classes within an organ of a single patient is superior to an analysis using the results of a cohort data analysis. We argue that for future application of DRS into clinical practice such as breast tissue biopsy, emphasis should therefore be put on individual tissue analysis. As a next step towards a clinical application we aim to confirm these results in an *in-vivo* setting.

References

1. Gioux S, Choi H, Frangioni J. Image-guided surgery using invisible near-infrared light: fundamentals of clinical translation. Mol Imaging 2010; 9: 237-255.

2. Keereweer S, Kerrebijn J, van Driel P et al. Optical image-guided surgery--where do we stand? Mol Imaging Biol. 2011; 13: 199-207.

3. Brown J, Vishwanath K, Palmer G, Ramanujam N. Advances in quantitative UV-visible spectroscopy for clinical and pre-clinical application in cancer. Curr Opin Biotechnol 2009; 20 119-131.

4. Sćepanović O, Volynskaya Z, Kong C et al. A multimodal spectroscopy system for real-time disease diagnosis. Rev Sci Instrum 2009; 80: 043103.

5. Zhu C, Palmer G, Breslin T et al. Diagnosis of breast cancer using fluorescence and diffuse reflectance spectroscopy: a Monte-Carlo-model-based approach. J Biomed Opt 2008; 13: 034015.

6. Ariga R, Bloom K, Reddy V et al. Fine-needle aspiration of clinically suspicious palpable breast masses with histopathologic correlation. Am J Surg 2002; 184 410-413.

7. Burns R, Brown J, Roe S et al. Stereotactic core-needle breast biopsy by surgeons: minimum 2-year follow-up of benign lesions. Ann Surg 2000; 232 542-548.

8. Chaiwun B, Settakorn J, Ya-In C et al. Effectiveness of fine-needle aspiration cytology of breast: analysis of 2,375 cases from northern Thailand. Diagn Cytopathol 2002; 26 201-205.

9. Youk J, Kim E, Kim M et al. Missed breast cancers at US-guided core needle biopsy: how to reduce them. Radiographics 2007; 27: 79-94.

10. Kennedy S, Geradts J, Bydlon T et al. Optical breast cancer margin assessment: an observational study of the effects of tissue heterogeneity on optical contrast. Breast Cancer Res Treat 2010; 12: R91.

11. Vishwanath K, Yuan H, Barry W et al. Using optical spectroscopy to longitudinally monitor physiological changes within solid tumors. Neoplasia 2009; 11 889-900.

12. Volynskaya Z, Haka A, Bechtel K et al. Diagnosing breast cancer using diffuse reflectance spectroscopy and intrinsic fluorescence spectroscopy. J Biomed Opt 2008; 13 024012.

13. Keller M, Majumder S, Kelley M et al. Autofluorescence and diffuse reflectance spectroscopy and spectral imaging for breast surgical margin analysis. Lasers Surg Med 2010; 42 15-23.

14. Brown J, Wilke L, Geradts J et al. Quantitative optical spectroscopy: a robust tool for direct measurement of breast cancer vascular oxygenation and total hemoglobin content in vivo. Cancer Res 2009; 69 2919-2926.

15. Zhu C, Palmer G, Breslin T et al. Diagnosis of breast cancer using diffuse reflectance spectroscopy: Comparison of a Monte Carlo versus partial least squares analysis based feature extraction technique. Lasers Surg Med 2006; 38 714-724.

16. Bigio I, Bown S, Briggs G et al. Diagnosis of breast cancer using elastic-scattering spectroscopy: preliminary clinical results. J Biomed Opt 2000; 5 221-228.

17. Breslin T, Xu F, Palmer G et al. Autofluorescence and diffuse reflectance properties of malignant and benign breast tissues. Ann Surg Oncol 2004; 11 65-70.

18. Nachabé R, Hendriks B, Desjardins A et al. Estimation of lipid and water concentrations in scattering media with diffuse optical spectroscopy from 900 to 1,600 nm. J Biomed Opt 2010; 15 037015.

19. Nachabé R, Hendriks B, van der Voort M et al. Estimation of bilogical chromophores using diffuse optical spectroscopy - benefit of extending the UV-VIS wavelength range to include 1000 to 1600nm. Optics Express 2010; 18: 1432-1442.

20. Nachabé R, Evers D, Hendriks B et al. Diagnosis of breast cancer using diffuse optical spectroscopy from 500 to 1600 nm: a comparison of classification methods. J Biomed Opt 2011; 16: 087010.

21. Farrell T, Patterson M, Wilson B. A diffusion theory model of spatially resolved, steady-state diffuse reflectance for the noninvasive determination of tissue optical properties in vivo. Med Phys 1992; 19: 879-888.

22. Nachabé R, Evers D, Hendriks B et al. Effect of bile absorption coefficients on the estimation of liver tissue optical properties and related complications in discriminating healthy and tumorous samples. Biomed Optics Express 2011; 2: 600-614.

23. Zonios G, Perelman L, Backman V et al. Diffuse reflectance spectroscopy of human adenomatous colon polyps in vivo. Appl Opt 1999; 38: 6628-6637.

24. Breiman L, Friedman J, Olshen R, Stone C. Classification and Regression Trees. Belmont, CA. : Wadsworth Publishing Company 1984.

25. Kruskal W, Wallis W. Use of Ranks in One-Criterion Variance Analysis. Journal of the American Statistical Association 1952; 47: 583-621.

26. Majumder S, Keller M, Boulos F et al. Comparison of autofluorescence, diffuse reflectance, and Raman spectroscopy for breast tissue discrimination. J Biomed Opt 2008; 13 054009.

27. Zhu C, Breslin T, Harter J, Ramanujam N. Model based and empirical spectral analysis for the diagnosis of breast cancer. Biomed Opt Express 2008; 16: 14961-14978.

Chapter 10

Real-time *in vivo* characterization of primary liver tumors with diffuse optical spectroscopy during percutaneous needle interventions

Rami Nachabé

Benno H. W. Hendriks

Ross Schierling

Jasmine Hales

Judy M. Racadio

Drazenko Babic

John M. Racadio

Abstract

This study presents the first *in vivo* real-time tissue characterization during image-guided percutaneous intervention with diffuse optical spectroscopy (DOS) sensing at a tip of a needle with integrated optical fibers. A total of 9 percutaneous needle insertions in three woodchucks with primary hepatocellular carcinoma were performed under 3D fluoroscopy and ultrasound; DOS measurements were continuously acquired during needle insertion and clinically relevant parameters were extracted from the optical data along the needle paths. The derived real-time tissue characterization enabled identification of the tissue type at the needle tip during the transition from healthy liver to tumor tissue. Statistically significant differences in tissue properties between the tumor and the healthy liver enabled discrimination between these two types of tissues. Tissue blood content, oxygenation level, lipid content and tissue density were the main parameters that showed significant differences when the needle tip was guided from healthy tissue to tumor.

1. Introduction

Diffuse optical spectroscopy (DOS) is an emerging technique for real-time tissue characterization. This technique consists of studying the spectral light response after illuminating tissue with a light source. The collected optical spectra are translated into clinically relevant parameters such as blood, water and lipid fractions, tissue oxygenation levels and tissue density related to the scattering of light [1]. In recent research, several advances have been made in integrating optical fibers into needle-like probes for DOS measurements at the distal end of the devices [2-5]. Most of the DOS clinical studies have addressed the diagnostic performance of such a tool in discriminating tumors from normal tissue. These clinical experiments consisted of performing several point measurements at different locations in tumors and healthy tissue. The diagnostic performance of DOS has generally been evaluated by comparing the outcome of a statistical classification with pathology [3, 5] or with diagnostic medical images used as reference [2,3,6]. A few *in vivo* studies have been conducted to demonstrate that DOS measurements enable tissue discrimination [3,4,6]. In most of these cases, image guidance was used to advance the tip of the probe into the region of interest [2,3,6]. Point measurements were then performed at various positions in tumors and in normal tissues. DOS data collected from various patients were gathered together by type of tissue and diagnostic performance in discriminating tumor from normal tissue was thereby evaluated. However, no continuous DOS measurements were performed during the insertion of the needles in the subjects. Continuous measurements are of great relevance during percutaneous procedures, because they enable detection of the transition from healthy tissue to tumor based on the clinical parameters derived from optical spectroscopy. Additionally, continuous measurements provide a profile of the tissue along the needle path yielding data on intra-subject heterogeneity.

To this aim, we applied continuous DOS measurements under 3D fluoroscopy and ultrasound guidance in woodchucks with hepatocellular carcinoma (HCC) tumor to evaluate the added-value of continuous measurements during percutaneous insertions.

2. Materials and methods
2.1. Animal model and handling

In this study, we used three woodchucks with HCC tumor induced by the woodchuck hepatitis virus infection. Similar to hepatitis B virus, the woodchuck hepatitis virus infects the liver, may cause acute and chronic hepatitis and usually leads to development of HCC within three years. The woodchucks were ordered from Northeastern Wildlife Inc. (Harrison, ID, USA) and weighed an average of 2.5 kg. The animals were initially sedated with an intramuscular injection of 5mg/kg of Xylazine (Fort Dodge Labaratories, Fort Dodge, Iowa) and 50mg/kg of Ketamine (Fort Dodge Labaratories, Fort Dodge, Iowa). For intravenous contrast agent administration, a 20 gauge angiocatheter was placed into the femoral vein using direct ultrasound guidance. All procedures in this study followed the guidelines of the Institutional Animal Care and Use Committee of Cincinnati Children Hospital Medical Center and were approved by the ethics committee.

2.2. Needle with sensing capabilities and optical setup

A research prototype setup that allows optical spectroscopy measurements of tissue via optical fibers integrated in a needle was used in this study [7]. In short, the setup includes a light source and two optical spectrometers that enable light detection in the visible and near infrared wavelength range. A custom-made needle is connected to the light source and to both spectrometers via 200 micrometer diameter optical fibers. The 18 gauge needle has a polished angle tip of 70 degrees while the fiber ends were cut straight. The light emitted at the tip of the needle travels through the tissue before reaching the collecting optical fiber and is subject to optical absorption and scattering. The measurement acquisition time per spectrum is 300 ms and an analytical model was used to derive the various physiological and morphological properties from each spectrum. The spectral measurements enable estimation of physiological and morphological information such as biological volume fractions (e.g. blood, water, lipid, bile, etc.), oxygenation level of blood and light scattering due to tissue density using a mathematical model that describes tissue-light interaction [7]. The blood volume fraction corresponds to hemoglobin (oxygenated and deoxygenated) assuming a concentration of 150 g of hemoglobin per liter of plasma. The lipid volume fraction corresponds to a density of 0.86 g/ml.

2.3. Image guidance

The needle insertions were performed under 3D fluoroscopy and ultrasound guidance to advance the tip of the needle into the tumor. Whereas ultrasound is a common imaging technique used for needle guidance, 3D fluorosocopy is a more recent technique that consists of overlaying live X-ray fluoroscopy with cone beam CT (CBCT) [8]. A 3D soft tissue CBCT dataset was acquired after injection of contrast agent (Optiray 350, Covidien) for better visualization of the tumor and the surrounding healthy tissue. From the 3D data set, an optimal CT-like slice with the tumor being clearly visible was selected to define a planned needle path. The needle planning was interactively performed by drawing a line from the center of the tumor towards the skin surface. **Figure 1.A** shows a CBCT image of the tumor within the liver as well as the planned needle path whereas **Figure 1.B** shows the 3D fluoroscopy with the tip of the needle reaching the target. Live fluoroscopy and ultrasound imaging were acquired simultaneously with DOS acquisition in order to assure registration of the tissue characterization with the actual location of the needle tip. A total of 9 insertions were performed in the animals. At the end of the experiment, the liver was excised for gross tissue investigation. A cut-through was performed along the needle path in the tumor to observe the tissue structure.

Real-time in vivo characterization of primary liver tumors with diffuse optical spectroscopy during percutaneous needle interventions
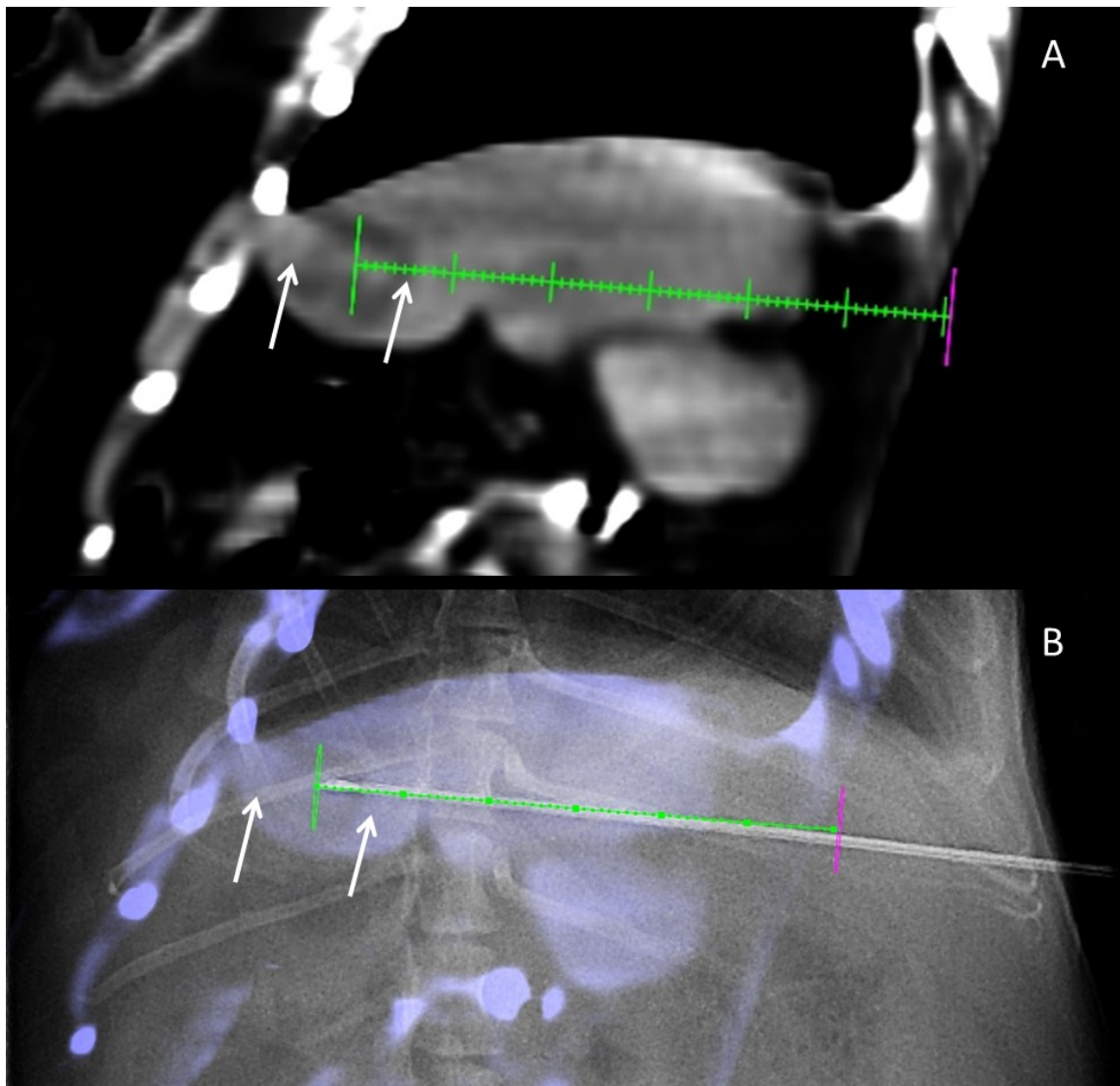
Chapter 10

Figure 1. (A) Cone beam CT slice depicting a virtual needle path (green line) with entry point (magenta marker) defined at the skin surface and the end target in the middle of the round tumor. The small and large dash markers along the virtual line correspond to mm and cm spacing, respectively. The white arrows indicate the boundaries of the tumors along the virtual line (B) Cone beam CT overlayed with live fluoroscopy (i.e. 3D fluoroscopy) demonstrating tumor in liver. The green line corresponds to the virtual needle trajectory. The needle tip is in the center of the tumor

3. Results

When comparing the data acquired within the normal liver tissue and within the tumor from the 9 insertions, statistical differences (P-value < 0.05) were noted for parameters such as blood volume fraction, tissue oxygenation level, lipid volume fraction, and scattering amplitude. The set of boxplots in the top row of **Figure 2** shows that blood and lipid volume fractions and the tissue oxygenation were significantly greater in normal liver as opposed to tumors, whereas the scattering amplitude was greater in tumors than in normal liver tissue. In all reported *in vivo* studies in literature, collective data acquired from all enrolled subjects were statistically compared [3,4,6]. However, it is interesting to

evaluate the statistical differences within one needle insertion. The bottom row of **Figure 2** shows boxplots of the parameters of interest for a single insertion from normal to tumor tissue. It can be seen that the trends are similar to the collective data set. What is interesting to note is the fact that outliers (cross markers in boxplots) for blood and tissue oxygenation values correspond to transition values from one tissue type to another.
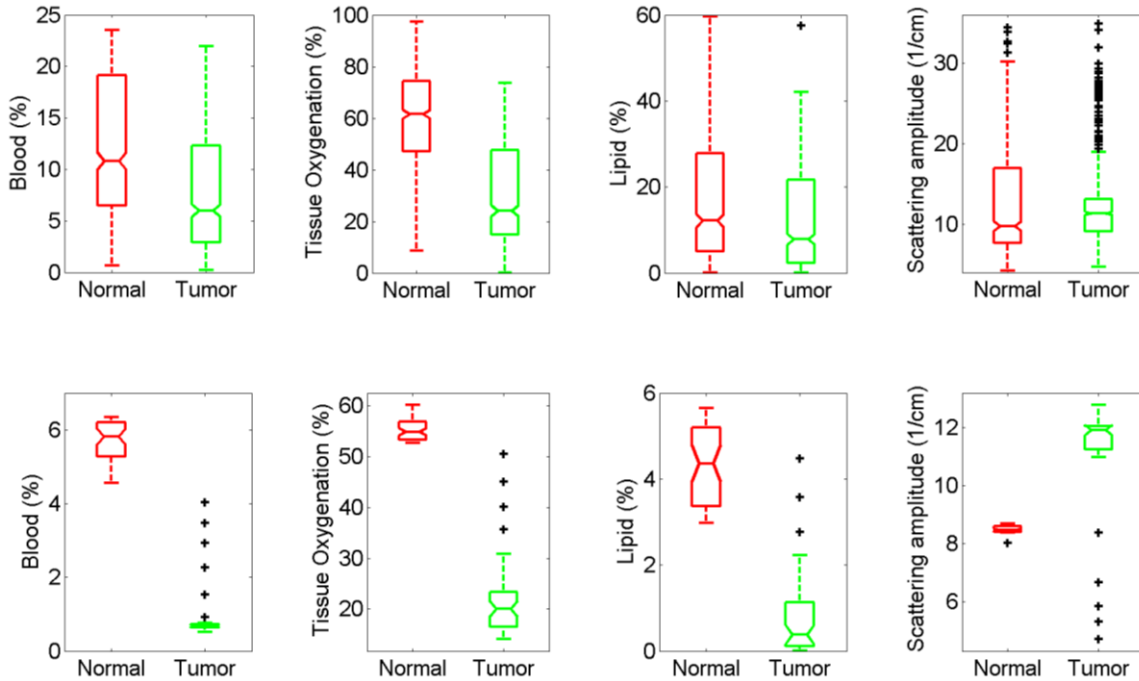
Figure 2. Boxplot of collective data for normal and tumor tissues (top tow) and for a single insertion (bottom row) of blood, lipid volume fractions as well as tissue oxygenation and scattering amplitude.

Figure 3 depicts estimated values of the four derived parameters while inserting the needle from normal to tumor tissue from which the boxplots in the bottom row of **Figure 2** were obtained.
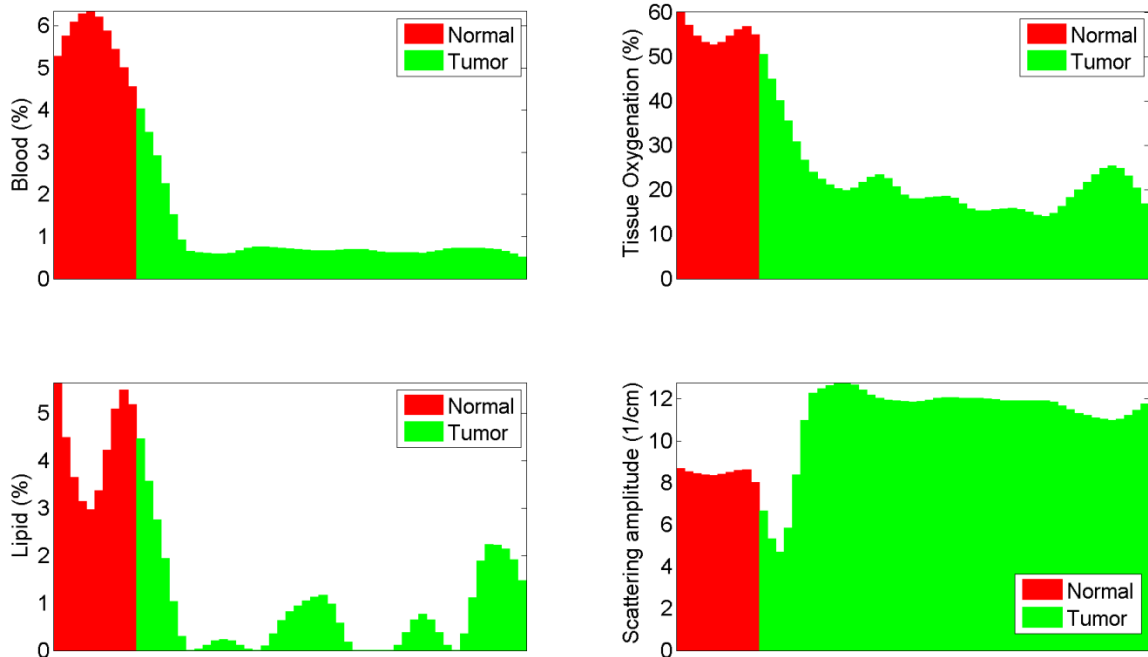
Figure 3. Histogram of blood volume fraction, tissue oxygenation, lipid volume fraction and scattering amplitude derived from DOS measurements when needle being inserted from normal to tumor tissue.

4. Discussion

Several observations can conjointly be drawn from **Figure 2** and **3**. First, the total amount of blood is significantly higher in healthy liver as opposed to tumor tissue. This observation correlates with the macroscopic investigations after tissue resection depicted in **Figure 4**. Second, the oxygenation saturation level of blood is lower in the tumor as compared to the healthy liver. Furthermore, parts of the tumors are hypoxic with oxygenation levels as low as 10%, while regions close to the boundaries have higher oxygenation levels. Third, the lipid volume fractions are very low at the boundaries between the tumor and the healthy liver tissue. Finally, the scattering amplitude of the probed healthy liver tissue is homogeneous whereas it is heterogeneous in the tumor; this correlates with the macroscopic observation shown in **Figure 4** where the tumor tissue has a more granular structure. Additionally, the difference in tissue homogeneity between the tumor and the healthy part of the liver is visible macroscopically on the CBCT images displayed in **Figure 1**. These findings were consistent for all insertions except for one case in which the blood content in tumor was higher than in normal tissue; this was confirmed by ultrasound to be a hemorrhagic part of the tumor.

Figure 4. Photograph of the liver with a cut section through the tumor. The thickness of the tumor is roughly one centimeter as it can also be seen on Figure 1.

To our knowledge, there have been no previous *in vivo* liver tumor DOS studies, although there have been a few *ex vivo* studies demonstrating higher blood content in the healthy liver as compared to tumor; however, care should be taken in interpreting *ex vivo* human studies because the tissue properties can change very quickly after excision of the tissue [9,10]. Moreover, the *ex vivo* studies were done in liver with colorectal metastases whereas the present study addresses primary liver tumors. The comparison of the derived parameters is thus not straightforward. Therefore, this present *in vivo* animal study can be considered as a starting point for future investigational works in discriminating HCC from healthy liver tissue. The *ex vivo* studies available in literature showed higher scattering amplitude as well as lipid, blood and bile content in healthy liver as opposed to tumor. From the results depicted in **Figure 2**, we also demonstrate that blood and lipid content are greater in the healthy part of liver. There was no significant difference in bile content, which is most likely due to the fact that the tumors in our animals are primary tumors and not metastases from other organs; metastases are made of abnormal cells from the organ of origin and therefore no bile is expected in metastases [9].

The existing *in vivo* studies in the literature were mainly performed in breast [3,4] and lung [6]; therefore, only comparisons of physiological parameters (e.g., oxygenation

levels) in our study to these previous studies are valid, and tissue composition comparisons are not. Our results agree with the general reported findings from the *in vivo* human DOS studies that were conducted previously by different research groups [3,4,6]. Most of these studies demonstrated lower oxygenation levels in the tumor and higher scattering amplitude, as did our study.

The information provided by DOS, such as mapping of blood oxygenation levels along the needle path, can be of great relevance in the case of biopsy procedures. Hypoxic tissue is often associated with necrosis and therefore measuring the oxygenation level in tumors can allow the operator to avoid performing a biopsy in a necrotic region that would not allow conclusive tumor staging by pathologists. Hence, relying on the oxygenation level in blood is of great interest in performing biopsies [4].

In the HCC tumor, the estimated lipid volume fraction was non-uniformly distributed, which is expected because HCC is known to be associated with patchy macroscopic fatty change [11]. The scattering amplitude related to tissue density is also heterogeneous in the tumor, whereas it is homogenous in healthy liver. This observation is in agreement with existing findings on stiffness measurements with ultrasound or MR elastography, with tumors being harder than normal liver tissue [12]. Performing continuous measurements during a needle insertion as opposed to single point measurements in the different types of tissues as done in existing studies has the advantage of providing a full overview of the tissue characterization along the needle path to ensure better needle placement for biopsies.

5. Conclusion

In summary, this study shows the potential of real-time tissue characterization by diffuse optical spectroscopy measurements at the tip of a needle during percutaneous intervention. This first *in vivo* liver study using diagnostic imaging as a reference demonstrates that blood content and tissue oxygenation can be used as the primary discriminators for transition from normal tissue to tumor. Lipid content and scattering amplitude provide information on the heterogeneity of tumor tissues along the needle path, which contrasts to the homogeneity of the surrounding normal liver tissue.

References

1. Van Veen RL, Verkruysse W, and Sterenborg HJCM. Diffuse reflectance spectroscopy from 500 to 1060 nm by correction of inhomogeneously distributed absorbers. *Opt Lett.* 2002 Feb; 27(4): 246-248.

2. Rathmell JP, Desjardins AE, van der Voort M et al. Identification of the epidural space with optical spectroscopy: an *in vivo* swine study. *Anesthesiology.* 2010 Dec; 113(6): 1406-1418.

3. Brown JQ, Vishwanath K, Palmer GM et al. Advances in quantitative UV-visible spectroscopy for clinical and pre-clinical application in cancer. *Curr Opin Biotechnol.* 2009 Feb; 20(1): 119-31.

4. Van Veen RL, Amelink A, Menke-Pluymers M, et al. Optical biopsy of breast tissue using differential path-length spectroscopy. *Phys Med Biol.* 2005 Jun; 50(11): 2573-81.

5. Volynskaya Z, Haka AS, Bechtel KL, et al. Diagnosing breast cancer using diffuse reflectance spectroscopy and intrinsic fluorescence spectroscopy. *J Biomed Opt.* 2008 Mar-Apr; 13(2): 024012.

6. Kanick SC, van der Leest C, Djamin RS, et al. Characterization of mediastinal lymph node physiology in vivo by optical spectroscopy during endoscopic ultrasound guided fine needle aspiration. *J Thorac Onco.* 2010 Jul; 5(7): 981-987.

7. Nachabe R, Hendriks BHW, van der Voort M, et al. Estimation of biological chromophores using diffuse optical spectroscopy: benefit of extending the UV-VIS wavelength range to include 1000 to 1600 nm. *Biomed Opt Exp.* 2010 Nov; 1(5): 1432-1442.

8. Racadio JM, Babic D, Homan R, et al. Live 3D guidance in the interventional radiology suite. *AJR Am J Roentgenol.* 2007 Dec.; 189(6):W357-64.

9. Nachabe R, Evers DJ, Hendriks BHW, et al. Effect of bile absorption coefficients on the estimation of liver tissue optical properties and related implications in discriminating healthy and tumorous samples. *Biomed Opt Exp.* 2011 Feb; 2(3): 600-14.

10. Germer GC, Roggan A, Ritz JP, et al. Optical properties of native and coagulated human liver tissue and liver metastases in the near infrared range. *Lasers Surg Med.* 1998; 23(4): 194-203.

11. Prasad SR, Wang H, Rosas H, et al. Fat-containing lesions of the liver: radiologic-pathologic correlation. *Radiographics.* 2005 Mar-Apr; 25(2): 321-331.

12. Mariappan YK, Glaser KJ, and Ehman RL. Magnetic resonance elastography: a review. *Clin Anat.* 2010 Jul; 23(5): 497-511.

General discussion

Several research groups investigated over the last two decades the potential of diffuse optical spectroscopy for specific medical applications such as cancer diagnosis, treatment monitoring and surgery support. The recent technical advances in detectors, gratings, optical fibers and light sources enabled the possibility to perform quasi real-time measurements with miniaturized probes such as needles, endoscopes, catheters and the like.

This dissertation encompasses several research and development works in the field of clinical diagnosis with diffuse optical spectroscopy. Needle-like optical probes with similar characteristics than conventional medical needles were developed in such a way that the optical fibers were integrated in the cannula. Three optical fibers were embedded, one from which light is delivered while the two other fibers are connected to the detection unit composed of silicon and InGaAs detectors, respectively. The InGaAs detectors are relatively new and expensive enabling light detection above a micron wavelength. Formerly, PbS detectors were used to detect light with wavelength above a micron however the sensitivity of such detectors is poor. Other research groups only use silicon detectors due to its low price limiting the light detection to wavelengths below one micron. Therefore, most research groups have only evaluated blood-derived chromophores in the visible and near infrared wavelengths range because these are the man chromophores that have spectral absorption features in wavelength range detectable with silicon detectors. In the beginning of the century, researchers have tried to estimate water and lipid concentrations by trying to measure up to the limit of silicon detection of light roughly around 1100 nm. However, the reliability of the derived water and lipid concentrations could well be not very accurate because of the limitations and sensitivity of silicon detectors. By measuring simultaneously with silicon and InGaAs detectors, we were able to acquire spectra up to 1800 nm with a signal-to-noise ratio above 100:1 enabling accurate absorption coefficients measurement of biological chromophores such as water, lipid and collagen. The determination of absorption coefficients of these chromophores enables their use in mathematical models to derive their concentrations in tissue after spectral measurements with the optical probe. Therefore, the use of an InGaAs detector is relevant for accurate determination of additional biological substances that are not commonly used by other research groups.

The model we used to characterize tissue corresponds to an analytical expression derived from diffusion theory. In this dissertation the first parameterization of diffuse optical spectroscopy measurements over a wavelength range comprising the visible and the near infrared up to 1800 nm is presented. Validation of the method and the mathematical model to derive parameters relevant to the clinician was performed by means of phantoms studies and benchmarking with other existing techniques for biological substances concentration estimation. The validation is performed by comparing

the derived chromophores concentrations from the mathematical model with the actual concentrations in the phantom with known optical properties. The robustness of the model is evaluated by changing the average particles size in the phantom without modifying its content. Such a procedure enables to verify that the model does extract the same concentrations while the scattering properties are being changed. Comparison of quantifying concentrations of certain biological substances with other existing methods is also considered as a guaranty of the reliability of diffuse optical spectroscopy in determining proper values. Validation of the model in deriving the various parameters of interest is an essential and crucial step before interpreting the measurements performed in the clinic as the outcome should help the physician to make the proper diagnosis or make the right decision during a medical procedure. However, using a model derived from the diffusion theory has its limitations. In fact, in order to be applicable the scattering length of the photons i.e. the average distance between two scattering events should be small compared to the source-detector fiber distance. Recently, several studies by various research groups were conducted to model diffuse optical spectroscopy for side-by-side fibers as well as single fiber backscattering configurations. These models are developed based on either phantom measurements or probabilistic-based simulations (e.g., Monte-Carlo) with a wide range of optical properties corresponding to the one expected in tissue. In this dissertation, we have chosen to use probes in which the source-detector fiber distance is large compared to the average scattering length of the photons such that diffusion theory is applicable across the broad wavelength range of interest.

Most of the presented clinical studies in this dissertation were conducted in *ex vivo* settings and therefore the blood derived chromophores might be questionable although measurements were performed immediately after tissue excisions. Nevertheless, extending the wavelength range has clear benefits when comparing with results from other existing *ex vivo* clinical studies available in literature. The first *in vivo* experiments that were performed in animals with primary tumors showed the importance of real-time measurements and data analysis in order to identify the transition of needle placement in a tumor based on the changes in the derived parameters. Additionally, deriving the tissue oxygenation level along the needle path is of great relevance to avoid taking biopsies in hypoxic locations that potentially could be correlated to necrosis.

In this PhD research, several advances have been made with respect to measuring and investigating biological chromophores that are not commonly used in literature. Whereas the main focus of most of the research groups are investigating the difference between normal and dysplastic tissue in blood content and its oxygenation level, the presented preclinical and clinical studies in this dissertation showed that several additional chromophores can be relevant for tissue discrimination yielding better diagnosis performances. Diffuse optical spectroscopy has been widely used for diagnosis in the field of oncology where blood volume fraction, its oxygenation level and the reduced scattering amplitude are the main three derived parameters that allows discrimination of dysplastic and cancerous tissue from normal tissue. Having a wide wavelength range up to 1800 nm showed to be of great relevance for accurate water and

lipid volume fractions estimation. It was shown that proper estimation of water and lipid concentrations can significantly improves diagnosis performances in breast and liver cancer. Therefore, the thorough investigation in understanding which biological substances that could potentially play a role in discriminating abnormal from normal tissue is very important. For instance, bile showed to be a biological chromophore that is significantly higher in healthy liver as opposed to colorectal metastases tumors due to the presence of cancer cells originating from a different organ, hence not containing bile. In opposition, the *in vivo* study in animal with primary tumor showed no significant differences in bile content between normal and tumor samples measurements. However, it was shown that tissue oxygenation is lower in tumors as expected and proven in different *in vivo* studies presented by several research groups.

The main clinical applications addressed in this dissertation are focused on diagnosis but several other clinical applications can be addressed with diffuse optical spectroscopy sensing at the distal end of needle-like fiber optic probes. A wide range of clinical applications have been investigated by several research groups. Two of the topics that have been gaining a lot of interest are chemotherapy monitoring as well as tumor margin assessments. The possibility of measuring up to 1800 nm widens further the scope of clinical applications as it enables to derive many other biological substances that absorb lights in the infrared wavelengths range. In fact, the possibility of accurately quantifying lipid and water shows that diffuse reflectance spectroscopy has a great potential in steatosis quantification and non-alcoholic fatty liver disease diagnosis. This disease is considered to be positively diagnosed if the haptic fat is above 5% only, hence the need of accurate tools for reliable hepatic fat quantification. Diffuse reflectance spectroscopy can be an interesting alternative for magnetic resonance spectroscopy for accurate quantitative fat determination provided that measurements are performed in a very wide wavelength range comprising several fat and water absorption features. The work presented in this dissertation yielded additional clinical investigations addressing specific applications. For example, another clinical application of interest that can be addressed due to the lipid quantification from a broad wavelength range corresponds to epidural space identification. For instance, an *in vivo* study in swine showed the potential of diffuse optical spectroscopy in identifying the epidural space which is a lipid-rich space surrounding the cerebral spine fluid. It was shown that a confirmation of needle placement in the epidural space can be ensured based on the amount of lipid and blood present in the probed volume.

Further investigations in the wavelength ranges above a micron are still required. It has been demonstrated in this dissertation that absorption coefficients of water and lipid are sensitive to temperature and types of triglycerides, respectively. Thus additional research is advised to evaluate the possibility of temperature estimation from the spectral measurements or discriminating different types of fat in tissue. These topics are of a great challenge as the changes are very subtle and thus accurate signal processing is to be envisaged. Other chromophores should also be investigated in the infrared wavelengths

range as there are probably other biological substances that absorb light in the infrared such as for instance collagen as shown in this dissertation.

Ongoing *in vivo* human clinical studies using the technology and methods developed herein should further validate the clinical value in surgical and interventional procedures.

Summary

The goal of this dissertation is to present the potential of diffuse optical spectroscopy technique to characterize and differentiate types of tissue, including dysplastic and cancerous tissues, when measuring the tissue spectra during a surgical or an interventional procedure under medical image guidance.

This dissertation begins with a chapter that describes the different mathematical modeling of light transport in scattering media such as tissue. Each of the existing models used in literature is described including the way to extract the optical properties by applying it to the tissue measurements performed with fiber-optic handheld probes. An overview of the clinical applications investigated by the research groups is given as well as the performance of the diagnosis in discriminating different types of tissue based on the derived parameters.

Chapter 2 and 3 corresponds to the validation of the diffusion theory model applied to optical spectroscopy measurements performed in a wide wavelength range as compared to what has been already presented in literature. In fact, chapter 2 presents the very first validation available in literature of the applicability of diffusion theory approximation model to measurements performed from 900 to 1600 nm. Water and lipid absorption coefficients were measured for different temperatures and used to in the model to derive the concentration of these chromophores. The validation was performed by recovering the actual water and lipid content in custom made emulsions with known lipid content. The validation of the reduced scattering estimation was performed by correlating the estimated parameters related to the reduced scattering with the particles size of the emulsions after blending and investigating the particle size distribution. Chapter 3 presents the advantage of extending the commonly-used wavelength range from 400 to 1000 nm up to 1600 nm. Although water and lipid can be estimated from diffuse optical spectroscopy measurements up to 1000 nm, this chapter shows that the extension of the wavelength significantly improves the accuracy of the optical properties extraction and that the lack of spectral feature of water and lipid when measuring up to 1000 nm can not only yield inaccurate water and lipid content but as well influence the estimated blood concentrations and reduced scattering parameters.

Chapters 4 through 6 present the application of diffuse optical spectroscopy for diagnosis related to liver diseases. Chapter 4 is a benchmarking of optical spectroscopy with other techniques such as magnetic resonance spectroscopy (MRS), nuclear magnetic resonance spectroscopy (NMR), high performance thin layer chromatography (HPTLC) and histopathology for hepatic lipid quantification in mice. The derived hepatic fat fractions in the mice liver did not show any significant differences between the various techniques. Furthermore, it was shown that it was possible to clearly distinguish the group of mice on chow diet from the group of mice on high fat diet. The potential of diffuse

optical spectroscopy in quantifying hepatic lipid is of great interest for diagnosis of fatty liver disease where it is considered to be positive in patients for hepatic lipid fractions as low as 5%. Chapter 5 presents optical spectra acquired *ex vivo* on metastasis in liver and the surrounding healthy liver tissue in 14 patients. This chapter demonstrates the importance of including bile absorption coefficients to the model in addition to oxygenated-hemoglobin (HbO_2), deoxygenated hemoglobin (Hb), water and lipid as livers are rich in bile ducts. This study shows that it is possible to discriminate tumors from the surrounding healthy liver tissue based on the amount of bile, water and the reduced scattering amplitude. Chapter 6 describes the diagnosis performance of diffuse optical spectroscopy in discriminating the tumors from the healthy liver samples with two different methods: classifying the types of tissues using the derived clinical parameters from fitting the diffusion theory mathematical model to the measurements as well as applying a statistical method to classify the raw optical measurements. In this chapter, in addition to discriminating tumors from healthy tissue, the lipid content estimated with diffuse optical spectroscopy showed a strong correlation with hepatic fat estimation from the histological slides. These findings ultimately have impact on detecting tumors when performing a biopsy as well as defining the steatosis level in liver.

Chapter 7 demonstrates the capability of diffuse optical spectroscopy in discriminating tumor sites from the surrounding healthy lung tissues. An *ex vivo* study was conducted in samples excised from 10 patients with lung cancer. This study showed that hemoglobin volume fraction and the reduced scattering amplitude showed significant difference in both type of tissue by being lower in tumors as compared to the healthy lung sites. Additionally, the performance of diagnosis to discriminate the tumors from the healthy lung samples was evaluated and yielded sensitivity and specificity up to 86% and 85%, respectively.

Chapters 8 and 9 demonstrate the potential of diffuse optical spectroscopy to classify several types of breast tissues including malignant types. Chapter 8 corresponds to an *ex vivo* study on 54 excised breast samples that were measured at 5 different sites, namely adipose, glandular, fibroadenoma, invasive carcinoma and ductal carcinoma *in situ*. From the various optical parameters that are derived from the measurements and the chromophores volume fractions, statistical tests were performed to investigate which parameter shows significant difference between pairwise types of tissue. Furthermore, the performance of diagnosis in discriminating the 5 types of tissue yielded area under receiver operator curve (AUC) ranging from 86% to 100%. Additionally, the performance of classifying benign and malignant samples was made with different types of classification methods that were already applied by various research groups that conducted optical spectroscopy measurements on breast samples. The different classification schemes were compared and it was shown that the performance of the diagnosis can vary a lot depending on the type of classification that is used. Therefore this chapter emphasizes the importance of being very critical when selecting the classification scheme. Chapter 9 shows the differences in investigating the difference in optical properties and measurements between malignant and non-malignant tissue by comparing

intra and inter-patients variations. It was concluded that the diagnosis performance is best when comparing the tissues within single patients as compared to when all data from all patients are compared.

Chapter 10 presents the feasibility of real-time tissue characterization during needle insertions from healthy liver to hepatocellular carcinoma tumor where medical imaging such as 3D fluoroscopy and ultrasound were used as reference. Whereas in literature point measurements in healthy and in tumors are compared, this study shows that continuous diffuse reflectance measurements while advancing the needle enables the identification of the tumor boundaries based on the derived clinical parameter, namely blood oxygenation and volume fraction as well as the scattering amplitude.

Samenvatting

Het onderzoeksdoel van dit proefschrift is vaststellen in hoeverre diffuse optische spectroscopie gebruikt kan worden om verschillende weefsels, waaronder displastisch en kankerweefsel, van elkaar te onderscheiden tijdens chirurgische of onder beeldgeleiding uitgevoerde ingrepen.

In hoofdstuk 1 worden verschillende mathematische modellen uit de literatuur besproken die optische verstrooiingsparameters extraheren uit spectra die gemeten zijn met handzame op glasvezel gebaseerde meetinstrumenten. Tevens wordt er een overzicht gegeven van de klinische toepassingen die door de verschillende onderzoeksgroepen hiermee onderzocht zijn, evenals de behaalde nauwkeurigheid in onderscheidend vermogen van deze methodes.

In hoofdstuk 2 en 3 van dit proefschrift wordt de validatie van het diffusie theorie model onderzocht wanneer deze toegepast wordt op een groter golflengte gebied dan tot dus ver beschreven in de literatuur. Hoofdstuk 2 beschrijft voor het eerst de toepassing van het diffusie model voor het golflengte gebied van 900 tot 1600 nm. Water en vet absorptiecoëfficiënten zijn gemeten voor verschillende temperaturen en vervolgens gebruikt als invoerparameters in het model om de concentraties van deze chromoforen uit de gemeten spectra te bepalen. Dit model is vervolgens gevalideerd door verschillende water en vet emulsies met bekende vet concentraties te meten. De validatie van de gereduceerde verstrooiingscoëfficiënt is gebeurd door de voorspelde vetdeeltjesgrootte in de emulsies na menging te vergelijken met de gemeten deeltjesgrootte verdeling. Hoofdstuk 3 gaat in op het voordeel dat de uitbreiding van het golflengte gebied tot 1600 nm geeft vergeleken met de steeds gebruikte golflengte gebied van 400 nm tot 1000 nm. Hoewel vet en water concentraties ook geschat kunnen worden op basis van het spectrum tot 1000 nm laat dit onderzoeksdeel zien dat de uitbreiding van het golflengte gebied leidt tot een nauwkeurigere bepaling van deze parameters. Daarnaast wordt ook aangetoond dat de beperkte spectrale karakteristieken van water en vet in het golflengte gebied tot 1000 nm niet alleen leiden tot een onnauwkeurige schatting van water en vet concentratie maar dat ook de verstrooiingsparameters en bloedconcentratie schattingen nadelig beïnvloed worden.

In de hoofdstukken 4 tot en met 6 worden de toepassingen van de diffuse optische spectroscopie op leverziekten besproken. In hoofdstuk 4 wordt optische spectroscopie vergeleken met andere technieken zoals magnetische resonantie spectroscopie (MRS), nucleaire magnetische resonantie spectroscopie (NMR), hoge prestatie dunne laag chromatografie (HPTLC) en histopathologie op vetgehalte bepaling in muizenlevers. De verschillende technieken vertoonde geen significante verschillen tussen de bepaalde lever vetfracties. Verder wordt aangetoond dat het mogelijk is de groep muizen op chow voeding te onderscheiden van de groep muizen op voeding met hoog vetgehalte.

Kwantificeren van levervet met diffuse optische spectroscopie is van groot belang voor de diagnose van leververvetting waarbij patiënten met een vetpercentage van meer dan 5% al als positief beschouwd worden. In hoofdstuk 5 worden *ex vivo* spectroscopische meting aan uitgezaaide dikke darm tumoren in de lever van 14 patiënten besproken. In dit hoofdstuk wordt het belang van het toevoegen van gal aan de lijst van absorberende stoffen in de lever, waar galproductie plaatsvindt, naast die van oxyhemoglobine (HbO_2), desoxyhemoglobine (Hb), water en vet aangetoond. Deze studie laat zien dat het mogelijk is om deze uitgezaaide kankergezwellen te onderscheiden van normaal leverweefsel op basis van de gemeten hoeveelheid gal, water en de gereduceerde verstrooiingscoëfficiënt. Hoofdstuk 6 beschrijft het diagnostische vermogen van diffuse optische spectroscopie om lever kankergezwellen van normaal leverweefsel te onderscheiden waarbij twee onderzoeksmethoden gebruikt zijn: classificatie op basis van de bepaalde optische parameters door het diffusie theorie model te fitten aan de spectra alsook door een statistische classificatie methode toe te passen op de ruwe optische metingen. Daarnaast is in dit hoofdstuk ook gekeken naar het vetgehalte in de lever bepaalt uit de optische metingen en dit vergeleken met de vetgehalte schatting op basis van pathologisch gekleurde weefselcoupes, hetgeen een goede correlatie liet zien. Beide bevindingen zijn waardevol, daar ze het biopteren van kankergezwellen kunnen verbeteren en tevens de risico's bij levertransplantaties kunnen verkleinen door snel en nauwkeurig de steatose graad van de lever te bepalen.

Hoofdstuk 7 laat de mogelijkheden van diffuse optische spectroscopie zien bij het onderscheiden van kankergezwellen in longweefsel. Een *ex vivo* studie werd uitgevoerd aan weefselmonsters van 10 patiënten met longkanker. Dit onderzoek toonde aan dat de hemoglobine concentratie en gereduceerde verstrooiingsamplitude significant verschilden in het kankerweefsel vergeleken met het omringende normale weefsel. De sensitiviteit en specificiteit waarmee longkankergezwellen van normaal longweefsel onderscheiden kunnen worden, zijn respectievelijk 86% en 85%.

In hoofdstukken 8 en 9 wordt onderzocht in hoeverre met diffuse optische spectroscopie verschillende vormen van borstweefsels, inclusief borstkankergezwellen, te onderscheiden zijn. Hoofdstuk 8 bespreekt een *ex vivo* studie aan 54 verwijderde borstkankergezwellen waarbij aan 5 verschillende soorten weefsels metingen verricht zijn, namelijk aan vetweefsel, klierweefsel, fibroadenomen, invasieve carcinomen en ductaal carcinoma's *in situ*. Door statistische proeven uit te voeren aan de verschillende geëxtraheerde optische parameters is bepaald welke parameters significante verschillen opleveren tussen de verschillende weefseltypes. Bovendien is het onderscheidend vermogen waarmee de 5 weefseltypes van elkaar te onderscheiden zijn bepaald door het oppervlak onder de "receiver operator curve" (AUC) te berekenen, dat varieerde van 86% tot 100%. Daarnaast is het onderscheidend vermogen om kwaadaardige kankergezwellen van normaal en goedaardig afwijkend weefsel bepaald met behulp van verschillende soorten classificatie methoden die al door diverse onderzoeksgroepen, die optische spectroscopie metingen uitvoeren, gehanteerd zijn. Bij het vergelijken van de verschillende classificatiemethoden volgde dat het onderscheidend vermogen afhankelijk

is van de gekozen methode. Het is dus van belang om een zorgvuldige keuze van de classificatiemethode te maken. In hoofdstuk 9 is gekeken in hoeverre het onderscheiden van kwaadaardige kankergezwellen van normaal en goedaardige gezwellen in borstweefsel met diffuse optische spectroscopie beïnvloed wordt door de variaties die er zijn tussen verschillende patiënten. Geconcludeerd kon worden dat het onderscheidend vermogen beter wordt bij het vergelijken van de weefsels binnen één patiënt in vergelijking met wanneer de gegevens van alle patiënten gezamenlijk vergeleken wordt.

In hoofdstuk 10 is onderzocht wat de toegevoegde waarde is van real-time optische weefsel karakterisering tijdens medische naald interventies in combinatie met medische beeldvorming zoals röntgen doorlichting en echografie. Vooral naald interventies aan primaire lever tumoren in bosmarmotten zijn daarbij onderzocht. Terwijl tot dusver in de literatuur puntmetingen in gezond weefsel en kankerweefsel vergeleken worden, blijkt uit deze studie dat continue diffuse optische reflectie metingen het opsporen van de kankergezwelgrenzen op basis van de waarden van bloed concentratie, bloedoxygenatie en verstrooiing amplitude duidelijk verbeterd.

Scientific output

Publications:

Rami Nachabé, Benno H. W. Hendriks, Adrien E. Desjardins, Marjolein van der Voort, Martin B. van der Mark, and Henricus J. C. M. Sterenborg. "Estimation of lipid and water concentrations in scattering media with diffuse optical spectroscopy from 900 to 1600 nm", *Journal of Biomedical Optics* **15**: 037015, May 2010. (*Chapter 2 of this thesis*)

Rami Nachabé, Benno H. W. Hendriks, Marjolein van der Voort, Adrien E. Desjardins, and Henricus J. C. M. Sterenborg. "Estimation of biological chromophores using diffuse optical spectroscopy: benefit of extending the UV-VIS wavelength range to include 1000 to 1600 nm", *Biomedical Optics Express* **18**: 1432-1442, November 2010. (*Chapter 3 of this thesis*)

James P. Rathmell, Adrien E. Desjardins, Marjolein van der Voort, Benno H. W. Hendriks, **Rami Nachabé**, Stefan Roggeveen, Drazenko Babic, Michael Söderman, Marcus Brynolf, and Björn Holmström. "Identification of the epidural space with optical spectroscopy-An in vivo swine study", *Anesthesiology* **113**: 1406-1418, December 2010.

Rami Nachabé, Daniel J. Evers, Benno H. W. Hendriks, Gerald W. Lucassen, Marjolein van der Voort, Jelle Wesseling, and Theo J. M. Ruers. "Effect of bile absorption coefficients on the estimation of liver tissue optical properties and related implications in discriminating healthy and tumorous samples", *Biomedical Optics Express* **2**: 600-614, March 2011. (*Chapter 5 of this thesis*)

Adrien E. Desjardins, Benno H. W. Hendriks, Marjolein van der Voort, **Rami Nachabé**, Walter Bierhoff, Guus Braun, Drazenko Babic, James P. Rathmell, Staffan Holmin, Michael Söderman, and Björn Holmström, "Epidural needle with embedded optical fibers for spectroscopic differentiation of tissue: *ex vivo* feasibility study", *Biomedical Optics Express* **2**: 1452-1461, June 2011.

Rami Nachabé, Daniel J. Evers, Benno H. W. Hendriks, Gerald W. Lucassen, Marjolein van der Voort, Emiel K. Rutgers, Marie-Jeanne Peeters, Jos A. ven der Hage, Hester S. Oldenburg, Jelle Wesseling, and Theo J. M. Ruers, "Diagnosis of breast cancer using diffuse optical spectroscopy from 500 to 1600 nm: comparison of classification methods", *Journal of Biomedical Optics* **16** (8): 087010 August 2011. (*Chapter 8 of this thesis*)

Rami Nachabé, José W. A. van der Hoorn, Roland van de Molengraaf, Rolf Lamerichs, Jeroen Pikkemaat, Charles F. Sio, Benno H. W. Hendriks, and Henricus J. C. M. Sterenborg, "Validation of interventional fiber optics spectroscopy with MR spectroscopy, MAS-NMR spectroscopy, high performance thin layer chomatography and histpathology for accurate fat quantification", *Investigative Radiology* **47**(4): 209-216, April 2012. *(Chapter 4 of this thesis)*

Daniel J. Evers, **Rami Nachabé**, Houke M. Klomp, Johanna W. van Sandick, Michel W. Wouters, Gerald W. Lucassen, Benno H. W. Hendriks, Jelle Wesseling, and Theo J. M. Ruers, "Diffuse reflectance spectroscopy: a new guidance tool for improvement of biopsy procedures in lung malignancies", *Accepted for publication in Clinical Lung Cancer in March 2012. (Chapter 7 of this thesis)*

Rami Nachabé, Benno H. W. Hendriks, Henricus J. C. M. Sterenborg, "Modeling diffuse reflectance spectroscopy: a review", *Submitted to Journal of Biomedical Optics in December 2011. (Chapter 1 of this thesis)*

Daniel J. Evers, **Rami Nachabé**, Daphne Hompes, Frits van Coevorden, Gerald W. Lucassen, Benno H. W. Hendriks, Loes van Velthuizen, Jelle Wesseling, and Theo J. M. Ruers, "Diffuse reflectance spectroscopy for the discrimination of liver tumors and steatosis quantification", *Submitted to Annals of Surgical Oncology in February 2012. (Chapter 6 of this thesis)*

Rami Nachabé, Benno H. W. Hendriks, Ross Schierling, Jasmine Hales, Judy M. Racadio, Drazenko Babic, , and John M. Racadio, "Real-time *in vivo* characterization of primary liver tumors with diffuse optical spectroscopy during percutaneous needle interventions", *Submitted to American Journal of Roentgenology in March 2012. (Chapter 10 of this thesis)*

Daniel J. Evers, **Rami Nachabé**, Emiel J. Rutgers, Marie-Jeanne Vrancken Peeters, Jos A. van der Hage, Hester S. Oldenburg, Gerald W. Lucassen, Benno H. W. Hendriks, Jelle Wesseling, and Theo J. M. Ruers, "Diffuse reflectance spectroscopy for real time imaging of tumor tissue in liver", *Submitted to Breast Cancer Research and Treatment in April 2012. (Chapter 9 of this thesis)*

Conference proceedings:
Rami Nachabé, Rik Harbers, Adrien E. Desjardins, Marjolein van der Voort, Guus A. L. Braun, and Benno H. W. Hendriks, "Extracting optical properties from diffuse optical spectroscopy", *Proc. SPIE* **7187**, 71871C (2009).

Rami Nachabé, Benno H. W. Hendriks, and H. J. C. M. Sterenborg, "Determination of water and lipid concentrations by diffuse optical spectroscopy in lipid emulsions in the wavelength range of 1000 to 1500 nm" in *Biomedical Optics*, OSA paper BTuD88 (2010).

Conference presentations:

Rami Nachabé, Rik Harbers, Adrien E. Desjardins, Marjolein van der Voort, Guus A. L. Braun, and Benno H. W. Hendriks, "Extracting optical properties from diffuse optical spectroscopy", SPIE Photonics West , January 2009, San José, California, USA, Poster presentation.

Rami Nachabé, Benno H. W. Hendriks, and H. J. C. M. Sterenborg, "Determination of water and lipid concentrations by diffuse optical spectroscopy in lipid emulsions in the wavelength range of 1000 to 1500 nm" OSA Biomedical Optics, April 2010, Miami, Florida, USA, Poster presentation.

Rami Nachabé, Benno H. W. Hendriks, Marjolein van der Voort, Adrien E. Desjardins, Martin M. B. Van der Mark, and Henricus J. C. M. Sterenborg, "Estimation of chromophore concentrations with diffuse optical spectroscopy in the near infrared wavelength range up to 1600 nm" SPIE Photonics West, January 2011, San Francisco, California, USA, Poster presentation.

Rami Nachabé, "UV/VIS/NIR spectroscopy *In Vivo*", Fotonica Evenement, March 2011, Nieuwegein, The Netherlands, Oral presentation.

José W. van der Hoorn, Roland van de Molengraaf, **Rami Nachabé**, Marijn Vlaming, Charles F. Sio, Rolf Lamerichs, Jeroen De Groot, Oliver C. Steinbach, "*In vivo* MRS analysis of Non-Alcoholic Fatty Liver Disease in a translational model for the metabolic syndrome", XVII International DALM symposium on Diabetes, Obesity, and the Metabolic Syndrome, March 2011, Doha, Qatar, Poster presentation.

José W. van der Hoorn, Roland van de Molengraaf, **Rami Nachabé**, Jeroen Pikkemaat, Marijn Vlaming, Charles F. Sio, Rolf Lamerichs, Jeroen De Groot, Oliver C. Steinbach, "*In vivo* MRS analysis of Non-Alcoholic Fatty Liver Disease in a translational model for the metabolic syndrome", 6th European Molecular Imaging Meeting, June 2011, Leiden, The Netherlands, Poster presentation.

Rami Nachabé, Daniel J. Evers, G. W. Lucassen, Benno H. W. Hendriks, J. Wesseling, and Theo J. M. Ruers, "Tissue composition estimated with an interventional fiber optical probe during liver tissue resection", European Multidisciplinary Cancer Congress, September 2011, Stockholm, Sweden, Oral presentation.

José W. van der Hoorn, Roland van de Molengraaf, **Rami Nachabé**, Jeroen Pikkemaat, Marijn Vlaming, Charles F. Sio, Rolf Lamerichs, Jeroen De Groot, Oliver C. Steinbach, "*In vivo* MRS analysis of Non-Alcoholic Fatty Liver Disease in a translational model for the metabolic syndrome", World Molecular Imaging Congress, September 2011, San Diego, California, USA, Poster presentation.

Marjolein van der Voort, Arthur Adams, Jurgen E. Mourik, Willem Mali, Tim Nielsen, Martin B. Van der Mark, Daniel J. Evers, **Rami Nachabé**, Gerald W. Lucassen, Benno H. W. Hendriks, Jelle Wesseling, and Theo J. M. Ruers, "Optical spectroscopy for the detection of breast cancer", 4th Annual World Cancer Congress of Breast Cancer, November 2011, Guangzhou, China, Oral presentation.

Rami Nachabé, Benno H. W. Hendriks, Ross Schierling, Jasmine Hales, Judy M. Racadio, Drazenko Babic, , and John M. Racadio, "Real-time *in vivo* characterization of primary liver tumors with diffuse optical spectroscopy during percutaneous needle interventions", Society for Pediatric Radiology 55th annual meetings and postgraduate course, April 2012, San Francisco, California, USA, Oral presentation.

Curriculum Vitae

Rami Nachabé is born 30th August 1983 in Lebanon. He obtained his bachelor in Mathematics and Physics from the Université de Nice-Sophia Antipolis in 2003 and obtained in 2006 his Master degree in Physics from Université Louis Pasteur in Strasbourg as well as an Engineering degree in medical imaging and robotics. During his studies, he performed several internships related to optical simulations such as in the LSIIT laboratory in Strasbourg (2004) where he had to write a code to compute light scattering from rough surfaces; and at Sony in Stuttgart (2005) where he programmed an algorithm to compute grating diffractions of electromagnetic fields. He performed his master degree project at Philips Research within the biomedical photonics group (2006) where he implemented an algorithm for signal and image processing of protein bindings in assays imaged with fluorescence confocal microscopy. In 2007, he worked as an imaging scientist within the CTO department of Philips Healthcare in Best, the Netherlands. He conducted several phantoms studies, reconstruction code integration and clinical studies within an optical mammography project. In 2008, he started his PhD fellowship in Philips Research within the minimally invasive healthcare group. His work was conducted under the supervision of Dr. Benno Hendriks from Philips Research and Prof. Dr. Henricus Sterenborg from Erasmus Medical Center in Rotterdam. During the course of his PhD period, he started with the understanding of the fundamentals of diffuse optical spectroscopy. He developed and validated mathematical models to derive clinically relevant parameters and subsequently gained experience in experimenting, writing papers and collaborating with clinical staff such as surgeons, radiologists, anesthesiologists, pathologists, etc. Rami spent the last half year of his PhD period at Cincinnati Children's Hospital Medical Center in the USA where he was working with the interventional radiology department in an animal lab equipped with a Philips FD-20 flat detector C-arm. He learned from this period how to write protocols, perform experimental procedures in an interventional radiology room as well as brainstorming with interventional radiologists on new ways of performing procedures.

Acknowledgements

It has been a long journey and I would have never reached the final destination without an incredible crew full of talent.

First of all, I would like to express my gratitude to Dr. Benno Hendriks thanks to whom I managed to succeed in my work. Dear Benno, without your guidance and your diligent supervision of my work, I honestly think that I could have never reached the scientific level I have now. You have been an outstanding mentor and I learned so much from you. Besides the professional relation we had together, the private relation was fantastic. I also would like to thank you for always being on my side when needed and providing me with the right advice. I am truly proud of working for a genuine person like you and I am sure that our adventure will continue. You are simply my role model for whom I have blind trust.

I would like to thank Professor Dr. Henricus Sterenborg. Dear Dick, being a PhD student of one of the most famous persons in the field of biomedical spectroscopy is a big honor. Thank you for the challenging scientific discussions we had. Your very critical view to my results and your way of trying to pull the best out of my research was very useful. The several discussions I had with you helped me a lot in being efficient at work.

I would also like to thank the members of the radiotherapy department at Erasmus Medical Center, namely Dr. Arjen Amelink and Dr. Stephen Kanick for the technical discussions we had about diffuse spectroscopy as well as for providing me with very insightful information on writing scientific publications.

Furthermore, I would like to express my gratitude to the former and current members of the so-called "photonic needle" project. In the beginning, I worked with Guus the needle master, Adrien from whom I learned to write scientific papers, Rik my friend and lab teacher, Leon who has been a great coach, and Marjolein the first person who taught me how to set up clinical experiments. In a later stage of the project, Gerald joined us and I discovered a great person that was always of great support. Dear Gerald, I always see myself in you as a worker and as a person as well. You have been of a great support! Stefan joined at the same period and he was so fun to work with as well as Walter the man with the gold fingers. Although she joined for a very short time, I would definitely like to thank my friend Joyce Henselmans. Thanks Joyce for the great moments we had! During the last period of my PhD, several members: Jeroen, Jasper, Manfred, Susanne, Christian, Vishnu, Arnold, Antonie, Geert and Florian. Thanks guys for the team spirit!

Additionally, I want to thank my colleagues from the "Minimally Invasive Healthcare" group in Philips Research, especially the wild scientist Dr. Martin van der Mark, Gert 't Hooft known as the walking encyclopedia, and Erik Harks my office mate, confident and Dutch teacher.

not work a lot with you, I can assure you that I had a lot of fun at every single moment we spent together and I am sure there is still more to come.

Special thanks to all the co-authors of the publications we had during my PhD period: Dr. Rathmell from Massachussetts General Hospital, Dr. Brynolf from Karolinska Institute; Dr. Wesseling, Dr. Rutgers, Dr. Peeters, Dr. Van der Hage, Dr. Oldenburg, Dr. Klomp, Dr. Van Sandick, Dr. Wouters, Dr. Hompes, Dr. van Coevorden, and Dr. Van Velthuizen from the Dutch Cancer Institute; Dr. van der Hoorn from TNO; Dr. Molengraaf, Dr. Lamerichs, Dr. Pikkemaat, and Dr. Sio from Philips Research; and Dr. Judy Racadio from Cincinnati Children's Hospital Medical Center.

Et le meilleur pour la fin. Je tiens à remercier mes amis de toujours; notamment, Thomas, Oriane, Nicolas, Jordi, Olga, Sébastien, et Marangai. Je voudrais remercier tout particulièrement mes frangins et mes parents sans qui rien n'aurait été possible. Merci pour les valeurs transmises et l'éducation reçue. Sachez que malgré la distance qui nous sépare, vous avez toujours étaient tout proche de mon cœur. Maman, papa, je vous adore énormément!

« Eduque-toi mon fils car si un homme averti en vaut deux, un homme instruit en vaut trois », 3 février 2012.

Rami Nachabé.